Fermilab FERMILAB-THESIS-2002-06

THE UNIVERSITY OF CHICAGO

MEASUREMENTS OF DIRECT CP-VIOLATION AND CPT-INVARIANCE IN THE NEUTRAL KAON SYSTEM

A DISSERTATION SUBMITTED TO
THE FACULTY OF THE DIVISION OF THE PHYSICAL SCIENCES
IN CANDIDACY FOR THE DEGREE OF
DOCTOR OF PHILOSOPHY

DEPARTMENT OF PHYSICS

BY
VALMIKI PRASAD

CHICAGO, ILLINOIS
JUNE 2002

Copyright © 2002 by Valmiki Prasad
All rights reserved

TABLE OF CONTENTS

LIST OF FIGURES ix

LIST OF TABLES xiv

ACKNOWLEDGEMENTS xvi

ABSTRACT xix

1 INTRODUCTION 1
- 1.1 Understanding CP-Violation 3
  - 1.1.1 Theoretical Progress 3
  - 1.1.2 Experimental Progress 5
- 1.2 Outline of Thesis 7
- 1.3 Kaon Phenomenology 8
  - 1.3.1 CP-violation in neutral $K \to 2\pi$ decays 12
  - 1.3.2 CPT Conservation 13
  - 1.3.3 CPT Violation 15
  - 1.3.4 Predictions of CPT Conservation 17

2 EXPERIMENTAL TECHNIQUE 19
- 2.1 The KTeV Technique 20
  - 2.1.1 The Double Beam Technique 20
  - 2.1.2 K_L and K_S Production 21
  - 2.1.3 Regeneration and Its Usefulness 22
- 2.2 Alternate Methods of Measuring $Re(\epsilon'/\epsilon)$ 29

3 KTEV EXPERIMENTAL APPARATUS 31
- 3.1 The Beamline 31
  - 3.1.1 Primary Beam and Target 31
  - 3.1.2 Secondary Beam 33
- 3.2 The KTeV Detector 35
- 3.3 Regenerator 36
- 3.4 Charged Spectrometer 38
  - 3.4.1 Drift Chambers 38
  - 3.4.2 Analysis Magnet 40
  - 3.4.3 Calibration and Alignment 40
- 3.5 Cesium Iodide Calorimeter 41

3.6 Trigger and Veto Counters 41
3.6.1 The Mask Anti 41
3.6.2 The Collar Anti 41
3.6.3 Trigger Hodoscopes 43
3.6.4 Ring Counters and Spectrometer Antis 43
3.6.5 The Back Anti, Hadron Anti and Muon Counters 44
3.7 Trigger and Data Acquisition 46

4 CSI CALORIMETER 48
4.1 Crystals 48
4.2 Readout 53
4.2.1 Photomultiplier tubes (PMTs) 53
4.2.2 Digitization 55
4.3 Cosmic Ray Hodoscope 62
4.4 Laser System 65
4.5 Energy Calibration and Cluster Reconstruction 70
4.5.1 Cluster Reconstruction 70
4.5.2 Energy Calibration 89
4.6 Effect of Radiation on Performance of CsI Crystals 93

5 DATA COLLECTION 101
5.1 Data Periods 101
5.2 Problems during Data-taking 102
5.2.1 Drift Chambers 103
5.2.2 Calorimeter-related problems 103
5.2.3 Other Problems 105
5.3 Data Samples used in this Dissertation 105

6 ANALYSIS AND RECONSTRUCTION OF $K_{L,S} \to \pi^+\pi^-$ DECAYS 108
6.1 Trigger Requirements 108
6.1.1 Level 1 108
6.1.2 Level 2 109
6.1.3 Level 3 109
6.2 Offline Reconstruction 110
6.3 Analysis Cuts 115
6.3.1 Data Quality Cuts 115
6.3.2 Reconstruction Cuts 115
6.3.3 Background Suppression Cuts 116
6.3.4 Apertures 119
6.3.5 Fiducial cuts 120
6.4 Charged Mode Background 121
6.4.1 Background Subtraction 123

6.4.2 Final $\pi^+\pi^-$ Background Levels 128
6.5 Total event counts 130

7 ANALYSIS AND RECONSTRUCTION OF $K_{L,S} \to \pi^0\pi^0$ DECAYS 133
7.1 Trigger Requirements 133
7.1.1 Level 1 133
7.1.2 Level 2 134
7.1.3 Level 3 138
7.2 Reconstruction of $K_{L,S} \to \pi^0\pi^0$ events 139
7.2.1 Photon Energy and Position Reconstruction 140
7.2.2 Reconstruction of Kaon Kinematic Variables 140
7.3 Data-Monte Carlo Neutral Mode Energy Scale Difference 144
7.3.1 Effect of Neutral Mode Energy Scale on $Re(\epsilon'/\epsilon)$ 147
7.4 Analysis Cuts 151
7.4.1 Common $K_{L,S} \to \pi^0\pi^0$ and $K_{L,S} \to \pi^+\pi^-$ Cuts 152
7.4.2 Kinematic and Event Quality Cuts 153
7.4.3 Background-suppression Cuts 153
7.4.4 Aperture Cuts 158
7.5 Background Subtraction 158
7.5.1 Sources of Background 159
7.5.2 Background Normalization and Subtraction 161
7.5.3 Final $\pi^0\pi^0$ Background Levels 164
7.6 Total Event Counts 166

8 THE MONTE CARLO SIMULATION 169
8.1 Introduction to Monte Carlo in KTeV 169
8.2 Kaon Production, Evolution, Decay and Transport 171
8.2.1 Kaon Production 171
8.2.2 Kaon Transport 171
8.2.3 Kaon Evolution 173
8.2.4 Kaon Decay 173
8.3 Accidentals 174
8.4 Simulation of the Trigger and Detector 175
8.4.1 Drift Chambers 175
8.4.2 Calorimeter 178
8.4.3 Trigger 186
8.4.4 Veto, Trigger and Aperture Elements 189
8.5 Generation of Monte Carlo Samples 191
8.6 Monte Carlo Samples 193

9 SYSTEMATIC UNCERTAINTIES IN $K_{L,S} \to \pi^0\pi^0$ AND $K_{L,S} \to \pi^+\pi^-$ DECAYS 194
9.1 General Comments . . . 194
9.2 Neutral Mode Systematic Studies . . . 195
9.2.1 Triggers . . . 195
9.2.2 Analysis Cuts . . . 196
9.2.3 Energy Scale . . . 201
9.2.4 CsI Reconstruction and Energy Resolution . . . 203
9.2.5 Acceptance . . . 204
9.2.6 Calorimeter Size and CsI Position Bias . . . 206
9.2.7 Apertures . . . 206
9.2.8 Background . . . 208
9.2.9 Accidentals . . . 212
9.2.10 Summary of Neutral Mode Systematic Errors . . . 213
9.3 Charged Mode Systematic Studies . . . 213
9.3.1 Triggers . . . 213
9.3.2 Drift Chamber Simulation . . . 214
9.3.3 DC Resolution . . . 214
9.3.4 Momentum Scale . . . 214
9.3.5 Acceptance . . . 215
9.3.6 Analysis Cuts . . . 215
9.3.7 Detector Alignment and Calibration . . . 217
9.3.8 Limiting Apertures . . . 217
9.3.9 Background Subtraction . . . 218
9.3.10 Summary of Charged Mode Systematic Errors . . . 218

10 DETERMINATION OF $RE(\epsilon'/\epsilon)$ 221
10.1 Extracting $Re(\epsilon'/\epsilon)$ . . . 221
10.1.1 The Prediction Function . . . 222
10.1.2 The Acceptance and Fit to Data . . . 224
10.1.3 Fitting Parameters . . . 225
10.2 Systematic Errors due to the Fit . . . 226
10.3 Total Systematic Error . . . 227
10.4 $Re(\epsilon'/\epsilon)$ Fit Result . . . 229
10.5 Cross-checks of $Re(\epsilon'/\epsilon)$ Measurement . . . 231
10.5.1 Reweighting Analysis . . . 234
10.6 Measurement of Other Physics Parameters . . . 235
10.6.1 Measurement of Δm and τ_S in the Neutral Mode . . . 235
10.6.2 Measurement of $\Delta\phi$ . . . 239

11 CONCLUSION 243
11.1 Measurement of $Re(\epsilon'/\epsilon)$ 243
11.1.1 Re-analysis of KTeV Published $Re(\epsilon'/\epsilon)$ Result 244
11.1.2 Discussion of $Re(\epsilon'/\epsilon)$ Measurements and Theoretical Predictions 245
11.2 KTeV Measurements of $\Delta\phi$, Δm and τ_S 246
11.3 Concluding Remarks on CP-violation 250

A COMMENTS ON THE RECONSTRUCTION OF ELECTROMAGNETIC CLUSTERS 253
A.1 Cluster Position Lookups 253
A.2 Transverse Energy Lookups 254
A.3 Readout threshold correction 254
A.4 Treatment of Close Clusters 255
A.5 Sneaky Energy 257
A.6 Linearity Correction 258

B NEUTRAL MODE ENERGY SCALE SYSTEMATICS STUDIES 259
B.1 Decay Modes used in Neutral Mode Energy Scale Study 259
B.1.1 Hadronic Interactions at the Regenerator 259
B.1.2 $K_L \to \pi^0\pi^0\pi^0$ Decays 260
B.1.3 $K^* \to \pi^0 + K_S$ Decays at the Regenerator 260
B.1.4 Hadronic Interactions in the Vacuum Window Region 263
B.1.5 $K_L \to \pi^+\pi^-\pi^0$ Decays 263
B.1.6 $\eta \to \pi^0\pi^0\pi^0$ at the Vacuum Window 265
B.1.7 $K_{L,S} \to \pi^0\pi^0$ Dalitz Decays 268
B.2 Data-Monte Carlo Energy Scale Comparisons 268
B.3 Assignment of Systematic Uncertainty 271

C STUDIES OF ENERGY AND POSITION RECONSTRUCTION IN THE NEUTRAL MODE 274
C.1 Data-Monte Carlo Reconstruction Differences 274
C.2 Determining the Effect on $Re(\epsilon'/\epsilon)$ of Data-Monte Carlo Reconstruction Differences 281
C.2.1 Cluster Reconstruction near the Holes 284
C.3 Systematic Uncertainty due to Energy and Position Mis-reconstruction in $K_{L,S} \to \pi^0\pi^0$ Events 295

REFERENCES 297

Ad Majoram ARSENAL Gloriam !

LIST OF FIGURES

1.1 Experimental Measurements of $Re(\epsilon'/\epsilon)$ before June 2001 6
1.2 Geometric Representation of Relationship between η_{+-}, η_{00},ϵ and ϵ' in the Complex Plane. 17

3.1 KTeV Secondary Beamline 32
3.2 KTeV Collimation System 34
3.3 $K_L \rightarrow \pi^0\pi^0\pi^0$ Centre-of-Energy Distributions at the calorimeter for vacuum beam data 35
3.4 Plan View of the KTeV Detector 36
3.5 Final Regenerator Module 38
3.6 Drift Chamber Cell Geometry and Track Separation Cut "Cell" . . . 39
3.7 Geometry of Mask-Anti (MA) 42
3.8 The Collar-Anti 43
3.9 The Trigger Hodoscopes 44
3.10 The Back-Anti, Hadron-Anti and Muon Systems 45

4.1 Cross-sectional View of the CsI Calorimeter 49
4.2 CsI Longitudinal Response With and Without Reflective Wrapping. . 50
4.3 KTeV Readout System 54
4.4 Expected Nonlinearity and Rate Dependance of CsI PMTs 56
4.5 DPMT Block Diagram 57
4.6 FADC Response versus Input Charge in Intime-Slice. 59
4.7 A Transverse Cosmic-Ray Event in the CsI Calorimeter. 63
4.8 The Cosmic Ray Hodoscope 64
4.9 CsI ADC Distribution for Transverse-going Cosmic Ray Muons 65
4.10 Laser System used for CsI Monitoring 67
4.11 Deviations from a Linear Charge Response Before and After DPMT Calibration. 68
4.12 Average CsI Gain Drift versus Absolute Spill in 1997 69
4.13 Definition of Clusters near the Holes 72
4.14 Electron E/p resolution near the CsI Beam Holes 78
4.15 Effect of Readout Threshold Correction on K_{e3} Electron Energy Linearity. 79
4.16 Mean Energy Response Relative to an 8 GeV Photon Shower 83
4.17 Effect of Longitudinal Uniformity Correction on K_{e3} Electron Energy Linearity. 84

4.18 Transverse Variation of K_{e3} Electron Energy Response Within a CsI Block . . . 85
4.19 Tranverse Variation of Fraction of $e^{\pm}$ Energy within a Nominal Cluster 86
4.20 E/p Resolution for K_{e3} Electrons With and Without Transverse Non-uniformity Correction . . . 87
4.21 K_{e3} Electron E/p Linearity in Individual Channels . . . 88
4.22 $e^{\pm}$ Energy Linearity for Different Charge Integration Periods . . . 92
4.23 Electron Energy Resolution and Linearity in 1997 . . . 94
4.24 Change in CsI Gain vs Radiation Dose . . . 95
4.25 Change in $e^{\pm}$ E/p resolution after Average Radiation Dose of 2 krad 95
4.26 Variation in the Total Radiation Dose Over the CsI Calorimeter . . . 96
4.27 Change in CsI Longitudinal Uniformity after Irradiation . . . 98
4.28 Longitudinal Response of a Typical Crystal at the Start of Data-Taking and After 2.3 krad of Radiation . . . 99
4.29 Longitudinal Response of a Highly Radiation-sensitive Crystal at the Start of Data-Taking and After 5.2 krad of Radiation . . . 100

5.1 Data-Taking Periods in KTeV . . . 102
5.2 Cesium Iodide Calorimeter Online Monitoring Display . . . 106

6.1 Event Display for a $K_{L,S} \to \pi^+\pi^-$ Event . . . 113
6.2 Definition of p_T^2 in the Charged Mode Analysis . . . 114
6.3 Vertex χ^2 Distributions for Vacuum and Regenerator Beam $\pi^+\pi^-$ Data Before Background-Subtraction . . . 116
6.4 $K_{L,S} \to \pi^+\pi^-$ p_T^2 distributions for Vacuum and Regenerator Beam Data Before Background-subtraction . . . 118
6.5 $K_{L,S} \to \pi^+\pi^-$ invariant $\pi^+\pi^-$ mass distributions for Vacuum and Regenerator Beam Data Before Background-subtraction . . . 120
6.6 x- and y-positions of the Vacuum Beam $K_{L,S} \to \pi^+\pi^-$ Decay Vertex projected back to z-position of the Defining Collimator for Data Events 125
6.7 p_T^2 v $m_{\pi^+\pi^-}$ Distribution for $K_{L,S} \to \pi^+\pi^-$ Data Events before Background-subtraction . . . 127
6.8 $K_{L,S} \to \pi^+\pi^-$ p_T^2 distributions for Vacuum and Regenerator Beam Data Before Background-subtraction with Normalized Background Components overlaid . . . 129
6.9 Vacuum and Regenerator Beam Kaon Vertex z-position Distributions for 1997 $\pi^+\pi^-$ Data after all Analysis Cuts and Background Subtraction 131
6.10 Vacuum and Regenerator Beam Kaon Energy Distributions for 1997 $\pi^+\pi^-$ Data after all Analysis Cuts and Background Subtraction . . . 132

7.1 Layout of ET and HCC System . . . 134
7.2 E-Total Trigger Efficiency vs Total Energy in the Calorimeter . . . 135
7.3 Distribution of HCC Thresholds in 1997. . . . 137

7.4 Effect of Dynode Pulse Timing on HCC Bit Efficiency 138
7.5 A $K_{L,S} \to \pi^0\pi^0$ Event. 141
7.6 Kaon Vertex Reconstruction of a $K_{L,S} \to \pi^0\pi^0$ Decay 143
7.7 Data and Monte Carlo $K_{L,S} \to \pi^0\pi^0$ Reconstructed z-vertex at the Regenerator Before and After Applying Final Energy Scale 146
7.8 Data-Monte Carlo Difference in Regenerator Downstream Edge z-position Before Edge Matching vs Kaon Energy. 148
7.9 Energy Scale Used to Match the $K_{L,S} \to \pi^0\pi^0$ Data and Monte Carlo Regenerator Edge Distributions 150
7.10 Pairing χ^2 Distributions for 1997 $2\pi^0$ Data before Background Subtraction 154
7.11 Comparison of Maximum χ^2_{shape} Distributions in $2\pi^0$ Data after Background Subtraction and $3\pi^0$ Background Monte Carlo 155
7.12 Vacuum and Regenerator Beam $\pi^0\pi^0$ Invariant Mass Distributions in 1997 $2\pi^0$ Data Before Background Subtraction 156
7.13 Ring Number Distributions for 1997 $2\pi^0$ Data before Background Subtraction 157
7.14 Vertex Distribution for $K_L \to 3\pi^0$ Background 159
7.15 Vacuum and Regenerator Beam Neutral Mode Ring Number Distributions in 1997 163
7.16 Vacuum and Regenerator Beam $\pi^0\pi^0$ Invariant Mass Distributions for 1997 Data and Background 165
7.17 Vacuum and Regenerator Beam Kaon Energy Distributions for 1997 $K_{L,S} \to \pi^0\pi^0$ Data 167
7.18 Vacuum and Regenerator Beam Kaon Vertex z-position Distributions for 1997 $\pi^0\pi^0$ Data 168

8.1 The Effect of Common Absorber Scatters in $2\pi^0$ Events 172
8.2 Missing Hit Probability for DC1X Plane 1 176
8.3 Vacuum Beam p_T^2 Distribution for $\pi^+\pi^-$ Events for data and Monte Carlo with and without Maps and Accidentals 177
8.4 Monte Carlo Electromagnetic Shower Position Bins 179
8.5 Data and Monte Carlo Energy Resolutions before Smearing in Monte Carlo 180
8.6 The Effect of CsI Longitudinal Response Simulation on Energy Linearity and Resolution 183
8.7 Fraction of Cluster Energy in Central Block With and Without CsI Longitudinal Response Simulation 184
8.8 1997 Monte Carlo K_{e3} Electron E/p Linearity Before Calibration . . 187
8.9 HCC Bit Efficiency for a Channel in 1997 189
8.10 HCC Bit Efficiency for a Channel with High Energy HCC Inefficiencies in 1996 190

9.1 Study of $Re(\epsilon'/\epsilon)$ Bias due to HCC Thresholds 197
9.2 Variation of the Neutral Mode Single Ratio versus the Minimum Photon Energy Cut in 1997 198
9.3 Data-Monte Carlo Comparison of Ring Number in $K_{L,S} \to \pi^0\pi^0$ Events in 1997 200
9.4 Data-Monte Carlo Difference in the Reconstructed Vertex Z-Position for Various Modes as a Function of Z-Vertex 202
9.5 Data-Monte Carlo $z_{2\pi^0}$ Distributions for Hadronic Interactions at the Vacuum Window 203
9.6 Data-Monte Carlo Comparison of z_K Distributions in $K_{L,S} \to \pi^0\pi^0$ and $K_L \to \pi^0\pi^0\pi^0$ Events 207
9.7 Comparison of Data and p_T^2 Fit in $K_{L,S} \to \pi^+\pi^-$ Events 211
9.8 Data-Monte Carlo Comparison of z_K Distributions in $K_{L,S} \to \pi^+\pi^-$ and $K_L \to \pi^\pm e^\mp \nu$ Events 216

10.1 The Effect of Interference of K_L and K_S Amplitudes 222
10.2 Variation of $Re(\epsilon'/\epsilon)$ as a Function of Kaon Energy for the 1997 Neutral and 1997b Charged Data Sets. 232
10.3 Cross-checks of $Re(\epsilon'/\epsilon)$ Measurement 233
10.4 Vacuum and Regenerator Beam $K_{L,S} \to \pi^0\pi^0$ Events before and after Event Reweighting 236

11.1 Comparison of KTeV $Re(\epsilon'/\epsilon)$ Measurement with Other Recent Measurements 245
11.2 Comparison of KTeV Δm Measurement with Other Measurements . . 248
11.3 Comparison of KTeV τ_S Measurement with Other Measurements . . . 249
11.4 Comparison of KTeV $\Delta\phi$ Measurement with Other Measurements . . 250
11.5 Comparison of KTeV Measurements of ϵ'/ϵ with other Measurements 252

A.1 Total Energy Below Readout Threshold/Cluster in 1996 and 1997 K_{e3} Data 256
A.2 Transverse Energy Distribution of Electron Shower 257

B.1 Comparison of Regenerator "Junk" and $K_{L,S} \to \pi^0\pi^0$ Data Distributions 261
B.2 Comparison of Minimum Photon Separation Distributions between "Junk" and $K_{L,S} \to \pi^0\pi^0$ Data. 262
B.3 Comparison of Vacuum Window "junk" and $K_{L,S} \to \pi^0\pi^0$ Data Distributions 264
B.4 Variation of the π^0 Mass with Charged Vertex Position in $K_L \to \pi^+\pi^-\pi^0$ Decays 266
B.5 Distributions of 1997 $K_L \to \pi^+\pi^-\pi^0$ Data Events in the Vacuum Beam 267

C.1 Variation of Kaon Mass with Kaon Energy 275

C.2 Variation of Kaon Mass with Kaon Vertex Z-position 276
C.3 Kaon Mass Variation with Photon Angle 277
C.4 Variation of Kaon Mass with Minimum Photon Separation 278
C.5 Kaon Mass versus Kaon Energy in $2\pi^0$ Events 285
C.6 Variation of Kaon mass versus Kaon Energy for $2\pi^0$ Events in 1997 . 286
C.7 Kaon Mass versus z_K for Distortions based on Shower Mean 287
C.8 Kaon Mass vs z_K for Distortions based on Overlapping Photons . . . 288
C.9 Kaon mass vs Minimum Photon Separation for Distortions based on Shower Mean 289
C.10 Kaon Mass vs Minimum Photon Separation for Distortions based on Overlapping Photons 290
C.11 Data-Monte Carlo Regenerator Edge Position and z_K-agreement for $2\pi^0$ Events 291
C.12 $2\pi^0$ Data-Monte Carlo Regenerator Edge and z_K-agreement for Shower Mean-based Distortions 292
C.13 $2\pi^0$ Data-Monte Carlo Regenerator Edge and z_K-agreement for Energy-Nonlinearity-based Distortions 293

LIST OF TABLES

4.1 Energy and Charge Ranges covered by each QIE Exponent. The ranges vary slightly from channel. 58
4.2 Photon Illumination in $2\pi^0$ Vacuum and Regenerator Beam Events . 73

6.1 Background Levels for the $K_{L,S} \to \pi^+\pi^-$ Events 128
6.2 Number of Background-subtracted $K_{L,S} \to \pi^+\pi^-$ Events in 1997 Data 130

7.1 Change in $Re(\epsilon'/\epsilon)$ due to Energy Scale Correction of 0.9993 149
7.2 Neutral Mode Analysis Efficiency for Selected Cuts in 1997 151
7.3 Background Normalization Factors with respect to Data for the $K_{L,S} \to \pi^0\pi^0$ Events in 1997 161
7.4 Background Levels for the $K_{L,S} \to \pi^0\pi^0$ Events in 1996 and 1997 . . 166
7.5 Number of background-subtracted $K_{L,S} \to \pi^0\pi^0$ events in the 1996 and 1996 dataset 166

8.1 Statistics for coherent $K \to \pi^0\pi^0$ and $K \to \pi^+\pi^-$ Monte Carlo samples. 193

9.1 Dependance of $Re(\epsilon'/\epsilon)$ on Minimum Photon Energy cut 197
9.2 Dependance of $Re(\epsilon'/\epsilon)$ on $\chi^2_{\pi^0}$ 200
9.3 Systematic Errors due to Background in the $K_{L,S} \to \pi^0\pi^0$ Analysis. . 209
9.4 Systematic Uncertainties on $Re(\epsilon'/\epsilon)$ from the $K_{L,S} \to \pi^0\pi^0$ Analysis 219
9.5 Systematic and Monte Carlo Statistical Errors on $Re(\epsilon'/\epsilon)$ in $K_{L,S} \to \pi^+\pi^-$ Events 220

10.1 Table of systematic errors on $Re(\epsilon'/\epsilon)$ for the COMBINED 1996 and 1997 analyses. 228
10.2 Table of systematic errors on $Re(\epsilon'/\epsilon)$ for the 1996 neutral and 1997a charged mode analyses. 229
10.3 Table of systematic errors on $Re(\epsilon'/\epsilon)$ for the neutral mode 1997 and charged mode 1997b analyses. 230
10.4 $Re(\epsilon'/\epsilon)$ Fit Results 231
10.5 Summary of systematic uncertainties on Δm and τ_S in the $K_{L,S} \to \pi^0\pi^0$ mode 238
10.6 Systematic Errors on $\Delta\phi$ 241

11.1 Some recent theoretical predictions of $Re(\epsilon'/\epsilon)$ 246

B.1 Usefulness and Drawbacks of Using Various Modes to Study Neutral Mode Energy Scale 269

C.1 Study of CsI Reconstruction near the Beam Holes 294
C.2 Effect of Reconstruction Distortions on $Re(\epsilon'/\epsilon)$ in 1997 296

ACKNOWLEDGEMENTS

First and foremost, my gratitude goes to my advisor, Ed Blucher. I am very grateful for his patience, understanding, wisdom and close friendship during the last seven years. Learning from him has truly been a wonderful experience.

I am grateful to Nari Mistry for having started me off on the exciting path of experimental physics several years ago. His training and advice have proven essential over the years. I also thank Bruce Winstein for sharing his insight and understanding of physics and Yau Wah for many interesting discussions.

I owe a huge debt of gratitude to my fellow students who have made the Chicago KTeV group a stimulating and fun place to work in. I thank Jim Graham, my friend and fellow student in this analysis, for all his help and friendship through the years. I wish him the best for the future. Thanks also to Peter Shawhan, Colin Bown, Greg Graham, Breese Quinn, Steve Bright, Eric Zimmerman, Elizabeth Turner and Miguel Barrio for all their help with the analysis as well as for their company. I am grateful for having had such a lively and exciting group of fellow students to work with.

I am also grateful to Rick Kessler for teaching me a whole variety of things, from performing a thorough analysis to carrying lead bricks; Aaron Roodman for introducing me to the wonders of the calorimeter; Sasha Glazov for many stimulating and important physics discussions and Elliott Cheu for teaching me how to write good analysis code and spell correctly !

The success of the KTeV experiment was due to the hard work of several fine people. I thank them all. My KTeV experience would never have been the same without the cesium iodide calorimeter. For having put up with my endless stream of questions and helping build a superb detector, I am grateful to Peter Shanahan, Julie Whitmore, Hogan Nguyen, Bob Tschirhart and Sydney Taegar.

For helping me navigate through the difficulties of graduate school and dissertation writing as painlessly as possible, I am grateful to Nobuko McNeill, Aspasia Sotir-Plutis and Marty Dippel.

I would never have been able to survive graduate school without the support of many close friends, all of whom I am very grateful to. I mention only a few of them: I thank Pia Negandhi, Atul Kumar, Katja and Konstantin Gavrilov, Kavita and Rajesh Krishnan, Samir and Sujay Parekh, Michael Eastwood, Alexis Amadon, Yogen Rajah, Filip Sain, Siva Kasiraja, Jennifer Allen, Navinder Singh, V.Ramana and Tony Olson for tolerating my frustration, sharing my joys, putting up with my idiosyncracies and keeping me sane and balanced during the last seven years. To Sarah Sellergren, what can I say after all these years ? Her support, friendship, company, love and hospitality have kept me going in the most difficult of times. I am very grateful to her for having made the last few years so pleasant.

I thank my brother, Vyasa, and sisters, Vidya and Elaine, for their love and encouragement as well as for keeping me responsible. Finally, I thank my parents and my grandparents without whose love, faith and undying support, this work would have been impossible.

ABSTRACT

We present a measurement of the CP-violating parameter, $Re(\epsilon'/\epsilon)$, by the KTeV experiment at Fermilab. Using the 1996 and 1997 E832 datasets, we measured $Re(\epsilon'/\epsilon)$ to be $(20.7 \pm 1.6(stat) \pm 2.4(syst)) \times 10^{-4}$. This result demonstrates the existence of direct CP-violation. We also present measurements of the phase difference between η_{+-} and η_{00}, $\Delta\phi \equiv \phi_{00} - \phi_{+-}$, the $K_L - K_S$ mass difference, Δm, and the K_S lifetime, τ_S. Our measurement of $\Delta\phi = (0.41 \pm 0.22(stat) \pm 0.48(syst))^\circ$ is consistent with CPT conservation. Δm and τ_S were determined to be $\Delta m = (5262 \pm 15(stat + syst)) \times 10^6 \hbar s^{-1}$ and $\tau_S = (8965 \pm 6(stat + syst)) \times 10^{-14} s$.

CHAPTER 1
INTRODUCTION

The concept of symmetry has been an important part of science and art for over two thousand years with the search for symmetries often driving the creative aspects of both artistic and scientific endeavour. There are many examples of symmetries such as geometrical, spatial and even literary but in all cases, it refers to a regularity of form under certain transformations. Symmetry considerations are important in several scientific areas including developmental and evolutionary biology [1], chemistry [2] [3], and mathematics [3].

There are also many examples of symmetry in art forms with some of the more spectacular architectural and artistic representations of decorative symmetry and periodicity found in the medieval Islamic art forms [4] and the work of M.C.Escher [5]. Although many artists prefer to describe their work as beautiful and harmonious rather than "symmetrical" or "regular", the role of symmetry in art had already been recognised by Albrecht Dürer in 1528 in his extensive work "De symmetria partium".

With symmetry playing such an important role in the scientific and creative pursuit, it is not surprising that physics in the 20th century was largely motivated by the ideas of symmetry as well. The concept of symmetry in physics is important because it relates to how physical laws behave under certain transformations. For example, a physical law which obeys a certain symmetry is invariant under the respective symmetry transformation. Since symmetries are so closely related to the behaviour of physical laws, recognizing and understanding symmetries leads to a fundamental understanding of nature.

The symmetries in physics that are most relevant to this thesis are those that involve particle-antiparticle exchange (C), spatial inversion (P) and time-reversal (T). Since this thesis is concerned with the invariance principles related to the C, P and T transformations, we shall discuss the history and development of the C, P and

T symmetries in physics to understand how these symmetry principles were first recognized and applied.

Time-reversal (T) invariance was recognized in the late 1870s and it was shown by Boltzmann [6] that classical electrodynamics was T-invariant. Although the classical equations of motion themselves were T-invariant, time-reversal symmetry was rarely exploited until 1932, when Wigner showed that the "Kramers degeneracy" [7] was a result of T-invariance in quantum theory.

The invariance of fundamental physical laws under spatial inversion or the parity transformation was also suggested by Wigner [9]. In order to explain the observation that there were two non-overlapping subsets of energy levels of iron atoms by Laporte [10] in 1924, Wigner realised that the two subsets were of opposite parity. Wigner introduced the parity operator, P, and parity conservation, and also realised that the parity operation is a quantum mechanical one.

Charge-conjugation (C-) invariance is also inherently non-classical as it requires the existence of anti-particles and thus is only consistent in a quantum theory. Soon after the discovery of the first anti-particle, Heisenberg [11] proposed that nature was invariant under the interchange of particles and anti-particles. This proposition was later described in the language of C-conjugation by Kramers [12] in 1937.

The consequences of C-, P- and T-invariance led to the prediction of several results in particle and nuclear physics culminating in the development of the CPT-theorem [13] [14] [15]. The CPT-theorem, which requires that interactions be invariant under the combined operations of C, P and T, is based on the basic structure of quantum field theory in terms of local field operators, proper Lorentz invariance and the requirement that all real observables be Hermitian products of field operators. It is a fundamental prediction of quantum field theory and predicts that the particle and anti-particle have identical masses, decay lifetimes and magnetic moments.

While the early part of 20th Century physics was involved with the development and application of C-, P- and T-invariance of the physical laws, the latter 44 years of the century have been concerned with the observation and understanding of how these symmetries are broken. In 1956, experiments [16] [17] [18] showed that parity symmetry was maximally violated by weak interactions. These experiments demon-

strating parity violation also showed discovery of parity violation in weak interactions also showed that C-symmetry was violated [19]. Although the breaking of C- and P-symmetries was not expected, shortly before the discovery of C- and P-violation, Landau [20] and Yang [21] had proposed that even if C- and P- were violated, the combination of C and P, CP, could still be a good symmetry. However, in 1964, the observation of the decay of the long-lived neutral kaon to two charged pions [22] suggested that the weak interaction exhibited a small CP-violation. The observation of the coherence of long- and short-lived neutral kaons a year later by Fitch *et al.* [23] removed any doubt that the CP symmetry was indeed being broken in weak interactions.

Having observed CP-violation, it was conceivable (though discomforting) that even CPT-symmetry could be broken. However, despite many stringent searches for CPT-violation, CPT-invariance has continued to hold true.

1.1 Understanding CP-Violation

Since the discovery of CP-violation about 35 years ago, much effort has gone into investigating the nature of the CP-violation both theoretically and experimentally.

1.1.1 Theoretical Progress

The theoretical work on CP-violation focussed on describing CP-violation in the kaon sector, understanding how CP-violation could be included into the gauge theories, predicting the amount of CP-violation in other (non-kaon) sectors, and exploring the importance of CP-violation in cosmology. We briefly touch upon these theoretical directions.

Soon after the first observation of CP-violation by Christenson *et. al.* [22] in 1964, there was a considerable theoretical work [24] on laying out the formalism for describing CP-violation in the kaon sector. It was shown that CP-violation in the kaon sector could proceed through an "indirect" channel due to the asymmetric mixing of CP eigenstates and/or a "direct" channel due to CP-violation in the decay amplitude.

The existence of direct CP-violation would mean that there is a difference between the partial decay rates of particles and anti-particles.

Once CP-violation had been discovered, there were many attempts to accommodate it in gauge theories. Very soon after the announcement of the observation of CP-violation, Wolfenstein [25] proposed the existence of a superweak force, $\sim 10^{-9}$ weaker than the weak force to explain the origin of CP-violation in neutral kaons. Since it was hypothesised that this superweak force only led to CP-violation by causing an asymmetric mixing of CP eigenstates, the observation of direct CP-violation would "kill" the "superweak force" hypothesis.

It was also predicted that the breaking of the Higgs symmetry could lead to the occurrence of CP-violation in gauge theories. In the Standard Model, CP-violation is allowed by including a non-zero complex phase in the CKM quark-mixing matrix [26]. Both direct and indirect CP-violation are predicted by the Standard Model. Indirect CP-violation is described by the asymmetric mixing of particle and anti-particle states and is represented by a "box" diagram, while direct CP-violation required a penguin diagram contribution [27].

The inclusion of CP-violation into gauge theories also allowed theorists to investigate the possibility of CP-violation in other sectors such as in B- and D-mesons. In recent years, the B-sector has become a focus for studies in CP-violation.

The importance of CP-violation in cosmology was first demonstrated by Sakharov [28] in 1967 when he described CP-violation as one of the necessary conditions for baryogenesis. It was also shown by Peccei [29] and others that CP-violation in the kaon sector was probably unrelated to the matter-antimatter asymmetry in the early universe and was too small to account for it. New models for CP-violation during baryogenesis continue to be an area of active theoretical investigation.

Despite the theoretical effort in understanding CP-violation, there has been no clear, quantitative explanation of either the origin of CP-violation or the experimentally observed level of CP-violation.

1.1.2 Experimental Progress

The discovery of CP-violation in 1964 led to a series of experiments to study CP-violation in the kaon sector as well as more recently searches for CP-violating effects in other sectors such as in the B-system.

There were many elegant experiments that set out to determine the nature of CP-violation in kaons. While there were experiments that investigated CP-violation in $K \to 2\pi$ decays, there were also measurements which studied CP-violating effects in semileptonic and non-2π final states. Since this thesis is concerned with CP-noninvariance in $K \to 2\pi$ decays, we briefly describe the experimental progress in understanding CP-violation in this decay channel.

By measuring the ratio of CP-violating to CP-conserving decays in the $2\pi^0$ and $\pi^+\pi^-$ final states [30], it was shown early on that the CP-violation in kaons was mainly due to the asymmetric mixing of CP eigenstates.

Although indirect CP-violation had been observed in the kaon sector, it was difficult to detect direct CP-violation since the effect was expected to be 10^{-4} to 10^{-3} times smaller than indirect CP-violation. Experimentally, direct CP-violation in the kaon sector was measured by the parameter, $Re(\epsilon'/\epsilon)$. As described in Section 1.3, a non-zero value of $Re(\epsilon'/\epsilon)$ is an unambiguous signal of direct CP-violation.

Although there were several experiments which searched for direct CP-violation, it was only in the early 90s that experiments were within reach of measuring a non-zero value of $Re(\epsilon'/\epsilon)$. The results of the NA31 experiment at CERN and the E731 experiment at Fermilab both measured $Re(\epsilon'/\epsilon)$ with a precision of $\sim 6\times 10^{-4}$ as shown in Figure 1.1. However, while the NA31 result [31], $Re(\epsilon'/\epsilon) = (23 \pm 6.5) \times 10^{-4}$, showed that $Re(\epsilon'/\epsilon)$ was non-zero at the 3.5σ level, the E731 result [32], $Re(\epsilon'/\epsilon) = (7.4 \pm 5.9) \times 10^{-4}$, was consistent with $Re(\epsilon'/\epsilon) = 0$. In order to resolve this difference, two new experiments, KTeV at Fermilab and NA48 at CERN, were designed. The published results from KTeV [34], $Re(\epsilon'/\epsilon) = (28.0 \pm 4.1) \times 10^{-4}$, and NA48, $Re(\epsilon'/\epsilon) = (15.3 \pm 2.6) \times 10^{-4}$, both showed that $Re(\epsilon'/\epsilon)$ is non-zero and hence, there is CP-violation in the kaon decay amplitudes. The results also proved unambiguously that Wolfenstein's superweak force [25] is not solely responsible for CP-violation.

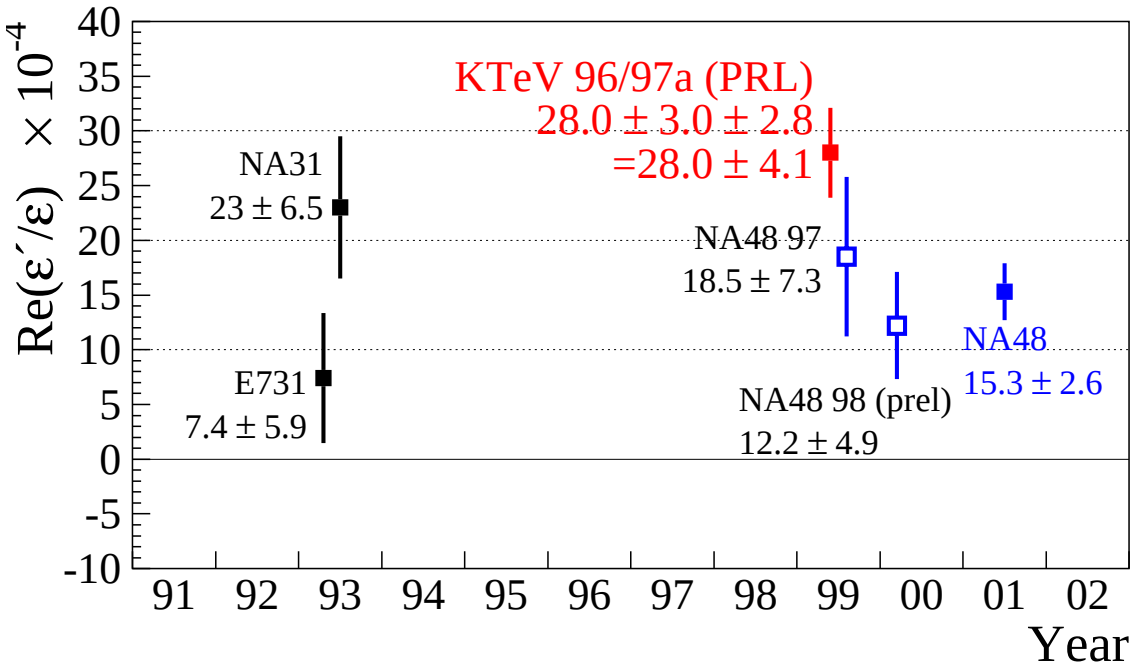

Figure 1.1: Experimental measurements of $Re(\epsilon'/\epsilon)$ before June 2001. Measurements before 1990 are not shown. The open squares indicate that the NA48 results from 1997 and 1998 were included in the 2001 NA48 result.

Searches for CP-violation and T-violation have been carried out experimentally in various other (non-kaon) sectors.

Recent experiments at Belle [37] and Babar [38] have both successfully measured CP-violation in the B-sector using $B \to \psi K_S$ decays. CP-violation in other B-decay modes are currently being investigated.

T-violation which is complementary to CP-violation by way of the CPT-theorem has been studied in searches for the neutron electric dipole moment. The presence of a non-zero neutron electric dipole moment is a sign of T-violation. According to the Standard Model, the neutron electric dipole moment is expected to be very small ($10^{-27} - 10^{-25}$e-cm [35]). A non-zero neutron electric dipole moment has not been observed experimentally and the current upper limit is 6.3×10^{-26}e-cm [36].

1.2 Outline of Thesis

The focus of this thesis is the measurement of $Re(\epsilon'/\epsilon)$ at KTeV. It is important to measure $Re(\epsilon'/\epsilon)$ precisely because predicting the amount of direct CP-violation in the K-sector is a crucial test of any theory which describes CP-violation. We see from Figure 1.1, however, that despite the conclusive evidence for direct CP violation in neutral kaons, the experimental results show a large scatter, with a probability of 1% that they all come from the same normal distribution. To measure the amount of direct CP-violation in the kaon-sector precisely, we need to reconcile the differences between the most recent experimental measurements. With this in mind, the $Re(\epsilon'/\epsilon)$ measurement of a statistically-independent and enhanced sample of KTeV data is presented. We also present an updated analysis of the previously published data sample.

This thesis also describes the KTeV measurement of the difference between the CP-violating phases in the $\pi^0\pi^0$ and $\pi^+\pi^-$ final states, $\Delta\phi$. As described in Section 1.3, the comparison of the CP-violating phases in the $\pi^+\pi^-$ and $\pi^0\pi^0$ final states is a test of CPT invariance.

Besides, describing the KTeV measurements of $Re(\epsilon'/\epsilon)$ and $\Delta\phi$, the thesis discusses the measurement of the short-lived kaon lifetime, τ_S, and the mass difference between the long- and short-lived kaons, Δm. The latter two measurements were performed using $K \to \pi^0\pi^0$ and $K \to \pi^+\pi^-$ decays. We emphasize the $K \to \pi^0\pi^0$-based measurements in this thesis, since the $K \to \pi^+\pi^-$-based measurements have been discussed in detail in [39].

The rest of this chapter summarizes the aspects of kaon phenomenology which are relevant to the measurement of $Re(\epsilon'/\epsilon)$ and $\Delta\phi$. In Chapter 2, the KTeV technique of measuring $Re(\epsilon'/\epsilon)$ is described. The details of the KTeV detector are discussed in Chapter 3. The electromagnetic calorimeter is an integral part of the KTeV detector, so its design and performance are explained in great detail in Chapter 4. After introducing the data samples that were used in the measurement in Chapter 5, we describe the data analysis in Chapters 6 and 7. A precise determination of the fraction of events collected by the detector (acceptance) and an accurate assignment of the

systematic uncertainties are crucial to the measurement of $Re(\epsilon'/\epsilon)$. The acceptance and the systematic studies are discussed in Chapters 8 and 9. Having described the acceptance calculation and systematic studies, we explain how $Re(\epsilon'/\epsilon)$, $\Delta\phi$, Δm and τ_S are obtained from the acceptance-corrected analysis in Chapter 10.

1.3 Kaon Phenomenology

In this section, we summarize the phenomenology describing CP-violation in kaons. We begin by describing the treatment of CP-violation in the neutral kaon system which pertains to all decay channels and then focus on the formalism regarding CP-violation in neutral $K \to 2\pi$ decays. In our discussion of CP-violation in neutral $K \to 2\pi$ decays, we first introduce the formalism which is independent of any assumption regarding CPT-invariance and then treat the CPT-conserving and CPT-violating scenarios separately. This section concludes with a discussion of tests of CPT-invariance in neutral $K \to 2\pi$ decays. Much of the formalism is based on Sachs [24] and further details can be found there.

The charge-conjugate neutral kaon states, $K^0(\overline{s}d)$ and $\overline{K^0}(s\overline{d})$, are eigenstates of strangeness with eigenvalues of 1 and -1, respectively. Although strangeness, S, is seen to be conserved in strong and electromagnetic interactions, the observation of $|\Delta S| = 1$ decays such as $K^0 \to \pi^+\pi^-$ and $\overline{K^0} \to \pi^+\pi^-$ showed that strangeness was not a good quantum number in weak interactions. In addition to strangeness-violating weak decays, the existence of K^0 and $\overline{K^0}$ decays to the the same final state, $\pi^+\pi^-$, showed that the two states were degenerate and could be coupled by a second-order ΔS=2 weak interaction. As a result of the K^0-$\overline{K^0}$ coupling, the kaon eigenstates of the full Hamiltonian were re-defined by Pais and Gell-Mann [40] to be C-conjugation eigenstates:

$$\begin{aligned} |K_1> &= \frac{1}{\sqrt{2}}(|K^0> + |\overline{K^0}>) \\ |K_2> &= \frac{1}{\sqrt{2}}(|K^0> - |\overline{K^0}>). \end{aligned} \tag{1.1}$$

Even after C-violation was observed, K_1 and K_2 were still considered to be the eigenstates of the complete Hamiltonian since they were also CP-eigenstates.

By connecting the K^0 and $\overline{K^0}$ states, the weak interaction split the degeneracy between the eigenstates, resulting in a small mass difference between K_1 and K_2. The states, K_1 and K_2, also had very different lifetimes since they decayed to final states with different number of particles [1].

To determine the CP-eigenvalues of K_1 and K_2, it is necessary to define a phase convention relating K^0 to $\overline{K^0}$. Since the strong and electromagnetic interactions do not connect K^0 and $\overline{K^0}$, the phase convention is determined by the weak interaction alone. The weak interaction allows an arbitrary choice of phase as long as the phase is consistent (i.e. CP(CP$|K^0>$)=$|K^0>$). We choose the following convention relating K^0 and $\overline{K^0}$:

$$\begin{aligned} CP|K^0> &= |\overline{K^0}> \\ CP|\overline{K^0}> &= |K^0> . \end{aligned} \tag{1.2}$$

Based on this phase convention, K_1 and K_2 are the CP-even and CP-odd eigenstates respectively.

The discovery of CP-violation in the kaon system led to the conclusion that the full eigenstates were not pure CP-eigenstates but were a mixture of CP eigenstates. To determine the kaon eigenstates, we need to determine the full Hamiltonian, $\mathcal{H}$, which includes second-order weak (or superweak) interactions. $\mathcal{H}$, which is given by

$$\mathcal{H} = M - \frac{i}{2}, , \tag{1.3}$$

consists of an absorptive term, , , and a "mass matrix" term, M. The form of these

[1] Since the CP-violating effect is very small, this conclusion holds true even when we account for CP-violation.

terms is described by Kabir [41] as

$$< j|, |k >= \sum_f A^*_{fj} A_{fk} \tag{1.4}$$

and

$$\begin{aligned} < j|M|k > &= m_K \delta_K + < j|H_w|k > \\ &\quad -\frac{1}{2\pi} P \int \frac{dE}{E - m_K} \sum_c A^*_{cj}(E) A_{ck}(E), \end{aligned} \tag{1.5}$$

where j,k = 1,2 refer to K^0 and $\overline{K^0}$ states respectively, H_w is the Hamiltonian describing the second-order weak interaction, A_{fj} is the decay amplitude to final state, f, and $A_{cj}(E)$ refers to the virtual decay amplitude to channel, c, with energy, E. The virtual amplitude is normalized such the $A_{cj}(E)$=0 if the channel is not energetically accessible. Only the principal value of the integral term in Equation 1.5 is considered. The integral term is known as the "dispersive" term and is responsible for CP-violation.

We solve the eigenvalue equation,

$$\mathcal{H}|\alpha >= (M - \frac{i}{2},)|\alpha >= \lambda_\alpha |\alpha >, \tag{1.6}$$

to determine the kaon eigenstates. The eigenvalues, $\lambda_\alpha = m_\alpha - \frac{i}{2}, {}_\alpha$, are complex since $\mathcal{H}$ is not Hermitian even though M and , are.

The kaon eigenstates, K_S and K_L are found to be

$$\begin{aligned} |K_S > &= \frac{1}{\sqrt{1 + |\epsilon - \Delta|^2}} (|K_1 > +(\epsilon - \Delta)|K_2 >) \\ |K_L > &= \frac{1}{\sqrt{1 + |\epsilon + \Delta|^2}} (|K_2 > +(\epsilon + \Delta)|K_1 >) \end{aligned} \tag{1.7}$$

to first order in ϵ and Δ. From Equation 1.7, we see that the eigenstates consist

mainly of a pure CP-eigenstate with a tiny CP-impurity[2].

Expressed in the $|K^0>$ and $|\overline{K^0}>$ basis, the kaon eigenstates are

$$\begin{aligned} |K_S> &= \frac{1}{\sqrt{2(1+|\epsilon-\Delta|^2)}}((1+\epsilon-\Delta)|K^0>+(1-\epsilon+\Delta)|\overline{K^0}>) \\ |K_L> &= \frac{1}{\sqrt{2(1+|\epsilon+\Delta|^2)}}((1+\epsilon+\Delta)|K^0>-(1-\epsilon-\Delta)|\overline{K^0}>). \end{aligned} \tag{1.8}$$

ϵ and Δ are defined by

$$\epsilon = \frac{(<\overline{K^0}|\mathcal{H}|K^0> - <K^0|\mathcal{H}|\overline{K^0}>)}{2\Delta m + \frac{i}{2}(\Delta, \ )} \tag{1.9}$$

and

$$\Delta = \frac{(<K^0|\mathcal{H}|K^0> - <\overline{K^0}|\mathcal{H}|\overline{K^0}>)}{2\Delta m + \frac{i}{2}(\Delta, \ )} \tag{1.10}$$

where Δm is the mass difference, $m_{K_L} - m_{K_S}$, and $\Delta, \ = \ , \ _{K_S} - \ , \ _{K_L}$. From Equations 1.4 and 1.5, we find that ϵ is a measure of CP-violation since it transforms as $\epsilon \leftrightarrow -\epsilon$ under the CP-transformation.

To understand the significance of Δ, we observe that CPT conservation leads to the same lifetimes and total decay amplitudes for particle and anti-particle. Therefore, if CPT is conserved,

$$<K^0|\mathcal{H}|K^0> = <\overline{K^0}|\mathcal{H}|\overline{K^0}>, \tag{1.11}$$

and $\Delta = 0$. Hence, Δ is a measure of CPT conservation.

CPT conservation also results in the condition

$$<K^0|\mathcal{H}|\overline{K^0}> = <\overline{K^0}|\mathcal{H}|K^0>^* \ . \tag{1.12}$$

Therefore, assuming CPT conservation,

$$\epsilon = \frac{Im(M_{12}) - \frac{i}{2}Im(, \ _{12})}{i\Delta m - \frac{1}{2}\Delta,} \tag{1.13}$$

[2]The CP-impurity is small because CP-violation is a small effect.

where M_{12} and , $_{12}$ are $< K^0|M|\overline{K^0} >$ and $< K^0|$, $|\overline{K^0} >$ respectively.

1.3.1 CP-violation in neutral $K \to 2\pi$ decays

The ratio of CP-violating to CP-conserving kaon decays to 2π is given by

$$\eta_{\pi\pi} = \frac{A(K_L \to 2\pi)}{A(K_S \to 2\pi)}. \tag{1.14}$$

Substituting Equation 1.8 into Equation 1.14, we find that

$$\eta_{\pi\pi} = \epsilon + \Delta + \kappa_{\pi\pi} \tag{1.15}$$

where

$$\kappa_{\pi\pi} = \frac{A_{2\pi} - \overline{A}_{2\pi}}{A_{2\pi} + \overline{A}_{2\pi}} \tag{1.16}$$

and $A_{2\pi}$ and $\overline{A}_{2\pi}$ are the decay amplitudes to 2π for K^0 and $\overline{K^0}$ respectively.

If the decay amplitudes for K^0 and $\overline{K^0}$ are CP-invariant, then $A_{2\pi} = \overline{A}_{2\pi}$ and $\kappa_{\pi\pi} = 0$. Therefore, $\kappa_{\pi\pi}$ is a measure of CP-violation in the decay amplitude (direct CP-violation). From Equation 1.15, we see that the direct CP-violating contribution to neutral $K \to 2\pi$ decays can only be determined by comparing $\eta_{2\pi}$ in the $\pi^+\pi^-$ (η_{+-}) and the $\pi^0\pi^0$ (η_{00}) modes. To compare η_{+-} and η_{00}, we decompose the $K^0 \to \pi^+\pi^-$ and $K^0 \to \pi^0\pi^0$ decay amplitudes, A_{+-} and A_{00}, based on the isospin content, I, of the final state. The final 2π state is in the I=0 and I=2 isospin states. The I=1 state is forbidden since the final state obeys Bose statistics. The initial K^0 state has I=$\frac{1}{2}$, so the $K^0 \to 2\pi$ decay consists of $\Delta I = \frac{1}{2}$ and $\Delta I = \frac{3}{2}$ transitions.

The 2π decay amplitudes are given by

$$\begin{aligned} A_{+-} &= \frac{1}{\sqrt{3}}(\sqrt{2}a_0 e^{i\delta_{WY}} e^{i\delta_0} + a_2 e^{i\delta_2}) \\ A_{00} &= \frac{1}{\sqrt{3}}(a_0 e^{i\delta_{WY}} e^{i\delta_0} - \sqrt{2}a_2 e^{i\delta_2}) \end{aligned} \tag{1.17}$$

where a_0 and a_2 represent the reduced amplitudes to the I=0 and I=2 final states respectively. In this form, Equation 1.17 shows the roles of the relative phase be-

tween the coefficients, a_0 and a_2, δ_{WY}, as well as the $(\pi\pi)_{I=0}$ and $(\pi\pi)_{I=2}$ final state scattering phase-shifts, δ_0 and δ_2[3]. Since the choice of the phase, δ_{WY}, is arbitrary, we adopt the Wu-Yang phase convention [42] by setting $\delta_{WY} = 0$.

Until now, we have not considered the effect of the CPT theorem. To account for the CPT-theorem, we discuss the predictions assuming CPT conservation and then study the consequences of CPT violation.

1.3.2 CPT Conservation

If CPT is conserved then the weak Hamiltonian, H_w, which is responsible for CP-violation is unchanged under the CPT transformation:

$$(CPT)H_w(CPT)^{-1} = H_w. \tag{1.18}$$

From the anti-unitary nature of the CPT operation and Equation 1.18, we find based on Watson's Theorem [43] and the Wigner phase convention that the K^0 and $\overline{K^0}$ reduced amplitudes, a_I and $\overline{a}_I$ are related by

$$a_I = \overline{a}_I^* \tag{1.19}$$

where I is the isospin of the 2π final state.

By substituting Equation 1.17 into the definition 1.16 and applying Equations 1.19 and 1.14, we find that in the Wu-Yang phase convention [42] where $\delta_0 = 0$,

$$\begin{aligned} \eta_{+-} &= \epsilon + \frac{\epsilon'}{1+w} \\ \eta_{00} &= \epsilon - 2\frac{\epsilon'}{1-2w} \end{aligned} \tag{1.20}$$

where

$$w \equiv \frac{1}{\sqrt{2}} e^{i\delta} \frac{Re(a_2)}{a_0}, \tag{1.21}$$

[3]The final state phases are the same for the K^0 and $\overline{K^0}$ to 2π decays since the strong interaction is CP-invariant.

$$\epsilon' \equiv \frac{1}{\sqrt{2}} i e^{i\delta} \frac{Im(a_2)}{a_0} \tag{1.22}$$

and $\delta \equiv \delta_2 - \delta_0$.

Ignoring terms of order ϵ, w can be expressed as

$$|w| \approx \frac{1}{\sqrt{2}} \left| \frac{A(K_S \to 2\pi)_{I=2}}{A(K_S \to 2\pi)_{I=0}} \right|. \tag{1.23}$$

We see from Equation 1.23 that w describes the ΔI $= \frac{1}{2}$ enhancement seen in kaon decays. Experimentally, $|w| \sim \frac{1}{22}$. The smallness of w allows us to make the approximation,

$$\begin{aligned} \eta_{+-} &\approx \epsilon + \epsilon' \\ \eta_{00} &\approx \epsilon - 2\epsilon'. \end{aligned} \tag{1.24}$$

We see from the definition of ϵ', Equation 1.22, that CP-violation in the kaon decay amplitude only occurs if there is a phase difference between the partial isospin amplitudes a_0 and a_2. Empirically, it is observed that $\eta_{+-} \approx \eta_{00}$ implying that direct CP-violation is a small effect and that CP-violation in the $K \to 2\pi$ decay is dominated by ϵ.

To determine the contributions of the decay amplitude, $Im(,_{12})$, to ϵ (Equation 1.13), we see from Equation 1.4 that

$$Im(,_{12}) = Im(A^*_{2\pi}\overline{A}_{2\pi} + A^*_{\pi l\nu}\overline{A}_{\pi l\nu} + A^*_{3\pi}\overline{A}_{3\pi} + \sum_{raredecays} A^*_{rare}\overline{A}_{rare}). \tag{1.25}$$

By our choice of phase convention, $A^*_{2\pi}\overline{A}_{2\pi}$ is only imaginary for $\Delta I = \frac{3}{2}$ transitions, which are suppressed. The contribution to Im$(,_{12})$ due to semileptonic and 3π is also small because of the $\Delta S = \Delta Q$ rule [44] and the smallness of the ratio, $,_{K_L}/,_{K_S}$, respectively. As a result, we see that the decay amplitude contribution to ϵ is very small and that the CP-violation parameter, ϵ, is dominated by the dispersive term in the mass matrix, M.

ϵ' is expected to be much smaller than ϵ, which has a value, $|\epsilon| = 2.28 \times 10^{-3}$,

based on the average of $|\eta_{+-}|$ and $|\eta_{00}|$ measurements [45]. Therefore, to measure direct CP-violation in $K \to 2\pi$ decays, it is experimentally easier to measure the ratio, $|\eta_{+-}/\eta_{00}|$, which is proportional to ϵ'/ϵ, rather than the difference, $(\eta_{+-} - \eta_{00})$, which is proportional to ϵ'. From Equation 1.24, we find that, to first order in ϵ'/ϵ,

$$\begin{aligned} \left|\frac{\eta_{+-}}{\eta_{00}}\right|^2 &= \frac{,\,(K_L \to \pi^+\pi^-)/,\,(K_S \to \pi^+\pi^-)}{,\,(K_L \to \pi^0\pi^0)/,\,(K_S \to \pi^0\pi^0)} \\ &\approx 1 + 6Re(\epsilon'/\epsilon). \end{aligned} \tag{1.26}$$

A non-zero value of $Re(\epsilon'/\epsilon)$ shows that direct CP-violation is present in the kaon system.

Using the definition of ϵ', Equation 1.22, and the approximation, $\phi_\epsilon \approx \phi_{+-}$, the phase of ϵ'/ϵ is found to be

$$\begin{aligned} \phi_{\epsilon'/\epsilon} &= \delta + \frac{\pi}{2} - \phi_\epsilon \\ &\approx \delta + \frac{\pi}{2} - \phi_{+-}. \end{aligned} \tag{1.27}$$

Based on measurements of the $\pi - \pi$ isospin scattering lengths, the difference in the $\pi - \pi$ phase shifts, $\delta \equiv \delta_2 - \delta_0$, was determined to be (-42±4)° [46]. Combining the measurement of δ with the the measured value of ϕ_{+-}, (43.4±0.5)° [47] [48], we find that $\phi_{\epsilon'/\epsilon} = (5 \pm 4)^\circ$ and hence, $|\epsilon'/\epsilon| \approx Re(\epsilon'/\epsilon)$.

1.3.3 CPT Violation

Having discussed the phenomenology of CP-violation in neutral $K \to 2\pi$ decays assuming CPT conservation, we now consider the effect of CPT-violation on neutral $K \to 2\pi$ decays.

The CPT condition, Equation 1.18, which was used in the previous section is now modified to be

$$(CPT)H_w(CPT)^{-1} = H_w'' \tag{1.28}$$

where $H_w \neq H_w''$. Based on this relationship, we find by Watson's Theorem [43] and

the Wigner phase convention, that the reduced amplitudes are related by

$$\overline{a}_I = (a''_I)^*. \tag{1.29}$$

Since any deviation from CPT invariance is expected to be small, the CPT-violating contribution is treated as a small perturbation, μ_I, such that

$$\begin{aligned} a''_I &= a_I - 2\mu_I a_I \\ \overline{a}''_I &= a^*_I - 2\mu^*_I a^*_I \end{aligned} \tag{1.30}$$

with $|\mu_I| \ll |\eta_{\pi\pi}|$.

Adopting the Wu-Yang phase convention by setting a_0 to be real, leads to the relationship :

$$\overline{a}_0 = a_0 - 2\mu^*_0 a_0. \tag{1.31}$$

Proceeding as we did in the previous section, we find

$$\begin{aligned} \kappa_{+-} &= \epsilon'' + \mu^*_0 \\ \kappa_{00} &= -2\epsilon'' + \mu^*_0 \end{aligned} \tag{1.32}$$

where

$$\epsilon'' \equiv \epsilon' + \frac{1}{\sqrt{2}} e^{i\delta} \frac{\mu^*_2 \mu^*_2}{a_0} - w\mu^*_0. \tag{1.33}$$

Using the relationships 1.15 and 1.33, η_{+-} and η_{00} are given by

$$\begin{aligned} \eta_{+-} &= \epsilon + \Delta + \epsilon'' + \mu^*_0 \\ \eta_{00} &= \epsilon + \Delta - 2\epsilon'' + \mu^*_0 \end{aligned} \tag{1.34}$$

and

$$\eta_{+-} - \eta_{00} = -3\epsilon''. \tag{1.35}$$

Before we conclude this discussion on the consequences of CPT violation, it is important to emphasize that we have assumed unitarity in the discussion above.

This assumption is inherent in our treatment of the mass matrix, M (Equation 1.5) where we consider the second-order weak interaction operator, H_w, to be Hermitian.

In a rigorous treatment of CPT-violation, however, we should remove the unitarity requirement. This consideration has been treated by Sachs [49] who has shown that CPT conservation is valid even when considering weak interactions which are non-Hermitian based on the experimental limits on unitarity.

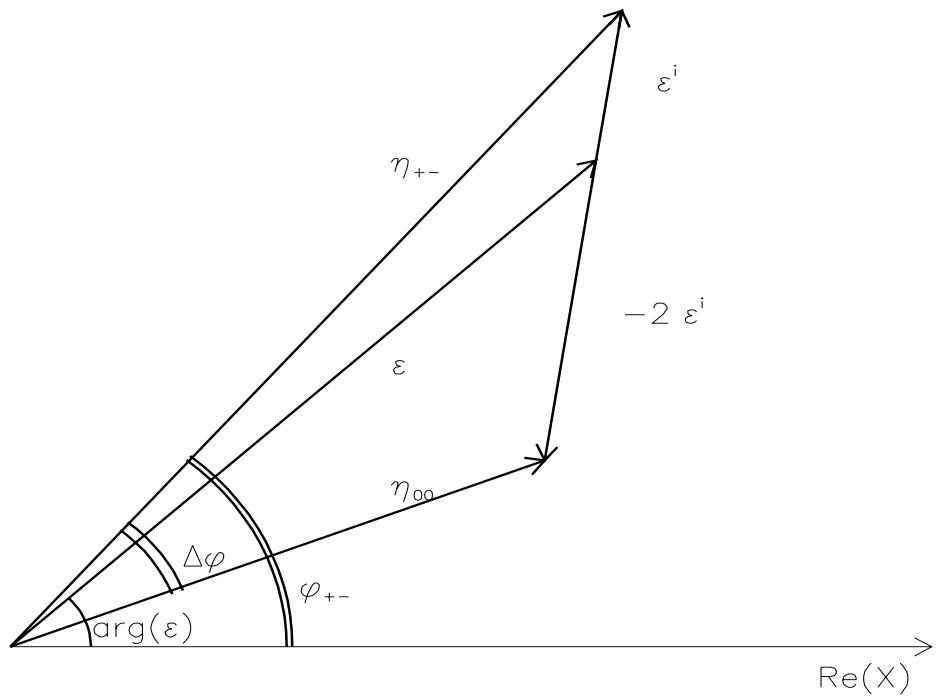

Figure 1.2: Geometric representation of relationship between η_{+-}, η_{00}, ϵ and ϵ' in the complex plane. $\Delta\phi$ is defined to be $(\phi_{00} - \phi_{+-})$. The figure is not drawn to scale.

1.3.4 Predictions of CPT Conservation

We see from Equations 1.34 and 1.35 that both $\eta_{\pi\pi}$ and $(\eta_{+-} - \eta_{00})$ consist of at least 2 CPT-violating terms. This implies that there could be a possible cancellation of CPT-violating terms in neutral $K \to 2\pi$ decays. As a result, a measurement which is consistent with the predictions of CPT conservation cannot rule out the presence of CPT-violation in the kaon system.

Although the neutral $K \to 2\pi$ system cannot be used to disprove the existence of CPT violation in the kaon sector, the neutral $K \to 2\pi$ system is nevertheless useful in testing the predictions of CPT conservation. Based on the relationship between η_{+-} and η_{00} described in Equation 1.24 and shown in Figure 1.2, we find, to first order in ϵ'/ϵ,

$$\Delta\phi(radians) \equiv \phi_{00} - \phi_{+-} \approx -3Im(\epsilon'/\epsilon). \tag{1.36}$$

Since $\phi_{\epsilon'/\epsilon} = (5 \pm 4)^\circ$ based on CPT conservation, we expect

$$|\Delta\phi(radians)| < 1 \times 10^{-3}, \tag{1.37}$$

if CPT is invariant. If CPT is violated, we see from Equation 1.33 that $\Delta\phi \approx 0$ only if there is a fortuitous phase cancellation such that $\phi_{\epsilon''} \approx \phi_\epsilon$.

Based on Equation 1.13, CPT conservation also predicts that

$$\phi_{+-} \approx \phi_\epsilon = tan^{-1}(\frac{2\Delta m}{\Delta,}). \tag{1.38}$$

The term, $(\frac{2\Delta m}{\Delta\Gamma})$, is referred to as the superweak phase, ϕ_{SW}. The KTeV measurement of $|\phi_{+-} - \phi_{SW}|$ which tests CPT-invariance is presented in [39].

CHAPTER 2
EXPERIMENTAL TECHNIQUE

KTeV is a fixed target experiment located at Fermilab. The goal of the E832 part of this experiment is to measure $Re(\epsilon'/\epsilon)$ at the 1×10^{-4} level. As the Standard Model predictions for $Re(\epsilon'/\epsilon)$ are of order $10^{-4} - 10^{-3}$, KTeV was designed to be sensitive enough to test the Standard Model predictions and observe direct CP-violation.

As seen from Equation 1.26, the measurement of $Re(\epsilon'/\epsilon)$ at the 10^{-4} level requires the measurement of the double ratio of K_L and K_S decays to both $\pi^0\pi^0$ and $\pi^+\pi^-$ final states at a precision better than 10^{-3}. The $K_{L,S} \rightarrow \pi^+\pi^-$ decay channels are referred to as the **charged** mode while the $K_{L,S} \rightarrow \pi^0\pi^0$ channels are called the **neutral** mode. Although, in essence, the $Re(\epsilon'/\epsilon)$ measurement is a simple counting experiment involving four decay channels, challenges arise because of the high level of precision required to make the measurement. The main challenges are the minimization of measurement biases which may affect one channel more than another, the need for an excellent understanding of the detector in order to minimize and determine accurately the systematic errors, a precise understanding of the fraction of events that are detected (the acceptance), and the collection of millions of events in each of the four decay channels in order to have a statistical error on $Re(\epsilon'/\epsilon)$ of $\sim 10^{-4}$.

This chapter will describe the technique used by the KTeV E832 experiment to measure $Re(\epsilon'/\epsilon)$ and explain how the challenges mentioned above are met. The process of regeneration that is used in the KTeV experiment will be described as well. The details and performance of the KTeV detector will be left for the chapters 3 and 4. This chapter will end with a brief description of a few alternate techniques of measuring $Re(\epsilon'/\epsilon)$.

2.1 The KTeV Technique

The KTeV experiment uses two neutral kaon beams to produce K_L and K_S decays to 2π. The two neutral beams enter a decay region ~90 m from the target at which they were produced. At this distance from the target, the kaons in the neutral beam are almost all K_L. To produce K_S, one of the beams passes through a plastic regenerator. Although K_S are produced through various interactions in the regenerator, only coherently regenerated K_S in the forward direction are selected. The importance and advantages of the double-beam technique and regeneration are discussed in Sections 2.1.1 and 2.1.3, respectively.

Since the K_L and K_S beams share the same decay volume, the large difference in lifetimes causes the two beams to have very different decay vertex distributions. As a result, the acceptance within the KTeV decay region must be understood very well to avoid a first-order bias in the ratio of K_L to K_S decays. To determine the acceptance accurately, KTeV uses a detailed Monte Carlo simulation which accounts for the kaon evolution and simulates the detector geometry and response. The Monte Carlo simulation is described in detail in Chapter 8.

2.1.1 The Double Beam Technique

The use of the double beam technique is advantageous because it enables KTeV to collect K_L and K_S decays at the same time and under the same conditions. By doing so, biases due to temporal fluctuations during data collection such as changes in beam intensity and variations in detector response with time are reduced. Furthermore, by counting decays from all four channels at the same time, biases that affect charged and neutral modes identically will cancel out in the double ratio measurement as well.

The two neutral beams are produced from a primary beam of high-energy protons at high intensity hitting a target. The high-intensity primary beam results in a higher kaon flux which in turn leads to a higher rate of collecting kaon decays. Using kaons of higher momentum is also useful because the sensitivity of the neutral mode reconstruction is improved. For example, the decay vertex resolution in the neutral mode is ~30 cm, more than ten times smaller than the K_S decay length of ~4 m at

the mean kaon energy in the KTeV regenerator beam, ~70 GeV.

By using two neutral beams collimated from a single beam, KTeV is able to ensure that the beams are similar to each other in content and shape. Having beams of similar content and shape cause primary beam-related intensity effects to cancel out in the double ratio. By using two identical beams, biases due to the different level of activity in the kaon beams arising from neutrons and other neutral hadrons produced in the interaction at the target are also suppressed.

2.1.2 K_L and K_S Production

By placing the decay region far away from the target, we allow almost all the K_S produced at the target to decay before they reach the decay region. This not only ensures that both kaon beams are almost purely K_L but it also allows short-lived neutral particles like Λ to decay. It also provides more room for sweeping away charged particles in the beam and placing absorbers to reduce the photon and neutron content in the beam.

K_S are regenerated from one of the K_L beams by using a plastic regenerator. The incoming pure K_L beam is converted to a mixed kaon beam, $K_L + \rho K_S$, where ρ is the regeneration amplitude. $|\rho|$ is $\sim 3\%$ for the KTeV regenerator. The beam containing regenerated K_S is referred to as the regenerator beam while the other beam is called the vacuum beam. By placing a regenerator in one of the beams, we become susceptible to left-right biases between the beams and detector response. To overcome these biases, the regenerator is made to alternate from one beam to the other every minute.

KTeV places an additional ("shadow") absorber upstream of the regenerator to reduce the flux of particles on the regenerator. Decreasing the flux on the regenerator, reduces the activity in the regenerator as well as the number of K_S produced. Reducing the regenerator activity is important, since we trigger on regenerator activity. Having excessive activity will "swamp" the trigger and decrease the data collection efficiency. By reducing the number of K_S decays, the number of 2π decays in the regenerator and vacuum beams become comparable. In this way, the CP-violating

$K_L \to 2\pi$ events are not overwhelmed by the CP-conserving K_S decays. Since the statistically limiting decay channel in the $Re(\epsilon'/\epsilon)$ measurement is $K_L \to \pi^0\pi^0$, it is important that we maximize the number of such decays collected.

The rate of $K \to 2\pi$ decays in the regenerator beam, $R_{2\pi}^{reg}(t)$, is

$$R_{2\pi}^{reg}(t) \propto F(p)T(p)\left[|\rho|^2 e^{-\frac{t}{\tau_S}} + |\eta|^2 e^{-\frac{t}{\tau_L}} + 2e^{-\frac{t}{2}(\frac{1}{\tau_S}+\frac{1}{\tau_L})}|\rho||\eta|cos(\Delta mt - \phi_\eta + \phi_\rho)\right], \tag{2.1}$$

where t is the proper time, $\tau_{S,L}$ are the $K_{S,L}$ lifetimes, Δm is the K_S-K_L mass difference, ϕ_η is the phase of η, and p is the kaon momentum. $F(p)$ describes the momentum-dependance of the incoming beam, $T(p)$ represents the transmission through the regenerator and shadow absorber, and $|\rho|$ and ϕ_ρ are the regeneration amplitude and phase, respectively. In the vacuum beam, the rate of 2π decays, $R_{2\pi}^{vac}(t)$, is

$$R_{2\pi}^{vac}(t) \propto F(p)|\eta|^2 e^{-\frac{t}{\tau_L}}, \tag{2.2}$$

if we ignore the small amount of high-energy K_S that were produced at the target and had not decayed before reaching the decay region.

One sees from expressions 2.1 and 2.2 that by measuring the ratio of 2π decays in the regenerator to vacuum beam, the primary beam flux dependances cancel out since the two beams are identical upstream of the regenerator. The ratio of 2π decays in the two beams is proportional to powers of $|\rho/\eta|$ with a constant of proportionality, $T(p)$, which depends only on the geometry of the regenerator and upstream absorber.

To be less sensitive to the understanding of $T(p)$, we select the charged and neutral mode decay regions and kaon energy ranges to be the same. Effects on $Re(\epsilon'/\epsilon)$ due to kaon evolution, such as the relative number of K_L and K_S in the beam, are also reduced by choosing a common decay region and kaon energy range.

2.1.3 Regeneration and Its Usefulness

The process of kaon regeneration is essential to the KTeV measurement of $Re(\epsilon'/\epsilon)$. To exploit the advantages as well as to reduce the drawbacks of using a regenerator

as a source of K_S, it is necessary to understand the different types of regeneration and scattering processes.

Regeneration Processes

When a K_L beam enters and interacts within the regenerator, strong and electromagnetic interactions dominate the scattering off nuclei. In order to determine the outgoing kaon state, it is therefore necessary to consider the scattering of the strong kaon eigenstates, K^0 and $\overline{K^0}$. Since the strong interaction conserves strangeness, interactions such as $\overline{K^0}p \rightarrow \Lambda\pi^+$ have no K^0 corollary. As a result,

$$\sigma_T(\overline{K^0}N) > \sigma_T(K^0N), \tag{2.3}$$

where σ_T is the total cross-section. From the optical theorem and the difference in the total K^0 and $\overline{K^0}$ nucleon scattering cross-sections, one finds that the forward scattering amplitudes for K^0 and $\overline{K^0}$, $f(0)$ and $\overline{f}(0)$, respectively, are different. As a result, an incoming K_L state emerges as a mixed K_L and K_S state, $\Psi(0)$, where

$$\Psi(0) = \frac{(f(0) - \overline{f}(0))}{2}K_S + \frac{(f(0) + \overline{f}(0))}{2}K_L. \tag{2.4}$$

An incoming K_L state which scatters at a non-zero angle will also emerge as a mixed K_L and K_S state.

Since the fractional difference in the Compton wavelengths of K_S and K_L is less than 10^{-14}, the phase difference between an incoming K_L and an emerging K_S with the same energy remains constant over large distances. Although kaons scatter coherently off nucleons in the same nucleus, they only scatter coherently off different nuclei over a coherence length, L_c, which is given by [50]

$$L_c = \frac{p}{\Delta m m_K}. \tag{2.5}$$

The coherence length, L_c, is 8 m at ~70 GeV, the mean kaon energy in the KTeV regenerator beam. This is much greater than the KTeV regenerator length, so forward scatters off different nuclei in the regenerator are coherent. Coherence for scatters

off separate nuclei is lost very rapidly as the angle of scatter increases. At the mean kaon energy in KTeV, scatters off different nuclei are coherent only if the scattering angle is less than 10^{-5} mrad. The regeneration amplitude, ρ, for coherent scatters due to a regenerator of finite thickness is

$$\rho = i\pi NL(\frac{f(0) - \overline{f}(0)}{k})\delta(L,p), \tag{2.6}$$

where L is the regenerator length, N is the nucleon density and $\delta(L,p)$ is a geometrical factor based on the K_L-K_S evolution difference.

Diffractive scattering occurs when a kaon scatters incoherently off nuclei with a small amount of momentum transfer causing the kaon to scatter at a non-zero angle. Diffractive K_S regeneration can occur either through an incoherent regenerative scatter to K_S or through a combination of an incoherent non-regeneratitve K_L scatter followed by coherent regeneration. Comparing the amplitudes for $K_S \to 2\pi$ and $K_L \to 2\pi$ for n diffractive scatters in the forward direction [51], we find that

$$\frac{\rho_{diff}}{\eta} = -(\frac{2n - x}{x})\frac{\rho_{coh}}{\eta}, \tag{2.7}$$

where x is the number of interaction lengths of the regenerator, and ρ_{diff} and ρ_{coh} are the diffractive and coherent regeneration amplitudes, respectively.

From Equation 2.7, we see that single diffractive scatters are minimized for a 2-interaction length regenerator - the same length which maximises coherent $K_S \to 2\pi$ decays! In KTeV, the regenerator length is chosen to suppress single diffractive scatters, so multiple diffractive scattering is the dominant source of incoherent regenerator scattering. We also see from Equation 2.7 that the regeneration amplitudes for diffractive forward scatters and coherent scatters have opposite phases if the regenerator is less than 2 interaction lengths long. Since the "regeneration phases" are different for diffractive and coherent scatters, the K_L-K_S interference patterns for diffractive and coherent scatters are different as well.

Besides scattering coherently and diffractively, kaons can also scatter inelastically off nuclei in the regenerator. This results in large momentum transfers causing the nuclei either to break up or to be transferred to an excited state. Several other parti-

cles may be produced in the interaction as well. The emerging kaon state for K_L that scatter inelastically is mostly K_S. The kaons that are inelastically scattered usually have large scattering angles. Regeneration can also occur due to the electromagnetic interaction between the kaon charge radius and the electrons and nucleons in the regenerator but this effect is very small [51]. Both K_S and K_L can also be produced in the regenerator via neutron interactions such $n + N \rightarrow K^0 + \Lambda$. The process can be either diffractive or inelastic but in both cases, extra strange particles are produced at the same time. Such events can be identified and rejected by detecting the extra particles.

Why forward scatters ?

In the KTeV $Re(\epsilon'/\epsilon)$ measurement, the regenerator is optimized to select coherent scatters and reduce diffractive and inelastic scatters, since only coherent regenerator scatters are used in the final analysis to extract $Re(\epsilon'/\epsilon)$. The main advantage of using coherent scatters is that they occur in the forward direction and hence, we avoid the difficulties involved in reconstructing large angle scatters accurately. Unlike the $K \rightarrow \pi^+\pi^-$ mode where the kaon decay can be fully reconstructed, KTeV is unable to reconstruct the kaon transverse momentum and measure the kaon scattering angle accurately in the $K \rightarrow \pi^0\pi^0$ mode.

If we were to include scatters at a non-zero angle in the $Re(\epsilon'/\epsilon)$ measurement, we would need to measure the scattering angle accurately and understand the acceptance as a function of kaon angle very well.

The scattering angle is used to identify kaons that have scattered from the regenerator beam into the vacuum beam. If this is not done the kaon would be assigned to the wrong beam, thus causing a bias in $Re(\epsilon'/\epsilon)$. Measuring the scattering angle is also important because the regeneration phase varies with the scattering angle. Since the regeneration phase affects the distribution of 2π decays in the regenerator beam, it is important to understand the regeneration phase well. The scattering angle is also useful in distinguishing between inelastic scatters and diffractive scatters since both types of scattering have different angular dependances.

By including non-forward scatters, we would need to understand the differences in the acceptance between the two beams very well to avoid any biases in $Re(\epsilon'/\epsilon)$. This is because the response of the KTeV detector depends on the the kaon angle. Because of the dependance of the acceptance on the kaon angle, non-zero angle scatters can cause the acceptance in the regenerator and vacuum beams to be different for kaons at the same energy and decay vertex position. In the case of forward scatters, the acceptance for kaons with the same energy and decay distance from the target is the same because the angular distribution of the kaons is the same in the two beams [1].

Since a small fraction of diffractive scatters occur in the forward direction, we could in principle, select both diffractive and coherent forward scatters. This would require accounting for regeneration phase differences in the two types of scatters. Since this is difficult, we only select coherent forward scatters. If we were to select diffractive scatters, it would only increase the number of K_S decays collected. However, since the statistically limiting channel is $K_L \to \pi^0\pi^0$, the potential improvement in statistical error is small.

Advantages of Regeneration

There are three advantages to using a regenerator to produce K_S. Firstly, by selecting coherent forward scatters, the acceptance in both beams is the same for kaons at the same energy and decay position. This has been discussed in the previous section. Secondly, by measuring the regeneration parameters using the charged and neutral modes separately, we can compare and check that the $K_{L,S} \to \pi^0\pi^0$ and $K_{L,S} \to \pi^+\pi^-$ analyses are consistent. Thirdly, the presence of both K_L and K_S in the regenerator beam allows us to use the interference in the amplitudes to measure several important kaon parameters. This is an additional cross-check of the $Re(\epsilon'/\epsilon)$ measurement.

As seen from Equations 2.1 and 2.2, the ratio of 2π decays in the vacuum and regenerator beams is a function of $|\rho/\eta|$. As a result, in order to measure $Re(\epsilon'/\epsilon)$ at KTeV, we need to measure the regeneration amplitude and phase. The measurement

[1] Effects due to the regenerator attenuation and underlying event activity due to hadron interactions in the regenerator are considered to be small.

of the regeneration parameters at KTeV is greatly simplified since the regeneration amplitude is dependent on the kaon momentum. According to Regge theory, regeneration in an isoscalar material such as carbon is dominated by the exchange of the ω-meson [52]. The exchange of a single Regge pole predicts a momentum-dependent power law behaviour for the regeneration amplitude, where

$$|\frac{f(0)-\overline{f}(0)}{k}| \propto p^{\alpha}. \tag{2.8}$$

Through analyticity, the power, α, and the regeneration phase are related by

$$arg(\frac{f(0)-\overline{f}(0)}{k}) = -\frac{\pi}{2}(2+\alpha). \tag{2.9}$$

Since deviations from the power law (arising from exchanges other than a single Regge pole) decrease with kaon energy and are small for kaon energies above $\sim$10 GeV, the power law assumption is well-suited for kaons at KTeV which have energies in 20 GeV to 200 GeV range.

From the distribution of 2π decays in the regenerator beam, we are able to measure both $|\frac{f(0)-\overline{f}(0)}{k}|$ at a kaon momentum of 70 GeV and the power law exponent, α, in the $K_{L,S} \rightarrow \pi^+\pi^-$ and $K_{L,S} \rightarrow \pi^0\pi^0$ modes separately. It is harder to compare $|\frac{f(0)-\overline{f}(0)}{k}|$ at a kaon momentum of 70 GeV since the charged and neutral mode measurements of $|\rho/\eta|$ will be different if ϵ'/ϵ is non-zero. On the other hand, the power law is independent of the measurement of ϵ'/ϵ, so the comparison of α in the charged and neutral modes is a useful cross-check of the two analyses.

Using a regenerator to produce K_S allows us to use the interference of K_L and K_S amplitudes in the regenerator beam to measure the kaon parameters Δm, ϕ_{+-}, ϕ_{00} and $\Delta\phi$. In addition, the K_S lifetime, τ_S, can be measured using 2π decays in the first few K_S decay lengths after the regenerator. The measurement of these parameters are important cross-checks of the event reconstruction and analysis in the charged and neutral modes and in the case of the phase measurements, are also tests of CPT conservation.

Disadvantages of Regeneration

Although there are several advantages to using a regenerator in the $Re(\epsilon'/\epsilon)$ measurement, there are a few drawbacks to the regenerator technique. The drawbacks are primarily due to scattering in the regenerator, although uncertainties due to the regeneration amplitude measurement as well as interactions of the beam in the regenerator also affect $Re(\epsilon'/\epsilon)$ to a small extent.

The biggest disadvantage to using a regenerator is the presence of diffractive and inelastic scatters. Noncoherent and inelastic scatters are a background to coherent forward scatters in the regenerator beam. The large-angle regenerator scatters in the neutral mode can also result in the mis-assignment of events to the vacuum beam.

As described earlier, the KTeV technique is sensitive to the measurement of the regeneration amplitude, ρ. Although the power law behaviour allows one to determine ρ experimentally and to be less sensitive to a theoretical description of the regeneration process, even at KTeV energies, there are small deviations from the power law arising from screening processes within the regenerator. Deviations from the power law affect the determination of $|\rho|$ and the regeneration phase, ϕ_ρ. $|\eta|$ is affected by the measurement of $|\rho|$, so deviations from the power law affect $Re(\epsilon'/\epsilon)$. However, since $Re(\epsilon'/\epsilon)$ involves the ratio, $|\frac{\eta_{+-}}{\eta_{00}}|$, power law deviations have only a second order effect on $Re(\epsilon'/\epsilon)$. On the other hand, uncertainties in the measurement of ϕ_ρ affect the ϕ_{+-} measurement to first order but almost cancel out in the measurement of $\Delta\phi$, the phase difference beween ϕ_{+-} and ϕ_{00}.

Since the regenerator is only present in the regenerator beam, the level of detector activity due to interactions between the neutral particles (other than kaons) in the beam and the beam elements are different in the vacuum and regenerator beams. These and other interactions that result in extra detector activity which is uncorrelated with kaon interactions are referred to as **accidental** events. The different level of accidental activity in the two beams introduces a bias in $Re(\epsilon'/\epsilon)$. To determine the bias, the effect of accidental activity on the detector response and acceptance needs to be understood.

2.2 Alternate Methods of Measuring $Re(\epsilon'/\epsilon)$

There are several other techniques of measuring $Re(\epsilon'/\epsilon)$. Some of these techniques can be applied to the KTeV experiment and therefore can be used as cross-checks of the nominal KTeV technique.

To be less reliant on the understanding of the detector acceptance in the KTeV experiment, one could re-scale the events in the vacuum beam so that the regenerator and vacuum beam distributions would have similar shapes. In this way, the acceptance would affect both beams in the same way and biases due to the acceptance cancel out in the double ratio. Although this method leads to a reduced dependance on the Monte Carlo simulation, the statistical error increases by a factor of $\sim$1.7. The re-scaling of events in one beam to match the decay distributions of events in the other beam is also performed in the NA48 experiment described below. The measurement of $Re(\epsilon'/\epsilon)$ at KTeV using the "re-scaling" method is discussed further in Chapter 10.

$Re(\epsilon'/\epsilon)$ can also be measured in KTeV using the interference in the regenerator beam. If a shorter regenerator is used, the number of K_L decays increases at the expense of the CP-conserving K_S decays. Regenerator beam-vacuum beam flux differences due to the attenuation of the regenerator are avoided by just using one beam to measure $Re(\epsilon'/\epsilon)$. However, this method is statistically less favourable than the nominal KTeV technique and in addition, the rate of diffractive scatters increases.

The following methods of measuring $Re(\epsilon'/\epsilon)$ require a different experimental design.

The NA48 experiment at CERN measures $Re(\epsilon'/\epsilon)$ using two separate targets to produce K_S and K_L; the targets are located at different distances from the detector, By tuning the kaon production angles and alignment of the two beams, the detector illuminations and energy spectra for $K_S \to 2\pi$ and $K_L \to 2\pi$ decays are made very similar. Any remaining acceptance differences are removed by re-scaling the $K_L \to 2\pi$ events to match the $K_S \to 2\pi$ decay distributions, and by using a Monte Carlo simulation. The NA48 measurement technique was designed to be less sensitive to the understanding of the acceptance than KTeV. However, the drawback in the NA48

technique is that differences in the flux and underlying event activity in the K_L and K_S beams need to be understood very well.

$Re(\epsilon'/\epsilon)$ can also be measured using K^0 (or $\overline{K^0}$) produced from a target and measuring the interference of K_L and K_S decays to 2π. In this case, the rate of decays to 2π, $R_{K\to 2\pi}$(t), is given by

$$R_{K\to 2\pi}(t) \propto [e^{-\frac{t}{\tau_S}} + |\eta|^2 e^{-\frac{t}{\tau_L}} + 2e^{-\frac{t}{2}(\frac{1}{\tau_S}+\frac{1}{\tau_L})}|\eta| cos(\Delta m t - \phi_\eta)], \tag{2.10}$$

where t is the proper time. By selecting $K \to 2\pi$ decays with proper time, t, $\approx 11\tau_S$, the first and last terms of Eq. 2.10 are comparable and one can determine η. However, this method has a serious drawback in that one must know the amount of the K^0 in the beam and the $\overline{K^0}$ contamination from the target precisely. One way of identifying K^0 is by triggering off Λ and other strange particles which are produced in the same target interaction. However, this method of identifying K^0 will not work if more than 2 strange particles are present. The use of a very low energy beam below the $K^0 - \overline{K^0}$ production threshold is also useful in reducing $\overline{K^0}$ contamination. The backgrounds from target interactions must also be understood well. Both of these problems are practically very difficult to solve.

Finally, by producing Φ from e^+e^- collisions and then observing the 2π decays of K_S and K_L which are produced to back-to-back, $Re(\epsilon'/\epsilon)$ can be measured. This method is being used by the KLOE experiment [53] at Frascati, Italy.

CHAPTER 3
KTEV EXPERIMENTAL APPARATUS

The KTeV experimental apparatus was designed to measure $Re(\epsilon'/\epsilon)$ (E832) at a high precision as well as to search for and measure rare kaon decays (E799). This chapter will describe the elements of the apparatus that are important in making a measurement of $Re(\epsilon'/\epsilon)$.

To describe the location of the beam and detector elements, it is necessary to define a coordinate system. The KTeV coordinate system is right-handed and is defined such that the target is at the origin. The neutral beam travels horizontally in the positive z-direction. The positive y-direction is vertically upwards.

3.1 The Beamline

The KTeV experiment used two neutral beams which were precisely matched in size and kaon momentum to make systematic effects due to beam-to-beam differences as small as possible. To reduce the rate of accidental activity, the neutral beam should be as free from photons as possible and maximise the kaon to neutron ratio in the beam. In addition, the two neutral beams should have a minimal beam halo. The beam halo causes radiation damage to the cesium iodide (CsI) calorimeter and increases the trigger rate. These requirements were achieved by employing a stable targetting system and a well-tuned collimation system. The KTeV beam geometry is shown in Figure 3.1.

3.1.1 Primary Beam and Target

The primary 800 GeV-proton beam came from the Fermilab Tevatron. The Tevatron had an RF frequency of 53 MHz and the protons arrived in ~1 ns pulses every 18.9

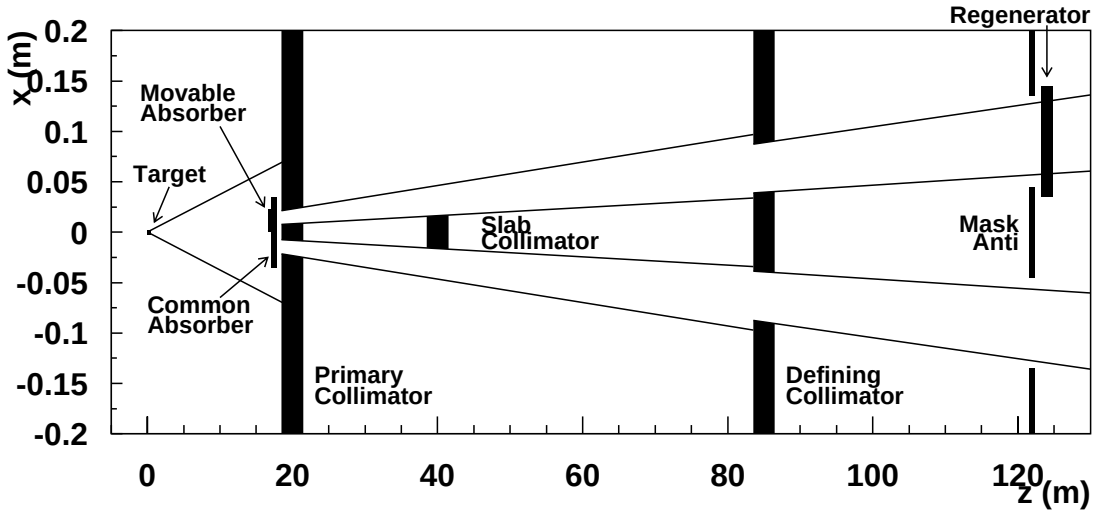

Figure 3.1: Plan view of the KTeV secondary beamline.

ns. During the 1996 and 1997 KTeV runs[1], the Tevatron had a 1-minute spill cycle in which the protons were injected and accelerated for 40 s and then delivered to the target for 20 s. These periods are referred to as off-spill and on-spill, respectively.

The protons impinged upon a beryllium oxide (BeO) target at a rate of $\sim 2\times 10^{11}$ Hz when running at normal intensity. The target had a cross section of 3 mm$\times$3 mm and was 30.5 cm (1.1 interaction lengths) long. BeO was chosen because it has a high density, a short interaction length and a low atomic number, Z, in order to reduce neutron production. Kaon production is optimized at $\sim$1.35 interaction lengths [54] but since a shorter target was more practical, a 1.1 interaction-length target was used. BeO is also cooled easily, so potential melting due to energy deposited by 800 GeV protons was adequately dealt with.

The proton beam was at a vertical angle of 4.8 mrad to the secondary beam in order to reduce the secondary neutron flux which peaks when the proton beam is parallel to the secondary beam. The kaon-to-neutron ratio improved by an order of magnitude by targetting the proton beam at 4.8 mrad. The proton beam at the target had an RMS width of less than 250 μm horizontally and vertically. The beam

[1]See Chapter 5.

position was stable to within 100 μm horizontally and vertically. This was a vast improvement compared to the the E773 experiment where the beam moved about by ± 600 μm [55]. The stability of the beam was very important in reducing the smearing of the secondary beam profile on the detectors.

About half of the $\sim 3 \times 10^{12}$ protons per spill interacted in the target while the rest was absorbed in a beam dump.

3.1.2 Secondary Beam

The secondary beamline in KTeV consisted of sweeping magnets, collimators and absorbers which defined two neutral beams and increased the kaon-to-neutron ratio of the beam.

Besides primary protons, the beam contained muons and other charged particles that were produced in the absorbers, collimators and upstream decays. A series of sweeping magnets removed these charged particles from the secondary beam. The last sweeping magnet was located 90 m away from the target just upstream of the decay volume used in the analysis. After removing charged particles from the beam, the neutral secondary beam consisted mainly of neutrons and kaons.

At $z = 18.7$ m, the KTeV beam passed through the Common absorbers which were used to eliminate photons and reduce the neutron flux in the secondary beam . The Common absorbers were made of 3" of lead, which was used to absorb photons, and 21" of beryllium, which increased the kaon-to-neutron ratio. The Common absorbers transmitted $\sim$19% of the incident kaons and $\sim$10% of the incident neutrons [55]. In addition to the Common absorbers, there was also a 18" beryllium absorber which alternated from beam to beam every spill and was sychronized to the regenerator motion. This absorber is referred to as the "shadow absorber" and its purpose was to reduce the flux incident on the regenerator, thereby reducing the accidental and inelastic scattering rate in the regenerator. The attenuation of the shadow absorber was 2.3. The kaon-to-neutron ratio was $\sim$0.77 in the vacuum beam and $\sim$1.25 in the regenerator beam after the absorbers [56].

The experiment also required a well collimated beam that passed cleanly through

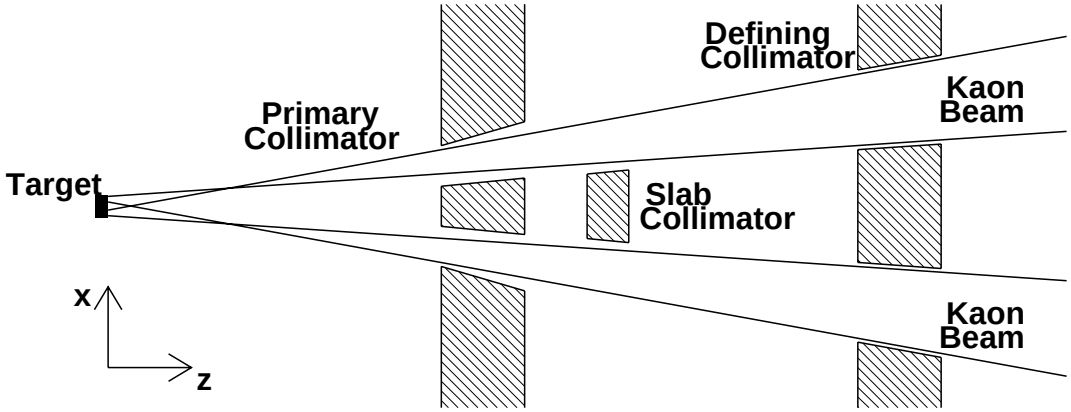

Figure 3.2: Schematic of the KTeV collimation system illustrating the taper of the collimators and the slab collimator. Both reduce collimator scattering. The figure is not to scale and the absorbers are not shown.

the CsI calorimeter beam holes. The collimation system is illustrated schematically in Figure 3.2. The primary collimator, located just downstream of the absorbers, provided the initial collimation and helped to reduce the beam halo. The taper of the collimators minimized backgrounds from kaons which scatter in the collimator. Downstream of the primary collimator was the slab collimator which was a 10 ft long steel block placed between the 2 neutral beams. The slab collimator prevented kaons which scattered in the primary collimator from crossing over from one beam to the other beam. The final beam size was set by the defining collimator which was located at z=85 m. The defining collimator was as far downstream as possible so that the motion of the primary beam would have a minimal effect on the two neutral beams emerging from the collimator. After passing through the defining collimator, the two secondary neutral beams subtended an angle with respect to the target of ± 0.8 mrad horizontally (i.e., in the x-direction). The effect of the well-collimated beam can be seen in Figure 3.3, which shows the kaon centre-of-energy distribution at the CsI calorimeter using reconstructed $K_L \to \pi^0\pi^0\pi^0$ decays. Only a very small fraction of kaons lay outside the calorimeter beam hole region, showing that the radiation

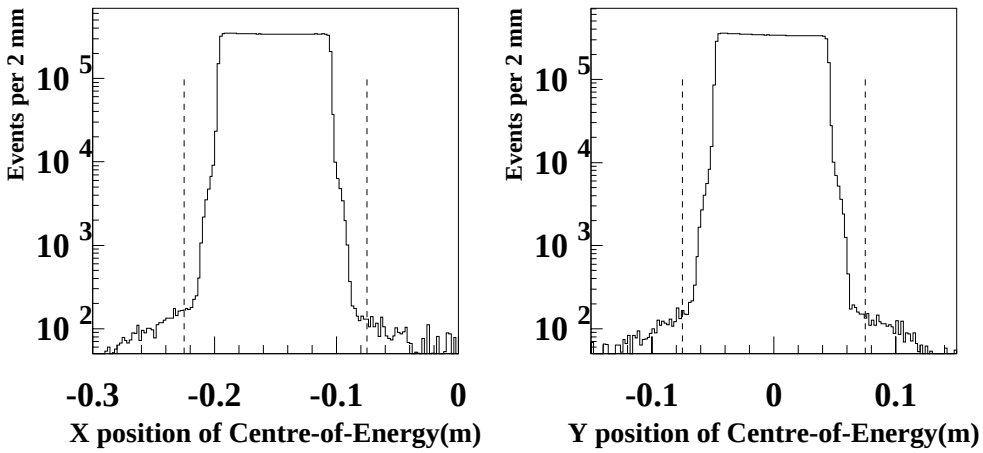

Figure 3.3: $K_L \to \pi^0\pi^0\pi^0$ X- and Y-centre-of-Energy distributions at the calorimeter for vacuum beam data after subtraction of background due to scattering in the regenerator. The dashed lines indicate the position of the edges of the calorimeter beam hole.

damage to the CsI crystals due to the secondary beam was minimal. The absence of a significant beam halo was a major improvement over previous Fermilab kaon experiments (E731 and E773).

3.2 The KTeV Detector

The KTeV detector shown in Figure 3.4 was located more than 90 m away from the target. At this distance, almost all the K_S produced at the target have decayed away.

The KTeV beam elements downstream of the primary collimator and the fiducial decay region were in an evacuated section which began with a vacuum pipe at z=28 m and extended into the decay tank which ends at z=159 m. The pressure in the tank during data-taking was $\sim 10^{-6}$ torr to reduce scattering within the decay region. The kevlar-mylar vacuum window at the end of the vacuum decay region was 1.4×10^{-3} radiations length thick.

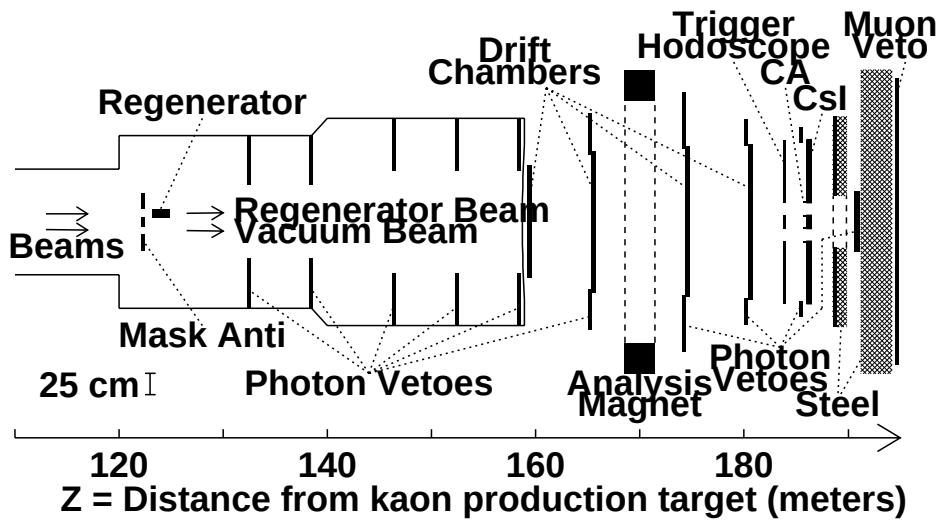

Figure 3.4: Plan view of the KTeV detector.

3.3 Regenerator

In order to collect K_S and K_L decays simultaneously, we used a regenerator in one of the beams to produce K_S. The downstream end of the regenerator was located at z=125.476 m and the regenerator was 1.70 m long with a transverse cross-section of 10 cm$\times$10 cm. The transverse cross-section was larger than the size of the neutral beam at the regenerator, so the beam was fully contained in the regenerator[2].

The length of the regenerator was chosen to be 1.83 interaction lengths as a compromise between the reduction of diffractive scatter background and the increase of coherent yield. The number of regenerated K_S arising from single diffractive scatters is minimized for a 2 interaction length regenerator (Equation 2.7) with the number of single diffractive scatters increasing by $\sim$ 5% for a regenerator of 1.83 interaction lengths. On the other hand, the number of coherent scatters is maximised with a 1.6 interaction length regenerator, with the coherent yield only decreasing by $\sim$ 1%

[2]On extremely rare occasions, kaons could scatter in the defining collimator and miss the regenerator.

for a 1.83 interaction length regenerator. Inelastic scatters were less of a consideration when choosing the length of the regenerator because inelastic interactions could be reduced by rejecting events with considerable energy in the regenerator.

The regenerator consisted of 84 modules of plastic scintillator and a final module at the downstream end. The final module was made of a lead-scintillator sandwich consisting of two 6 mm lead pieces and two 4 mm pieces of scintillator that were interleaved as shown in Figure 3.5. The regenerator was made "active" by attaching 2 phototubes (PMTs) to each module above and below the scintillator. The PMTs were used to veto inelastic kaon and neutron regenerator interactions and to reject kaons that decayed within the regenerator. By vetoing inelastic interactions, not only was the inelastic background in the regenerator beam suppressed, but the number of scattered kaons that crossed over from the regenerator beam into the vacuum beam was also reduced. Reducing the inelastic background helped in understanding the diffractive scattering background as well. It was also important to reject kaons that decayed within the regenerator since we would otherwise have to understand the acceptance for such decays by simulating decays within the regenerator in detail.

The PMTs helped to reject inelastic interactions and $K \to \pi^+\pi^-$ decays in the regenerator by detecting the energy deposited by the charged particles produced in decays and regenerator interactions. $K \to \pi^0\pi^0$ decays within the regenerator were suppressed since the photons from the decay were converted in the lead pieces. There was also some photon conversion in the scintillator.

Although we tried to reject decays within the regenerator, there was a small probability that $K \to 2\pi$ decays which occurred in the last regenerator module would not be vetoed. As a result, the effective regenerator edge, shown in Figure 3.5, was inside of the final regenerator module. The effective regenerator edge was different for the charged and neutral modes because of the different regenerator veto efficiencies. The effective regenerator edge needed to be determined accurately when predicting the number of $K \to 2\pi$ decays (Section 10.1.2) because a small change in the effective regenerator edge position caused a large change in the number of K_S decays predicted. The determination of the effective regenerator edge position is described in the Chapters 6 and 7.

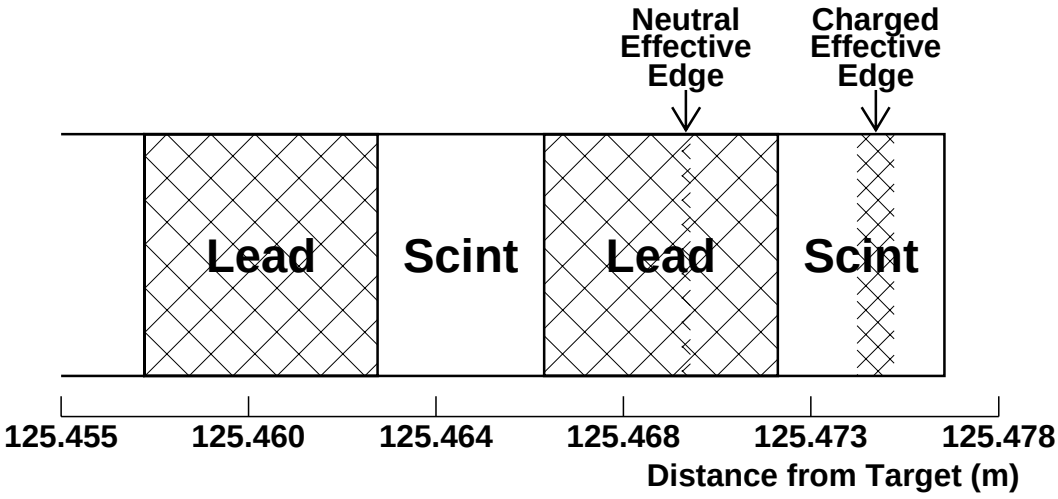

Figure 3.5: Downstream end of the regenerator showing the final regenerator module and the charged and neutral mode effective edges.

The net transmission of the neutral beam after passing through the regenerator and the shadow absorber was $\sim 7.8\%$ for K_L and $\sim 3.1\%$ for neutrons. About 0.1% of the coherent kaons that emerged from the regenerator are K_S.

3.4 Charged Spectrometer

To reconstruct $K_{L,S} \to \pi^+\pi^-$ decays, KTeV used a charged spectrometer. The KTeV charged spectrometer consisted of four drift chambers with an analyzing magnet between the second and third drift chambers. A brief description of the spectrometer and its calibration is presented below. Further details of the charged spectrometer can be found in [39].

3.4.1 Drift Chambers

Each drift chamber contained two planes of horizontal and vertical sense wires which were used to determine positions in the x- and y-views. The drift chamber wires were strung in a hexagonal cell pattern with six field wires surrounding each sense wire as shown in Figure 3.6. Each plane of sense wires within a drift chamber were arranged

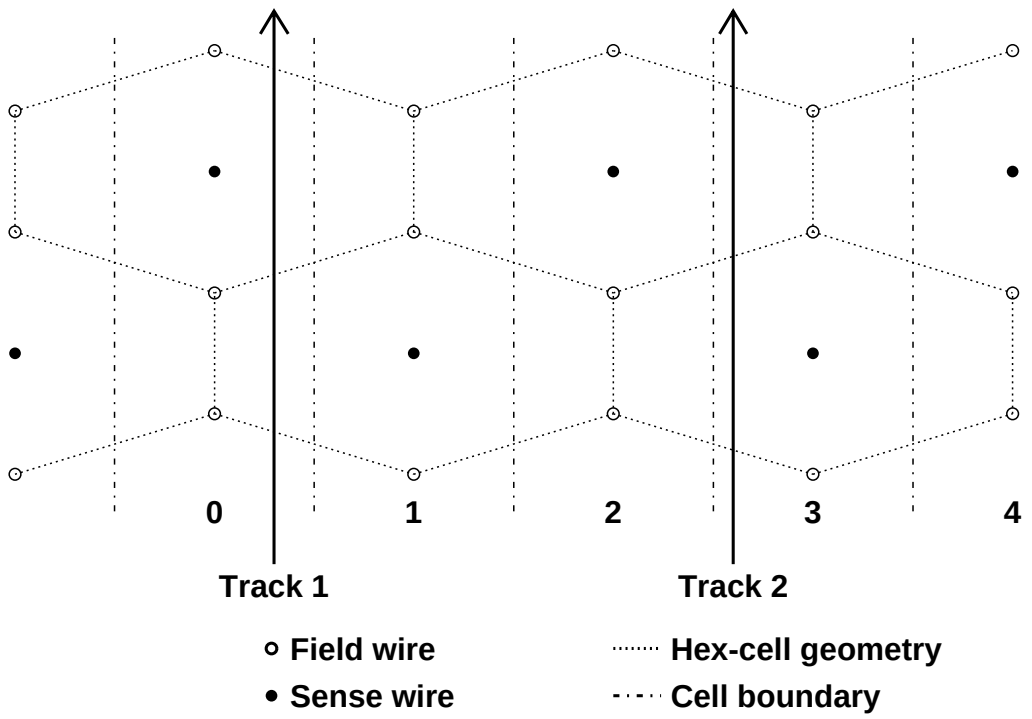

Figure 3.6: The drift chamber hexagonal cell geometry with the sense wire in the centre and the field wires at the vertices of the hexagon. In the track separation cut (Chapter 6), the edges of the "cell" are defined by the dashed vertical lines shown. The distance between two adjacent dashed lines is 6.35 mm. The two tracks in the figure are 3 "cells" apart.

such that the two planes with the same view were offset by 6.35 mm which was half a cell spacing. By offsetting the two similar planes in the drift chamber, one was able to determine on which side of a sense wire a track passed.

The drift chambers were filled with a 50-50 mixture of argon and ethane, and there were bags of helium between the chambers in order to reduce multiple scattering. The drift chambers were operated between -2450 V and -2500 V, resulting in a nearly constant drift velocity of $\sim$50 μm/ns over the drift cell. The drift times were measured using TDCs which had a precision of 0.5 ns/count.

3.4.2 Analysis Magnet

The KTeV analysis dipole magnet was operated at 1600 A and provided a momentum kick in the x-direction of ~412 MeV/c to charged particles. The transverse momentum kick was determined from $K_{L,S} \to \pi^+\pi^-$ data by setting the mean $\pi^+\pi^-$ mass to the kaon mass. The uniformity of the field was much better than 1%. A correction was applied because of a small fringe field which extended to chambers 1 and 4.

3.4.3 Calibration and Alignment

The drift chamber TDC calibration was a 2-step process. The first step was to align the timing of each wire by determining the timing offset for each wire. The next step was to determine the relationship between the drift distance, x, and the drift time, t. This was done assuming that the track illumination was uniform across each cell. The TDC values were corrected for missing hits in a cell as well as for the propagation time along the wire. Inefficiencies close to the sense wires were accounted for as well. After calibration, the resolution of each chamber plane was ~110 μm.

Having calibrated the drift chambers, we needed to determine their alignment. The transverse alignment was determined using muons from special runs with the analysis magnet turned off. From these special muon runs, the transverse offsets and the rotations of chambers 2 and 3 with respect to chambers 1 and 4 were determined. The relative transverse alignment was measured to 10 μm and the relative rotation of the chambers was determined to 20 μrad. Two-track events originating from a single common vertex were then used to determine the relative rotation about the z-axis of chambers 1 and 4. In doing this, we implicitly assumed that any rotation between chambers 1 and 2, which was not accounted for by muon runs, was due to corkscrew rotations between chambers 1 and 4. After determining the transverse offsets and relative rotations of the drift chambers, we found the alignment with respect to the target and calorimeter by projecting the kaon momentum back to the target z-position and using electrons from $K_L \to \pi^\pm e^\mp \nu$ decays to point to the calorimeter. The drift chamber positions were adjusted such that the reconstructed target and calorimeter positions agreed with the survey positions.

3.5 Cesium Iodide Calorimeter

$K_{L,S} \to \pi^0\pi^0$ events were reconstructed using a pure cesium iodide (CsI) calorimeter. The calorimeter and its performance will be described in detail in the following chapter.

3.6 Trigger and Veto Counters

Besides the charged spectrometer and calorimeter which were used to reconstruct charged and neutral mode decays, the KTeV detector employed trigger and veto counters to select signal events, reduce backgrounds, and define sharp apertures for selecting events.

3.6.1 The Mask Anti

In order to limit the upstream acceptance for the vacuum beam, as well as to prevent decays upstream of the regenerator from crossing over from one beam to another, a mask anti (MA) was placed at z=122.65 m. The geometry of the MA is shown in Figure 3.7. The MA consisted of a lead-scintillator sandwich which was 16 radiation lengths thick. Photons converted in the lead while charged particles deposited energy in the scintillator. The energy in the scintillator was detected by phototubes that were attached to the scintillator. As seen in Figure 3.7, the MA beam holes were larger than the beam size but smaller than the transverse dimensions of the regenerator, so kaons passing through the MA holes could not sneak by the regenerator.

3.6.2 The Collar Anti

To define the calorimeter inner aperture, we used two tungsten-scintillator detectors that were placed around the beam holes as shown in Figure 3.8. Each detector was called a collar-anti (CA) and there was one detector around each beam hole. Since the edges of the two CAs could be well-measured using K_{e3} electrons, the inner aperture could be sharply-defined. It was important to define the CsI inner apertures

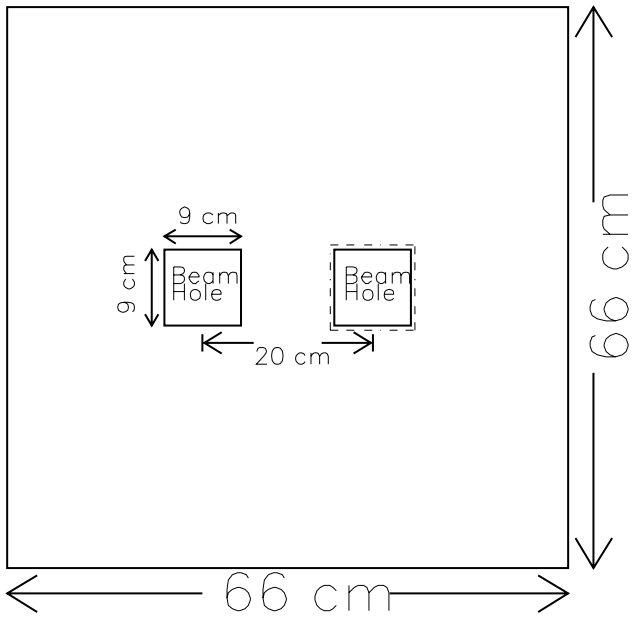

Figure 3.7: Geometry of mask-anti (MA) showing the beam holes. Both beam holes are 9 cm×9 cm in dimension. The dashed box indicates the tranverse dimensions of the regenerator. The MA is located at z=122.65 m

accurately since the acceptance varied rapidly near the hole due to the poor photon energy and position resolutions in this region of the calorimeter.

The CA was 1.5 cm wide and the inner edge was aligned with the calorimeter beam hole as shown in Figure 3.8. The CA was a 2.9 radiation length thick sandwich of tungsten and scintillator. Fibres transmitted the signals from the scintillators to phototubes placed at the outer edge of the calorimeter. To prevent photons from sneaking by the CA and hitting the calorimeter, the CA was placed directly in front of the crystals.

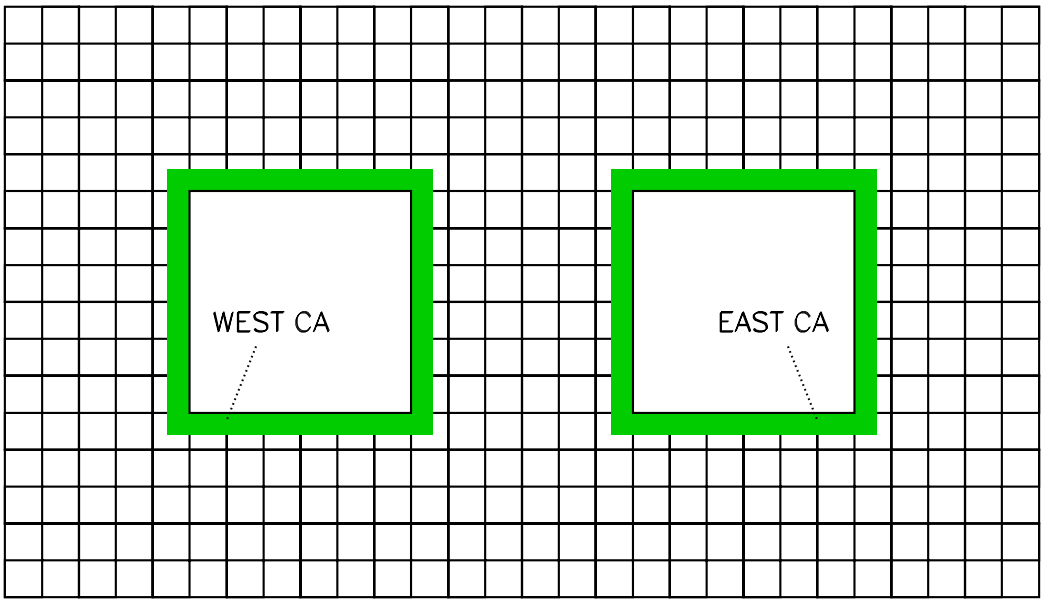

Figure 3.8: The geometry of the Collar Anti (CA) showing the 2 Collar-Anti around the CsI beam holes.

3.6.3 Trigger Hodoscopes

Trigger hodoscopes consisting of 2 vertical planes, labelled V and V', of 1 cm thick scintillator counters (0.013 radiation lengths) were used as part of the first level $K \to \pi^+\pi^-$ trigger. The arrangement of the trigger counters is shown in Figure 3.9. The two counters were offset in such a way that inefficiences due to dead space between the scintillation counters was minimized. The beam hole regions was cut out to reduce interactions from neutrons and kaons which would increase the radiation damage to the calorimeter.

3.6.4 Ring Counters and Spectrometer Antis

To suppress $K_L \to \pi^0\pi^0\pi^0$ decays, a series of photon veto counters were used. $K_L \to \pi^0\pi^0\pi^0$ decays where 1 or 2 photons were lost are a background to $K_{L,S} \to \pi^0\pi^0$ decays. Background due to inelastic scattering in the regenerator was also reduced by the veto counters. The 5 ring counters (RCs) were located along the vacuum decay region and the spectrometer antis (SAs) were positioned around the outer edges of the last three drift chambers and the calorimeter. With this arrangement, the vetos

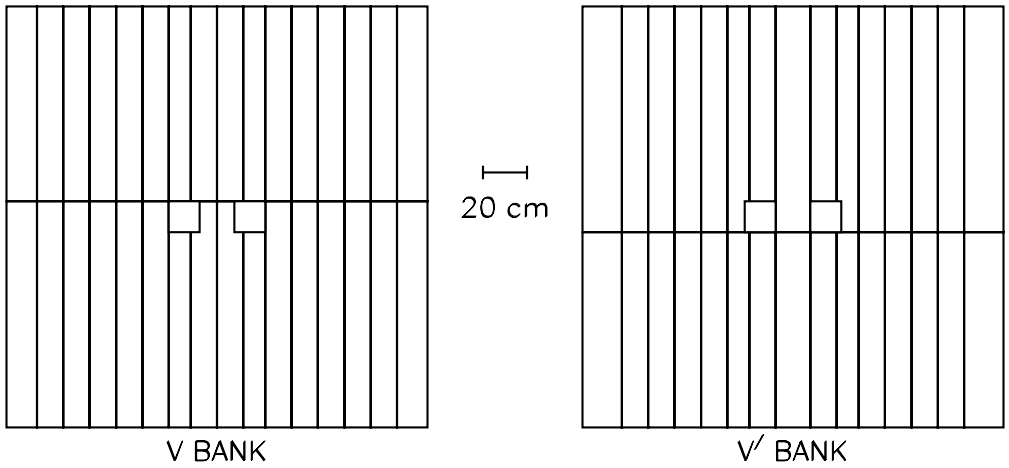

Figure 3.9: The geometry of the Trigger Hodoscope Counters (V,V')

were able to detect photons which were outside the CsI calorimeter acceptance region. The RCs and SAs consisted of a lead-scintillator sandwich of 16 radiation lengths and their signals were read out by phototubes and digitized. Photons which had energies > 160 MeV were rejected. The SA signals were part of the online trigger, and both the SA and RC vetoes were part of the offline analysis. The photon vetoes caused a factor of $\sim$1000 reduction in $3\pi^0$ background to $K_{L,S} \to \pi^0\pi^0$ decays.

3.6.5 The Back Anti, Hadron Anti and Muon Counters

The photon veto counters behind the calorimeter and the muon hodoscope counters are shown in Figure 3.10.

To reject events where one or more high-energy photons were lost down the CsI beam holes, a veto counter placed behind the calorimeter was used. This veto counter was called the Back-Anti (BA). The BA also served as a dump for the neutral beam. As shown in Figure 3.10, the BA was located behind a block of steel (MF1). The steel reduced any backsplash from the BA. The BA was made up of 30 radiation lengths of lead-scintillator sandwich but only the first 10 radiation lengths were used as a veto. Events with more than 5 GeV of equivalent photon energy in the BA

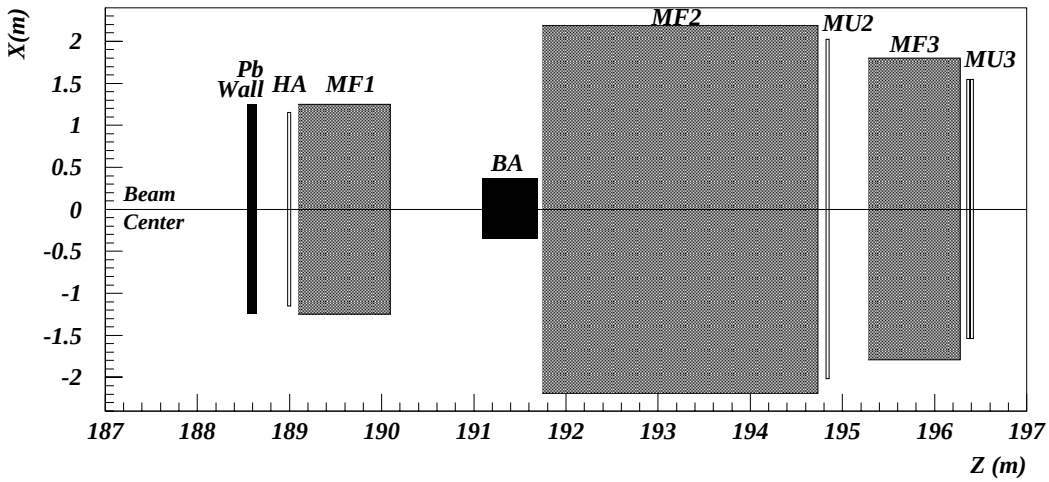

Figure 3.10: The Back-Anti (BA), Hadron-Anti(HA) and Muon systems. MF1, MF2 and MF3 are steel blocks.

were rejected. The BA was not part of the online trigger, but was very useful in suppressing $K_L \to \pi^0\pi^0\pi^0$ background in the offline analysis.

The hadron anti (HA) was a veto counter used for vetoing charged pions from $K_L \to \pi^\pm e^\mp \nu$ events. It was part of the online $K_{L,S} \to \pi^0\pi^0$ trigger during the 1997 E832 run. It consisted of scintillation counters placed behind the calorimeter. There was also a lead wall between the CsI and the HA to absorb electromagnetic showers from the back of the calorimeter. The lead wall was also used to cause hadrons to shower.

At the far downstream end of the KTeV detector were 3 blocks of steel, which were between 1 m and 3 m thick. The first block of steel (MF1) was in front of the BA. Behind the second (MF2) and third (MF3) blocks were scintillation counters which were used to identify muons. The first plane of muon counters (MU2) was part of the online charged mode trigger and helped reduce $K_L \to \pi^\pm \mu^\mp \nu$ background to $K_{L,S} \to \pi^+\pi^-$ decays. MU3 information was used in the offline charged mode analysis.

3.7 Trigger and Data Acquisition

When the experiment was running at nominal intensity, there were $\sim 2.5 \times 10^6$ kaons in the vacuum beam and $\sim 1 \times 10^6$ kaons in the regenerator beam (upstream of the regenerator) every second. Of these kaons, $\sim 10^5$ decayed in the KTeV decay volume. There were also a few MHz of detector activity due to neutron interactions. The data acquistion (DAQ) and data storage system could not handle the full rate of events and large data volume due to the high intensity at which KTeV ran. In order to reduce the number of events that reached the DAQ system, a 3-level event filtering scheme (trigger) was employed. The first level (Level 1) consisted of detector signals which required minimal processing (e.g., phototube output signals which passed through a discriminator). The Level 1 trigger operated at 53 MHz and was deadtimeless. On acceptance of an event by the Level 1 trigger, the digitization and readout process began. During typical running, the Level 1 rate was ~60 kHz.

The second level (Level 2) trigger consisted of several specially designed hardware processors which analyzed the detector signals and performed logic operations with them. The time taken for this stage varied for each Level 2 processor and ranged from ~500 ns to ~1.5 μs. While Level 2 processors were analyzing the data, the trigger did not accept any new events. If the event passed the Level 2 trigger, the digitization and data transfer to memory modules that buffered one spill of data, was allowed to finish. This took an additional ~15 μs. However, if the event failed the Level 2 filter, the detector signals were cleared and the readout process aborted. This took a few hundred nanoseconds. The rate of events passing the Level 2 trigger was 10 kHz.

Once the event had passed Level 2 and had been read out to the memory modules, the trigger was "live" again and ready to accept more Level 1 and 2 triggers. Events passing the Level 1 and Level 2 triggers were then analyzed by 34 CPUs which formed the third level (Level 3) trigger. The Level 3 trigger reconstructed events using the online detector calibration and applied loose analysis cuts. Events passing Level 3 were written out to DLT tapes for future offline analysis. The Level 3 filter had to process all the events passing Level 2 within the spill duration of 1 minute. About 2000 events per second passed the Level 3 requirement.

Each event was ~ 7 kB in size and 300 MB were written out every spill. The total amount of data written out during the E832 1996 and 1997 data-taking periods was $\sim$40 TB and the E832 trigger had a live time of about 65%.

The KTeV triggering system had 30 different triggers which were used for calibration, analysis and online monitoring. In order to collect as many $K \to 2\pi$ triggers as possible, high-rate triggers such as triggers with loose requirements or triggers of CP-conserving decays were pre-scaled. By pre-scaling a trigger, only a fraction of events that passed the trigger were written out. An extensive discussion of the KTeV trigger is presented in [57].

CHAPTER 4
CSI CALORIMETER

$K_{L,S} \rightarrow \pi^0\pi^0$ decays were reconstructed by determining the position and energy of the photons using a high precision cesium iodide (CsI) calorimeter. This chapter describes the KTeV CsI electromagnetic calorimeter, the calibration of the energy readout and the reconstruction of electromagnetic energy using the calorimeter. The effect of radiation on the performance of the calorimeter is also presented.

4.1 Crystals

The KTeV electromagnetic calorimeter consisted of 3100 pure cesium iodide crystals that were produced by 3 manufacturers: Horiba, Crismatec and Bicron. There were 2232 2.5 cm $\times$ 2.5 cm crystals in the centre and 868 5 cm $\times$ 5 cm crystals surrounding the smaller crystals as shown in Figure 4.1. The calorimeter measured 1.9 m $\times$ 1.9 m in transverse dimension. Each crystal was 50 cm (27 radiation lengths) long. Two 15 cm $\times$ 15 cm square beam pipes that were separated by 30 cm[1] allowed particles in the beam that had not decayed to pass without striking the crystals. The beam pipes were made of an ultra-high modulus carbon fiber/epoxy combination because they had to be as thin as possible to reduce radiation damage to the crystals as well as to minimize dead space, while at the same time, supporting the load of the crystals ($\sim$210 kg) above each pipe.

The CsI calorimeter was located in a light-tight steel blockhouse. The humidity and temperature in the blockhouse was strictly controlled since CsI was slightly hygroscopic and the light output of the crystals decreased by 1.5% per degree Celsius temperature increase. When the calorimeter was in operation, the lights in the blockhouse were turned off.

[1]The 30 cm separation of the beam pipes refers to the distance between the centres.

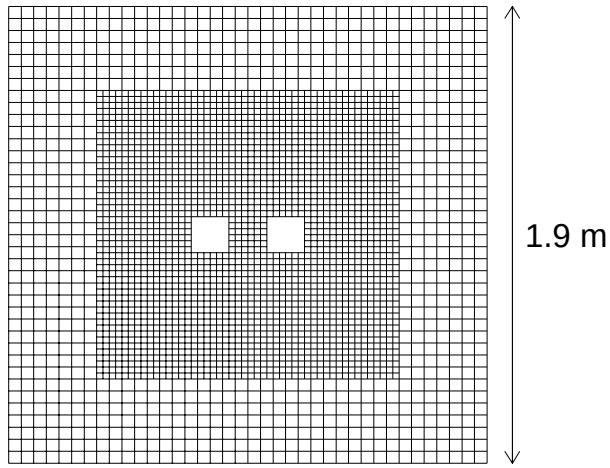

Figure 4.1: Cross-section of the 1.9 m×1.9 m CsI calorimeter.

Pure cesium iodide was well-suited for the KTeV experiment because it is a fast inorganic scintillator with a large light output compared to other fast scintillators, has a short radiation length and a moderate Moliere radius, and is radiation hard. The CsI scintillation light has two components: a fast component of peak wavelength, 315 nm, with decay constants of 10 ns and 36 ns, and a slow component of peak wavelength, 480 nm, with a decay time of 1 μs. 80% of the CsI scintillation light is due to the fast component making it suitable for the high-rate data-taking requirements of KTeV. Pure CsI has a radiation length of 1.85 cm and nuclear interaction length of 36.5 cm. This made it possible to distinguish electrons and photons, which produce electromagnetic showers, from pions, which only shower hadronically ∼67% of the time; ∼33% of the charged pions in the calorimeter are minimum ionizing. The Moliere radius of CsI is 3.8 cm, which reduced the number of overlapping showers, and yet allowed tbe use of 2.5×2.5 cm^2 crystals to provide good position resolution at the centre of the calorimeter.

Before installing the crystals in the blockhouse, we prepared the crystals and tested their performance in a crystal laboratory. The preparation of crystals involved wrapping each crystal in aluminized mylar to improve the longitudinal light response. The light output and length-wise response of the crystals were measured prior to

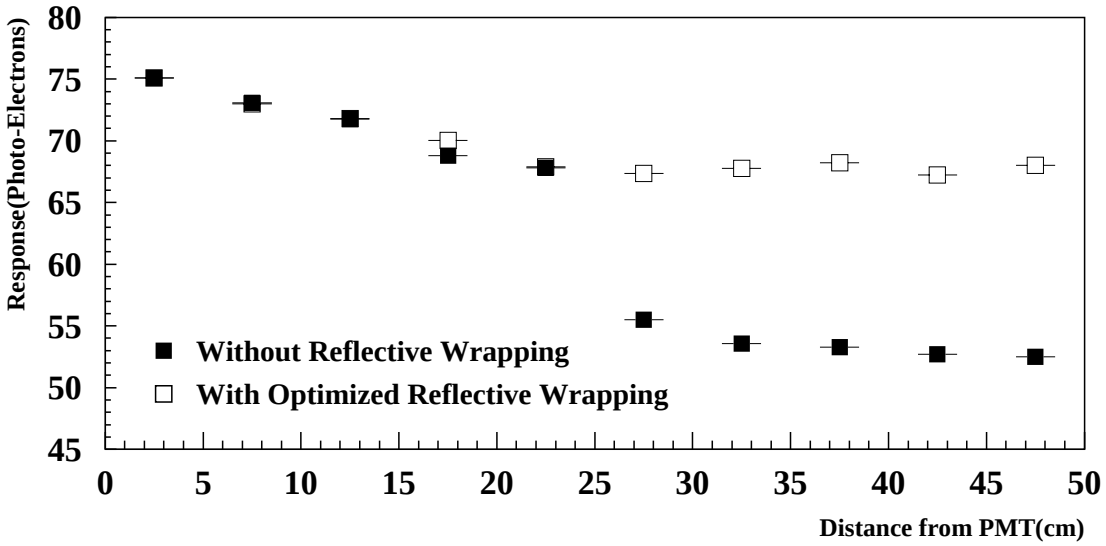

Figure 4.2: CsI longitudinal response of a 50 cm crystal made up of 2 25 cm pieces glued together. The response, which was measured with a ^{137}Cs source, is shown before and after wrapping with aluminized mylar. The curves are normalized such that the response is the same closest to the PMT. The error bars based on Poisson statistics are not shown.

installation.

80% of the crystals that were used were made up of two 25 cm pieces that were glued together; the remaining 20% of the crystals consisted of a single 50 cm crystal. The glue that was used has a refractive index of 1.5 whereas CsI has a refractive index of 1.85. This resulted in diffuse scattering at the glue joint. To improve the optical contact and minimize the scattering at the glue joint, the surfaces being glued together were polished. Because of the difference in the refractive indices, there was a step in the light collection efficiency at the position of the glue joint as shown in Figure 4.2. Crystals that were made up of a single 50 cm block of CsI showed a significant but smooth change in light collection efficiency along the length of the crystal.

The longitudinal response of a crystal affects the energy resolution and linearity. Therefore, it was important to make sure the energy response along the length of the crystal was as uniform as possible. To improve the energy resolution and linearity,

the response of each crystal was modified by wrapping each crystal with ~12 μm of aluminized mylar and adjusting the wrapping to optimize the longitudinal light response of the crystal. The mylar was black in order to prevent optical cross-talk between neighbouring crystals and the fraction of the wrapping that was reflective varied from crystal to crystal. Although higher reflectivity materials could have been used, aluminized mylar was chosen because it was thin and there was no optical contact with CsI surface. Since there was no optical contact with the crystals, the optical properties of the wrapping were not affected by radiation damage to the crystals. A thin wrapping material was selected so that less energy was absorbed by the wrapping; the fraction of dead material in the calorimeter was ~0.06%.

Before wrapping each crystal, we measured the energy response at ten different points along the length of the crystal in two different ways: measuring the (662 keV) photopeak of a ^{137}Cs source and determining the MIP peak of transverse cosmic ray muons. To increase the sensitivity to measuring the ^{137}Cs photopeak by collecting as much light as possible, a 2" phototube which covered the face of the crystal was used.

Optimizing the longitudinal light response involved varying the length and amount of reflector used, and the reflectivity at the upstream end of the crystal. To increase the response farther away from the phototube, the aluminized area at the upstream face of the crystal was increased, while to decrease the response, black ink was used to darken the aluminized section. Typically the aluminization would be higher upstream (farther away from the phototube), so that light that would otherwise not reach the phototube would be reflected downstream.

The longitudinal response of each crystal was adjusted until the predicted resolution for the crystal was within 20% of the resolution expected for a crystal with a uniform longitudinal response. The resolution was predicted using GEANT photon showers generated at six discrete energies: 2 GeV, 4 GeV, 8 GeV, 16 GeV, 32 GeV and 64 GeV. The energy distribution of the showers used matched that expected in $K_{L,S} \rightarrow \pi^0\pi^0$ events at KTeV. Although a crystal's longitudinal response was compared to that of a crystal with uniform response, the resolution is actually, optimized if the response very close to the phototube is higher than at other parts of the crystal.

Increasing the response close to the phototube compensates for energy leakage at the downstream face of the crystal.

After iterating the wrapping process several times, the response along the 50 cm length was uniform to ∼5%. The effect of wrapping a typical crystal is seen in Figure 4.2.

Besides optimizing the longitudinal uniformity of the crystals, the dimensions along the length of each crystal were measured to ∼10 μm in the crystal laboratory. Because CsI was a soft material, some of the crystals were bowed in the centre. The bowing was reduced by applying pressure to the crystals.

We also compared the radiation hardness and light output of a sample of crystals from each of the three manufacturers. The mean light output of the crystals was different for each manufacturer, with Horiba crystals having ∼30% less light than the other 2 manufacturers. The radiation hardness was determined by irradiating a small sample of crystals and studying the energy response. Based on this statistically-limited study, Horiba crystals were found to be the most radiation hard.

Once we had wrapped and tested the performance of the crystals in the crystal laboratory, we were ready to stack the crystals in the blockhouse. The location of each crystal in the calorimeter was specifically chosen based on the dimensions, radiation hardness, longitudinal photon response and reflectivity of the upstream face of the crystals. Each crystal was graded according to its longitudinal uniformity, upstream face wrapping and radiation hardness, with the highest grade crystals being the most longitudinally uniform and radiation hard. The radiation hardness was predicted based on the aforementioned radiation tests involving a small number of crystals. The highest grade crystals with no reflective upstream face were placed in the centre of the array while the crystals on the outer part of the array were of lower quality. The upstream face of crystals in the centre were chosen not to be reflective, so that the reflectivity could later be increased if the light collection efficiency upstream dropped due to radiation damage. Once a short-list of acceptable crystals for each region of the calorimeter had been made, the crystals were selected based on their dimensions. The orientation and positioning of the crystals was designed to minimize the dead space between crystals. An algorithm which matched the corners of neighbouring

crystals and kept the rows as flat as possible was used. To reduce the gaps between crystals and correct any bending within them, the crystals were compressed vertically by the weight of the crystals above and squeezed together horizontally by applying pressure at one end of each row of crystals.

The crystals were stacked in rows over a period of several months in 1996. The performance of the crystals and readout in each newly-placed row was tested and the flatness and width of each row was determined before the next row of crystals was stacked. It was imperative to verify that the crystals were not damaged during stacking, since the crystals could not be replaced once a new row had been stacked on top.

4.2 Readout

The calorimeter readout consisted of photomultiplier tubes (PMTs) that converted the light from the crystals to analog current pulses, a custom-built integrated circuit which digitized the PMT current and a bus (VME) system which stored the CsI data before transferring them to tape. Figure 4.3 shows a sketch of the KTeV calorimeter readout system.

Each CsI crystal and its readout is referred to as a CsI "channel" or "block". We describe the 2.5 cm$\times$2.5 cm cross-section crystals as "small" crystals and the 5 cm$\times$5 cm cross-section crystals as "large" crystals.

4.2.1 Photomultiplier tubes (PMTs)

In order to reconstruct photon energies and positions accurately, Hamamatsu photomultiplier tubes with low noise and high linearity were used in the KTeV calorimeter. We employed 5-stage 3/4" R5364 PMTs for the small crystals while 6-stage 1.5" Hamamatsu R5330 tubes were used for the large crystals. Each phototube was attached to a high-voltage divider chain which was specially selected to optimize the linearity. There were 5 different divider chains to choose from.

The photomultiplier tubes were optically coupled to the crystals to optimize the light collection efficiency by using a silicone "cookie". A $\sim$1 mm thick Schott UV

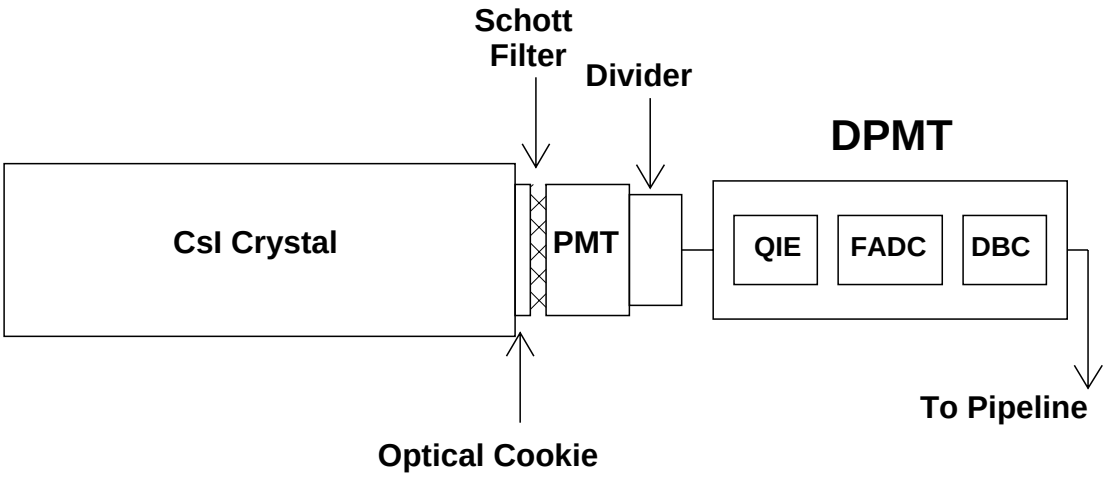

Figure 4.3: Layout of KTeV Readout System. The crystal, PMT and DPMT are inside the CsI blockhouse while the Pipeline system is outside the blockhouse.

filter was placed at the end of each phototube to reduce the slow component of the scintillation light by ∼50% [59]. The fast component was reduced by ∼15% by the filter. By reducing the slow component of light, the photon energy reconstruction was less susceptible to accidental effects due to calorimeter activity which occurred several 100 ns before the desired event.

Since the ∼25% quantum efficiency of the tubes coupled with the large light output of the CsI crystals led to a high light yield of about 25 photoelectrons/MeV, the typical phototube gains were between 2500 and 5000. To improve the linearity of the PMTs by operating them at higher gain, PMTs attached to crystals with high light output were partially masked to reduce the light output. The light output of 73% of small channels was reduced by 30%, and 3% of small channels had 60% of the light removed.

PMTs were matched to crystals in the calorimeter based on their linearities, rate stabilities and their expected operating voltages, which depended on the light output of the crystals. To match the photomultiplier tubes, small channels were divided into three zones based on their location with respect to the beam holes. There was only one zone for large channels. Crystals closest to the centre were assigned PMTs with

the best available nonlinearity and least PMT hysteresis while the most non-linear photomultiplier tubes were placed furthest away from the centre where the photon illumination was lowest.

To predict the non-linearity of a phototube when paired with a particular crystal, it was necessary to determine the expected peak current and gain of the phototube at that location. Based on the average photon energy from $2\pi^0$ events in each zone, the peak phototube currents predicted for the the three zones of small channels were 30 mA, 20 mA and 15 mA, with the peak current being highest closest to the centre. The peak phototube current for large channels was predicted to be 15 mA. The expected gain of the phototube was calculated assuming that the charge output for each channel was 12 fC/MeV.

When matching the PMTs to the crystals, we required that the expected operating voltage of the PMT be between the phototube specifications of 800 V and 1750 V. The operating voltage also affects the time between the scintillation pulse and the anode signal; the transit time varies by 4.7 ns between 800 V and 1700 V. To ensure that pulses for all channels had approximately the same transit time, we attempted to reduce the spread in voltages as much as possible. This was important because a large spread in the transit times would affect the efficiency of the Level 1 neutral mode trigger, which was made up of the analog sum of the dynode pulses.

Figure 4.4 shows that predicted range of nonlinearity and rate stability (the difference between the gain at the end and the start of a spill) after PMTs were matched to crystals. The expected a photomultiplier tube nonlinearity was better than 1%, and the rate stability was less than 0.5% in the presence of an average anode current of 3 μA. During data-taking, rate effects due to phototube hysteresis were stabilized by using a red LED which resulted in a constant anode current between 1 nA and 10 nA for each crystal.

4.2.2 Digitization

In order to collect a large amount of data with a high signal-to-noise ratio, the KTeV calorimeter required a high-rate, low-noise digitization system and a linearity better

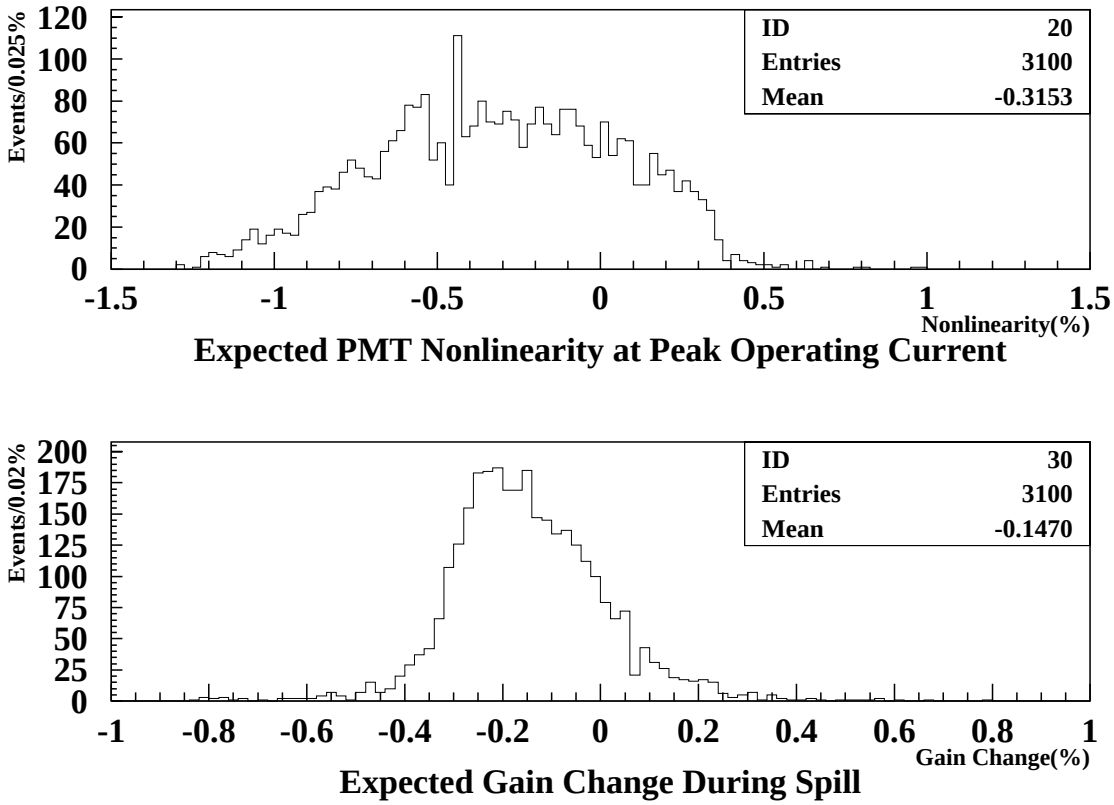

Figure 4.4: Expected nonlinearity at the peak operating current and rate stability (at 3 μA constant anode current) of CsI PMTs.

than 0.1%. The system also needed a large dynamic range to measure energies from a few MeV to 100 GeV.

These goals were met by the KTeV Digital Photomultiplier Base (DPMT) which was designed at Fermilab. The DPMT (Figure 4.5) was a multi-ranging, deadtimeless system which integrated the input phototube current, digitized the resulting charge and transferred the data to a buffer. The DPMT consisted of a conventional Flash ADC (FADC) and two custom application-specific integrated circuits (ASICS): the Charge-Integrator and Encoder (QIE) and the Driver/Buffer/Clock (DBC). As shown in Figure 4.3, the three DPMT components were mounted on a circuit board which was placed directly behind each PMT to minimize electronic noise that could be introduced by using long cables.

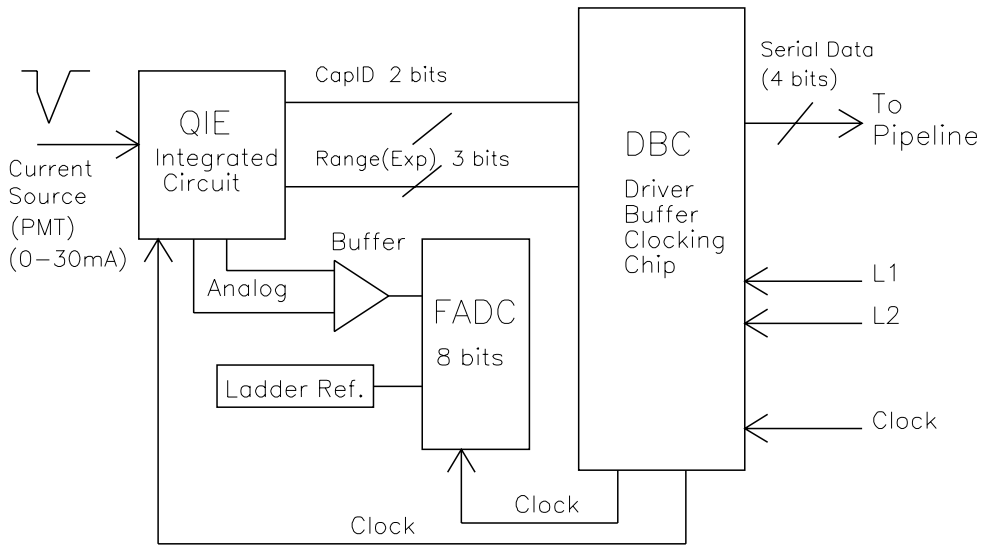

Figure 4.5: Block diagram of the DPMT.

To measure energies over four orders of magnitude accurately, the DPMT had 16 bits of dynamic range with an 8-bit resolution. The DPMT operated at the beam RF frequency, 53.1 MHz, to be less susceptible to out-of-time activity.

The Charge-Integrating Encoder (QIE)

The QIE [60] integrated the PMT current and determined the appropriate range of sensitivity needed to measure the charge. The QIE was a fully differential device, so temperature fluctuations, common mode noise and bias currents in the circuit did not affect the PMT current measurement.

The input PMT current, I, was first divided into 8 binary weighted ranges: $I/2$, $I/4$, $I/8$,...., $I/128$, $I/128$, before being integrated by 8 different 1 pF capacitors. Since the last 2 current ratios, $I/128$, were the same (due to space considerations on the chip), the integrating capacitance in the last range was doubled (i.e., to 2 pF). Based on the integrated charge over a clock period, the appropriate range of

QIE Range	Charge(pC)	Energy(GeV)
0	0 - 2.35	0 - 0.226
1	2.35 - 6.8	0.226 - 0.654
2	6.8 - 16.0	0.654 - 1.541
3	16.0 - 34	1.541 - 3.276
4	34 - 71	3.276 - 6.84
5	71 - 145	6.84 - 14.00
6	145 - 270	14.00 - 26.01
7	> 270	> 26.01

Table 4.1: Energy and Charge Ranges covered by each QIE Exponent. The ranges vary slightly from channel.

sensitivity was determined using a series of fast comparators. The selected range was digitized and grey-coded by a range encoder. An offset which was unique to each range was added to the analog output voltage, so that each QIE range (or QIE exponent) covered an exclusive range of the input charge while spanning the FADC region. The variation of the FADC value with the PMT charge (integrated over one clock cycle) in each QIE range is shown in Figure 4.6. Table 4.1 shows the typical energy and charge ranges corresponding to each QIE range[2].

To make the QIE operation deadtimeless, the system was pipelined by using four identical circuits to execute one of the four sequential operations performed by the QIE. The four operations performed by the QIE were the integration of all eight ranges, the selection of the proper range, the combination of the digitized exponent with the analog signal (due to the PMT current) and reference voltages across the integrators in the chosen range (multiplexing), and the resetting of all eight integrators for the next signal. Each of these operations took one clock period and each circuit performed a different one of the four operations during a clock cycle. The four circuits were identified by a phase or "capacitor identification" which ran from 0 to 3.

[2]There was a small channel-to-channel variation in the range of charges covered by each QIE exponent.

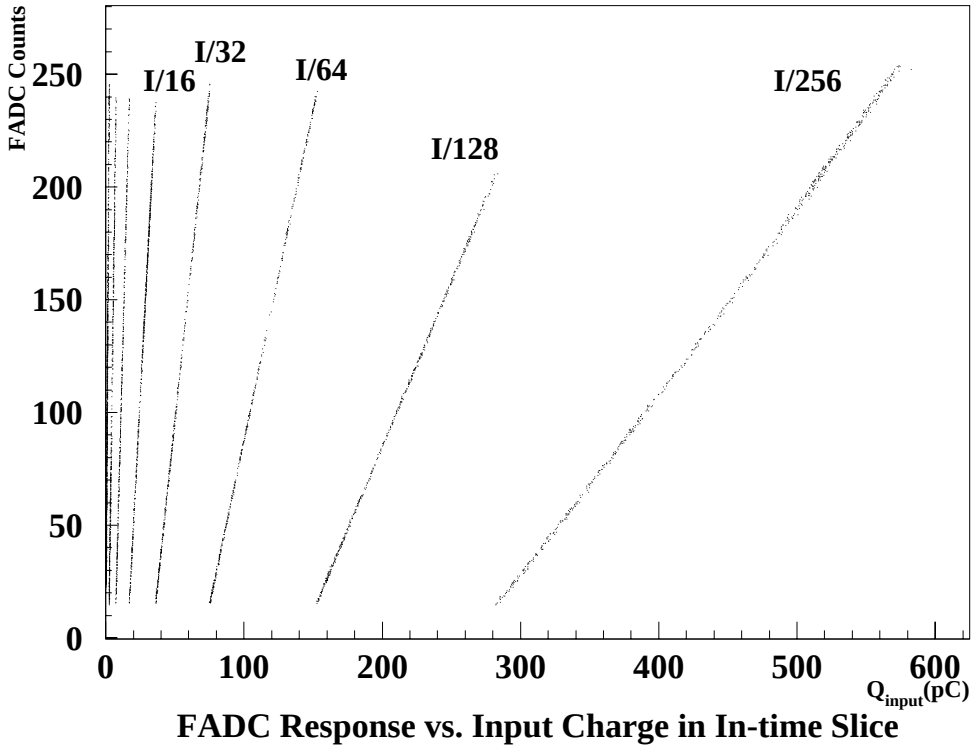

Figure 4.6: FADC response in all 4 QIE phases versus input charge in intime-slice (clock-cycle) for one channel. The response of each QIE phase in each range is very similar.

There were four sets of analog and digital data arising from the four identical circuits. The digital output of the QIE, which comprised a 3-bit "range" exponent and a 2-bit phase, was transferred to the DBC. The QIE analog output made up of a signal and a reference voltage, was converted to a single output using an operational amplifier before being transferred to the FADC for digitization. The sequential multiplexing of data from the same phase was achieved by using a timing circuit driven by a 4-stage ring-counter. The timing circuit also controlled the timing of the other three QIE operations.

The QIE was designed to minimize non-linearities in the charge integration. Although the linearity of the QIE was improved by making the device differential, non-linearities due to the finite impedance and parasitic capacitance of the current-

dividing circuit were still present.

Non-linearities due to the parasitic capacitance, C_p, arose because the capacitance affected the current integrated over each clock cycle. Since the shape of the PMT current pulse was not constant over an integration period, there was a voltage difference between the start and end of an integration period due to the finite impedance of the circuit. The voltage difference, Δv, caused a change in the charge, $Q_c = C_p \Delta v$, that was stored by the integrating capacitors. If the total PMT current pulse, which spanned several QIE integration periods, was small enough that the range of sensitivity did not change, the net change in charge over the QIE integration periods would be zero. However, if the total integrated current spanned several QIE ranges, differences in the parasitic capacitances between ranges would result in a net charge loss and a mismeasurement of the integrated PMT current. Furthermore, since the circuit impedance was non-linear, the charge loss did not vary linearly with the PMT current. To reduce non-linearities due to charge loss, the circuit components and the layout was designed to reduce differences in the parasitic capacitances and circuit impedances between ranges. In addition, a charge-loss compensation circuit was used to minimize non-linearities in the charge measurement. During the 1997 data-taking period (described in Chapter 5), some channels experienced failures in their charge loss compensation circuits. As a result, these channels exhibited non-linearities of up to 3% in a particular range.

Flash ADC (FADC)

The differential analog output voltage from the QIE was digitized by a conventional 8-bit Harris Flash ADC (HI1386). The linearity of the PMT, QIE and FADC can be seen in Figure 4.6. The spread in the data points within each range seen in Figure 4.6 shows the similarity of the responses of the four QIE phases. After digitization, the 8-bit output (mantissa) of the FADC was transferred to the DBC.

To reconstruct the charge with a resolution of $\sim$0.01%, the noise level of the DPMT had to be less than 9 fC over a 19-ns clock cycle. The QIE-FADC system had a noise level of $\sim$2.2 fC over a clock cycle. The main contribution to the system noise

was the QIE input noise. The QIE input noise became a smaller fraction of the input charge as the input charge increased. The noise at the output stage of the QIE was $\sim$1 fC and was comparable to that of the FADC. The component of the electronic noise from the FADC was the same for all QIE ranges [59]. Besides the electronic noise from the QIE and FADC, there was also an uncertainty of about 2.9 fC in the lowest range due to the digitization of the charge.

Driver/Buffer/Clock (DBC) and Pipeline System

The termination and synchronization of the digital data transfer from the QIE and FADC was controlled by the Driver/Buffer/Clock. The DBC also generated a clock for the operation of the FADC and QIE by using external clock signals, which were used to make the DPMT timing with respect to the PMT signal the same for every channel. The digital data from the QIE and FADC was delayed and buffered in a FIFO which could contain up to 40 clock cycles (slices) of data. Each clock cycle of data was stored in a 16-bit word. Upon receipt of a Level 1 signal, 32 slices were loaded into a second FIFO. If the event passed the Level 2 requirements, the data was transferred through a parallel-to-serial converter to a VME readout buffer called the "pipeline system". The data was driven 4 bits at a time at a rate of 26 MHz, taking 4.9 μs to transfer a 32 slice event.

Data from all 3100 CsI channels were sent to the pipeline system. To reduce the data volume as well as to shorten both online and offline data processing times, only data from channels whose energies exceeded a specific hardware threshold were saved for analysis. CsI readout thresholds were different for charged and neutral mode triggers since the energy reconstruction had to be known more accurately in the neutral mode. For the $\pi^0\pi^0$ and $3\pi^0$ triggers, the CsI readout thereshold was $\sim$5 MeV whereas for the $\pi^+\pi^-$ trigger, the threshold was $\sim$10 MeV.

The hardware threshold was set with respect to the baseline charge or pedestal of each channel. The pedestal, which is the charge read out by a channel when no energy had been deposited in the crystal, was measured by summing the DPMT mantissa counts over 4 clock cycles. By summing the mantissa value over 4 clock

cycles, the baselines of each QIE phase were accounted for. The QIE exponent for pedestal events was zero and the average pedestal for each channel was around 32 mantissa counts.

4.3 Cosmic Ray Hodoscope

A cosmic ray hodoscope was employed to monitor the longitudinal light response of the crystals throughout the data-taking period. The longitudinal uniformity information was used to correct for the non-linearities in the response of the crystals as well as to study the radiation damage to the crystals. The cosmic ray hodoscope was also used to calibrate the calorimeter (before protons were first delivered to KTeV) and monitor the calorimeter performance.

The cosmic ray hodoscope was essential to checking the performance of the CsI crystals and readout during stacking. We compared the longitudinal response that was measured in the blockhouse with the measurements from the crystal laboratory to make sure that the longitudinal uniformities were consistent and the crystals were not damaged. We also tested the readout of each channel.

The cosmic ray hodoscope detected muons that passed transversely through the calorimeter as shown in Figure 4.7. The hodoscope consisted of 3 sets of ~3 metre-long overlapping plastic scintillation counters, labelled U, D and T, placed above and below the CsI blockhouse as shown in Figure 4.8.

To select transversely-passing cosmic ray muons, the cosmic ray trigger required a coincidence in the U, D and T hodoscope "planes". In the offline reconstruction, cosmic ray events had to have at least one hit in each hodoscope plane[3]. To ensure that the reconstruction was correct, the projection of the track formed by connecting the hits in the U and D planes had to agree with the hit in the T plane. We identified muons that passed vertically through a crystal by requiring the crystal above and below to be "hit", while the crystals to the left, right and diagonal must have no deposited energy.

[3] If there were two hits in a plane, the hodoscope counters that had been hit had to be overlapping.

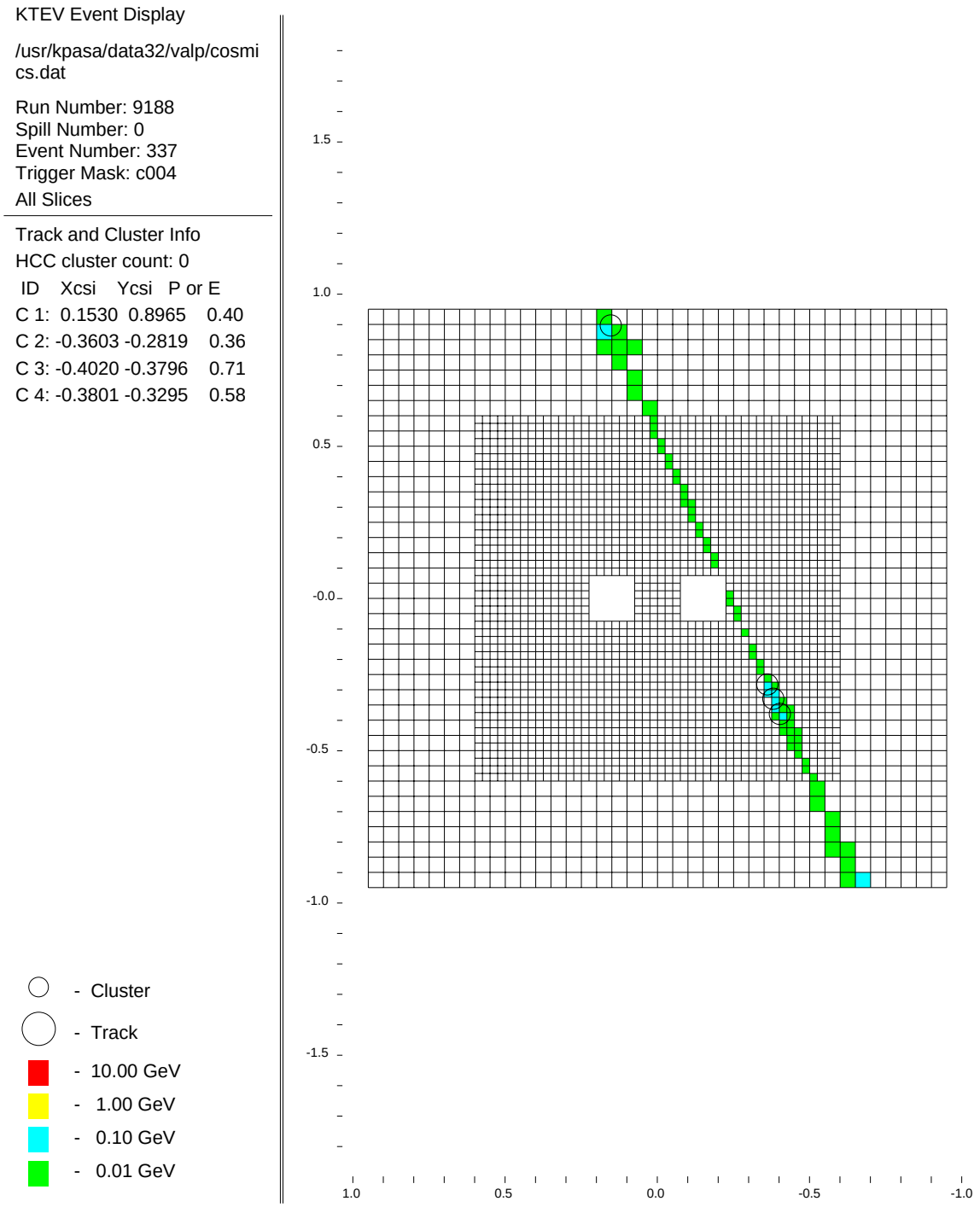

Figure 4.7: A transverse cosmic-ray event in the CsI calorimeter. (The kaon beam goes into the page.)

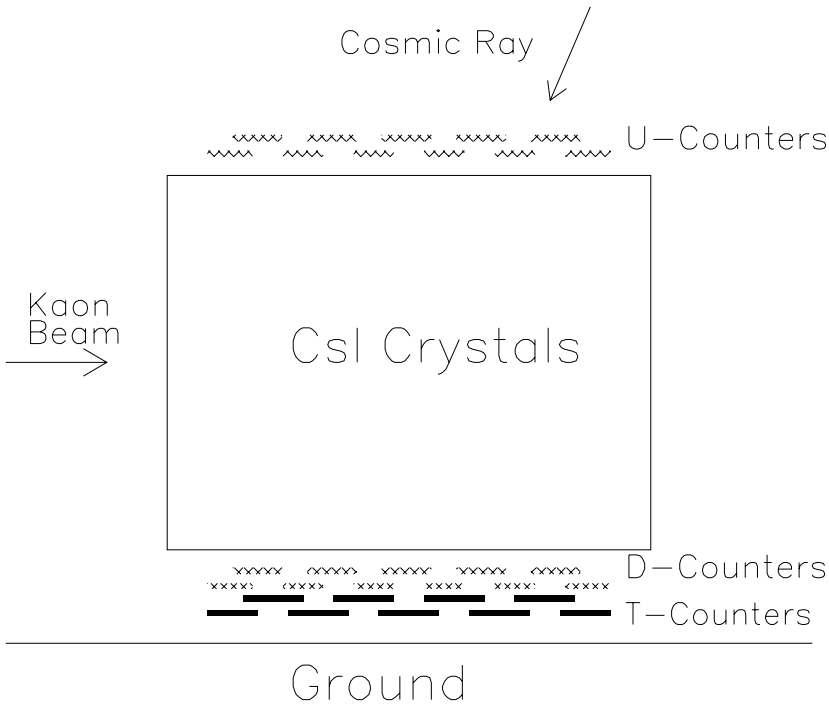

Figure 4.8: The cosmic ray hodoscope.

A minimum-ionizing particle (MIP) deposited a mean energy of 5.6 MeV/cm in CsI, so the energy deposited in a small and large crystal were about 14 MeV and 28 MeV, respectively.

By selecting minimum-ionizing muons that passed vertically through a crystal and determining where along the length of the crystal the muon passed, we studied the longitudinal response and performance of a CsI channel. The peaks of the ADC distribution for each channel (Figure 4.9) were also used to match the gains by changing the voltage of each channel until the ADC peaks lined up; the peak value for large channels being twice that of small channels. The gains were matched to within 20%. It was important for the neutral mode trigger that the gains were matched at this level when kaons were first delivered to KTeV because the neutral mode trigger efficiency would otherwise vary over the calorimeter leading to different efficiencies for collecting vacuum and regenerator $2\pi^0$ events.

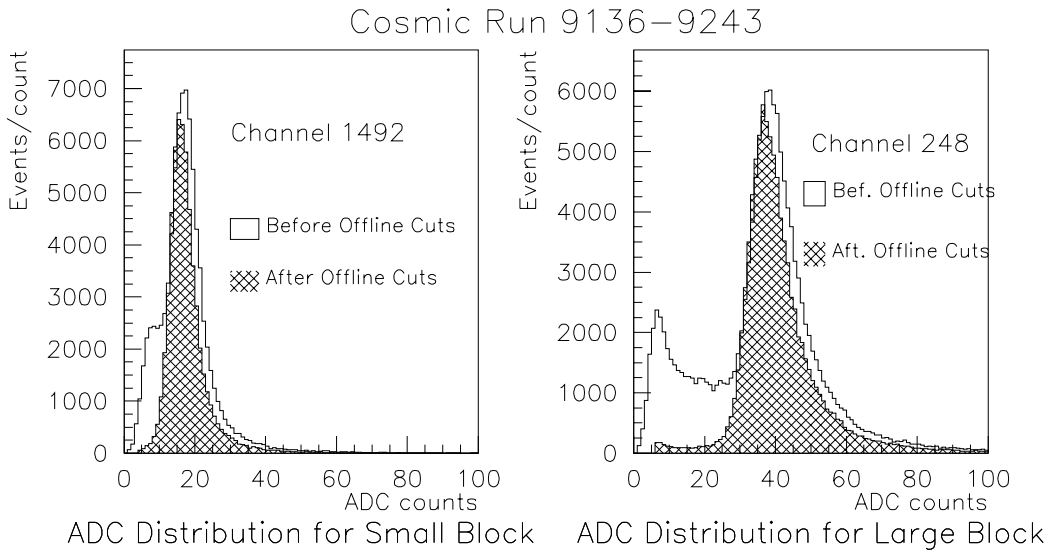

Figure 4.9: CsI ADC distribution for transverse-going for cosmic ray muons passing through a small (left) and large(right) block. The (shaded) distribution after offline cuts was used to study the response of the crystal.

The ADC distributions of events passing the cosmic ray trigger were also used in the online monitoring to identify readout problems. Although cosmic ray muons could only test the performance of the readout in the lowest range, they were extremely useful in debugging the calorimeter during stacking.

4.4 Laser System

A laser system was used to calibrate the DPMTs, monitor the performance of each CsI channel over the full dynamic range and correct the short-term gain fluctuations in each channel. To calibrate the DPMTs, it was important to be able to vary the intensity of the light reaching each channel, while to measure short-term CsI gain drifts, the laser system had to provide light at a fixed intensity.

The laser system shown in Figure 4.10 consisted of a Nb:YAG laser with frequency tripling optics. Filter wheels were placed after the tripling optics to vary the intensity of the laser light reaching the crystals to cover the full dynamic range of the QIE and

FADC. After the laser light passed through the filter wheels, it was sent to four "bowling balls" which contained a vial of N-Methyl-Carbazole dye in the centre. When illuminated with the laser light, the fluorescent dye emitted light with a peak wavelength of 380 nm. Quartz fibers were used to transmit the light from the bowling ball to each crystal; each fiber was attached to the PMT end of a crystal. Each bowling ball supplied light to a quadrant of the calorimeter. The light level supplied to each quadrant was measured by a highly stable and linear 1722 P-I-N diode whose output was digitized by a Burr-Brown (DDC101) 20-bit ADC.

Since the laser system was used to calibrate the DPMTs, it was important that DPMT non-linearities affect the laser light in the same way as scintillation light. As a result, care was taken to make the decay time of the light from the laser system as close as possible to that of the scintillation light from high-energy photons and electrons since non-linearity effects due to charge loss in the DPMT depended on the pulse shape and timing.

To calibrate the DPMTs, special runs were taken where 5 Hz laser pulses were used to scan the full dynamic range of the QIE. By comparing the integrated PMT current to the intensity measured by the P-I-N diodes, we calibrated the DPMT for each channel. A linear, least-squares fit was performed to determine the slopes and intercepts for each QIE range and phase. There were 64 parameters in the fit, corresponding to a slope and intercept for the 8 ranges and 4 QIE phases. The fit accounted for the effects of photo-statistics, DPMT noise and FADC digitization on the channel response. The PMT current was integrated over 5 clock cycles so that we could calibrate each phase separately. Integrating over an even number of clock cycles does not allow the fit to converge since the constants for two or more phases cannot be separated. The DPMT response was normalized by setting the slope for the fourth QIE phase in the highest range to be the same for every channel. After the online DPMT calibration, the deviation of the measured response from a linear fit was less than 0.2% as shown in Figure 4.11.

The calibration was checked throughout the run and in particular, when a DPMT was replaced. During the three-month-long 1997 E832 run, the DPMT performance was stable enough that the DPMT calibration used online did not have to be updated

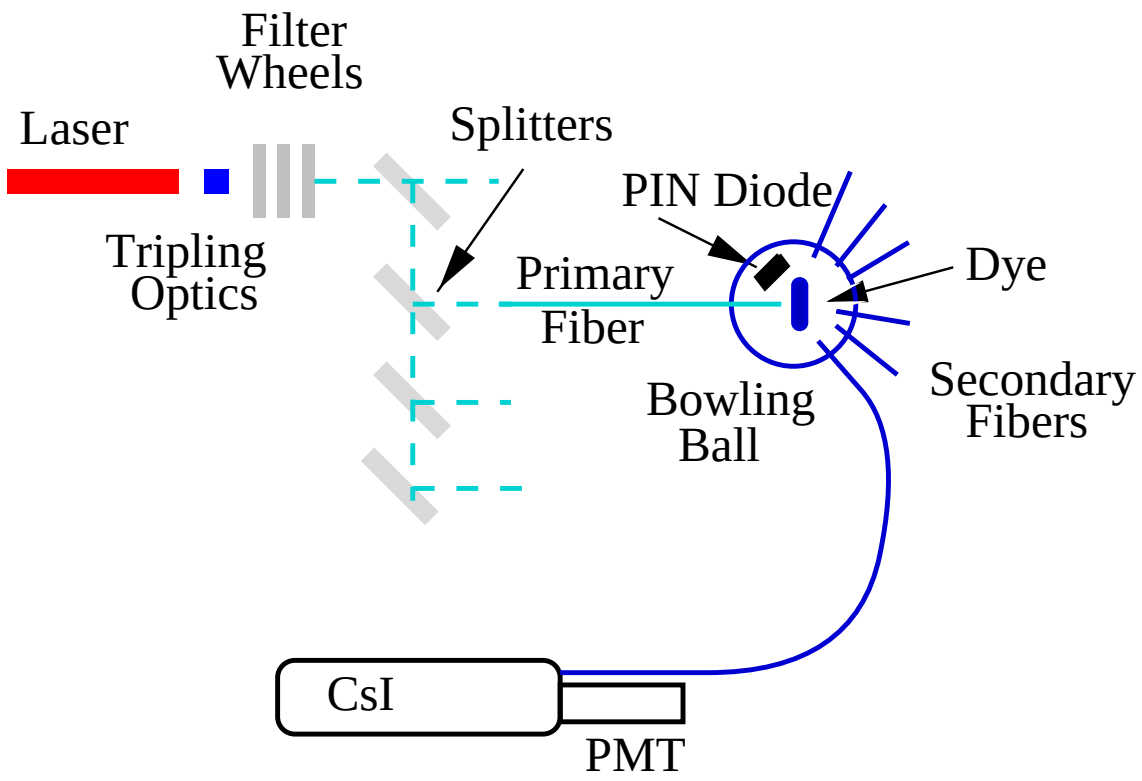

Figure 4.10: Laser System used for CsI Monitoring.

after it was first installed. The calibration for channels with replaced DPMTs were not updated during data-taking because the DPMTs were replaced with new ones with similar characteristics. In the offline analysis, new DPMT response parameters were determined and used for DPMTs that had been replaced.

Besides being used to calibrate the DPMTs, the laser system was also used during data-taking to monitor the performance of the CsI array. To identify problems in any DPMT range or phase, the laser system was used to scan the full dynamic range of the DPMT. "Laser scans" usually took place once every few days and no beam was delivered during the scan. To monitor the calorimeter while $Re(\epsilon'/\epsilon)$ data were being collected, the laser flashed every second at a fixed intensity, with about 2 GeV of energy being deposited in each crystal per laser flash. By operating the laser at a fixed intensity, spill-by-spill changes in a channel's average response and gain fluctuations within a spill could be measured.

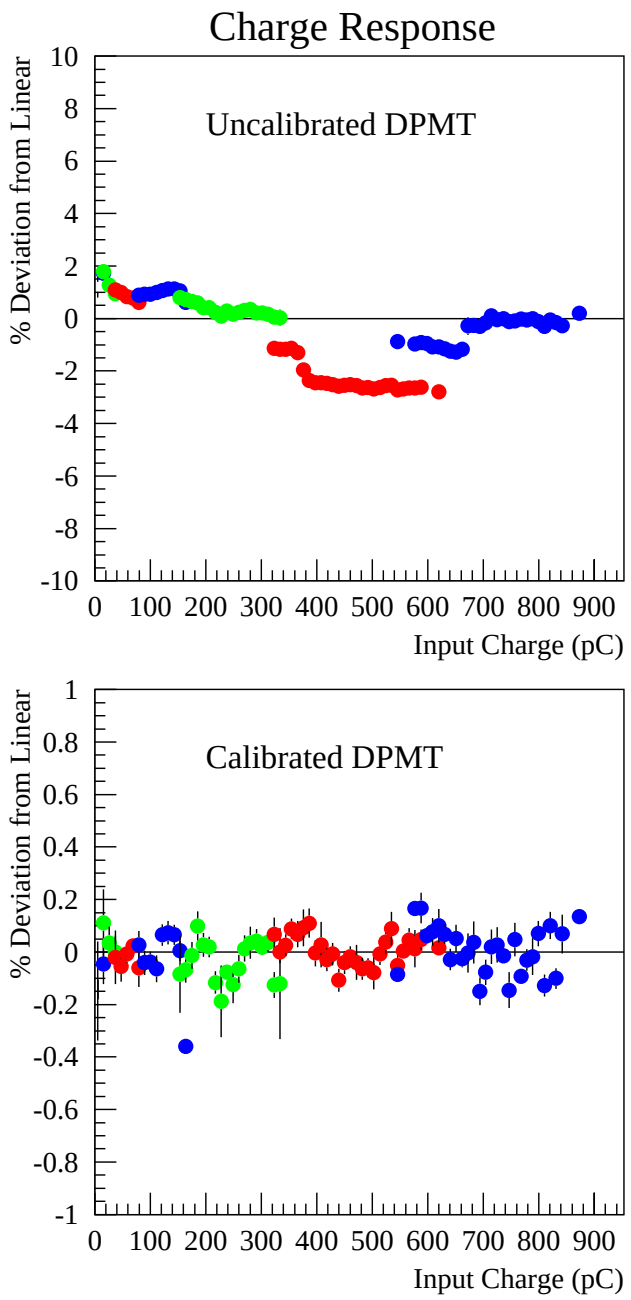

Figure 4.11: Deviations from a linear charge response before(top) and after(bottom) calibration of the DPMT for a single channel. Each QIE range is represented by a different colour.

Data from the 1 Hz fixed-intensity laser flashes were also used in the offline neutral mode calibration and analysis to correct for short-term changes in the response of each channel. We first measured the mean response of each channel over a spill by normalizing the charge read out by the CsI channel to the P-I-N diode intensity for each laser flash. The change in the response with respect to the first spill of the calibration period was then determined in order to obtain the correction to the channel's gain. On average, the response drifted by about 0.2% during a calibration period (1-3 days of data-taking). The average change in response with respect to the first good (high-quality) spill in each calibration period for the 1997 run is shown in Figure 4.12. The correction for short-term gain fluctuations improved the electron energy resolution by 0.12% in quadrature but had no effect on the energy linearity.

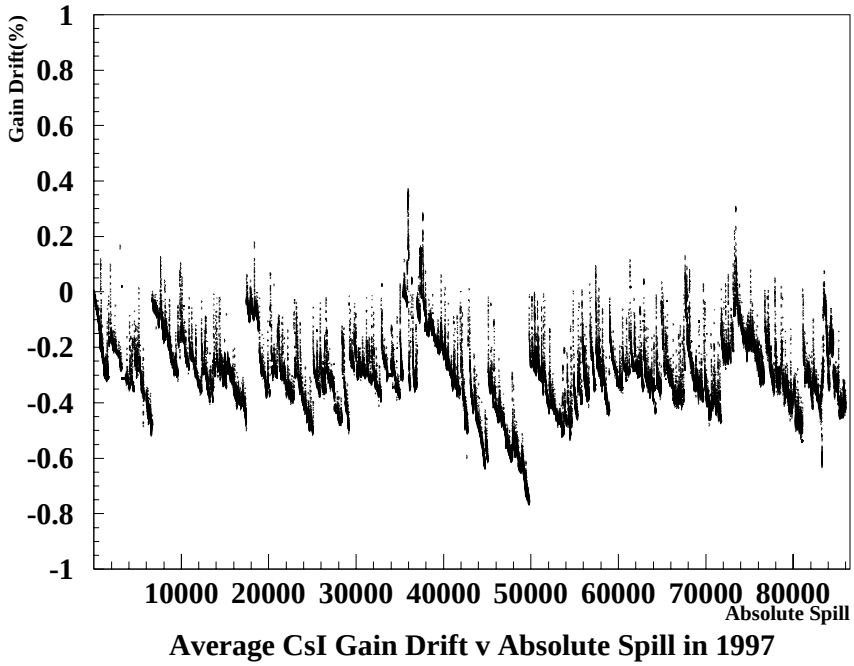

Figure 4.12: Average CsI gain drift measured using 1 Hz laser pulses versus absolute spill in 1997. The gain drift is measured with respect to the first "good" spill in each calibration period.

4.5 Energy Calibration and Cluster Reconstruction

The calibration of the calorimeter was a two-step process: the linearization of the DPMT response and the determination of the absolute energy scale or the "energy calibration". In this section, we will discuss the energy calibration. The DPMT calibration was presented in the previous section.

The energy calibration was performed using electrons from $K_L \to \pi^{\pm} e^{\mp} \nu$ (K_{e3}) events. By setting the mean electron energy-to-momentum ratio, E/p, for each channel to unity[4], we determined the "charge-to-energy" conversion (Q/E) for each channel. The electron shower energy, E, was reconstructed using the calorimeter while the momentum, p, was measured using the charged spectrometer.

Since the electron energy and position reconstruction are essential to the energy calibration, we will begin by describing the electromagnetic shower reconstruction and then describe how we determined the absolute energy scale for each channel. In this section, we will describe the general features and effects of the various stages of the cluster energy and position reconstruction. In Appendix A, we discuss certain aspects of the reconstruction that could have a systematic effect on the $Re(\epsilon'/\epsilon)$ measurement.

4.5.1 Cluster Reconstruction

We reconstruct the energies of electromagnetic showers in the calorimeter by first determining the energies of each channel that was read out and then identifying clusters of energy. The total energy within a cluster is obtained by summing the energies of the blocks within the cluster and correcting for energy losses due to geometrical and detector effects.

To determine the energy in each block that was read out, we first unpacked the digitized DPMT information in each slice (QIE clock cycle). Based on the DPMT calibration, the digitized information was converted to a "charge". The charge was then integrated over 6 in-time slices or 114 ns in the offline analysis. By integrating

[4]We set E/p for electrons to 1 because the electrons were highly relativistic.

over 114 ns, ~96% of the fast scintillation light was collected[5]. The integrated charge was converted to an energy using Q/E conversion factor. Finally, we corrected the energy in each block for short-term gain drifts by using the laser information.

Clustering

Energy clusters in the calorimeter were identified by blocks which were local energy maxima. A block was a local energy maximum if it had more energy than its closest neighbours[6]. The centre of the cluster was forced to lie within the block which was the local energy maximum or "seed block". A cluster was defined by a 7×7 array of small blocks ("small-region") or a 3×3 array of large blocks ("large-region") surrounding the local energy maximum or "seed block"; the size of the cluster was based on the size of the seed block. When the cluster seed was on a large-small crystal boundary ("mixed-region"), the cluster region was defined as a 3×3 grid of large blocks. If the 7×7 array of small blocks contained blocks that were in the beam hole, the cluster was defined in one of two possible ways, as shown in Figure 4.13. If the seed block was at the corner of the hole, then the cluster contained blocks on either side of the hole; whereas if a cluster was on the side of a beam hole, then the cluster only contained blocks on the same side of the beam hole. The illumination in the large-, small- and mixed-regions due to photons from $K \to \pi^0\pi^0$ events after all cuts is summarized in Table 4.2.

There are two categories of clusters: "hardware" clusters and "software" clusters. Hardware clusters were defined as clusters where the seed block had its Hardware Cluster Counter[7] (HCC) bit turned on. "Hardware Clustering" was used so that the clusters that were identified in the analysis would be consistent with those in the Level 2 trigger. Since the threshold for turning an HCC bit on was ~1 GeV,

[5]For reasons that are described in Chapter 5, the DPMT was operated at RF/3 (18 MHz) in 1996 and the charge was integrated over 4 RF/3 periods (228 ns).

[6]For a large (small) block, only the neighbours which were one large (small) block away is considered.

[7]The Hardware Cluster Counter is described in Chapter 7.

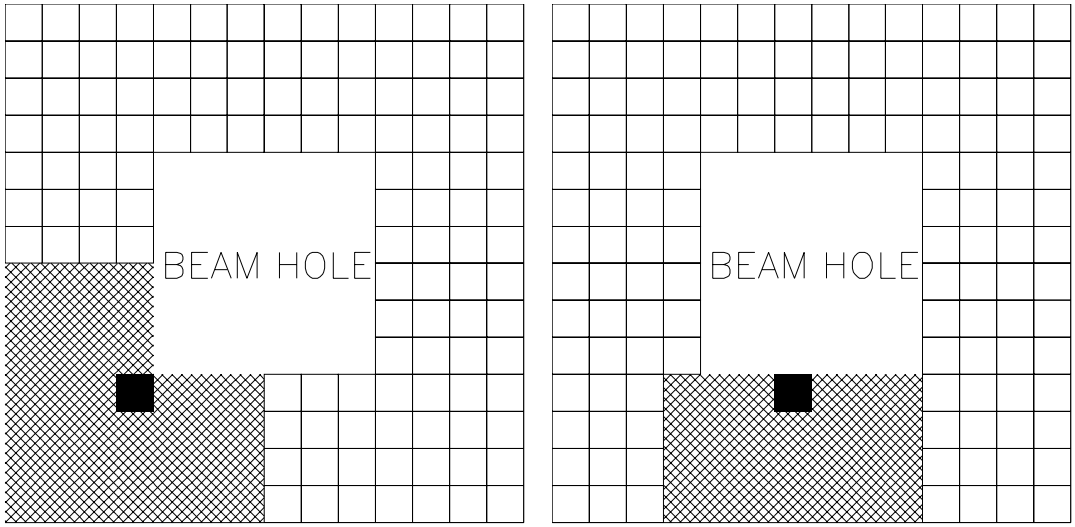

Figure 4.13: Definition of clusters near the hole. The seed crystal is in black and the blocks that are part of the cluster are shaded.

hardware clustering effectively required the cluster energy to have more than 1 GeV. Since hardware clusters were defined based on the HCC bit illumination, due to HCC errors, we would occasionally identify a seed block with very little energy but with its HCC bit on. To exclude such "fake" clusters, we required the hardware cluster seed energy to contain at least 100 MeV.

In software clustering, we required that the cluster seed not be a part of another hardware or software cluster, that the seed block energy be at least 100 MeV, and that the sum of energies of the blocks in the cluster be at least 250 GeV. Requiring that a software cluster seed not be part of another cluster meant that the minimum distance between a software cluster and any other cluster that was not in the hole region was 5 cm if one of the clusters contained a large block, and 7.5 cm if both

Region of Photon Illumination	Fraction in Vacuum Beam(%)	Fraction in Regenerator Beam(%)
Large-block region	11.3	15.6
Small-block region	79.2	73.3
Mixed block region	9.5	11.1
Within 7.5 cm of beam hole	26.5	21.0
Within 5.0 cm of calorimeter outer edge	0.9	1.3
Overlapping Photons (blocks common to $\geq$2 clusters)	7.1	6.5
2 or more photons next to the same hole	21.5	15.8

Table 4.2: Photon Illumination in $2\pi^0$ Vacuum and Regenerator Beam events. (Only loose analysis cuts were applied in all cases except the study of 2 or more photons where all final analysis cuts and corrections were applied)

clusters only contained small blocks.

The type of clustering that was performed was dependent on the trigger. For example, in the $2\pi^0$ mode, both hardware and software clustering were applied since we wanted to identify HCC clusters as well as remove events with additional low-energy clusters. On the other hand, in the $\pi^+\pi^-$ mode, only software clustering was performed, since the $\pi^+\pi^-$ trigger did not use the HCC.

Cluster Position Determination

Having identified the clusters of energy in the calorimeter, we were ready to determine their positions. The transverse positions of electromagnetic showers were defined to be the x- and y-centres-of-energy of each cluster. To determine the x- (y-) centre-of-energy, we calculated the ratio of the energy in the column (row) containing the cluster seed to the energy in the two adjacent columns (rows) and used a non-linear map[8], which assumed a uniform photon illumination over the face of the seed crystal,

[8]The map was non-linear because the transverse shower profiles were not flat.

to relate the ratio of energies to a position within the seed block. Unless the cluster centre was at the edge of a crystal, the cluster position was the weighted average of the cluster positions obtained from the left (top) and right (bottom) column (row) ratios[9]. If the cluster centre was at the edge of the crystal, we did not take a weighted average of the cluster positions, but only considered the energy in the column or row closest to the cluster centre. To convert the position within the seed block to a position in the KTeV coordinate system, the survey positions and sizes of the crystals were used.

The position lookups that were used to convert the ratio of column and row energies to a position within the seed block were generated using photons from $2\pi^0$ data events after all analysis cuts except the 3 GeV minimum photon energy cut. The minimum photon energy cut was removed, so that more accurate position lookups could be made for low energy photons. The position lookups were binned based on the cluster energy, size and region.

The position resolutions for electrons were 0.8 mm and 1.7 mm for small and large cluster seeds, respectively. The position resolutions were measured using the difference between the reconstructed cluster position and the track position extrapolated to the mean shower depth, 0.17 m, in the calorimeter.

Cluster Energy Reconstruction

To reconstruct the energy of a photon or electron, we applied a series of "geometrical" corrections to the sum of energies of the blocks in the cluster. We had to include the contribution due to channels with energies below the readout threshold ($E_{sub-thresh}$) since we only summed the energies of the the blocks that were read out. For clusters near the hole or the edge of the calorimeter, we also added the energy due to the part of the shower that was outside the calorimeter or went down the beam hole ($E_{missing}$). Although most of the shower was contained in the defined cluster, there was still about 5% of the shower energy which lay outside the defined (7×7 small-block/3×3 large-block) region. To account for this, we re-scaled the cluster energy

[9]Since a column (row) in a cluster could contain fewer blocks than its neighbouring column (row), we were careful to sum the energies over the same number of blocks when calculating the ratio of two column energies.

by $f_{out-of-cone}$.

Besides geometrical effects, we also corrected for detector-related energy effects. We observed variations in the response of the crystal along the length as well as across the face of the crystal; we corrected for these longitudinal and transverse non-uniformities by applying scale corrections, $f_{longitudinal}$ and $f_{transverse}$, respectively. Although we corrected for short-term gain variations ($f_{laser}(i)$) using the laser system, there were global time variations in the CsI scintillation response which had to be accounted for using a time-dependent scale factor, f_{spill}.

After applying the energy corrections mentioned above, we accounted for the residual non-linearities in the response seen in K_{e3} events. The correction, $f_{linearity}(i_{seed})$, which was different for each seed block (i_{seed}) was applied to both photon and electron showers.

In addition to geometrical and detector effects that affected both K_{e3} and $K_{L,S} \to \pi^0\pi^0$ events, in channels where there was energy from more than one electromagnetic shower, we had to make sure that the energy in each cluster did not include the energy from a neighbouring shower, $E_{overlap}$. When there were more than two showers near the same beam hole, we had to be careful to subtract the energy, E_{sneaky}, from one shower leaking across the beam hole into another shower.

In the $Re(\epsilon'/\epsilon)$ analysis, it was important that the data and Monte Carlo neutral mode energy scales agreed, Therefore, in order to match the data and Monte Carlo $K_{L,S} \to \pi^0\pi^0$ energy scales, we applied an additional energy scale factor, $f^{Data}_{Photons}$, to photons in the data after all other energy corrections were applied. The scale factor, $f^{Data}_{Photons}$, depended on the reconstructed kaon energy.

Based on the corrections described above, the energy of an electromagnetic shower, $E_{cluster}$, in the 1997 analysis[10] was given by

$$\begin{aligned} E_{cluster} &= f^{Data}_{photons}(E_{Kaon}) \cdot f_{linearity}(i_{seed}) \cdot f_{spill} \cdot f_{longitudinal} \cdot f_{transverse} \cdot f_{out-of-cone} \cdot \\ &\quad \left[E_{sub-thresh} + E_{missing} - E_{overlap} - E_{sneaky} + \sum_{i=1}^{N_{readout}} f_{laser}(i) \cdot E(i) \right], \end{aligned}$$

[10] In 1996, there were additional corrections because the DPMT was operated at 18 MHz. They are discussed later in this section.

(4.1)

where $E(i)$ was the energy in each block in the cluster that was read out. We now discuss each of the corrections and their effects on the energy linearity and resolution.

- Out-of-Cone Correction ($f_{out-of-cone}$): The "out-of-cone" correction accounted for energy that was outside the defined cluster region. The correction scaled the total energy of the cluster by 1.05921 for large- and mixed-region clusters and by 1.04178 for small-region clusters. The correction factors were obtained by using 8-GeV photon showers from GEANT[65]. Although the fraction of energy that lay outside the defined region depended on the position of incidence within the block and the cluster energy, the scale correction was independent of cluster energy and position within the central block. The position and energy dependance of a shower was accounted for instead by the transverse non-uniformity correction ($f_{transverse}$) and the longitudinal response correction ($f_{longitudinal}$), respectively.

- Missing Block Correction ($E_{missing}$): The "missing block" correction, $E_{missing}$, accounted for energy that was lost down the beam hole or outside the outer edge of the calorimeter. It was very important to account for such energy losses accurately, since the photon illumination at the beam holes and the outer calorimeter edges was different for vacuum and regenerator $K_{L,S} \to \pi^0\pi^0$ events (Table 4.2).

  The missing block correction is applied to clusters with seed blocks which are either in the outermost ring of crystals in the calorimeter, or within three small crystals of the beam hole. If a cluster seed is in the outermost ring of crystals, then the nominal 3×3 large-block region around the seed contains "blocks" that are outside the edge of the calorimeter. If a cluster seed was within three blocks of the beam hole, the 7×7 small-block region around the seed block would contain "blocks" that are within the beam hole and could also contain "blocks" that are not part of the defined cluster (Figure 4.13).

  To predict the amount of "missing energy", we used maps (transverse energy

lookups) based on the transverse energy distribution of a shower. The total energy due to missing blocks is given by

$$E_{missing} = \frac{\sum_{i=1}^{N_{missing}} frac(i) \times \sum_{i=1}^{N_{present}} E(i)}{\sum_{i=1}^{N_{present}} frac(i)}, \tag{4.2}$$

where $frac(i)$ is the fraction of total energy in block i and is obtained from the transverse energy lookups, and $E(i)$ is the energy in block i. As shown in Equation 4.1, the energy due to missing blocks is added to the sum of block energies.

The transverse energy lookups were made using photons from $2\pi^0$ events to which all analysis cuts other than the minimum photon energy cut was applied. Each lookup contained the average block energies in a 9×9 region of small blocks centered around the cluster seed. The maps were based on the cluster position within the seed block but were independent of the cluster energy. The lookups were made using photons with energies between 11.3 GeV to 22.6 GeV and only photons in the small-region which were away from the beam holes and were at least 40 cm away from any other cluster were selected. The effect of accidentals on the shower profile was reduced by the $\chi^2_{\pi^0}$ and χ^2_{shape} cuts described in Chapter 7.

The energy resolution for electrons near the hole after all energy corrections is shown in Figure 4.14. Beyond 1.25 cm from the beam hole, the energy resolution did not vary with the distance of the electron cluster from the beam hole, indicating that isolated clusters near the beam hole have been treated adequately.

- Readout Threshold Correction ($E_{sub-thresh}$): The readout threshold correction accounted for the energy in channels that were part of a cluster but were not read out. The energy in each block that was not read out was predicted based on the block-wise distance of the channel from the cluster seed, the readout

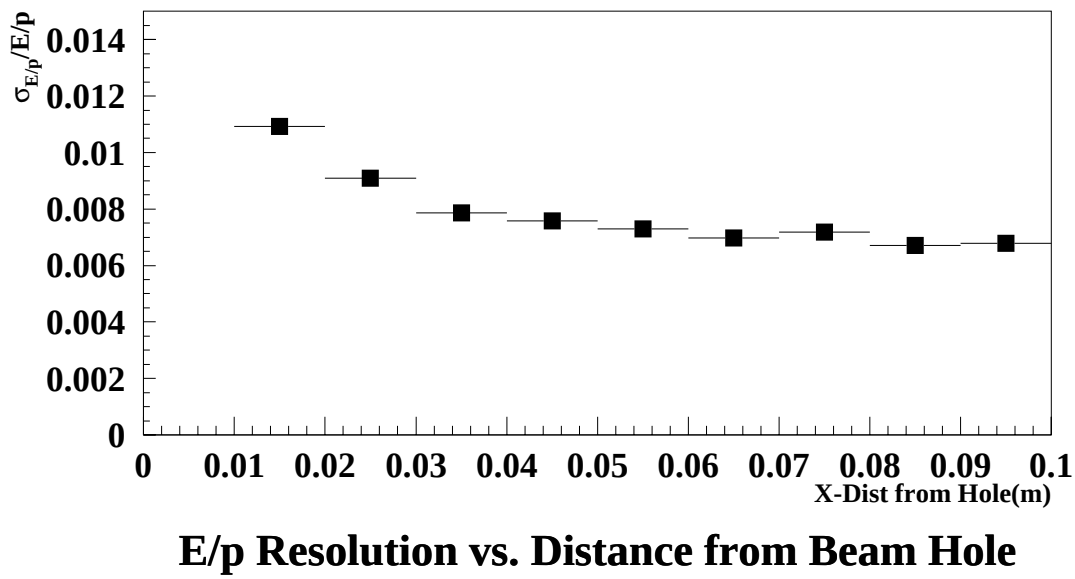

Figure 4.14: K_{e3} Electron E/p resolution as a function of x-distance from the beam hole. Any variation in the momentum resolution over the range of distances from the beam hole shown in the above plot is negligible.

threshold for the channel and the cluster energy[11]. The total energy due to channels with energies below the readout threshold, $E_{sub-thresh}$, was given by[12],

$$E_{sub-thresh} = \sum_{i=1}^{N_{sub-thresh}} E_{threshold}(i) \times (\alpha_r + \beta_r \ln(E_{cluster})) \,, \tag{4.3}$$

where $E_{threshold}(i)$ is the threshold energy for block i, and α_r and β_r are constants based on the block-wise distance, r, from the cluster seed. The total energy not read out, $E_{sub-thresh}$, was added to the cluster energy. The threshold correction was derived using K_{e3} electrons from a special run in 1996 when all the channels

[11]The predicted energy in each channel decreased as the further away it was from the cluster seed and the expected energy increased logarithmically with the total cluster energy.

[12]We only present the correction for triggers with a readout threshold of 6 counts above the baseline values since this was the readout threshold for calibration K_{e3} and $K_{L,S} \to \pi^0\pi^0$ events

were read out. The same correction was used when analyzing data and Monte Carlo in 1996 and 1997.

The "readout threshold" correction improved the energy linearity of showers below 15 GeV as shown in Figure 4.15, but did not affect the energy resolution significantly.

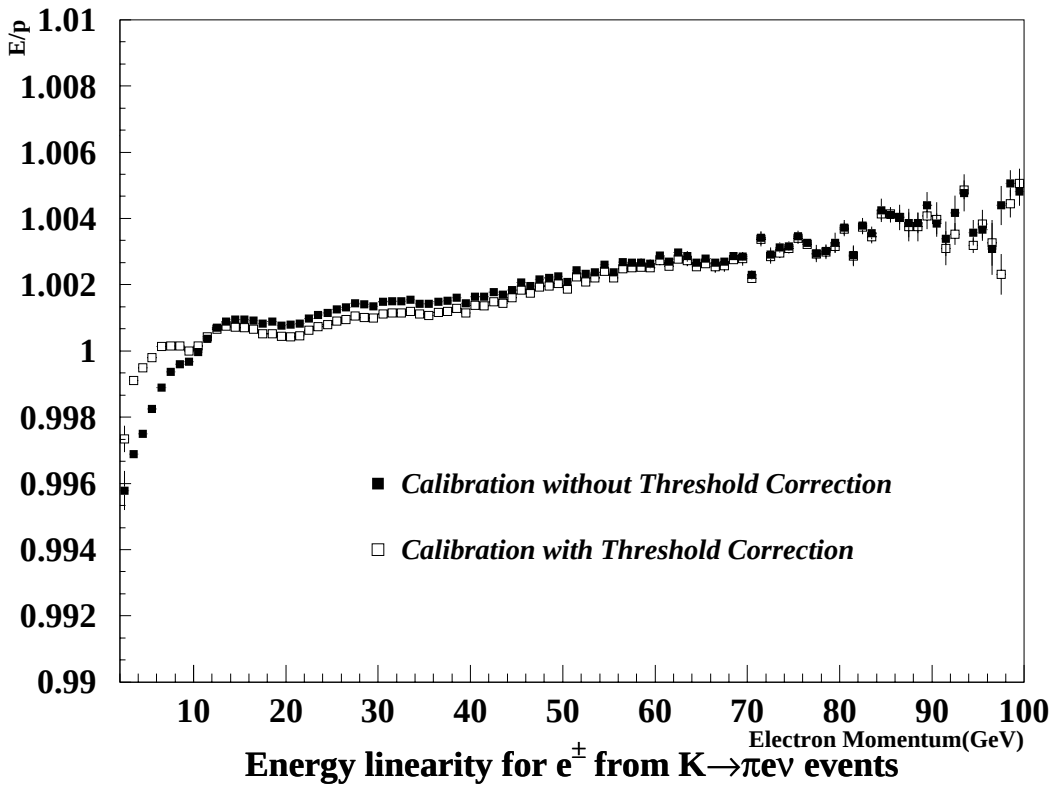

Figure 4.15: Effect of readout threshold correction on K_{e3} electron energy linearity.

- Distinguishing close clusters: In events where there were two or more electromagnetic showers in the calorimeter, the showers could be close enough to each other that a block contained energy from more than one cluster. To determine the amount of energy in the block that was due to each of the showers, we applied the "neighbour" and "overlap" corrections. The "neighbour" correction was applied to a block that was part of one cluster but contained energy from a

neighbouring shower, of which the block was **not** a part. In contrast, the "overlap" correction was applied to channels which were a part of more than one cluster. Clusters which contained channels that were common to other clusters were referred to as "overlapping" clusters. The total energy due to "neighbouring" and "overlapping" showers, $E_{overlap}$, was subtracted from the sum of the block energies in the cluster as shown in Equation 4.1.

The "neighbour" correction usually needed to be applied when one of the two nearby showers was due to a high-energy photon. To account for the energy contribution from the neighbouring shower ("neighbouring energy"), we determined the contribution in each block that was within 17.5 cm of the neighbouring cluster and subtracted the contribution from the block energy. Only neighbouring showers which were within 50 cm of the cluster seed were considered. The energy contribution from the neighbouring shower was determined using the transverse energy distribution of GEANT [65] electron showers over a 13×13 small block grid. The map was independent of cluster energy and the same map was used when analyzing data and Monte Carlo events.

7% of the photon clusters in $K_{S,L} \to 2\pi^0$ events contained overlapping clusters. To reconstruct the electromagnetic energy accurately, it was necessary to "separate" the showers by using transverse energy lookups to predict the fraction of energy in each block due to each overlapping cluster. The transverse energy lookups were the same as those used in the "missing block" correction. After separating a shower, the energy and position of each overlapping cluster were re-determined. The cluster separation process was iterated until the cluster energy was within 5 MeV and the cluster x- and y-positions were within 1 mm of the previous iteration.

- Sneaky Energy: The "sneaky energy" correction accounted for the "leakage" of energy across the beam hole from one electromagnetic shower into another. If the shower leakage across the beam hole was not accounted for, the measured energy of the showers would be higher than the true energy. The "sneaky energy" correction is very important in $K_{L,S} \to \pi^0\pi^0$ events where the num-

ber of photons near the same beam hole is different between the vacuum and regenerator beams (Table 4.2).

Although there are separate corrections for overlapping clusters as well as energy losses at the beam holes, by using transverse shower profiles made with photons away from the beam holes, it was tacitly assumed that the there was no empty space (*e.g.,* the beam holes) between the photon showers. To subtract the energy due to leakage from electromagnetic showers around the holes ("sneaky energy"), a map which was based on electrons from K_{e3} data was used.[13] The lookup predicted the amount of energy that had leaked into each block across the beam hole. Using K_{e3} electrons, it was observed that the energy leakage was proportional to the total cluster energy and also depended on the position of the cluster.

- Longitudinal Uniformity Correction ($f_{longitudinal}$): The longitudinal uniformity correction accounted for the longitudinal response of the CsI crystals as well as the energy dependance of the longitudinal distribution of photon and electron showers. Since the longitudinal distribution of electromagnetic showers depended on the energy of the incident electron or photon, there was a non-linearity in the energy response of the calorimeter due to the shower leakage through the back of the crystal as well as the uniformity along the length of the block. To correct for this non-linearity, the longitudinal uniformity correction convolved the length-wise response of each channel in the cluster with the average longitudinal distribution of a shower at the cluster energy, E_{clus}. The (convolved) responses of the blocks in the cluster were added together and normalized to the response of an 8 GeV photon shower. The longitudinal uniformity correction, $f_{longitudinal}$, was given by

$$(f_{longitudinal})^{-1} = \sum_{i=1}^{N_{blks}} \frac{E(i)}{\sum E(i)} \cdot \left(\frac{\int U_i(z) g(z)_{E_{clus}} dz}{\int U_i(z) g(z)_{E_\gamma = 8\ GeV} dz} \right), \tag{4.4}$$

where $E(i)$ is the energy of block i , N_{blks} is the number of blocks in the cluster,

[13] The electrons were required to be around the hole and well-separated from the pion.

$U_i(z)$ is the longitudinal response of the crystal i and, $g(z)_{E_{clus}}$ and $g(z)_{E_\gamma=8\ GeV}$ are the mean longitudinal distributions for a shower of energy E_{clus} and an 8 GeV photon, respectively. The mean longitudinal distribution, $g(z)$, was obtained from GEANT [65] showers and there were separate distributions for electrons and photons.

After accounting for the longitudinal response of the crystals, we find that the average response of the calorimeter ($f^{-1}_{longitudinal}$) to photons was higher than for electrons in data. This can be seen in Figure 4.16. Although the mean shower depth for photons was higher than for electrons, Figure 4.16 indicates that the effect of energy leakage through the back of the crystal was more than offset by the increased response close to the phototube.

Although the assumption that the shower was completely contained in a single block was not quite correct, accounting for the longitudinal shower variations in this way improved the energy linearity as seen in Figure 4.17. The effect of the correction on the energy resolution was negligible because the longitudinal response for most channels was flat to within 5%.

- Transverse Non-uniformity Correction ($f_{transverse}$): The transverse non-uniformity correction accounted for the variation of the energy response across the face of a block. Although the transverse "non-uniformity" in the response was first seen using K_{e3} electrons, we also observed a transverse variation in the energy response to muons that travelled longitudinally down a crystal. The response to electrons varied in both the $x-$ and $y-$directions over the face of the crystal, as seen in Figure 4.18, The change in the response across the face of a crystal was partly due to to the variation in the fraction of shower energy that was within the nominal cluster grid. The fraction of energy contained in a 7×7 small block and a 3×3 large block grid as a function of the cluster position within the central block is shown in Figure 4.19. Although Figure 4.19 was made using GEANT electron showers that were normally incident, the variation in the fraction of cluster energy across the face of the block due to electrons incident at angles of ∼8 mrad was expected to be of the same order. We see that the typical

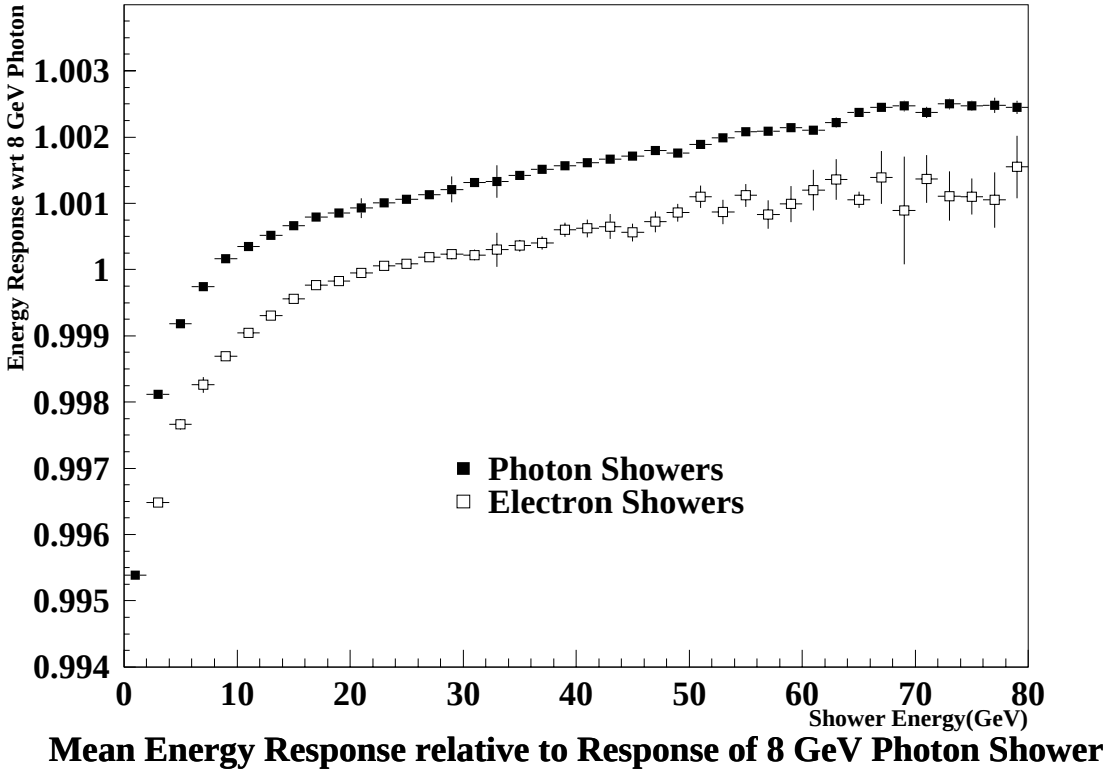

Figure 4.16: The mean energy response ($f^{-1}_{longitudinal}$) in data relative to the response of a 8 GeV photon shower. The longitudinal uniformity correction is applied by dividing the cluster energy by the energy response relative to an 8 GeV shower.

transverse variation in the energy response to electrons shown in Figure 4.18 was about five times larger than the response seen in Figure 4.19 indicating that there was indeed a variation in the transverse response of a crystal. The transverse variation in the response to minimum-ionizing muons was smaller but had the same shape as the response observed from K_{e3} electrons.

We corrected for the transverse non-uniformity by dividing the cluster seed block into a 5×5 grid and determining the mean response to electrons within each of the 25 regions. If a bin in the 5×5 grid had fewer than 5 electrons, then no correction was applied to clusters that were in that bin. The correction was normalized such that the average correction over the grid was unity. The

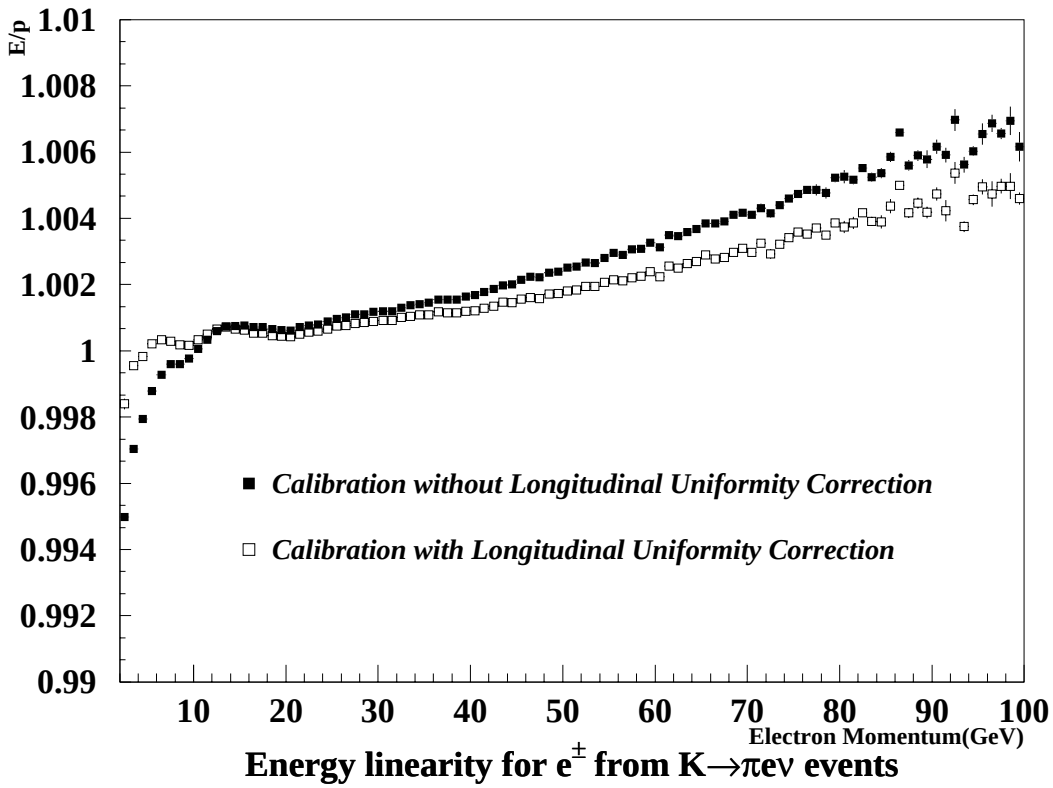

Figure 4.17: Effect of longitudinal uniformity correction on K_{e3} electron energy linearity.

transverse non-uniformity correction was applied by scaling the cluster energy.

Of all the corrections, the transverse non-uniformity correction caused the largest change in the energy resolution, improving the resolution by ~0.4% in quadrature, as shown in Figure 4.20. The effect on the energy linearity was negligible. The correction was applied to photons and electrons in data but not in the simulation. The effect of not applying this correction in Monte Carlo is discussed in Chapter 9.

- Linearity Correction ($f_{linearity}$): After applying all the cluster energy corrections described above, there was a residual non-linearity in the energy response seen in K_{e3} electrons (Figure 4.21). Part of this non-linearity was due to DPMT

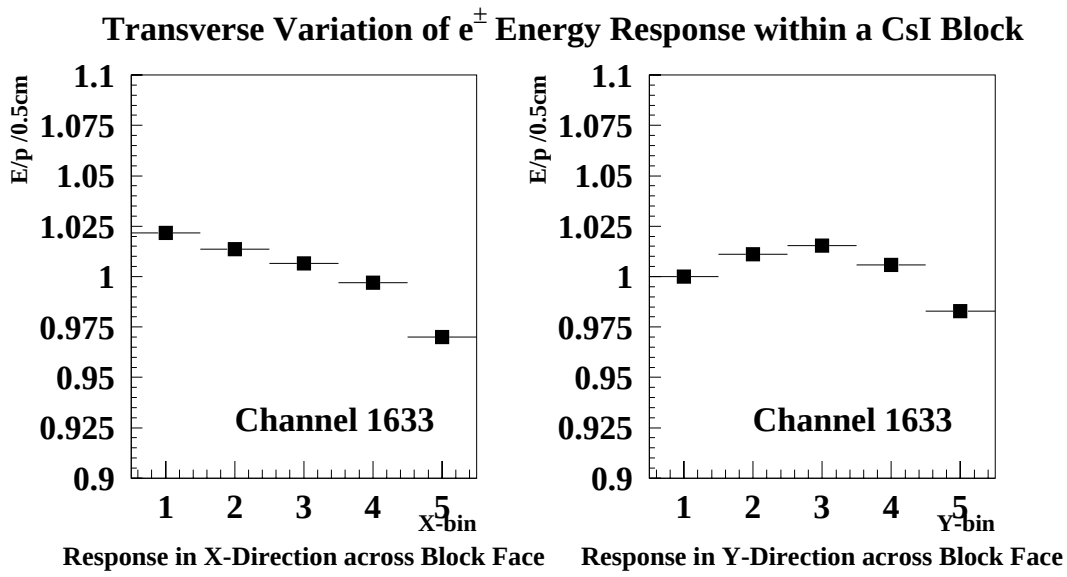

Figure 4.18: Variation of the $e^{\pm}$ energy response across the face of a small CsI block. The horizontal(x-) and vertical E/p variations in 0.5 cm bins are shown on the left and right respectively. The variations are normalized by setting the average variation of E/p to 1. Typical variations in response are about four times smaller.

linearity and readout threshold effects that were not fully corrected for. To correct for this non-linearity, we applied an energy linearity correction to each cluster seed, since as suggested in Figure 4.21, the non-linearity observed in the variation of the electron E/p with the electron momentum was different for each cluster seed. The correction was derived using K_{e3} electrons with energies between 2 GeV and 100 GeV over the full data-taking period. Separate linearity corrections were applied to the 1996 and 1997 analyses. After applying the energy linearity correction for each channel, the global variation of E/p versus the track momentum over the whole 1997 data-taking run was flat to 0.03%.

- Time-dependent Energy Scale Correction (f_{spill}): A spill-dependent scale correction, f_{spill}, was applied to each cluster to account for time-variations in the scintillation response of the whole calorimeter. The correction was the same for every channel in the calorimeter. Although the 1 Hz laser pulses corrected short-term gain fluctuations in each channel, the laser light was insensitive to

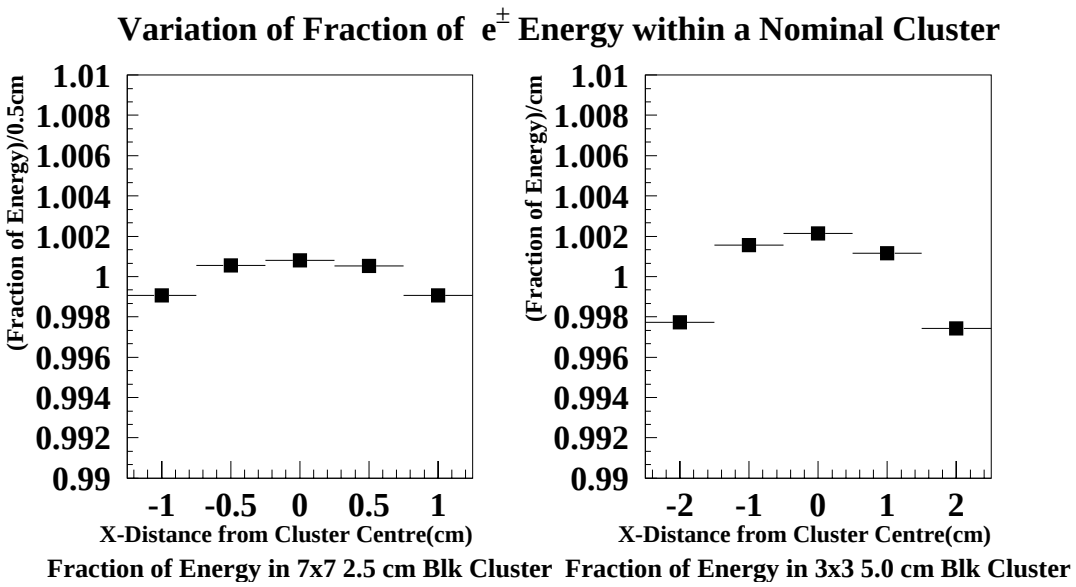

Figure 4.19: Variation of the fraction of $e^{\pm}$ energy in a (left) 7×7 Small Block and (right) 3×3 Large Block Clusters with cluster position. GEANT showers incident on the central block at 0° were used and the fraction of energy was normalized so that the average fraction was 1.

changes in the scintillation response of the crystals. For example, variations in the scintillation response due to temperature fluctuations in the blockhouse could not be observed in the laser light response. Changes in the scintillation response were corrected for by measuring the global response of the calorimeter to electrons every spill after applying all other corrections. The global response varied by about ±0.15% over the 1997 E832 run.

- Additional Cluster Energy Corrections in 1996: Two additional corrections, the "RF phase" correction and the "DPMT non-linearity" correction, were applied to the energy reconstruction of 1996 neutral mode data because the DPMT was not operated at the RF frequency of the beam in 1996. Since the QIE was operated at 17.7 MHz (RF/3) in 1996 but the protons were delivered by the beam at 53 MHz (RF), in-time photons could appear in 3 distinct periods or "RF phases" within the 57 ns integration slice. Because the current integration period, 228 ns, was the same for all 3 phases, the total charge was different

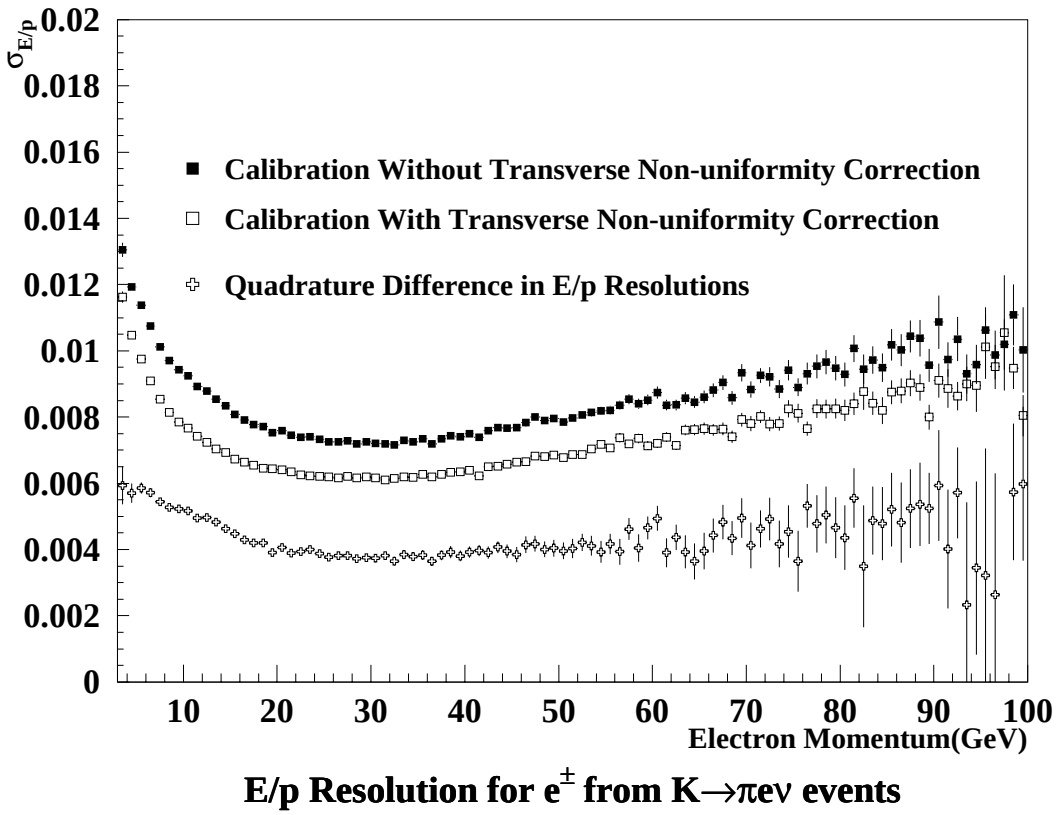

Figure 4.20: E/p resolution for K_{e3} electrons calibrated and analyzed with and without the transverse non-uniformity correction. The quadrature difference of the two distributions is also shown.

for the three phases. To correct for this difference, a phase-dependent scale correction was applied to the cluster energy. Since the charge in each 57 ns slice was very different when the DPMT was operated at RF/3, there was a greater susceptibility to energy non-linearities due to the charge-loss mechanism in the QIE. To account for these non-linearities, the "DPMT non-linearity" correction was applied to each channel that was read out. It was based on the QIE exponent of the slice with the maximum energy and the RF phase of the event.

Both the RF phase and DPMT non-linearity corrections were applied before the linearity correction, $f_{linearity}$.

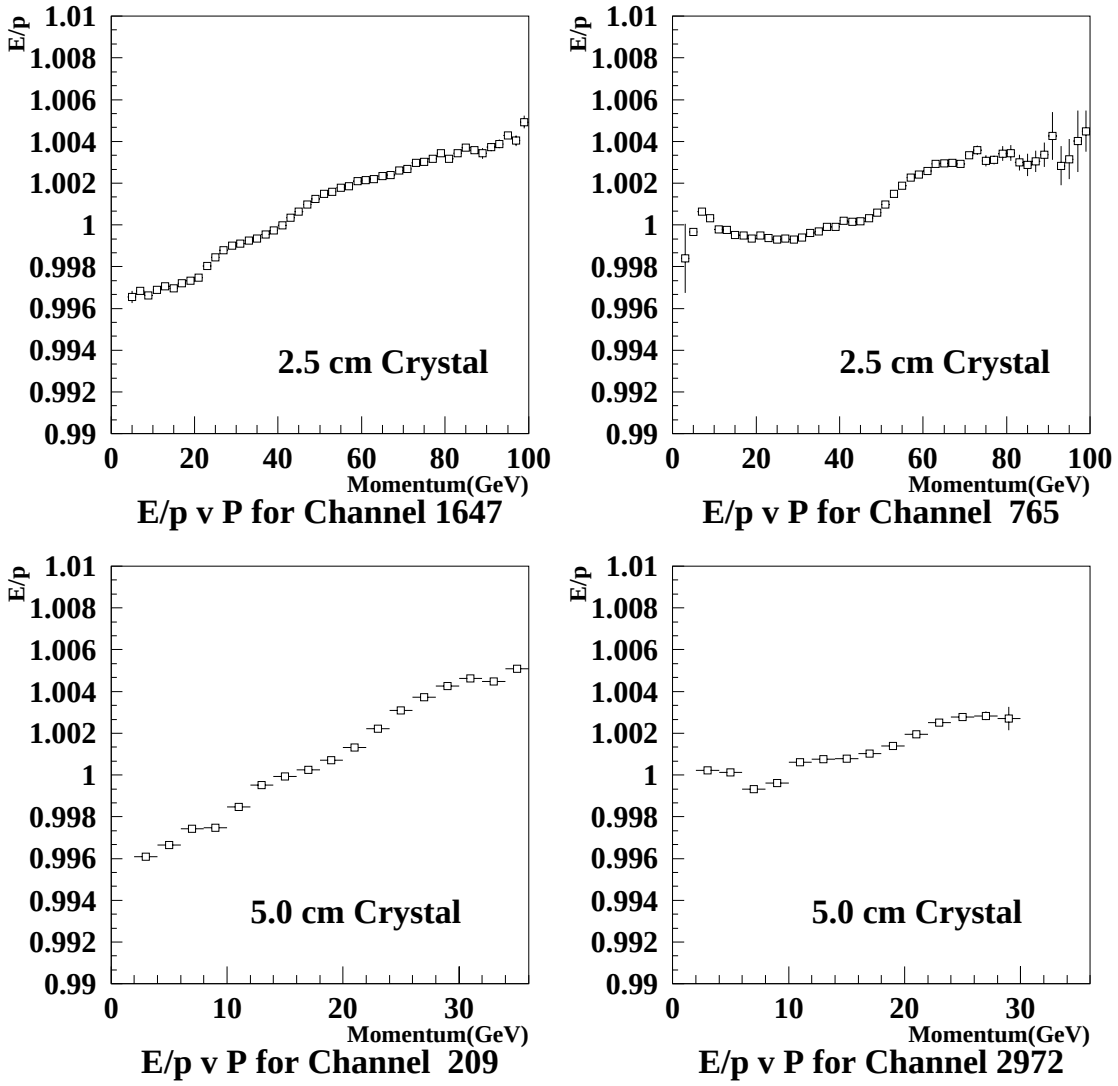

Figure 4.21: E/p linearity for K_{e3} electrons incident on four different channels. An correction is applied based on the E/p linearity in each channel.

- Energy Scale Correction for Photons An additional energy scale was applied to photons in $K_{L,S} \to \pi^0\pi^0$ data events to account for differences in the $K_{L,S} \to \pi^0\pi^0$ energy scale between the data and Monte Carlo. The energy scale will be discussed in detail in Chapters 7 and 9 and Appendix B.

4.5.2 Energy Calibration

We performed the energy calibration using electrons by adjusting the "charge-to-energy" conversion (Q/E) for each channel. The procedure was iterated until the electron E/p distribution for each channel was centred at 1 and the E/p resolution did not change significantly with further iterations. It was found that the energy resolution was stable after four gain iterations. The energy calibration procedure assumed that the measurement of the electron momentum was accurate and that the momentum non-linearity was negligibly small. The effect on $Re(\epsilon'/\epsilon)$ due to non-linearities in the momentum measurement during the energy calibration is discussed in Appendix B.

To calibrate each CsI channel to a statistical precision of about 0.05%[14], we required a large sample of electrons. It was also important that, as far as possible, the same clustering corrections be used when reconstructing calibration electrons and photons. To achieve an energy resolution better than 1%, we needed to identify the electron clusters clearly as well as measure the electron momentum and energy accurately .

K_{e3} electrons were used for the calibration because the $K_L \to \pi^\pm e^\mp \nu$ decay were copious, the electron energies ranged from 2 GeV to 100 GeV and it was easy to distinguish the electrons from the pions. The CsI readout threshold for K_{e3} calibration events was set to be the same as that of $K_{L,S} \to \pi^0\pi^0$ events so that differences between the electron and photon energy reconstruction due to the readout threshold correction were avoided. Although electrons were very useful in calibrating the calorimeter, using electrons in the energy calibration made us insensitive to the energy reconstruction of overlapping clusters which was important for $K \to \pi^0\pi^0$ events. We

[14]This was the desired precision of the offline energy calibration.

were also susceptible to photon-electron differences in the longitudinal shower development. The effect on $Re(\epsilon'/\epsilon)$ due to the electron-photon differences is discussed in Appendix B.

Electrons were selected from K_{e3} events with only two tracks which both pointed to clusters in the calorimeter and were identified by requiring the E/p of the electron to be greater than 0.8 and the E/p of the pion to be less than 0.8. Kinematic and veto cuts were applied to reduce the background due to $K_{L,S} \to \pi^+\pi^-$ decays.

We applied several selection cuts to improve the measurement of the electron energy and momentum. To minimize the energy from the pion leaking into the electron cluster, the pion track at the calorimeter had to be at least 30 cm away from the electron cluster if the pion was minimum-ionizing, and at least 50 cm away if the pion showered in the calorimeter. It was important to minimize the energy "overlap" from the pion because the overlapping pion shower energy affected the reconstructed energy linearity of the electron. Since pions and electrons were closer together at the centre of the calorimeter than at the outer regions, vacuum and regenerator beam $K_{L,S} \to \pi^0\pi^0$ events could be affected differently if we did not account for overlapping pion showers in the energy calibration. Besides applying a pion-electron separation cut, we also applied a tight cut on the transverse energy distribution of the electron shower to reduce the effect of accidentals on the electron cluster. To avoid mismeasuring the electron energy in events where the electrons scattered in the CA or where there was backsplash from the calorimeter into the CIA, we rejected events with energy in the CA and CIA. We also rejected events with electrons in the outer 2.5 cm of the calorimeter to improve the energy resolution for the cluster seeds at the outer edge of the calorimeter.

The energy calibration was performed "online", while we were collecting data, as well as offline. Although the offline and online energy calibration were essentially the same, there were slight differences because of the different goals of the online and offline calibrations. In the online calibration, we had to ensure that the calibration was fast, efficient and accurate enough that the Level 1, 2 and 3 triggers would not be inefficient. In the offline calibration, we wanted to achieve an energy resolution better than 1% and strove to ensure that the photon-electron differences and other

systematic effects on $Re(\epsilon'/\epsilon)$ were minimized.

The online energy calibration used the online DPMT and drift chamber calibration. The online energy calibration in 1996 and 1997 was performed by integrating the charge over 228 ns and 76 ns (4 QIE slices), respectively. Energy was summed over 5×5 blocks for clusters in the small-region, so that the energy calibration did not use too much CPU. Only software clustering was performed, so that the energy response could be measured at low energies. We did not correct for overlapping cluster energies and applied no cluster separation cuts in order to allow extra clusters from electrons that radiated downstream of the analysis magnet[15]. To speed up the calibration, we only accounted for energy losses at the beam holes, the outer calorimeter edges and outside the nominal cluster region, and did not apply any other corrections.

The online energy calibration was performed whenever the global electron E/p resolution exceeded ∼1.3% or the laser triggers indicated that the gain of several channels had changed by a few percent. The calibration was performed every one to two days. The Q/E for a particular channel was updated only if there were more than 3 electrons that hit that channel. The global E/p resolution was ∼1% during data-taking.

In the offline energy calibration, we used the offline tracking corrections, survey measurements, and drift chamber calibration to ensure that the momentum was determined accurately. To make the offline energy calibration and $K_{L,S} \to \pi^0\pi^0$ analysis as consistent as possible, we used the offline DPMT calibration in the electron energy reconstruction. The electron clusters were defined by the nominal 7×7 small-block and 3×3 large-block regions as in the $2\pi^0$ analysis. The PMT current was integrated over 6 QIE slices (114 ns) in the 1997 offline energy calibration and analysis[16]. Although the energy reconstruction was more susceptible to accidental effects the longer the charge integration period, the energy resolution and linearity improved substantially. By integrating the PMT current over 6 (instead of 4) QIE slices, the total charge increased by ∼7% and the energy resolution improved by 0.28% in quadra-

[15]Radiative K_{e3} decays upstream of the analysis magnet did not affect the E/p measurement since the momentum was measured after the photon had been radiated.

[16]The integration period in 1996 was the same for the online and offline calibrations.

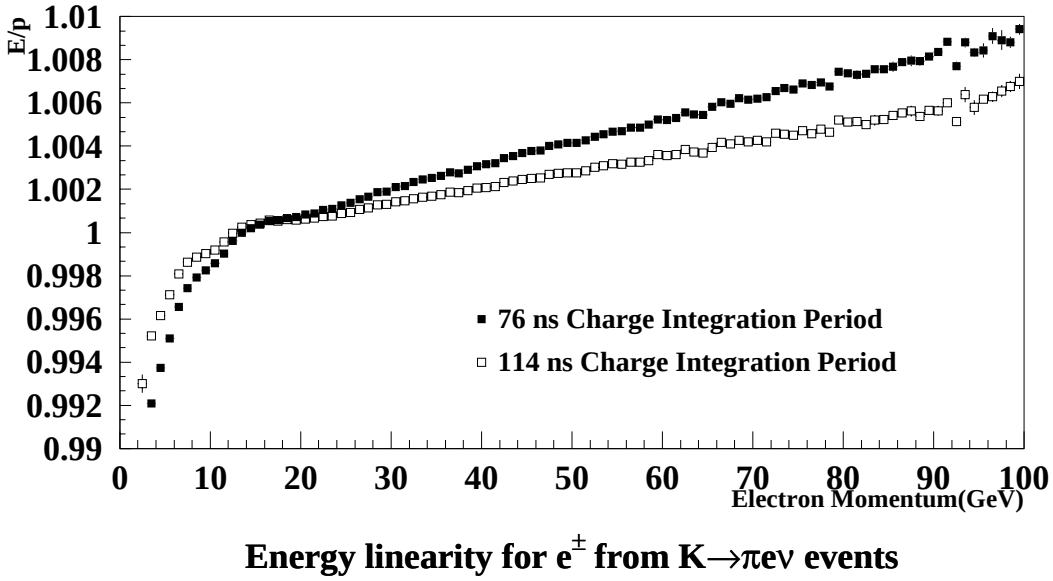

Figure 4.22: Energy linearity for e$^{\pm}$ from K_{e3} Data in 1997 for 76 ns and 114 ns charge integration periods. Although not all clustering corrections were applied, the same corrections were used in the comparison.

ture. The energy linearity improvement of ~0.4%/100 GeV is shown in Figure 4.22. As in the online calibration, we only performed software clustering, did not correct for overlapping clusters and accounted for energy losses down the beam holes, outer edges ($E_{missing}$) and outside the defined cluster regions ($f_{out-of-cone}$). In addition to the cluster energy corrections used in the online calibration, we also accounted for longitudinal and transverse variations in the response, energy that was not read out and short-term gain fluctuations in the offline energy calibration.

The 1996 and 1997 K_{e3} data was divided into several calibration periods. Each calibration period contained about one to three days of data. To ensure a high-quality electron sample, events with detector and data-taking problems as well as runs with special data-taking conditions were not used in the calibration. 420 million electrons were used to calibrate the 1997 data while 190 million electrons were used in 1996.

In each calibration period, the absolute energy scale for each channel was determined to better than 0.03% statistically. The energy linearity and energy resolution

for the full electron sample in 1997 after calibration are shown in Figure 4.23. The global E/p resolution in 1997 is 0.72%. As seen in Figure 4.23, the E/p distribution was slightly asymmetric. The "low-side" tail may have been partly due to energy losses in the dead space between the crystals. Photonuclear interactions of photons in the shower could also result in a lower measurement of E/p. A third possibility was the mis-identification of electrons in K_{e3} events. After subtracting the momentum resolution of the charged spectrometer in quadrature, the energy resolution, σ_E, was given approximately by

$$\sigma_E/E = 2\%/\sqrt{E} \oplus 0.4\%, \tag{4.5}$$

where E is the photon momentum in GeV.

4.6 Effect of Radiation on Performance of CsI Crystals

Cesium iodide was chosen for the KTeV calorimeter because it is a suitable scintillator for a high-speed environment and it could withstand high doses of radiation without a significant drop in performance. Published results [61] on the radiation-hardness of pure CsI were based on studies on a small sample of crystals that were performed over a short duration of a few days. The KTeV calorimeter presented ideal conditions for studying the performance of a large array of CsI crystals with varying amounts of radiation dosage. The rate of the radiation was much lower than in previous studies because the crystals were irradiated over several months. Hysteresis effects and the response of the crystals while they were being irradiated could also be monitored.

The CsI calorimeter was exposed to an average radiation dose per crystal of 2 krad over the 1996 and 1997 data-taking periods with crystals in the centre being exposed to a total of ~9 krad of radiation (see Figure 4.26). We measured the change in gain of each crystal over the 1996 and 1997 runs and observed that the light output of crystals exposed to about 8 krad of radiation was 75% of their light output before being irradiated (see Figure 4.24). We also compared the energy resolutions for each crystal after an average radiation dose of 2 krad to the resolutions after an average

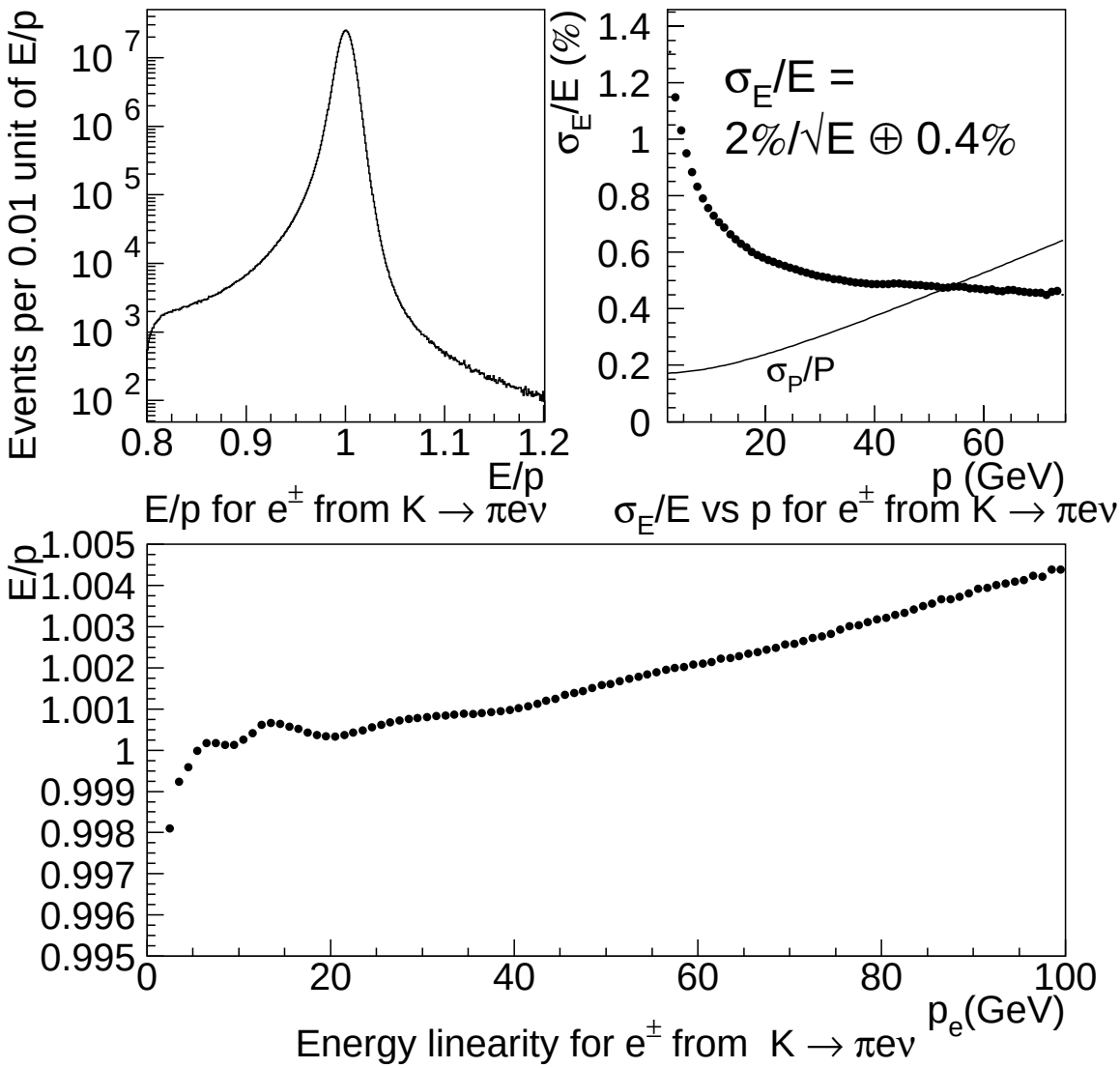

Figure 4.23: Top Left: E/p resolution for K_{e3} electrons in 1997. Top right: Energy resolution for K_{e3} electrons in 1997 after subtracting the momentum resolution (smooth curve). Bottom: The energy linearity for electrons from $K_L \to \pi^{\pm} e^{\mp} \nu$ events in 1997. The momentum non-linearity is assumed to be small. All 3 distributions were made using the full 1997 sample of 420 million electrons.

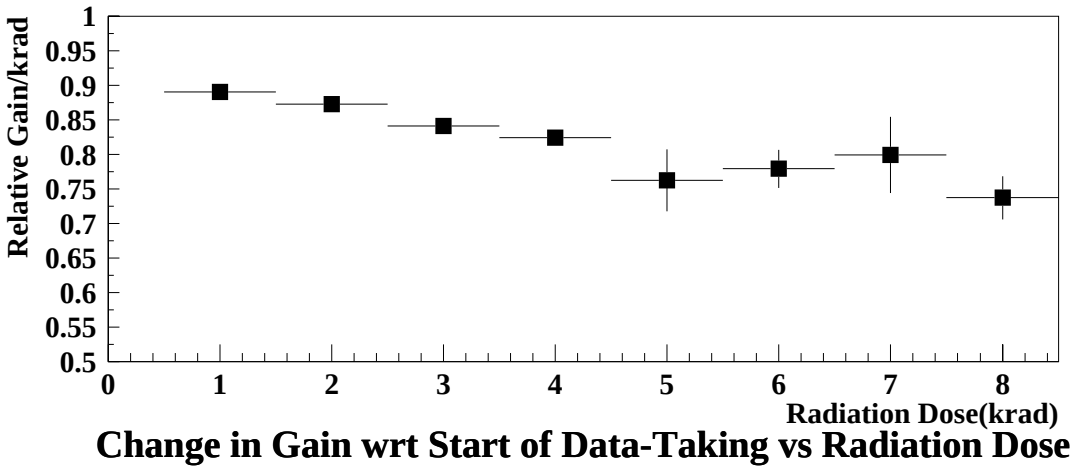

Figure 4.24: Change in CsI gain relative to the start of the data-taking period versus radiation dose. Gains were measured at the end of the E799 Summer data-taking period. Each point represents the average change in gain of crystals that had a total radiation dose indicated by the x-axis.

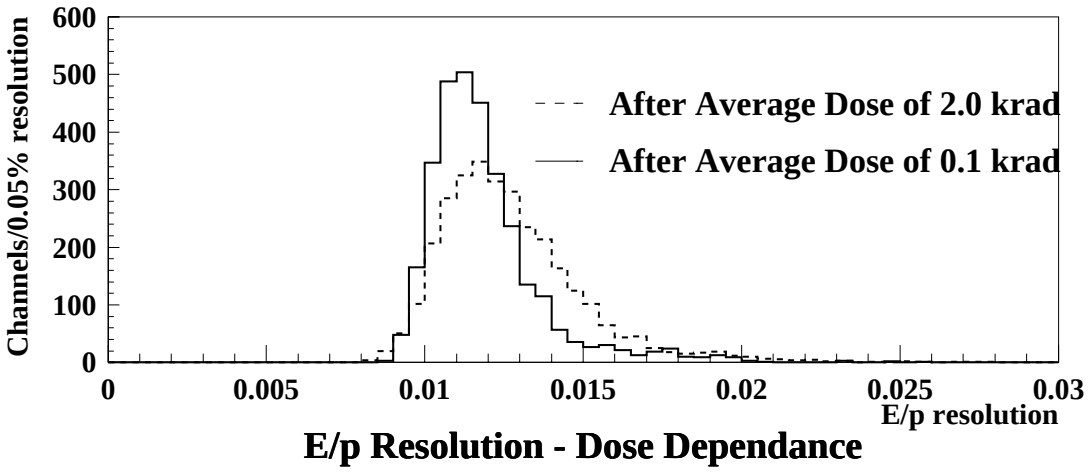

Figure 4.25: Distributions of electron E/p resolution after a mean dose of 0.1 krad and 2.0 krad. The mean and RMS of the E/p resolution after 0.1 krad were 1.2% and 0.18%, respectively. The mean and RMS of the E/p resolution after 2.0 krad were 1.3% and 0.23%, respectively.

radiation dose of 0.1 krad as seen in Figure 4.25. Only a small number of crystals experienced a change in resolution of greater than 0.6% (in quadrature).

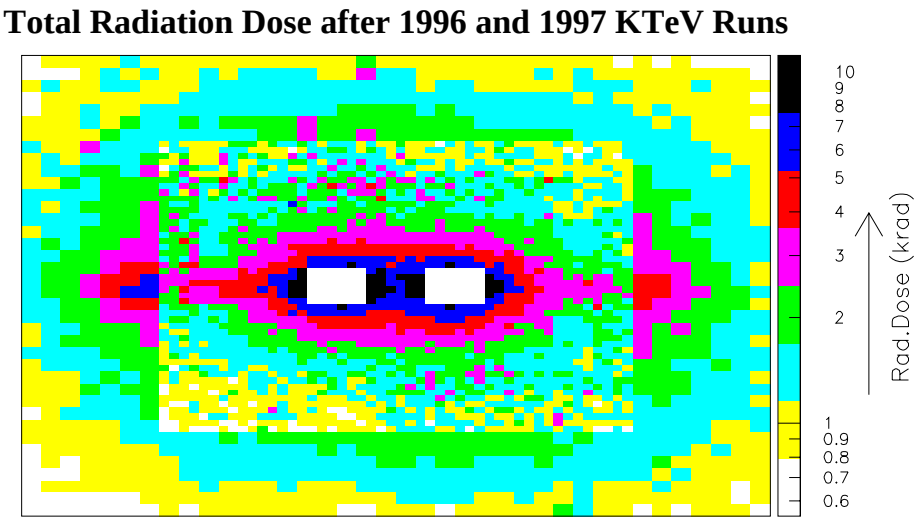

Figure 4.26: Variation in the total radiation dose over the calorimeter at the end of the KTeV run in 1997. Each pixel represents a CsI crystal.

The change in the longitudinal response of the crystals after irradiation was of significant concern. To measure the change in longitudinal response, we studied how the difference between the downstream (closer to the PMT) and upstream response (the uniformity step) was affected by radiation. The uniformity step, U_{step}, was given by

$$U_{step} = \frac{(Response_{Downstream} - Response_{Upstream})}{0.5 \times (Response_{Downstream} + Response_{Upstream})}. \tag{4.6}$$

We compared the uniformity step after an average exposure to 1.7 krad of radiation to the uniformity step at the start of data-taking. The change in the uniformity step, which was measured in units of standard deviations, is shown in Figure 4.27. A positive change in the uniformity step indicated that after radiation exposure, the drop in the response farther away from the PMT was higher than that closer to the PMT. We observed that for the longitudinal uniformity did not change significantly

for most crystals and that the crystals which showed a significant change in the uniformity were scattered over the calorimeter. For most of the crystals that showed more than a 3σ change in the uniformity after irradiation, we found that the change in longitudinal uniformity was small (<2%) and there was no clear correlation between the radiation dose and the change in uniformity. Figure 4.28 shows the change in the longitudinal response of a typical channel before and after irradiation. However, there were about 50 crystals which showed a large (>5%) change in the longitudinal response after radiation exposure. Figure 4.29 shows the longitudinal uniformity of highly radiation-sensitive channel after irradiation. As seen in the Figure, the light output at the upstream end dropped dramatically. The energy resolution also became worse for these crystals. It was observed that the crystals with the largest changes in longitudinal uniformity came from the same ingot or batch of crystals. Since these crystals were scattered all over the array, the change in response had less to do with the amount of radiation than the actual crystal production process. Moreover, contrary to earlier studies that were performed in the laboratory, crystals from all three crystal manufacturers showed similar radiation dependance.

Preliminary studies indicate that there was no significant dependance in the response across the face of the block (transverse uniformity) with radiation. The effect of radiation on the transverse response should be studied further.

Based on studies of the gain, energy resolution and longitudinal response of the crystals, we observed that the overall performance of the CsI calorimeter was not significantly degraded after ~9 krad of radiation. It will be interesting to study the response of the calorimeter at the end of the 1999 data-taking period because the total radiation dose was doubled by the end of the 1999 run. Moreover, we will be able to determine if there was significant recovery in the gain of the crystals between the 1997 and 1999 runs.

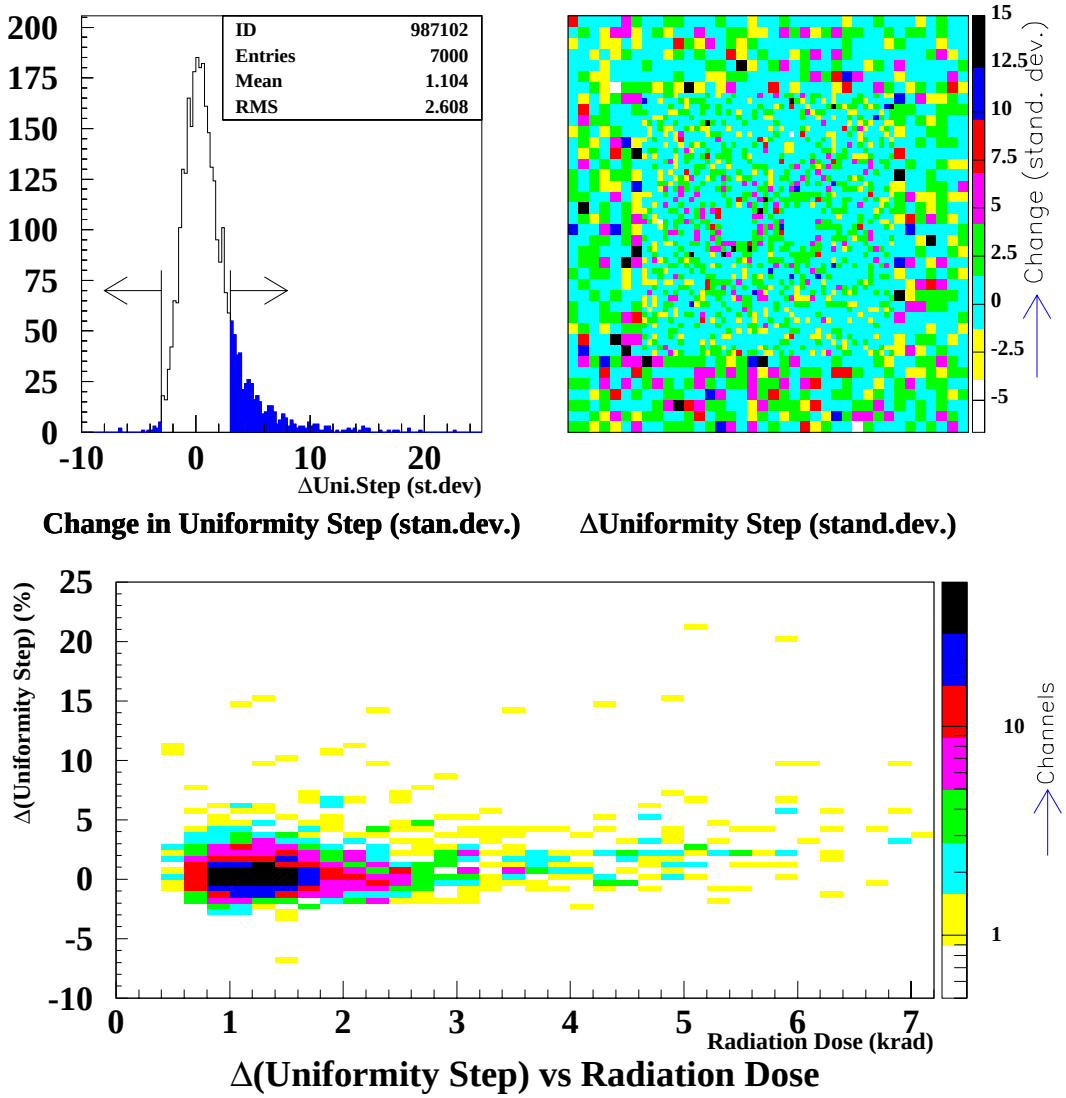

Figure 4.27: Change in CsI longitudinal uniformity after an average radiation dose of 1.7 krad. Top Left: Change in the Uniformity Step, ΔU_{step}, (Equation 4.6) in standard deviation (σ) units. The shaded region (indicated by arrows) shows crystals whose uniformity changed by more than 3σ. Top right: Variation in ΔU_{step} over the calorimeter. Each pixel represents a crystal. Bottom: ΔU_{step} (%) vs radiation dose (krad) for crystals with significant changes in uniformity step (shaded region in top left distribution).

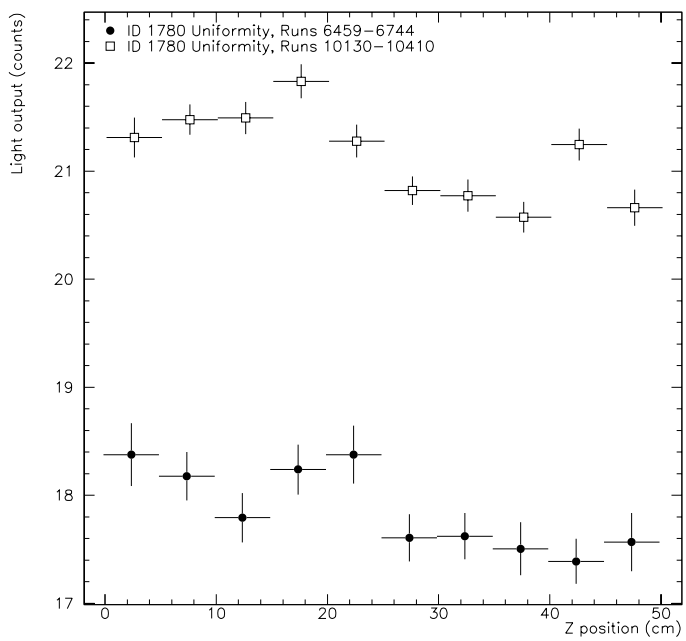

Figure 4.28: Longitudinal response of a typical crystal at the start of data-taking (Dark Circles) and after 2.3 krad of radiation (Empty Squares). The horizontal scale represents the distance from the Front Face of the Crystal. The overall light response for this crystal appears higher after irradiation because the PMT high voltage was adjusted during data-taking.

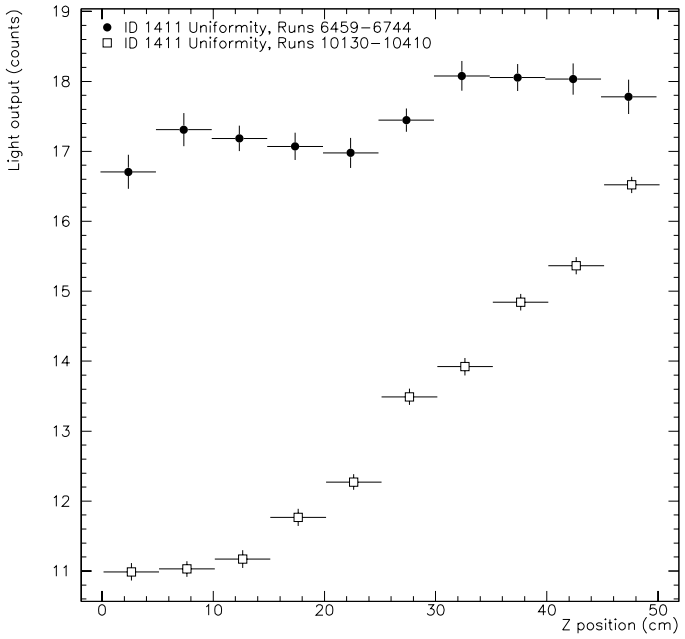

Figure 4.29: Longitudinal response of a highly radiation-sensitive crystal at the start of data-taking (Dark Circles) and after 5.2 krad of radiation (Empty Squares). The horizontal scale represents the distance from the Front Face of the Crystal.

CHAPTER 5
DATA COLLECTION

This chapter describes the data-taking periods in the KTeV experiment and discusses some of the problems that were encountered while collecting the data for the $Re(\epsilon'/\epsilon)$ measurement. The data samples that are used in this dissertation will be specified at the end of the chapter.

5.1 Data Periods

The KTeV detector was used for the E832 and E799 experiments. Since the experimental apparatus differed slightly between E832 and E799, the data-taking period was divided between the 2 experiments. The data-taking periods are shown in Figure 5.1. KTeV began with the E832 experiment and started collecting physics-quality data in October 1996. E832 data-taking ended in December 1996 and E799 began. Between the 1996 E832 and E799 runs, there were several detector upgrades. We were also able to identify and resolve several problems which improved the data collection efficiency during the E799 run in early 1997. The E832 experiment resumed again in April 1997 and although it ran for twice as long in 1997 as in 1996, we were able to collect almost 3 times as much useful $K \to 2\pi$ data. The Fermilab fixed target run ended in September 1997. After making substantial changes to the calorimeter and drift chambers, KTeV collected more E832 and E799 data during the fixed target run in 1999.

Besides collecting $K_{L,S} \to \pi^+\pi^-$ and $K_{L,S} \to \pi^0\pi^0$ data for the $Re(\epsilon'/\epsilon)$ measurement, we also carried out several "special" runs for calibration and detector studies. Although these special runs were very useful in understanding the detector, they were not included in the $Re(\epsilon'/\epsilon)$ analysis.

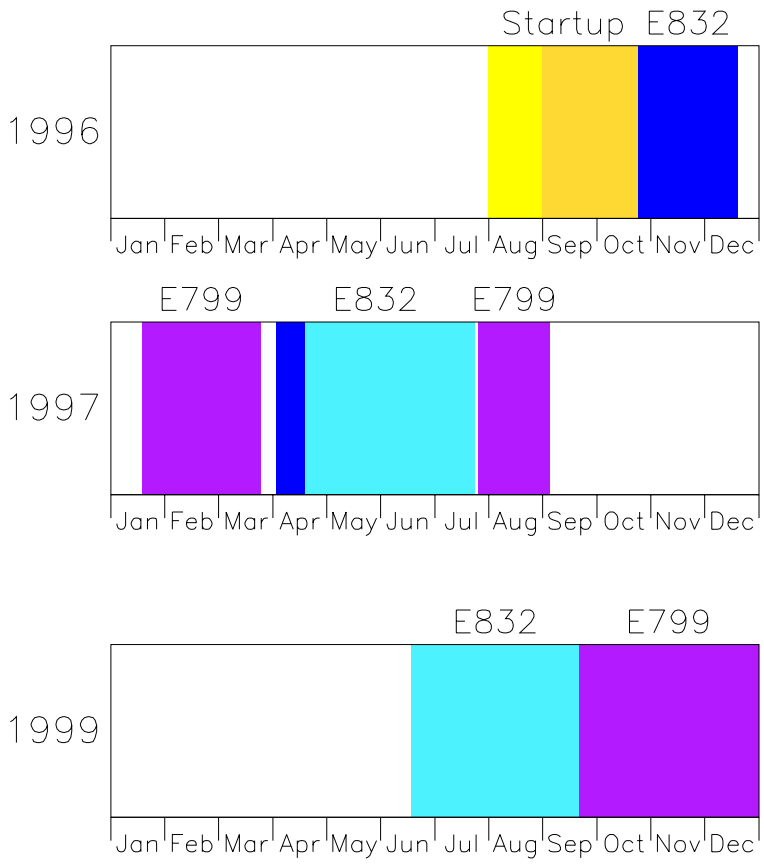

Figure 5.1: Data-Taking Periods in KTeV.

5.2 Problems during Data-taking

As is typical of most new experiments, the KTeV experiment faced several teething problems while collecting data in 1996 and 1997. Most of these problems were resolved during the 1999 data-taking run.

Since we wanted the final data sample to contain well-reconstructed events, we did not include events that had detector or data-taking problems in the $Re(\epsilon'/\epsilon)$ analysis. $\sim$12% of events were eliminated because they contained severe detector or data-taking problems, or were from special runs.

5.2.1 Drift Chambers

The drift chambers suffered several problems during 1996 and 1997 E832 running. Many of these problems involved noise in the drift chamber readout and the production of false hits due to drift chamber "oscillations". These problems are well-described in [62].

One of the largest problems that we faced in 1996 running was the "high-SOD" problem. Good events with two tracks were occasionally not accepted by the Level 3 charged mode filter code because the online track reconstruction did not identify both the charged tracks. The online tracking code did not identify a track if one of the hit-pairs that made up the track had a sum-of-distances (SOD) which was too high. Since the Level 3 $\pi^+\pi^-$ filter code required 2 good tracks, 22% of good charged mode events were rejected by the Level 3 trigger because one of the tracks had a "high-SOD" hit-pair.

The 'high-SOD' effect was found to depend on the operating voltage of the drift chambers, the chamber pressure and the beam intensity. Since the beam intensity was different in the regenerator and vacuum beams, the dependance of the beam intensity on the "high-SOD" effect resulted in a large $Re(\epsilon'/\epsilon)$ bias of $(10 \pm 5) \times 10^{-4}$. The bias on $Re(\epsilon'/\epsilon)$ was measured using a sample of events to which the Level 3 requirement was not applied. Although the "high-SOD" effect was modelled in the Monte Carlo simulation, we elected not to use the 1996 charged mode data because we could not determine the systematic error on $Re(\epsilon'/\epsilon)$ due to events that had been eliminated by the Level 3 filter code in 1996. Before the 1997 E832 run, the online track reconstruction was modified to allow tracks to have hit-pairs with high-SODs. Hence, although the 'high-SOD' effect was worse in 1997, we were not susceptible to the large bias due to the Level 3 filter which was present in the 1996 $\pi^+\pi^-$ data.

5.2.2 Calorimeter-related problems

The calorimeter encountered several readout problems in 1996 which resulted in the mismeasurement of cluster energies. Many of these problems were due to failures of the digitization hardware, with the QIE chips on the DPMTs being the most

vulnerable.

The QIE problems arose chiefly because of the design of the circuit components and layout of the chip. One of the main QIE failure modes in the 1996 E832 run was that the QIE assigned the wrong 3-bit exponent 0.1% of the time ("the exponent problem"). Since the operation of the exponent bit generator in the QIE was very sensitive to the QIE clock speed, slight variations in the clock speed would cause the exponent to be mis-assigned. This "exponent problem" was seen in chips from only one of the three QIE fabrication batches because the chips in the failing batch were slightly slower than the other batches. Since the QIE speed depended on the DPMT operating frequency, the "exponent problem" could be avoided by operating the DPMTs at a lower frequency.

Another common QIE failure mode was that the exponent in a QIE slice was assigned a non-zero value even though the integrated charge was in the lowest range of sensitivity (range 0). As a result of the mis-assignment of the QIE exponent, the energy in the channel was mis-measured. This failure mode occurred because the layout of the QIE contained metal traces which were too narrow. Electro-migration caused the impurities in the silicon to dissolve into the metal and form voids in the metal traces of the QIE. The voids resulted in the exponent being mis-assigned. Since voids would appear in the metal traces after about a million hours of QIE operation, this failure mode was first observed after a few weeks of running. Once a QIE experienced this failure mode, the channel would always read out the wrong energy.

As we were unable to redesign and replace the DPMTs without a considerable time delay, we decided to operate the DPMT at a frequency of RF/3 or 17.7 MHz in 1996 to reduce the rate of exponents being mis-assigned. Running at a lower clock frequency in 1996 made us more susceptible to accidental effects since the PMT current was integrated over a longer period. At the end of the 1996 E832 run, we replaced the QIEs from the failing fabrication batch and modified the DPMT boards to reduce the failure rate due to voids in the metal traces. Since the QIE layout was not modified in 1997, the QIE still had narrow traces. As a result, the QIEs continued to fail at a rate of 1 per 60000 hours of operation in 1997.

Besides QIE failures, there were also failures which were caused by the layout of the DBC chips. Some of the failure modes were first seen in 1996 but after several thousand hours of running in 1997, the problems became more frequent[1].

The bias on $Re(\epsilon'/\epsilon)$ due to a dead channel was $\sim 10^{-4}$ if we did not simulate the dead channel in the Monte Carlo. Since the bias was large, we decided to replace channels with readout problems as soon as possible during the run and to reject events which contained channels with readout problems. Occasionally, there were problems with either the calorimeter pipeline system, high voltage supplies, photomultiplier tubes or dividers. Events which had such problems were removed in the offline analysis.

The calorimeter channels were monitored in real time, so we were able to identify a CsI channel that had readout problems while we were collecting data and take the appropriate corrective action. Some of the histograms used to monitor the calorimeter performance are shown in Figure 5.2. The shift crew was alerted if a channel's readout was anomalous. For example, alarms would sound if a channel's gain (central plot in Figure 5.2) drifted by more than 5% or if the baseline (pedestal) level of the readout (top right plot in Figure 5.2) changed by more than 5 counts.

5.2.3 Other Problems

Besides calorimeter and spectrometer problems, we also faced difficulties involving the DAQ, trigger, regenerator and veto systems. Events with such problems were eliminated from the final data sample in the offline analysis.

5.3 Data Samples used in this Dissertation

The E832 datasets that were analyzed in this dissertation are from the 1996 and 1997 E832 runs. Due to the large Level 3 charged mode bias in 1996 described earlier, we did not use the 1996 $K_{L,S} \to \pi^+\pi^-$ sample. Although we excluded the 1996 charged

[1]The QIE and DBC chips were refabricated for the 1999 run and the DPMT failure rate was almost zero.

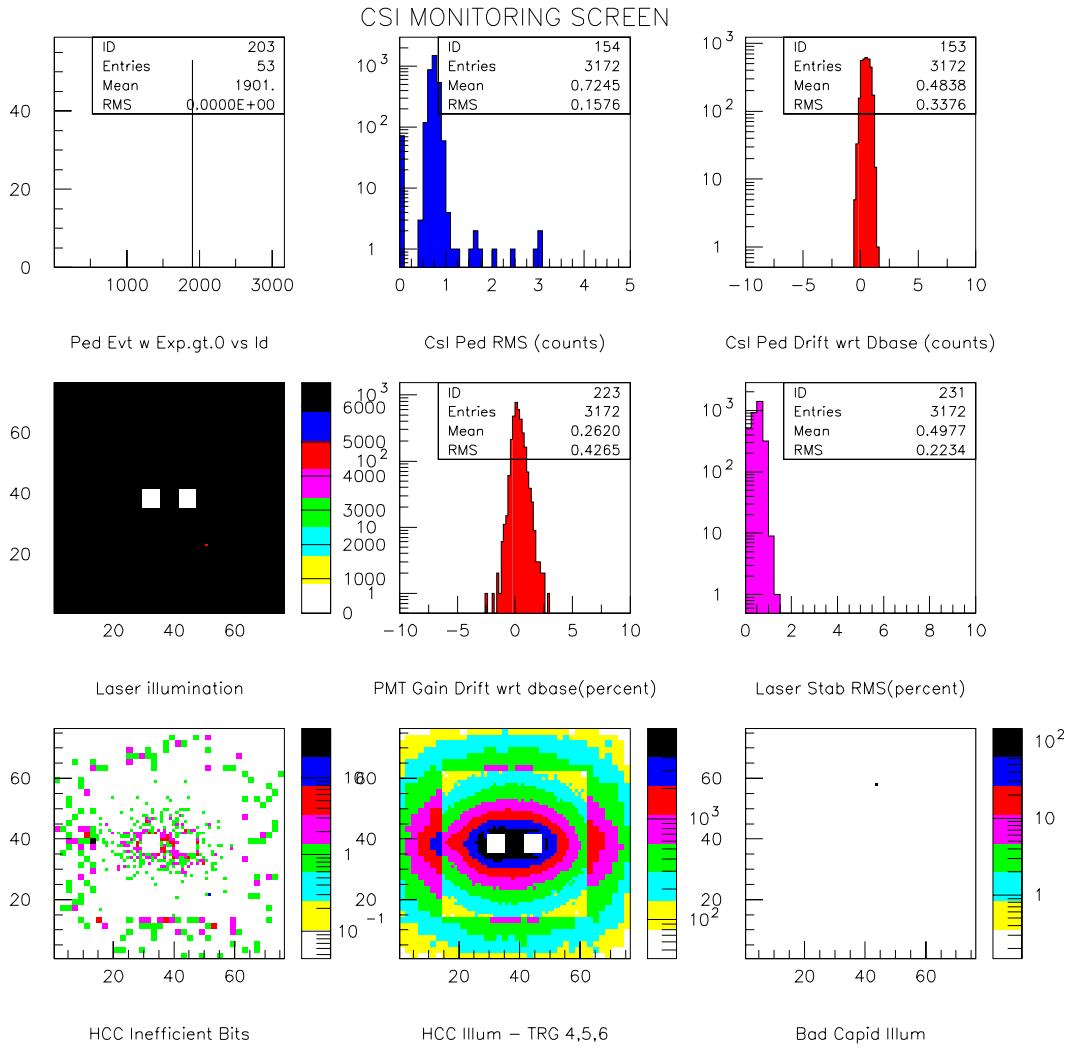

Figure 5.2: The cesium iodide calorimeter online display used to monitor the performance of the calorimeter during data-taking. These distributions were used to identify anomalous channels.

mode data from our final sample, the neutral mode data collected in 1996 was still useful. Since the measurement of $Re(\epsilon'/\epsilon)$ is statistically limited by the amount of neutral mode data, the statistical impact of excluding the 1996 charged mode data was small. The $K_L \to \pi^{\pm}e^{\mp}\nu$ and $K_{L,S} \to \pi^+\pi^-$ data in 1996 were still used to calibrate the calorimeter and to model the regenerator scattering in 1996. (This is discussed in Chapter 6.) Based on charged mode data from the the first 18 days of 1997 E832 running and the full 1996 neutral mode, we published a preliminary result [34]. In order to distinguish the 1997 charged mode data used for the publication and the rest of the 1997 charged mode dataset, we refer to the $K_{L,S} \to \pi^+\pi^-$ data from the first 18 days as the "1997a dataset" and the rest of the data as the "1997b dataset". The results presented in this thesis will be made up of the 1997a and 1997b charged mode datasets and the 1996 and 1997 neutral mode datasets.

CHAPTER 6
ANALYSIS AND RECONSTRUCTION OF $K_{L,S} \to \pi^+\pi^-$ DECAYS

The selection, reconstruction and analysis of the $K_{L,S} \to \pi^+\pi^-$ vacuum and regenerator beam samples will be described in this chapter. We will also describe the background subtraction scheme which is needed to yield the final $K_{L,S} \to \pi^+\pi^-$ data sample.

6.1 Trigger Requirements

Although the $K_{L,S} \to \pi^+\pi^-$ Level 1 and Level 2 triggers were designed to accept 2 track events with small net transverse momentum, the requirements were loose enough that other modes with two charged particles like $K_L \to \pi^+\pi^-\pi^0$ and $K_L \to \pi^\pm e^\mp \nu$ were accepted as well. The Level 3 $\pi^+\pi^-$ filter code then specially selected possible $K_{L,S} \to \pi^+\pi^-$ candidates.

6.1.1 Level 1

The Level 1 $K_{L,S} \to \pi^+\pi^-$ trigger required at least 3 hits in the V and V' counters with at least 1 hit in each counter. This loose 2-track requirement reduced the sensitivity to trigger hodoscope inefficiencies. We divided the trigger hodoscope counters into "East" and "West" sections with some overlap between "East" and "West" counters in the centre of the hodoscope. We also divided the counters into "Up" and "Down" sections with the 2 sections overlapping in the central region. The $K_{L,S} \to \pi^+\pi^-$ Level 1 trigger required at least 1 hit in each of the East, West, Up and Down sections[1]. An event with no net transverse momentum would always satisfy this

[1]The V-V' hit requirement is not consistent with the East-West-Up-Down trigger, since a single hit could illuminate both East and West or Up and Down counters at the same time.

"East-West-Up-Down" requirement. Inefficiencies in the "East-West-Up-Down" trigger affected regenerator and vacuum beam $K_{L,S} \to \pi^+\pi^-$ events differently because the $\pi^+\pi^-$ illuminations of the two beams were different. Since "East-West-Up-Down" trigger inefficiences affected the double ratio measurement to first order, the trigger performance needed to be well-understood.

The Level 1 tracking requirement involved the wires in the x and y views of drift chambers 1 and 2. The trigger demanded that three of the four views have at least one hit in a 90 ns time interval. To reduce accidental activity, scattering and decay background, the Level 1 $K_{L,S} \to \pi^+\pi^-$ trigger also rejected events with activity in the regenerator, MU2 counters (see Figure 3.10) and spectrometer-antis (SAs).

6.1.2 Level 2

The Level 2 $K_{L,S} \to \pi^+\pi^-$ trigger used two custom-made hardware processors: the Y-hit counter and the Y-track finder. Both of these processors involved the drift chambers. The Y-hit counter was a processor which looked for two hits in any three of the four chamber y-views with at least one hit in the remaining chamber. The Y-hit counter had several positive features. It was insensitive to chamber inefficiencies since it allowed hits to be missed by one of the four chambers. Furthermore, potential biases in $Re(\epsilon'/\epsilon)$ due to differences in wire inefficiencies were reduced because the same y-wires were used for both regenerator and vacuum beams (for the same regenerator position). The total processing time of the Y-hit counter was ~800 ns. The Y-track finder (YTF) required one y-track in both the upper and lower halves of the chambers. Tracks passing through the central section of the chambers were considered to be in both the upper and lower halves of the chambers. To allow for chamber inefficiencies, the YTF allowed one track to miss a hit in chambers 1 or 2 but needed both tracks to have all hits in chambers 3 and 4.

6.1.3 Level 3

The Level 3 filter code loosely selected $K_{L,S} \to \pi^+\pi^-$ events by requiring that there be at least two tracks and a two-track vertex with a combined mass greater than

450 GeV/c^2, assuming that both tracks were from pions. Each track also had to have an $E/p < 0.9$ where the energy, E, was measured using the calorimeter and the momentum, p, was determined using the charged spectrometer. We did not impose any requirements on how well the two tracks were matched at the vertex, so an event passed the Level 3 filter if any pair of tracks in the event satisfied the above conditions.

6.2 Offline Reconstruction

The $K_{L,S} \to \pi^+\pi^-$ event reconstruction consisted of first finding two tracks that originated from a common vertex point and matched clusters of energy in the calorimeter, and then reconstructing kinematic quantities such as the kaon momentum, invariant mass and the position of the kaon decay.

The first stage of the offline event reconstruction was the unpacking of the drift chamber hit information. The TDC information was unpacked and converted to drift distances using the $x(t)$ maps determined by the spectrometer calibration.

The next stage of the track reconstruction was to classify the hits and identify track candidates. Each hit was classified as either being a part of a hit pair or an "isolated single hit". A hit was part of a hit pair if there was a hit on an adjacent wire in the complementary drift chamber plane. For a wire with multiple hits, only the earliest hit in the 235 ns wide in-time window was considered for tracking. If the hit belonged to a hit pair, the hit was then classified based on the sum-of-distances (SOD) of the pair. A hit pair could have either a low-SOD, "good" SOD or a high-SOD. Unless a hit pair was in the x-view of the two downstream drift chambers, it was considered to have a good SOD if it was within 1 mm of a half-cell spacing, 6.35 mm (see Figure 3.6). For hit pairs in the x-view of the two downstream drift chambers where the track angles were larger, a good SOD had to be within 1.5 mm of a half-cell spacing.

Based on the classification of hits, a set of space points were determined. Each space point was assigned a weight which was later used to determine the quality of tracks. Hits forming good SODs were treated together as a pair forming a single space point; this type of space point was assigned the largest weight. Hits that were

part of low and high SODs were treated as two individual hits and were assigned a lower weight than hits from good SODs. Isolated singles were considered as 2 hits on either side of a wire. Occasionally there were events with an unusually large number of space points per pair of planes. In the 1997 charged mode analysis, the lowest quality space points like isolated singles were not considered for tracking if there were more than 32 space points in any of the 8 plane-pairs.

Once the hits had been classified, x- and y-track candidates were selected. y-track candidates were chosen by fitting the space points in the four chamber y-views to a straight line while x-track candidates were formed by selecting upstream and downstream track segments which matched at the central plane of the analysis magnet to within 6 mm. Each track candidate had to have a minimum number of hit pairs with a good SOD, and was only allowed to contain a limited number of isolated singles and hits that formed a low- or high-SOD. Track candidates were not allowed to share hits from the same wire unless the tracks passed on opposite sides of the sense wire.

Due to the orthogonality of the KTeV drift chamber system, there was no way to match the x-track candidates to the y-track candidates with only the spectrometer information, so the x- and y-track candidates were matched to clusters of energy in the calorimeter. A track was considered to match a cluster if the distance between the track and the cluster at the face of the calorimeter was less than 7 cm.

A series of corrections were applied to the (matched) track candidates. We adjusted the hit positions to account for chamber rotations, modified the drift distances to correct for the propagation time of the signal along the sense wires and recalculated the SODs after accounting for the angle of the track[2]. We also accounted for the effect of δ-rays which caused hit pairs to have low-SODs, by only choosing only the hit which led to a better agreement of upstream and downstream track segments at the magnet. We corrected for fringe field of the analyzing magnet, which extended to chambers 1 and 4, by moving the hits in the x-views of the chambers 2 and 3 [39]. Since the field of the magnet also had a small component in the x- and z-directions, we did not require the upstream and downstream y-track segements to lie in a straight

[2]After all corrections, each track was required to have at least 1 good SOD pair.

line.

Having selected the track candidates and corrected their positions, we determined the two-track vertices by matching the upstream segments of the tracks. We allowed the space points that made up the tracks to vary by 2 mm and required that the two tracks that made up the vertex not share any hits. For each two-track vertex candidate, we calculated a vertex χ^2 based on the agreement and position resolutions of the upstream x- and y-track segments. We also determined the agreement between the upstream and downstream track segments in the mid-plane of the magnet (offmag χ^2) for each track that made up a vertex candidate. In the calculation of both the offmag χ^2 and vertex χ^2, we accounted for both the chamber resolutions as well as the effect of multiple scattering on the tracks. The $\pi^+\pi^-$ vertex was selected to be the best vertex candidate based on the the vertex χ^2, the offmag χ^2, and the number of high-SOD pairs, low-SOD pairs and isolated singles that each track contained. The reconstructed z-vertex resolution for $K_{L,S} \to \pi^+\pi^-$ events was $\sim$30 cm.

From the tracking and vertex information, one could fully reconstruct a $K_{L,S} \to \pi^+\pi^-$ event. The track momentum was calculated using the field integral of a path extending from chambers 2 and 3 through the point in the mid-plane of the analysis magnet where the track passed. The "invariant mass" of the two tracks was determined using the track momenta assuming the tracks were due to charged pions. To determine which beam the kaon originated from, we used the vertex x-position for decays upstream of the downstream end of the regenerator. Since decays downstream of the regenerator may have originated from kaons that scattered in the regenerator and into the vacuum beam, to determine the kaon beam for a decay downstream of the regenerator, we first projected the total momentum vector of the vertex back to the z-position of the downstream face of the regenerator and then assigned the beam based on the x-position of the momentum projection.

A typical $K_{L,S} \to \pi^+\pi^-$ event reconstructed online is shown in Figure 6.1. In the figure, the two pion tracks are bent in the x-view by the field of the analysis magnet. In the event shown in Figure 6.1, one of the pions was minimum-ionizing while the other showered in the calorimeter.

In order to select coherent scatters and reduce other scattering background, the

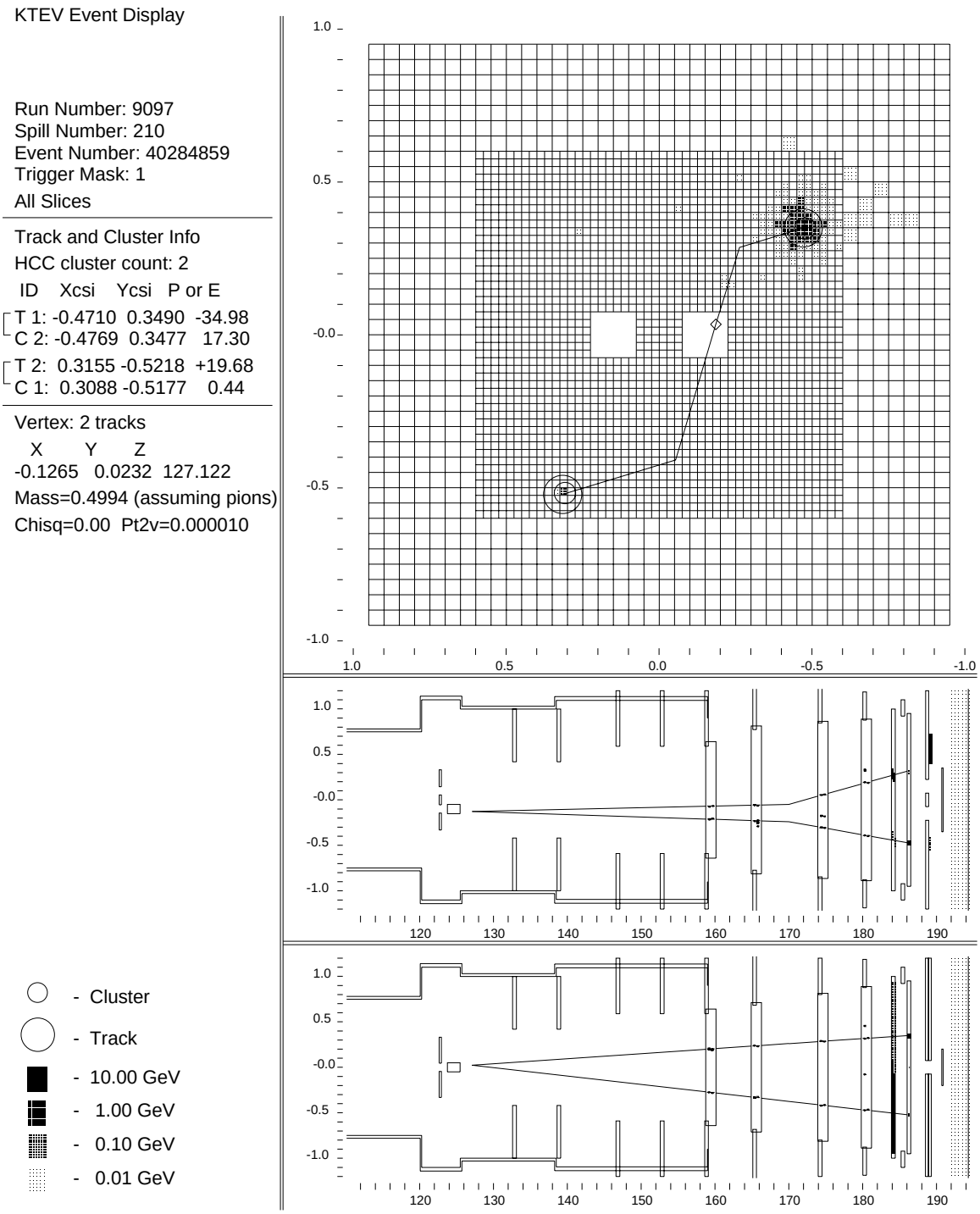

Figure 6.1: A $K_{L,S} \to \pi^+\pi^-$ event showing (top) the two clusters of energy at the calorimeter and (bottom) the x- and y-views of the tracks in the charged spectrometer. The kinematics of the event (*e.g.,* the track momenta, cluster energies and vertex position) determined by the online event reconstruction are shown on the left.

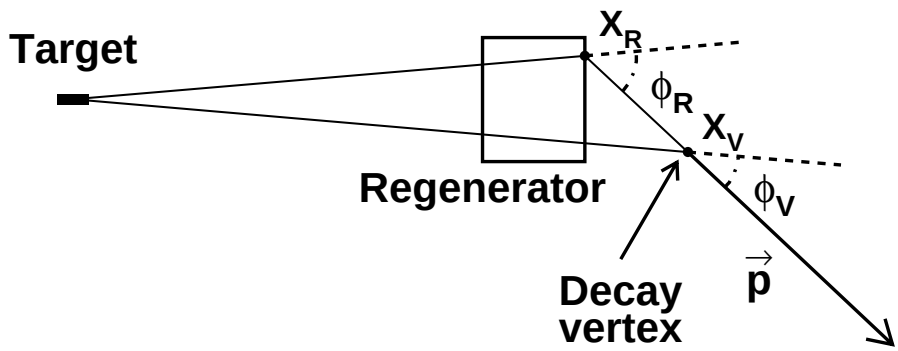

Figure 6.2: Definition of p_T^2 in the Charged Mode Analysis. The transverse momentum can be defined with respect to either the decay vertex (X_V) or the vertex projected back to the z-position of the regenerator (X_R). The latter definition is used in the $\pi^+\pi^-$ analysis.

transverse momentum of the kaon, p_T, had to be measured. As shown in Figure 6.2, the kaon transverse momentum could either be defined to be the 2-track momentum perpendicular to (a) the displacement vector from the target to the decay vertex position, X_V, or (b) the displacement vector from the target to the position of the total vertex momentum projected to the z-position of the downstream face of the regenerator, X_R. Since the kaon transverse momentum for $K_{L,S} \to \pi^+\pi^-$ events was non-zero for scattered kaons only, using the regenerator downstream face to define the kaon direction could be related to the physical scattering process more easily. Hence, we defined the kaon transverse momentum to be $|\vec{p}|sin\phi_R$ (instead of $|\vec{p}|sin\phi_V$) as illustrated in Figure 6.2. The definition of transverse momentum was the same for both vacuum and regenerator beam events.

6.3 Analysis Cuts

In order to make sure that the final $K_{L,S} \rightarrow \pi^+\pi^-$ event sample included well-reconstructed events which had a large signal-to-background ratio, several event selection cuts were applied. Analysis cuts were also applied to define the apertures. Using analysis cuts to define the apertures helped to reduce the sensitivity to the Monte Carlo simulation that was used to determine the acceptance.

6.3.1 Data Quality Cuts

We made sure that the final event sample only contained events that passed the online trigger. The V-V' counter hit requirement and the East-West-Up-Down trigger condition were verified by checking the matching of reconstructed tracks to hodoscope counter hits. $\sim$0.01% of events in both beams were rejected because the tracks did not match enough hit hodoscope counters. We also made sure that there were no hits in the MU2 counters by using the the muon counter TDC information. Events with activity in the MU3 counters were rejected as well. Lastly, we vetoed any event in which the regenerator trigger source TDC fired in either the in-time bucket or the buckets preceding or following the in-time bucket.

6.3.2 Reconstruction Cuts

To ensure that the data were well-reconstructed, we cut on the vertex χ^2 and the offmag χ^2 of both the pion tracks. Figure 6.3 shows that the vertex χ^2 distribution in both beams looked similar but had long tails due to hits caused by accidental activity and high-SOD effects. The offmag χ^2 distributions showed similar behaviour. Since the Monte Carlo did not simulate the effects that caused the tails in the distributions very well, we cut loosely on the two tracking variables to be less sensitive to the details of the simulation. The final event sample only contained events with a vertex $\chi^2 < 100$ and tracks with an offmag $\chi^2 < 500$.

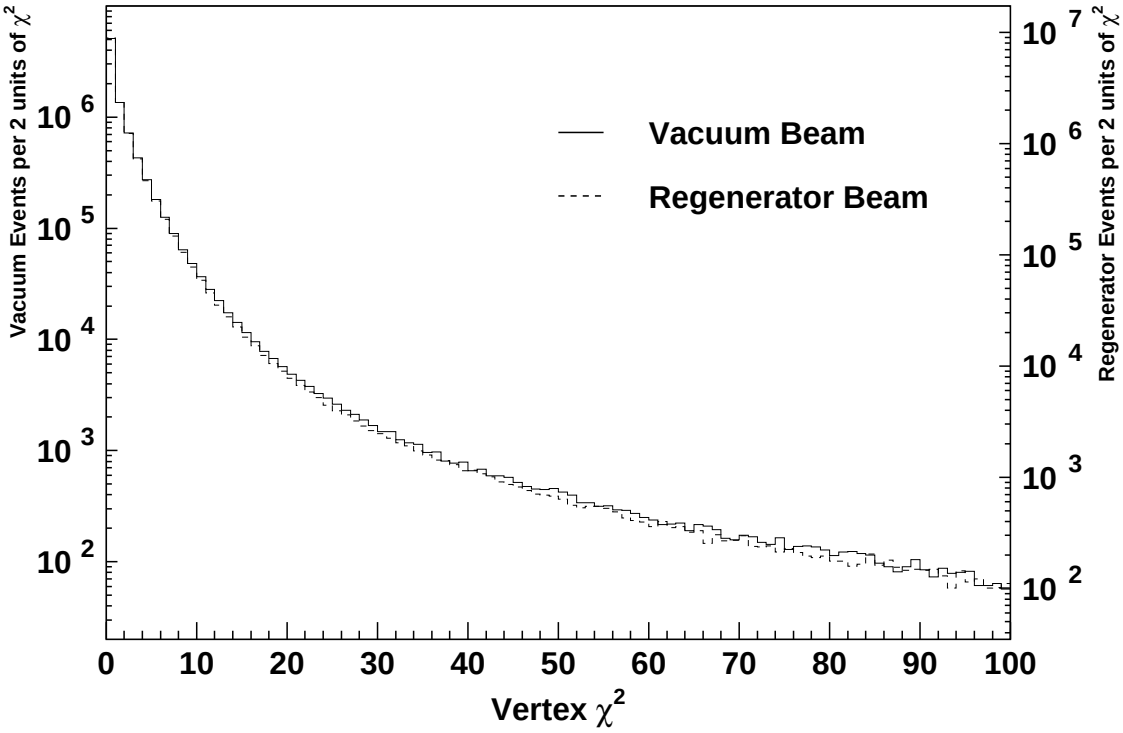

Figure 6.3: Vertex χ^2 distributions for vacuum and regenerator beam $\pi^+\pi^-$ data before background-subtraction and after all other analysis cuts

6.3.3 Background Suppression Cuts

We applied several cuts to reduce background to coherent $K_{L,S} \to \pi^+\pi^-$ events. We rejected events with activity in the regenerator and veto counters, and applied cuts to minimize extra activity in the detector. Background was also reduced by cutting on kinematic quantities such as the $\pi^+\pi^-$ invariant mass, kaon p_T^2 and the pion momenta.

Inelastic regenerator scatters were reduced by not allowing any regenerator module to have more than the equivalent energy of two minimum-ionizing particles (MIPs) or 8 MeV. We also required there to be less than the equivalent energy of 0.7 MIP in the last regenerator to define the downstream regenerator edge. The amount of energy in a regenerator module (see Figure 3.5) was calculated by subtracting the energy in the early time slice (i.e., the time slice before the in-time slice) from the energy in the in-time slice. This was done to account for baseline fluctuations in the

ADCs of the regenerator modules. Inelastic scatters were also reduced by rejecting events with significant activity in the veto counters. Events where the ring counter trigger source fired or where there was more than the energy equivalent of a 300 MeV photon in the SA were rejected. We also rejected events where the MA trigger source fired or the energy difference between any two MA channels was greater than the energy deposited by a 100 MeV photon. Cuts on MA activity reduced some upstream radiative $K_{L,S} \to \pi^+\pi^-$ decays.

Background due to scattering at a non-zero angle in the collimator and regenerator were reduced by requiring p_T^2 to be less than 250 MeV^2/c^2. Background from semileptonic decays and hadronic interactions in the regenerator were also reduced in this way. Figure 6.4 shows the vacuum and regenerator beam p_T^2 distributions before any background subtraction. The tails in the regenerator beam p_T^2 distribution are primarily due to the regenerator scatters while the tails in the vacuum beam are due to semileptonic decays and collimator scatters.

To improve the event reconstruction as well as to remove background due to mis-reconstructed events such as $K \to \pi^+\pi^-\gamma$, events with more than two tracks and with extra clusters in the calorimeter other than those due to the two pions were removed. To avoid rejecting good $\pi^+\pi^-$ events where a pion showered in the calorimeter or where a pion shower leaked across the beam hole, we only rejected events if the extra cluster was an in-time cluster with at least 1 GeV of energy and was not near the beam hole. The extra cluster must have also been more than 20 cm away from a pion cluster.

$K_L \to \pi^\pm e^\mp \nu$ background was reduced considerably by requiring each pion to have $E/p < 0.85$. This was a tighter cut than the Level 3 $\pi^+\pi^-$ requirement. To measure the pion E/p and $\pi^+\pi^-$ p_T^2 accurately, we had to avoid mis-matching the x- and y-tracks by requiring the x- and y-separation of tracks at the calorimeter to be at least 3 cm. Background due to $K_{\mu 3}$ decays with low energy muons that did not reach the muon counters was removed by ensuring that each track had a momentum greater than 8 GeV.

We selected events with a $\pi^+\pi^-$ invariant mass between 488 MeV/c^2 and 508 MeV/c^2 to reduce background due to mis-reconstruction. The $\pi^+\pi^-$ invariant mass, $m_{\pi^+\pi^-}$,

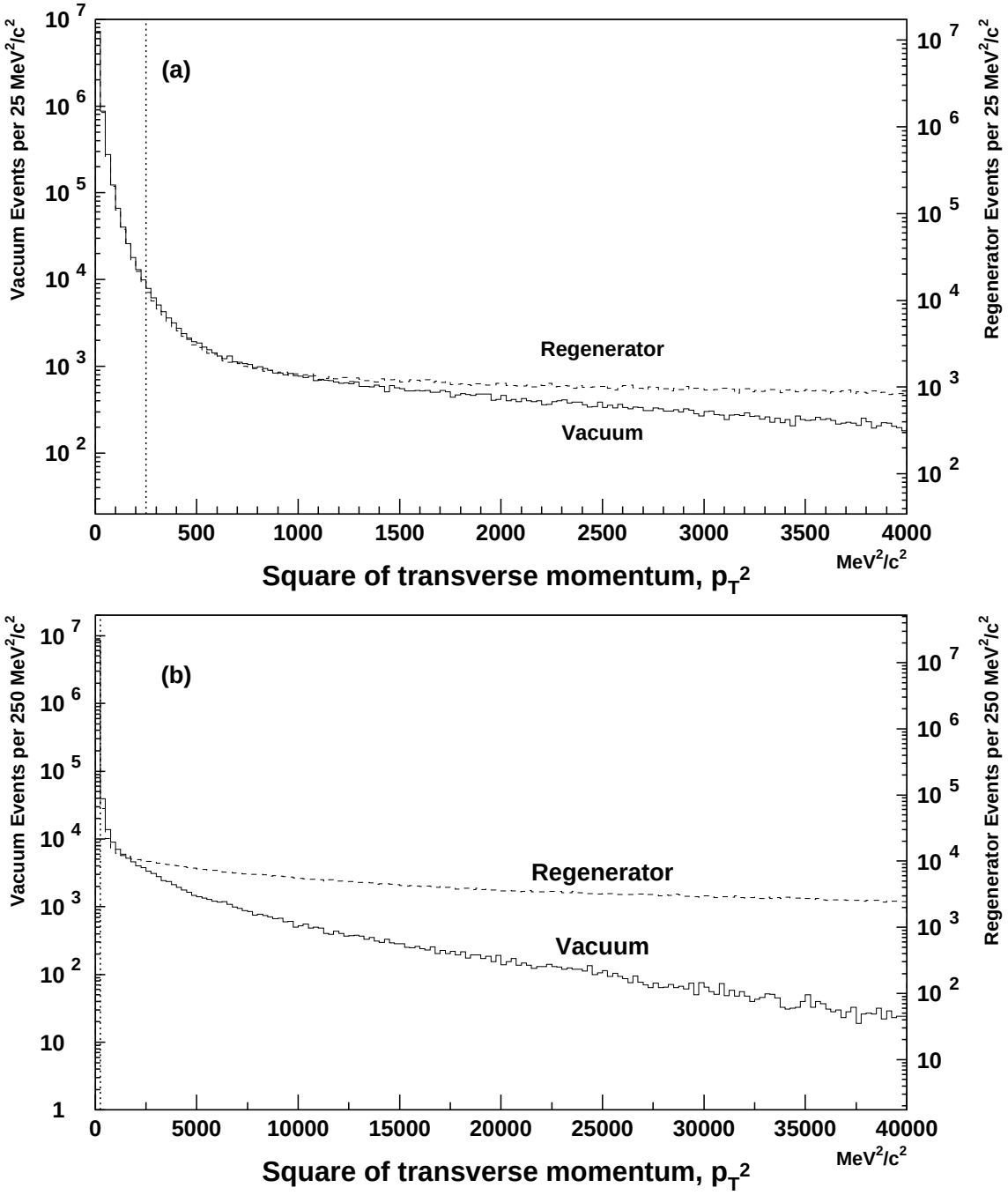

Figure 6.4: $K_{L,S} \to \pi^+\pi^-$ p_T^2 distributions for vacuum and regenerator beam data before background-subtraction and after all other analysis cuts. The top and bottom figures are the same distribution on different horizontal scales. The dotted line indicates the p_T^2 cut in the nominal $Re(\epsilon'/\epsilon)$ analysis.

distributions for both beams have a similar RMS resolution of ~1.6 MeV as shown in Figure 6.5. The low-side tail of the distributions was due to $K \to \pi^+\pi^-\gamma$ events. The tails in the vacuum beam were also due to semileptonic $K_{\mu 3}$ and K_{e3} events. The semileptonic background was smaller by a factor of ~13 in the regenerator beam due to the regenerator and shadow absorber attenuation.

Neutral Λ in the KTeV beam which decayed to $p\pi$ were a background to $K_{L,S} \to \pi^+\pi^-$ events. To remove this background, the invariant $p\pi$ mass was calculated assuming the higher momentum track was the proton. Events with invariant $p\pi$ mass between 1.112 GeV/c^2 and 1.119 GeV/c^2 were rejected regardless of the total $p\pi$ energy.

6.3.4 Apertures

Since charged pions could penetrate the physical apertures, we defined the apertures in the charged mode based on the projected track positions to be less senstive to the simulation at the physical apertures. The cuts on the projected track positions were made with respect to the positions of the physical apertures that were measured in a survey. Tracks were required to be 2 mm away from the CA, 2 mm outside the the beam holes of the trigger hodoscopes and 2.9 cm inside of the outer edge of the calorimeter. For decays upstream of the MA, tracks had to be 3 mm from the edges of the beam holes (see Figure 3.7). Since the calibration was poor at the outer edges of the drift chambers, events with tracks that passed too close to the outer edges of the chambers were not accepted. The drift chamber outer edge cut was different for each chamber; the cut varied from 14 to 62 drift chamber cells from the outer edge of the chambers.

Close tracks may result in mis-reconstructed hits with low-SODs. To avoid this, a track separation cut was applied. The track separation cut can also be thought of as a limiting inner aperture. To apply a track separation cut, we defined a drift chamber "cell" as illustrated in Figure 3.6. Each track was assigned to the "cell" belonging to the sense wire closest to the track. Tracks were required to be at least 3 drift "cells" apart in both the x- and y-views at every drift chamber. Since there

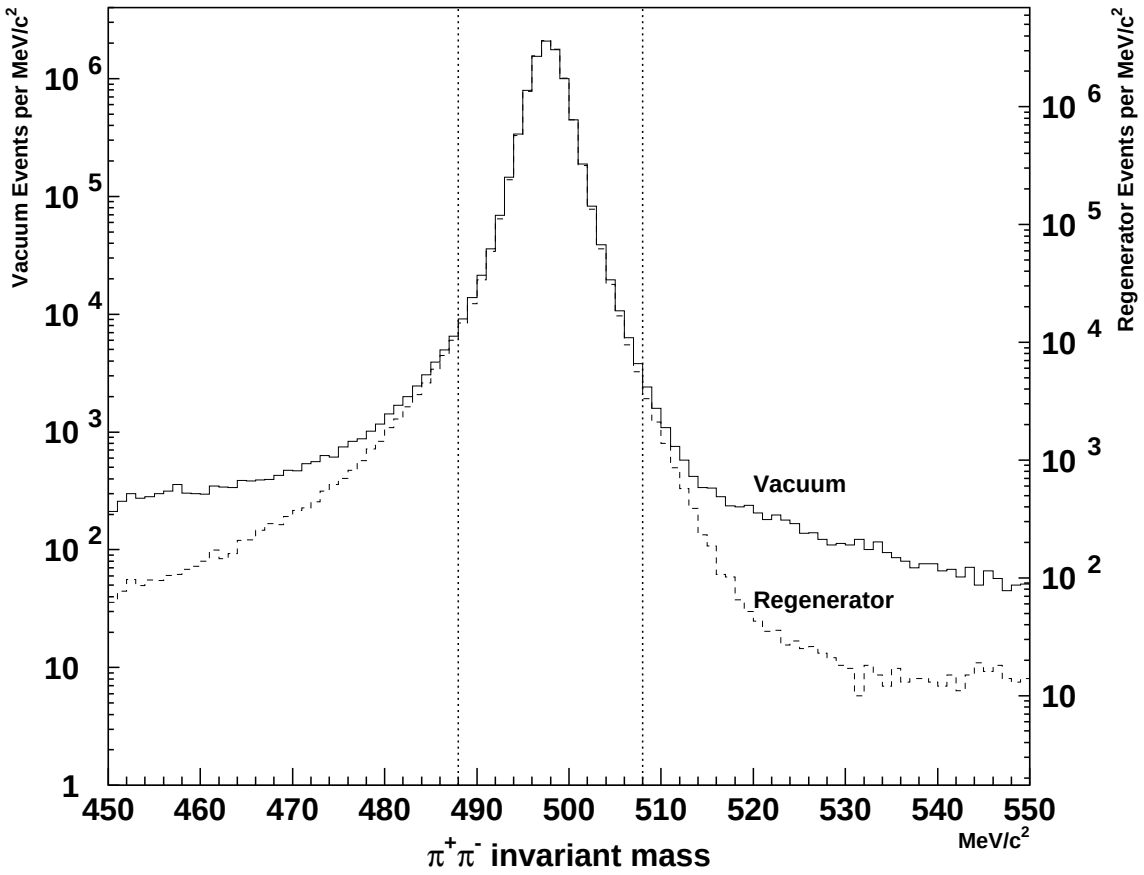

Figure 6.5: $K_{L,S} \to \pi^+\pi^-$ invariant $\pi^+\pi^-$ mass distributions for vacuum and regenerator beam data before background-subtraction and after all other analysis cuts. The dotted line indicates the $m_{\pi^+\pi^-}$ cut in the nominal $Re(\epsilon'/\epsilon)$ analysis.

were more vacuum beam $\pi^+\pi^-$ decays downstream, there were more vacuum beam events with smaller opening angles and hence the track separation cut affected the vacuum beam more than the regenerator beam. The track separation cut removes 18.4% and 10.2% of events in the vacuum and regenerator beams, respectively.

6.3.5 Fiducial cuts

The decay region was chosen to be between 110 m and 158 m from the target and the kaon energy range was between 40 GeV and 160 GeV.

The upstream edge of the regenerator beam in the charged mode depended on

the offline cut on the activity in the final regenerator module as well as the effect of the online Level 1 trigger source. To measure the effective regenerator edge, we first determined the probability, $P_{E<E_{veto}}$, that the total energy deposited by two minimum ionizing particles was less than the veto threshold. We then integrated $P_{E<E_{veto}}$ over the length of the last scintillator to find the effective regenerator edge. The effective regenerator edge for charged mode decays was (1.65±0.45) mm upstream of the physical downstream end of the regenerator.

There were a very small number of events which lay outside the beam region after all cuts. To reject such events, we projected the vertex momentum to the z-position of the downstream face of the regenerator and rejected the event if the projection lay outside a 75 cm^2 square region around the centre of the beam. The unscattered kaon beam reconstructed within a 60 cm^2 square region at the downstream end of the regenerator.

6.4 Charged Mode Background

There were two classes of background in $Re(\epsilon'/\epsilon)$ measurement - background due to mis-reconstructed decays which resembled 2π events and background due to kaon scattering.

Mis-reconstructed decays were potentially more insidious than scattering background as these decays were different in the charged and neutral modes. In the charged mode, $K_{L,S} \to \pi^+\pi^-$ events were mimicked by $K_{\mu 3}$ and K_{e3} decays, as well as by hadronic interactions in the regenerator which produced $\pi^+\pi^-$ and $\Lambda \to p\pi$. Background due to particle mis-identification was reduced considerably by having a good veto system and a detector system with excellent particle identification and resolution. The semileptonic decay background, at a level of 0.09%, was the primary background in the vacuum beam. It was much lower in the regenerator beam due to the attenuation of K_L in the regenerator. Background due to hadronic regenerator interactions was larger in the regenerator beam but even in that beam, it was at the 1×10^{-5} level.

Backgrounds due to kaon scattering were common to both charged and neutral

modes, so up to differences in η_{+-} and η_{00}, they were the same in both modes and hence should be less of a concern. However, since the charged and neutral mode reconstruction was very different, scattering background had a different effect in the two modes, thus causing a considerable impact on the $Re(\epsilon'/\epsilon)$ measurement if not accounted for. While the kinematics of $K_{L,S} \to \pi^+\pi^-$ events could be fully reconstructed, kinematic quantities such as the kaon transverse momentum could not be measured directly in $K_{L,S} \to \pi^0\pi^0$ events. In addition to reconstruction differences, the veto efficiencies for kaons that scattered inelastically to $\pi^+\pi^-$ and $\pi^0\pi^0$ final states were different. This resulted in different acceptances for inelastic scatters in the two modes.

The two main contributions to kaon scattering background were scattering in the defining collimators and scattering in the regenerator[3]. Kaons that scattered could either cross over from one beam to another or scatter at a small angle and remain in the same beam. The former caused a potential mis-reconstruction of the event in the wrong beam while the latter resulted in a different phase and acceptance for the scattered kaon with respect to an unscattered kaon.

Scattering in the collimator occurred in both beams and the scattered kaons were observed to be in both the K_L and K_S states[4]. In principle, there should be interference between the kaon states, but the data indicated that this was small. The scattered K_S in the KTeV decay region were mostly at high momentum because low-momentum K_S had already decayed before reaching the decay region. The K_S also had a broad p_T^2 spectrum which was typical of inelastic scatters. Scattered K_L were observed to have, on average, a lower p_T than scattered K_S. Background due to kaons that crossed over from one beam into the other after scattering in the collimators was reduced by the MA. Some of the scattered kaons that hit the MA but were not absorbed underwent regeneration. In the charged mode, the amount of collimator scattering was at the 0.01% level in both beams.

---

[3]Background due to scattering in the primary collimator was negligible because of the design of the collimation system (see Figure 3.2.

[4]The $K \to \pi^+\pi^-$ decay vertex distributions were described by a combination of K_L and K_S decay curves.

Kaons could scatter coherently, diffractively and inelastically in the regenerator. Kaons that scattered in the regenerator and into the vacuum beam consisted of both inelastic and diffractive scatters and were highly suppressed by the p_T^2 cut. Although kaons that scattered at a small non-zero angle in the regenerator beam were identified and reduced by the p_T^2 cut, kaons could also scatter inelastically and diffractively in the forward direction. This background was the largest source of background in the regenerator beam at a level of 0.074%.

6.4.1 Background Subtraction

The process of removing semileptonic decay and kaon scattering background from the data samples took place in three steps. Monte Carlo samples of the different types of background were first generated and analyzed using the same cuts as the data. These background samples were then normalized to the data samples. Finally, the normalized background samples were subtracted from the data to yield the final background-subtracted dataset for the $Re(\epsilon'/\epsilon)$ measurement.

Background due to hadronic regenerator interactions in the regenerator beam were subtracted by extrapolating from the distribution of events in the $\pi^+\pi^-$ invariant mass sideband, $m_{\pi^+\pi^-} > 510$ MeV/c^2, with a decay vertex z-position between 124 m and 126 m from the target, which was at the downstream end of the regenerator.

Generation of Background samples

The semileptonic decay samples were generated using the decay matrix elements; radiative semileptonic decays were simulated as well. The $\pi^+\pi^-$ trigger and offline analyses were applied to the semileptonic decay samples.

To generate kaons that scattered in the defining collimators, we had to identify a sample of collimator-scattered $K_{L,S} \to \pi^+\pi^-$ decays in the data and tune the simulation based on the data distributions. Collimator scatters were identified by projecting the kaon vertices from high p_T^2 $\pi^+\pi^-$ ($> 0.001\ GeV^2/c^2$) in the vacuum beam back to the z-position of the collimator and selecting events that were in the broad square bands shown in Figure 6.6. ~15% of events in this band consisted of coherent scatters

and semileptonic decays; these events were subtracted by extrapolating the distribution outside the sidebands.

The distribution of K_S collimator scatters was described by a single exponential p_T^2 term while the K_L component used two exponential p_T^2 terms. Both the exponential coefficients and weights for each scattering component were obtained by tuning the simulation to the vacuum beam $K_{L,S} \to \pi^+\pi^-$ data distributions. The simulation used the complete geometrical information of the collimator, accounted for the attenuation and regeneration of scattered kaons that punched through the MA, and described kaons that crossed over from one beam to the other[5]. The regenerator beam simulation was based on the vacuum beam simulation but accounted for the flux difference between the two beams. $K_L \to \pi^+\pi^-\pi^0$ events from collimator scatters were used to check the K_L scattering component.

The simulation of the incoherent and inelastic scattering of kaons in the regenerator was tuned using acceptance-corrected, background-subtracted $K_{L,S} \to \pi^+\pi^-$ decays. The $K_{L,S} \to \pi^+\pi^-$ data sample was analyzed using most of the nominal analysis cuts. To reduce semileptonic background, a greater separation of x-track segments at the calorimeter was required. $K^* \to \pi^0 + K_S$ background (where the K_S has a large p_T) was suppressed by applying stricter veto cuts on extra clusters. Any remaining background due to semileptonic decays and collimator scatters was subtracted from the $K_{L,S} \to \pi^+\pi^-$ data sample. Before parametrizing the scattering in the regenerator, we applied an acceptance correction to the data sample. The acceptance in kaon momentum, proper time and p_T^2 space was obtained by comparing the Monte Carlo after all analysis cuts with the generated Monte Carlo.

The $K_{L,S} \to \pi^+\pi^-$ data sample was fit in kaon momentum, proper time and p_T^2 space to parametrize the scattering in the regenerator. To reduce the number of mis-reconstructed coherent events that appeared to have a high-p_T[6], the fit was

[5]The simulation of MA punchthrough was more important for the neutral mode background subtraction, where it improved the agreement of the data and Monte Carlo kaon centre-of-energy distributions at distances greater than 10 cm from the centre of the beam hole (i.e., "ring numbers" >400).

[6]The p_T tail (p_T^2 >250 MeV^2/c^2) for mis-reconstructed coherent $K_{L,S} \to \pi^+\pi^-$ events extended to 13000 MeV^2/c^2 but about 75% of the events in the coherent tail had p_T^2 <2000MeV^2/c^2.

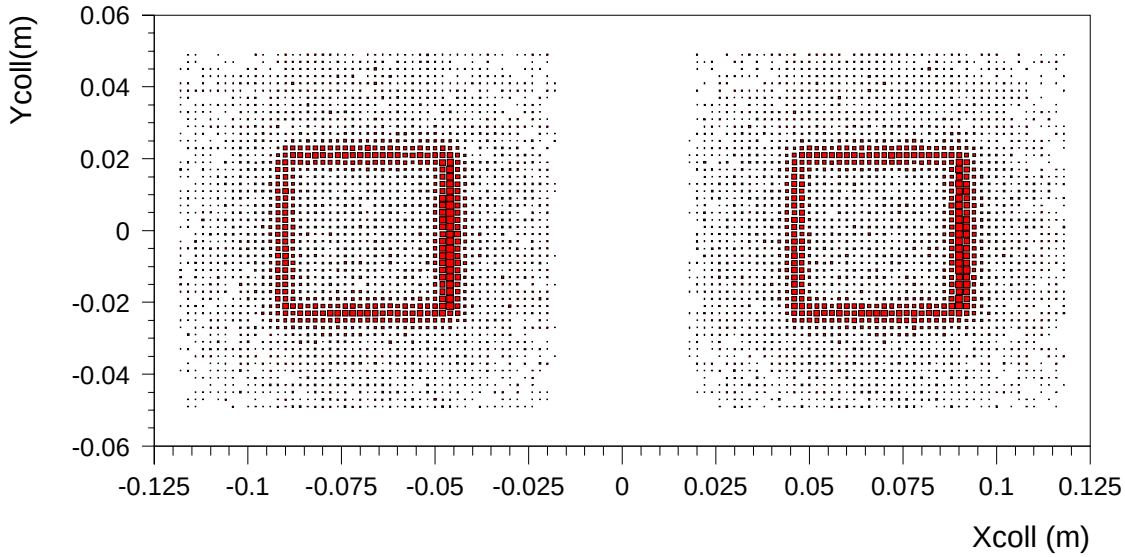

Figure 6.6: x- and y-positions of the vacuum beam $K_{L,S} \rightarrow \pi^+\pi^-$ decay vertex projected back to z-position of the defining collimator for data events with $p_T^2 > 0.001$ GeV^2/c^2. The dark square bands are due to collimator scatters and the background is due to semileptonic decays.

performed in the $p_T^2 > 2000$ MeV^2/c^2 region. Background due to hadronic regenerator interactions was suppressed by requiring the proper time to be greater than 0.2 K_S lifetime.

The parametrization of kaon scattering in the regenerator consisted of an incoherent sum of four elastic and two inelastic scattering terms. Each scattering term had a separate regeneration amplitude, phase, exponential p_T^2 dependance and normalization. The four elastic scattering terms described single scatters off carbon, lead and hydrogen and multiple scattering off carbon, respectively. Each of the elastic terms had different p_T^2 dependances and could be identified in this way. Additional phenomenological corrections were made to the lead and hydrogen scattering terms. The lead scattering term included a linear momentum dependance of the regeneration phase and the exponential p_T^2 slope, while the parametrization of kaons scattering off hydrogen had to account for the effect of the regenerator ADC cut. Since the kinetic energy of the hydrogen atom for p_T^2 transfers of $\sim$15000 MeV^2/c^2 was comparable to

the regenerator ADC cut, ~8 MeV, the reconstructed p_T^2 distribution for kaons which scattered off hydrogen was affected by the regenerator veto cut, We simulated the effect of the regenerator ADC cut on the p_T^2 distribution by applying a p_T^2-dependent cutoff for elastic kaon scatters off hydrogen.

The inelastic regenerator scatters consisted of both a K_L and a K_S component. The K_S component had a large regeneration amplitude and a broad p_T^2 distribution. Inelastic K_L scatters were studied using $K_L \to \pi^+\pi^-\pi^0$ decays, and were described using the same exponential p_T^2 dependance as inelastic K_S scatters. However, the normalization of the two inelastic components was different.

An overall kaon momentum-dependent correction of ~4% was applied to each regenerator scattering component to improve the agreement between the high-p_T $\pi^+\pi^-$ data and the fitting function used to determine the regenerator scattering simulation.

Regenerator scatters were simulated by first propagating a kaon up to the regenerator. Then a decision was made as to whether the kaon scattered coherently or incoherently. This decision was based on the probability of incoherent scattering which was kaon momentum-dependent. Once it was determined that the kaon scattered incoherently, one of the six scattering components was chosen and the kaon state was evolved based on the parametrization of the high-p_T data described above.

Normalization of Background Samples

The normalization of the background samples was performed by selecting regions in p_T^2 versus $m_{\pi^+\pi^-}$ space (see Figure 6.7) in which a particular type of background was dominant. Special cuts were applied and some $\pi^+\pi^-$ nominal analysis cuts were removed to enhance certain types of background in a selected p_T^2-$m_{\pi^+\pi^-}$ region. To obtain the normalizations in the nominal analysis, the normalizations determined from the background-rich regions were corrected using the efficiency of the additional cuts applied; the efficiency of the additional cuts was measured with Monte Carlo.

The K_{e3} normalization was obtained using events with $m_{\pi^+\pi^-}$ in the lower sidebands and p_T^2 in the 250 MeV^2/c^2 to 500 MeV^2/c^2 range. To enhance the K_{e3} events

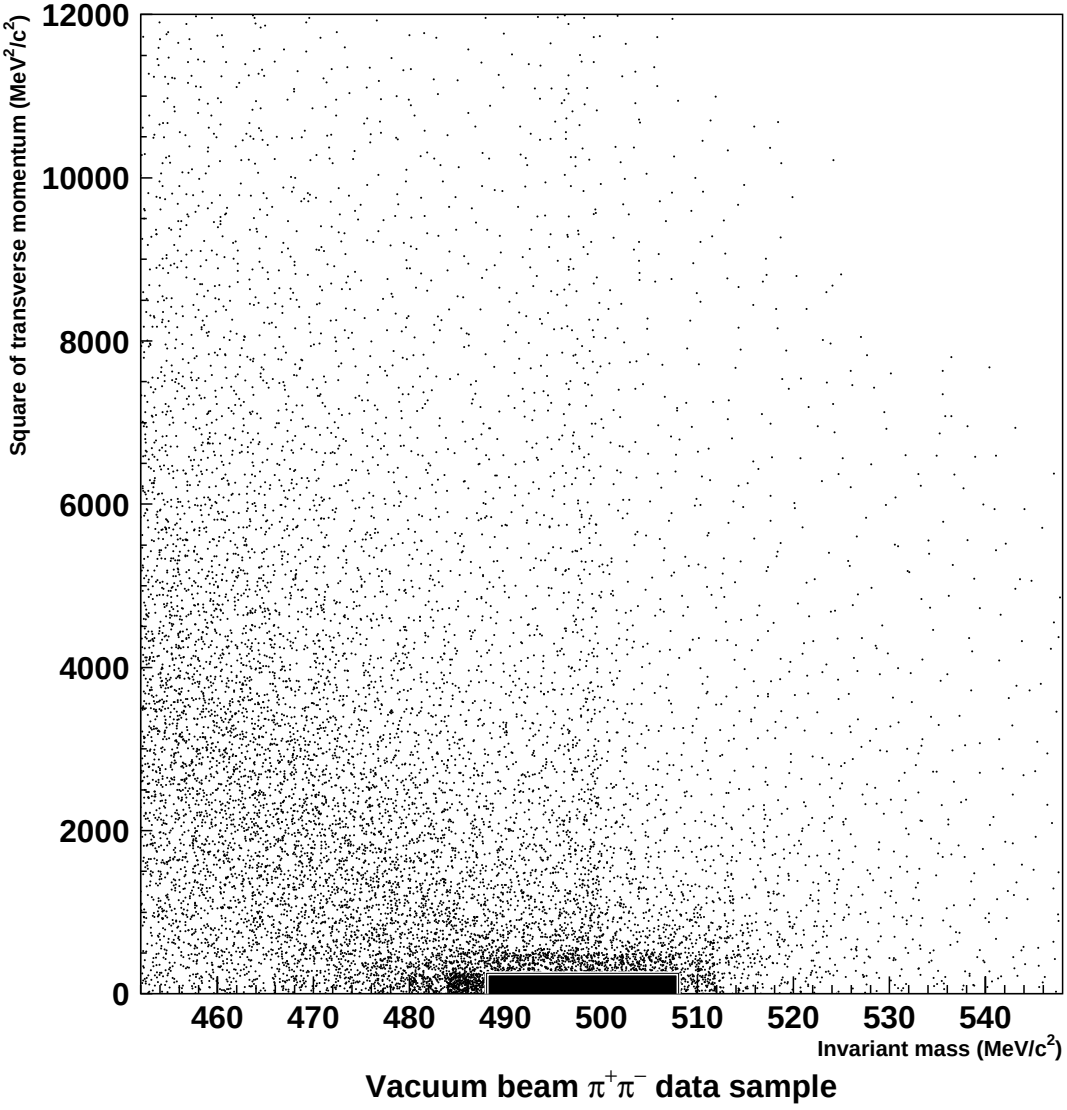

Figure 6.7: p_T^2 v $m_{\pi^+\pi^-}$ distribution for $K_{L,S} \to \pi^+\pi^-$ data events before background-subtraction and after all other analysis cuts. The rectangular box indicates the signal region for the $Re(\epsilon'/\epsilon)$ analysis

Background process	Vacuum (%)	Regenerator (%)
K_{e3}, e mis-identified as π	0.036	0.001
$K_{\mu 3}$, μ mis-identified as π	0.054	0.002
Kaon scattered in collimator	0.010	0.010
Kaon scattered in regenerator	-	0.074
Hadronic interactions produced at regenerator	-	0.001
Total	0.100	0.088

Table 6.1: Background Levels for the $K_{L,S} \to \pi^+\pi^-$ Events

and suppress the $K_{\mu 3}$ events in this region, the E/p of one of the particles was required to be greater than 0.75 and the other particle must have deposited at least 1 GeV in the calorimeter. The nominal E/p cut was removed.

$K_{\mu 3}$ background was also normalized using a low $m_{\pi^+\pi^-}$, high p_T^2 region. To enhance the $K_{\mu 3}$ background, the MU2 veto cuts were not applied and only events with one minimum ionizing particle in the calorimeter and another with $E/p < 0.5$ were selected.

The normalization for collimator scatters was obtained from vacuum beam $K_L \to \pi^+\pi^-\pi^0$ and $K_{L,S} \to \pi^+\pi^-$ events in a high p_T^2 region where the invariant $\pi^+\pi^-$ mass lay in the signal region. The total vertex momentum had to project back to the collimators.

The fit used to determine the regenerator scattering simulation yielded the normalization for diffractive (elastic) scatters in the regenerator. Inelastic regenerator scatters were normalized using events in the high-p_T^2, $m_{\pi^+\pi^-}$ signal region after subtracting collimator scatters and semileptonic backgrounds.

6.4.2 Final $\pi^+\pi^-$ Background Levels

The levels of the different background components after all analysis cuts are shown in Table 6.1. Figure 6.8 shows the p_T^2 distributions after all cuts in the vacuum and regenerator beams for $\pi^+\pi^-$ data and the various background contributions after normalization.

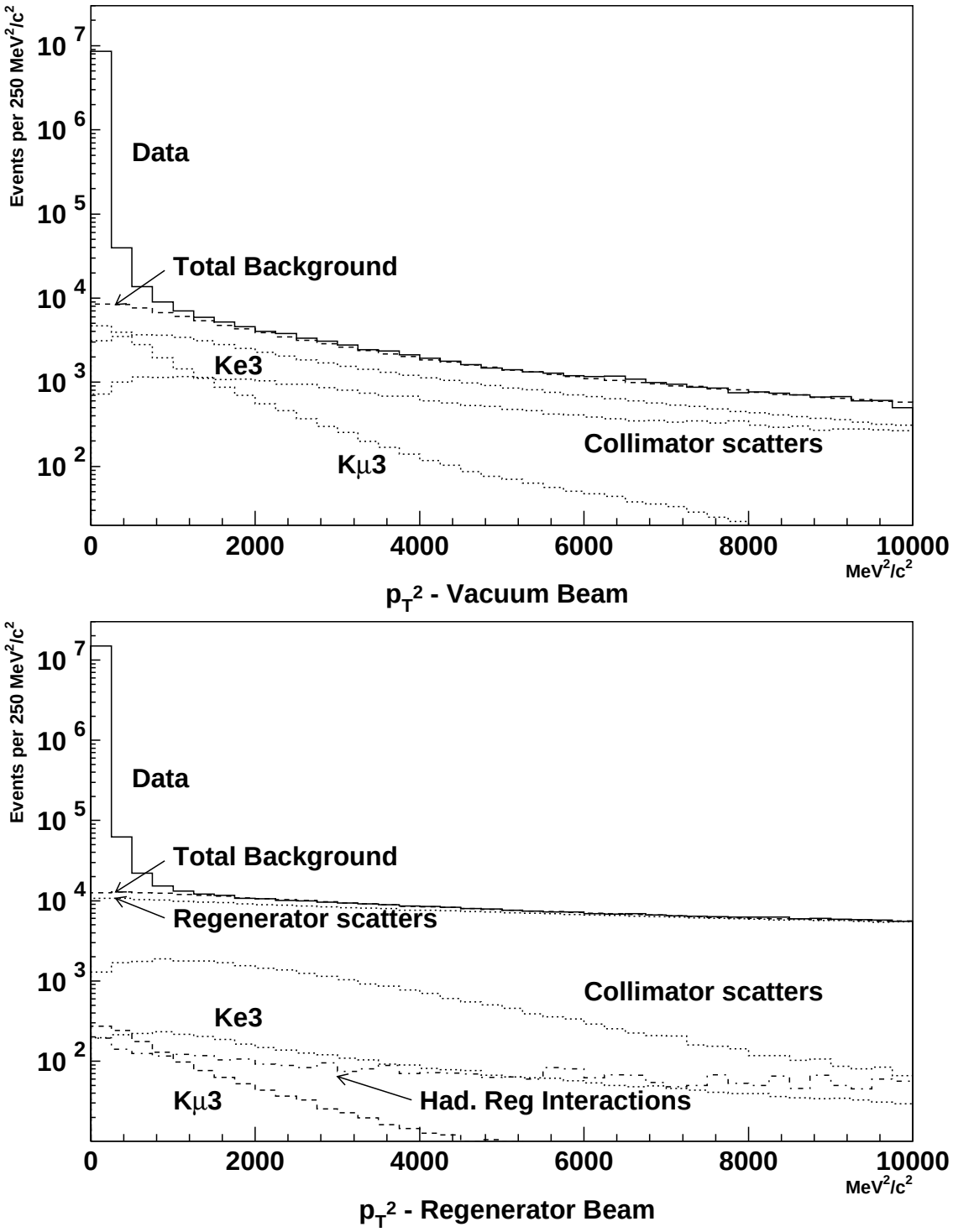

Figure 6.8: $K_{L,S} \to \pi^+\pi^-$ p_T^2 distributions for vacuum(top) and regenerator(bottom) beam data before background-subtraction overlaid with the normalized background components. All other analysis cuts have been applied.

Data Sample	Vacuum Beam	Regenerator Beam
1997a	2,532,504	4,386,518
1997b	8,593,739	14,903,091
Total	11,126,243	19,289,609

Table 6.2: Number of Background-subtracted $K_{L,S} \to \pi^+\pi^-$ Events in 1997 Data

6.5 Total event counts

Table 6.2 presents the background-subtracted statistics for the 1997 charged mode analysis. After all analysis cuts and background subtraction, the total number of $K_{L,S} \to \pi^+\pi^-$ events in the 1997 data sample was 11,126,243 and 19,289,609 for the vacuum and regenerator beams respectively. The kaon energy and vertex z-position distributions for the full 1997 $K_{L,S} \to \pi^+\pi^-$ data set are shown in Figures 6.9 and 6.10.

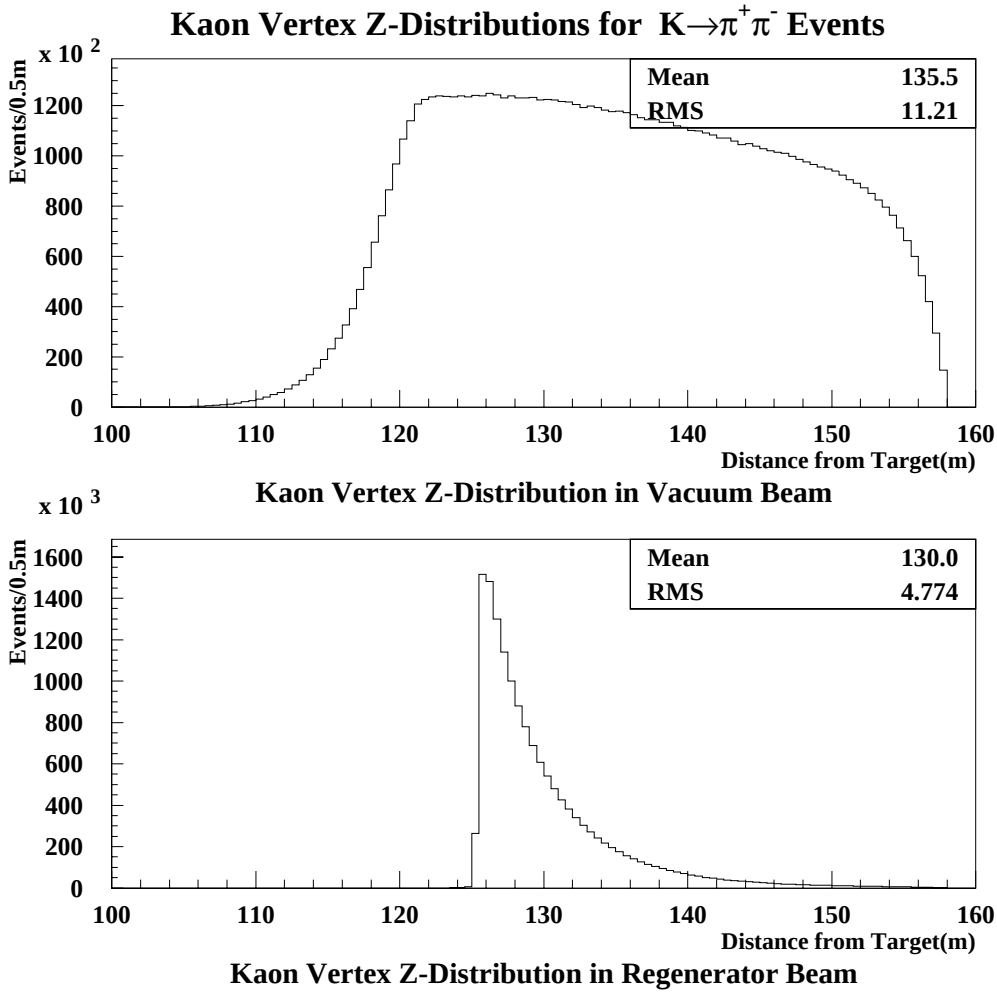

Figure 6.9: Vacuum and regenerator beam kaon vertex z-position distributions for the 1997 $\pi^+\pi^-$ data after all analysis cuts and background subtraction.

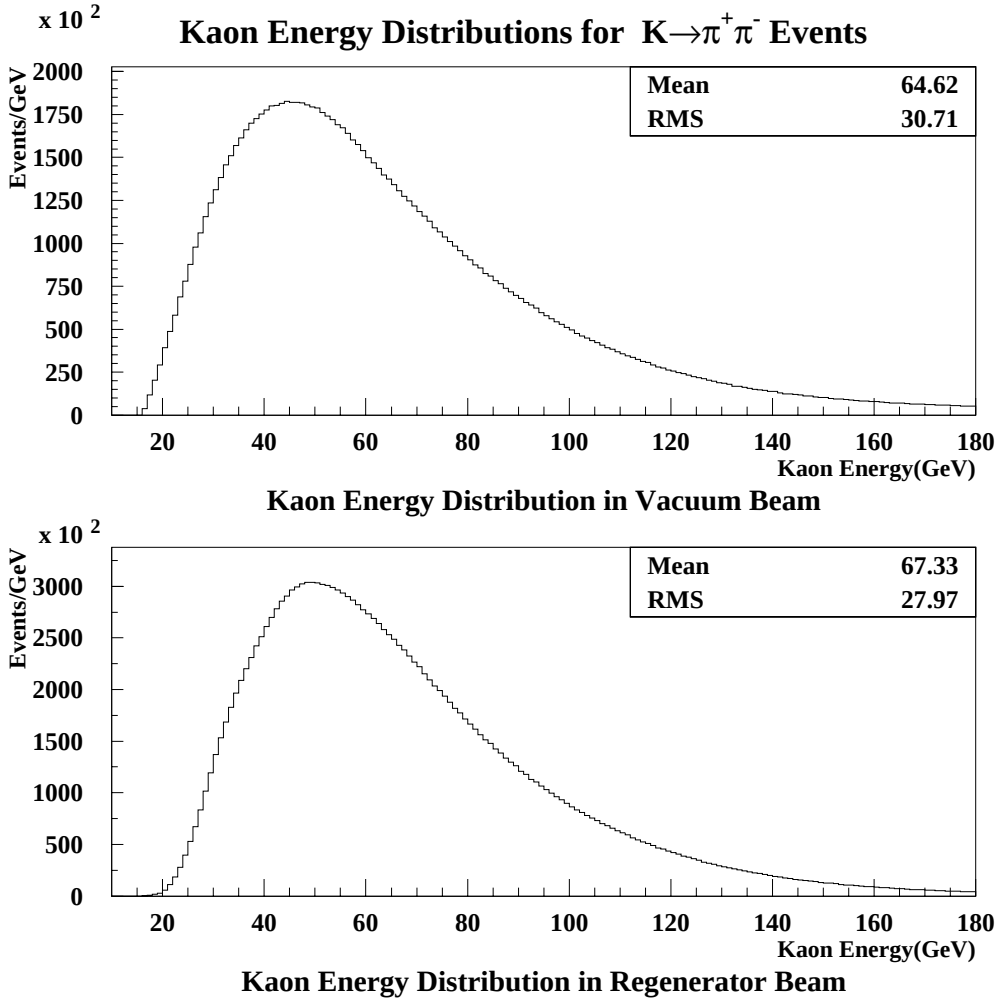

Figure 6.10: Vacuum and regenerator beam kaon energy distributions for the 1997 $\pi^+\pi^-$ data after all analysis cuts and background subtraction.

CHAPTER 7
ANALYSIS AND RECONSTRUCTION OF $K_{L,S} \to \pi^0\pi^0$ DECAYS

In this chapter, we describe the trigger selection, reconstruction and analysis of the $K_{L,S} \to \pi^0\pi^0$ data sample.

7.1 Trigger Requirements

The $K_{L,S} \to \pi^0\pi^0$ trigger was designed to collect as many $K_{L,S} \to \pi^0\pi^0$ events as possible and improve the efficiency of the offline analysis. The neutral mode trigger decreased the dead time during data collection by rejecting $K_{L,S} \to \pi^0\pi^0$ background events and events with a large amount of accidental activity. By reducing the number of $K_{L,S} \to \pi^0\pi^0$ background and poorly-reconstructed events written to tape, the offline analysis was sped up. The Level 1 and 2 $K_{L,S} \to \pi^0\pi^0$ triggers were based on the energy in the calorimeter and the activity in the veto counters. The neutral mode Level 3 trigger accepted loosely identified $K_{L,S} \to \pi^0\pi^0$ events.

7.1.1 Level 1

The Level 1 trigger for the $K_{L,S} \to \pi^0\pi^0$ mode used the E-Total (ET) system (see Figure 7.1) which was based on the total energy in the calorimeter. Events with a total calorimeter energy greater than the ~24 GeV ET threshold passed the ET trigger (see Figure 7.2). The ET threshold was chosen based on the reconstructed energy spectrum of kaons in the vacuum and regenerator beams. The ET system summed the analog signals from the dynodes of the PMTs attached to each crystal[1]; only the analog signals in the in-time 19 ns window (in both 1996 and 1997) were

[1]Using the digitized anode signals was considered but this would have taken too much time.

summed. The summed dynode signal (ΣET) was sent to a comparator whose output was the ET-trigger decision. Although the ET trigger decision was based on the analog signal in the in-time 19 ns window, the ET comparator threshold was set based on the energy sum over the 4-QIE-slice integration period of 228 ns and 76 ns in 1996 and 1997, respectively.

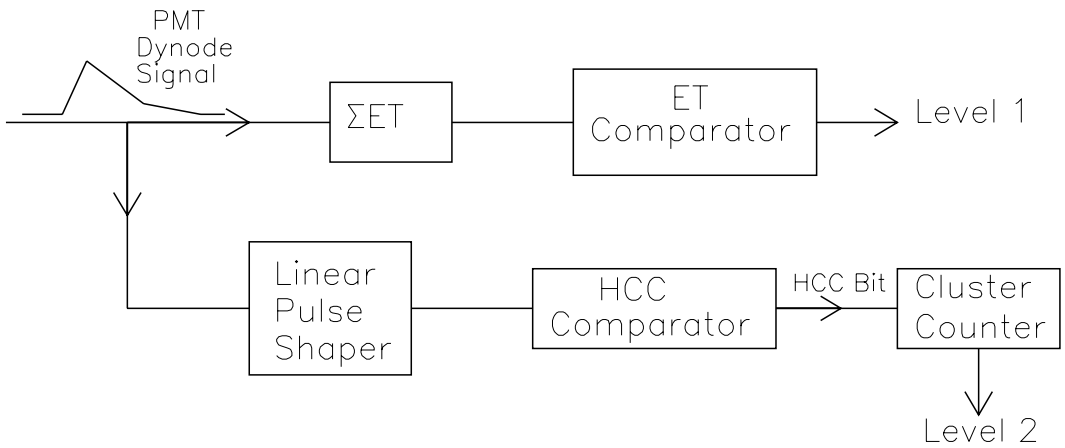

Figure 7.1: Layout of ET and HCC system.

Besides the ET system, the $K_{L,S} \to \pi^0\pi^0$ Level 1 trigger also had the regenerator, HA, SAs and the CA in veto to reduce the number of inelastic regenerator scatters and background due to mis-identified events such as $K_L \to \pi^0\pi^0\pi^0$ and $K_L \to \pi^+\pi^-\pi^0$.

7.1.2 Level 2

The Level 2 neutral mode trigger counted the number of isolated energy clusters[2] in the calorimeter and accepted events which had four[3] clusters with energies greater than ~1.5 GeV, consistent with the four photons from a $K_{L,S} \to \pi^0\pi^0$ decay. In this

[2]An isolated cluster was defined as a group of neighbouring CsI channels with energies exceeding a pre-assigned threshold, that were separated from other clusters.

[3]As discussed later, the neutral mode Level 2 trigger accepted events with four or five isolated clusters in 1996 and early 1997.

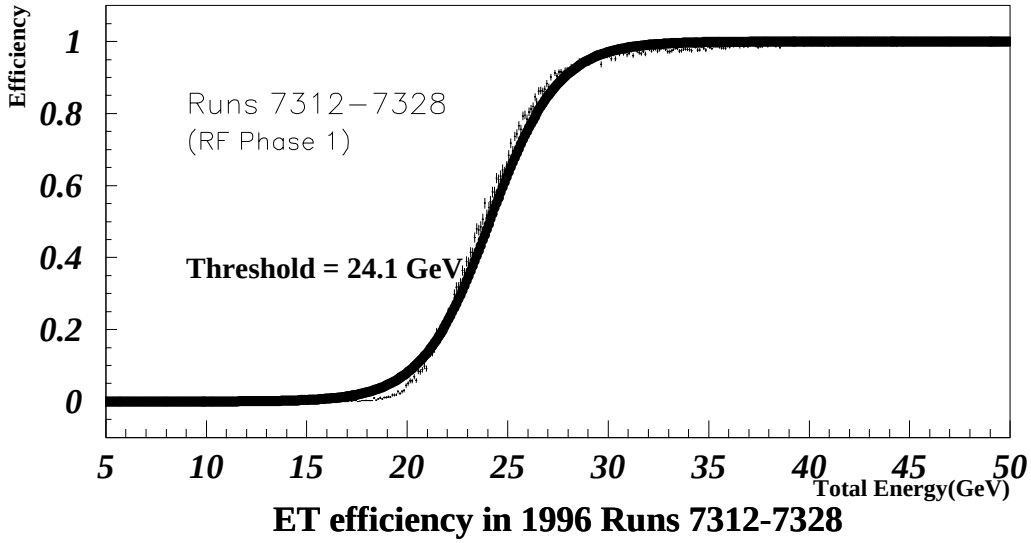

Figure 7.2: E-Total trigger efficiency close to the trigger threshold vs. total energy in the calorimeter in 1996. The solid line represents the fit to the data (dark points) which was used in the Monte Carlo simulation. The energy is integrated over 228 ns. The trigger threshold was defined to be the energy at which the ET system is 50% efficient and the "width" of the "turn-on" was the energy range within which the ET efficiency was between 10% and 90%. Only RF Phase 1 data from ECAL triggers, that read out but did not apply the ET trigger information, were used in this distribution.

way, background due to $K_L \to \pi^0\pi^0\pi^0$ and other decays with more or less than four photons in the final state were rejected by the Level 2 trigger.

To count the number of isolated clusters, the Level 2 neutral mode trigger used a custom-built hardware processor known as the Hardware Cluster Counter (HCC) [58]. The HCC system is shown in Figure 7.1. Each CsI channel was associated with an HCC bit that was set if the analog dynode signal in the 19 ns in-time window exceeded a threshold of $\sim$1 GeV. The HCC processor employed an algorithm which required that each isolated (HCC) cluster contain at least one channel with its HCC bit on (an HCC-illuminated channel). The HCC algorithm was based on the pattern of HCC-illuminated channels in a 2$\times$2 grid. The algorithm consisted of several discrete operations which could be performed simultaneously, thereby reducing processing

time. Furthermore, since the calorimeter had a fixed number of 2×2 grids, the cluster counting process took a fixed duration (independent of the calorimeter illumination). The processing time of the HCC was about 1.5 μs. A detailed description of the HCC hardware can be found in [58].

In 1996 and the first week of the 1997 E832 run, the Level 2 $K_{L,S} \to \pi^0\pi^0$ trigger accepted events with either four or five HCC clusters, while for the rest of the 1997 E832 run, the trigger required each event to contain exactly four HCC clusters. The event was allowed to contain five clusters for part of the data-taking period because during this time, some HCC bits would remain on for some time after the event had been read out. As a result, the cluster counter would occasionally identify clusters which contained negligible energy. HCC bits which exhibited this pathology were referred to as "hot" bits.

HCC Gain Adjustment and Performance

In order that the Level 2 acceptance could be better understood, we adjusted the HCC bit energy thresholds such that the HCC bit turned on at approximately the same energy for all channels. By setting the "HCC thresholds" to approximately ∼1 GeV (see Figure 7.3), we could model the acceptance more easily and apply a simple analysis cut which made us less sensitive to HCC bit inefficiencies.

The HCC threshold of each channel depended on the voltage threshold of each HCC comparator (see Figure 7.1), the pulse shape and the time delay of the timing of the pulse. Since there was a limited range within which we could adjust the comparator thresholds, we set the comparator voltages to the same value and adjusted the gains for each channel by changing the CsI PMT voltages.

There were two factors that had to be considered when matching the HCC thresholds. The first issue was that the voltages of the PMTs could only be modified between 800 V and 1700 V due to PMT non-linearity effects. As a result of this constraint, the HCC threshold matching was not perfect. The second factor was the sensitivity of the HCC bit to the pulse shape and timing. The pulse shape and timing was important because the HCC bit was only set if the rising edge of the dynode pulse exceeded the

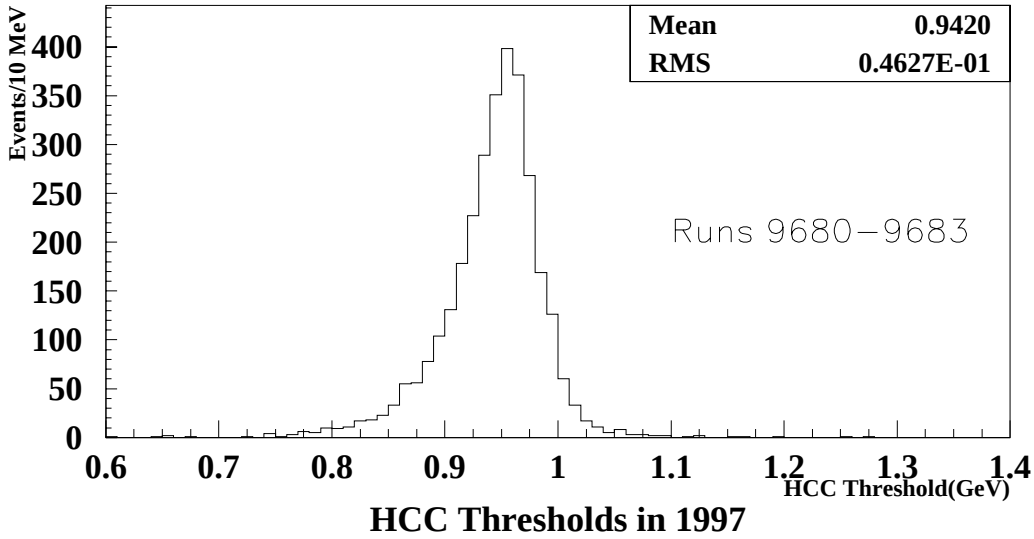

Figure 7.3: Distribution of HCC Thresholds in 1997. ECAL triggers were used in this distribution.

comparator threshold withing a specific 6-10 ns timing window. Since the rise time for high energy pulses was shorter than that of low-energy pulses, channels with dynode signals that arrived early with respect to the HCC timing window appeared to have an HCC bit inefficiency at high energy. For these channels, high energy pulses would cross the threshold too early and not fire the HCC bit, as shown in Figure 7.4(a). On the other hand, for channels with dynode pulses that arrived late with respect to the HCC timing window, there would be an HCC bit inefficiency at low energies since low energy pulses would cross the threshold too late (see Figure 7.4(b)). The gains of the CsI PMTs were adjusted so that HCC bit inefficiencies at both low- and high-energies were minimized, while at the same time making the HCC thresholds as uniform as possible over the calorimeter.

Matching the HCC thresholds of both large and small channels to the same energy affected the *ET* system. Since the dynode signals from large channels had a longer rise time than small channels, by matching the HCC thresholds of all channels to the same energy, the gains for large channels were systematically higher than for small

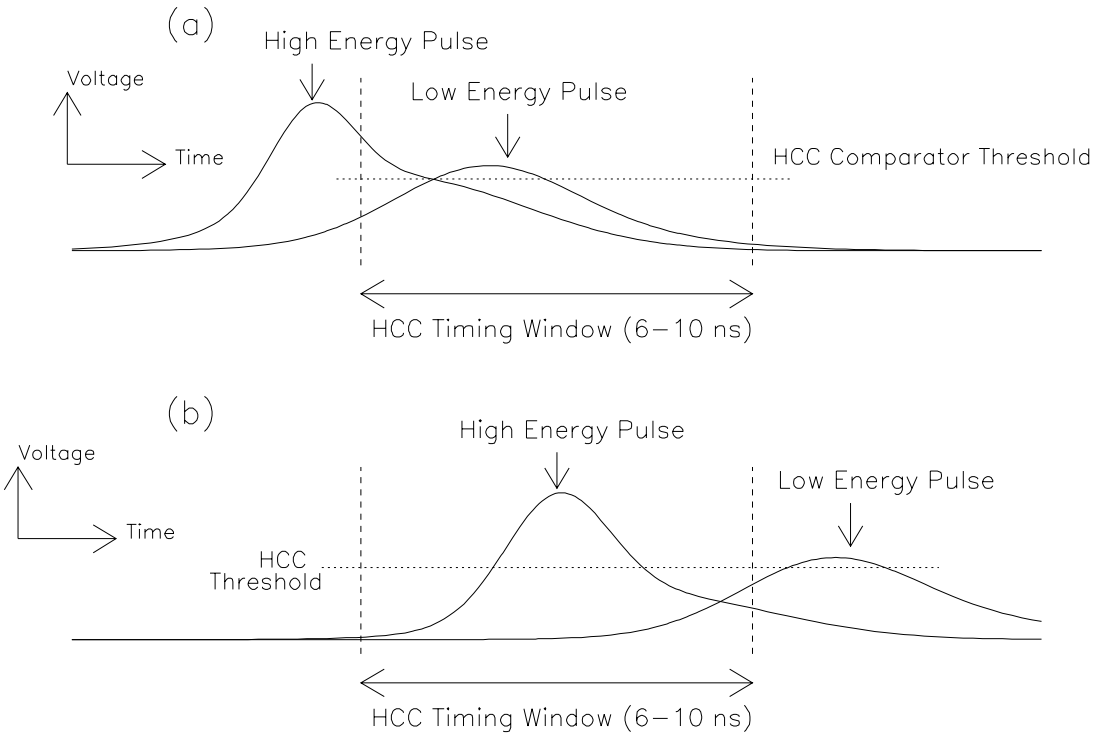

Figure 7.4: The effect of dynode pulse timing on HCC bit efficiencies. Figure (a) describes how high-energy HCC bit inefficiencies are due to dynode pulses which arrive early. Figure (b) shows how late dynode pulses affect the low-energy HCC bit efficiency.

channels[4]. As a result, large channel pulses were bigger than small channel ones at the same energy, so they contributed more to the ET sum. This effect had to be considered when understanding and simulating the $K_{L,S} \to \pi^0\pi^0$ Level 1 trigger acceptance.

7.1.3 Level 3

The $K_{L,S} \to \pi^0\pi^0$ Level 3 trigger identified $K_{L,S} \to \pi^0\pi^0$ candidates and reduced background due to mis-identified kaon decays by imposing loose requirements on

[4]Instead of having different gains for large and small channels, we could have added a delay to the small channel dynode signals that reached the comparators. We chose not to do so since this was practically difficult.

the invariant mass of the $2\pi^0$ and the agreement of the 2 π^0 vertices. Only loose $K_{L,S} \to \pi^0\pi^0$ requirements were applied so that good $K_{L,S} \to \pi^0\pi^0$ events that were not well-reconstructed using the online calibration would not be eliminated.

The Level 3 filter code required exactly four hardware clusters[5]. Events with four hardware clusters were reconstructed assuming the four clusters were photons and originated from a $K_{L,S} \to \pi^0\pi^0$ decay. Cluster energies and positions were determined using the online calibration. To speed up the CsI clustering, only hardware clustering was performed and the energy was summed over 5×5 small blocks and 3×3 large blocks for clusters in the small- and large-regions, respectively. Only the "missing block" and "out-of-cone" corrections (see Chapter 4) were applied. Overlapping clusters with common CsI channels were also separated.

Having identified four photons, the Level 3 code determined the the agreement of the 2 π^0 vertices for each combination of photon pairs. If the combination with the best vertex agreement passed a pairing quality, $\chi^2_{\pi^0}$, (described in Section 7.2.2) cut and the invariant $2\pi^0$-mass of the combination was greater than 450 MeV/c^2, the event passed the $K_{L,S} \to \pi^0\pi^0$ Level 3 requirement. Sometimes the second best combination of photon pairs would have a $2\pi^0$-mass which was greater than 450 MeV/c^2. In this case, if the quality of the second best pairing was sufficiently high, the event was accepted by Level 3.

7.2 Reconstruction of $K_{L,S} \to \pi^0\pi^0$ events

We reconstructed $K_{L,S} \to \pi^0\pi^0$ by determining the positions and energies of the four photons which originated from the decay of the two π^0s. The reconstruction of $K_{L,S} \to \pi^0\pi^0$ events is presented by first describing the energy and position reconstruction of the photons and then discussing the reconstruction of the kaon decay.

[5]Hardware clusters which were due to a "hot" HCC bit were not considered.

7.2.1 Photon Energy and Position Reconstruction

The reconstruction of photon energies and positions follows the procedure described in Chapter 4. Both hardware and software clustering were performed in the $2\pi^0$ event reconstruction. The photon clusters were defined by 7×7 small block and 3×3 large block regions. The photon clusters were required to be hardware clusters and to be consistent with the Level 2 HCC requirement; only events with exactly four hardware clusters were considered as $K_{L,S} \to \pi^0\pi^0$ candidates. The energy of each photon was given by Equation 4.1, where all the cluster energy corrections described in Section 4.5.1 were applied. A typical $K_{L,S} \to \pi^0\pi^0$ event is shown in Figure 7.5. To reconstruct the event in Figure 7.5 accurately, we need to reconstruct clusters near the hole and separate overlapping clusters.

7.2.2 Reconstruction of Kaon Kinematic Variables

Using the photon energies and positions, we were able to reconstruct the four-photon energy, the $2\pi^0$ invariant mass and the z-position of the reconstructed $2\pi^0$ vertex.

Essential to the reconstruction of $K_{L,S} \to \pi^0\pi^0$ decays was the correct assignment of the four photons to the two neutral pions. There were three possible combinations of photon pairings. For each combination of photon pairings, we calculated a pairing quality ($\chi^2_{\pi^0}$) based on the z-distance between the two 2-photon vertices, assuming that each 2-photon vertex was due to a π^0. The pairing quality or χ^2, $\chi^2_{\pi^0}$, was given by

$$\chi^2_{\pi^0} = \frac{(\overline{d^2_{\pi^0}} - \overline{d_{\pi^0}}^2)}{\sigma^2_{\overline{d_{\pi^0}}}} \tag{7.1}$$

where d_{π^0} was the distance along the beam axis between the π^0 vertex and the mean longitudinal shower position in the CsI, and $\sigma_{\overline{d_{\pi^0}}}$ was the uncertainty on the weighted mean, $\overline{d_{\pi^0}}$. Based on the Equation 7.1, we selected the combination of pairings with the lowest $\chi^2_{\pi^0}$ as the "correct" pairing. As described in the previous section, both the best and second best pairing χ^2 were considered when selecting events in the $2\pi^0$ Level 3 filter.

The distance along the beam axis between the π^0 vertex and the mean CsI longi-

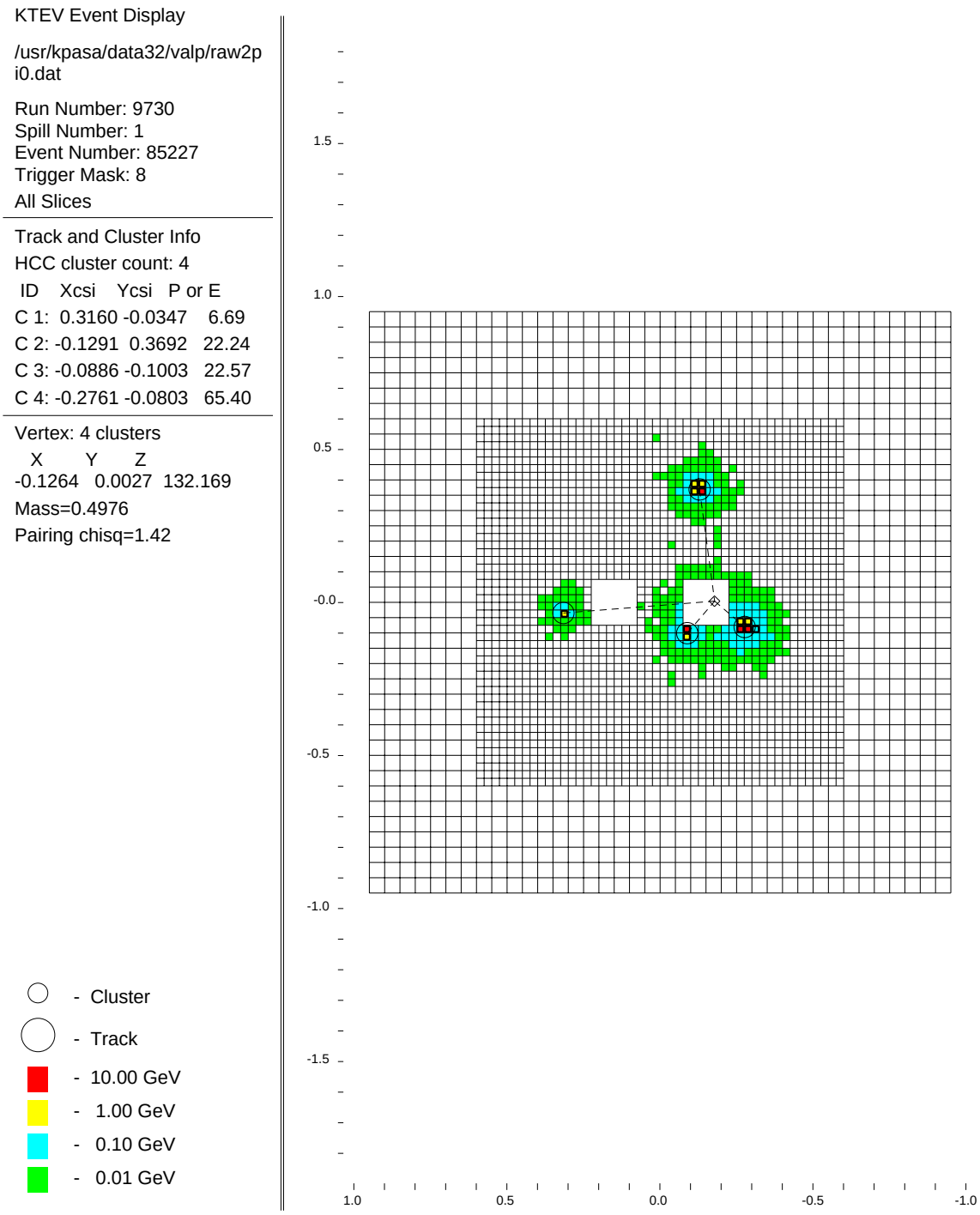

Figure 7.5: A $K_{L,S} \rightarrow \pi^0\pi^0$ event showing 4 clusters of energy in the calorimeter. The energies of the photons and the reconstructed kaon mass are on the left.

tudinal shower position, d_{π^0}, is given in the small angle approximation by

$$d_{\pi^0} = \frac{\sqrt{E_{\gamma_1} \times E_{\gamma_2}} \times r_{12}}{m_{\pi^0}}, \tag{7.2}$$

where r_{12} is the distance between the two photon showers, E_{γ_1} and E_{γ_2} are the reconstructed photon energies and m_{π^0} is the pion mass. We assume the Particle Data Group value [45] for the π^0 mass. Although the longitudinal shower profile varies logarithmically with the incident photon energy, the mean longitudinal shower depth of 0.17 m (with respect to the front face) was used for all photon energies. The systematic effect of using an energy-dependent shower mean is studied in Chapter 9 and Appendix C.

The $2\pi^0$ vertex z-position (relative to the target) was determined from the weighted mean of the vertex distances, d_{π^0}. The z-position of the front face of the calorimeter was obtained from survey measurements. The errors on the cluster energies and positions that were used in the determination of the weighted mean were given by the position and energy resolutions of electrons in K_{e3} events. The reconstructed z-position resolution of the $2\pi^0$ vertex was ~30cm.[6]

Since the only trace of a $K_{L,S} \to \pi^0\pi^0$ decay was the energy in the calorimeter, the transverse position of the kaon decay and the kaon momentum could not be measured directly. Instead, the kaon transverse position, (x_K,y_K), was estimated by assuming that the kaon vertex was at a distance, z_K, from the target on the line connecting target to the the kaon (or four-photon) centre-of-energy as shown in Figure 7.6. The implicit assumption was that the kaon had not scattered. The total kaon momemtum was also assumed to point along the vector from the target to the kaon centre-of-energy at the calorimeter. The kaon vertex $x-$position was used to determine whether the kaon originated from the regenerator or vacuum beam.

The $2\pi^0$ invariant mass, $m_{\pi^0\pi^0}$, was calculated using the kaon energy and momentum. The kaon energy, E_K, was obtained by summing the energies of the four

[6]We determined the vertex resolution using hadronic interactions which produced $2\pi^0$ at the downstream regenerator edge.

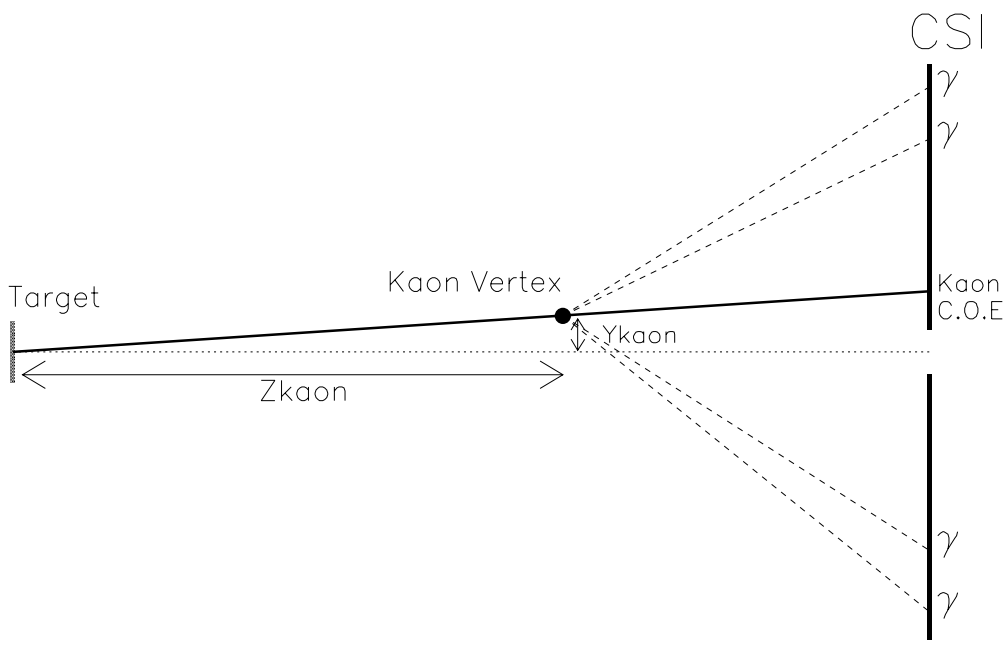

Figure 7.6: Kaon vertex reconstruction of a $K_{L,S} \rightarrow \pi^0\pi^0$ decay. The kaon trajectory has been mapped on to the $x - z$ plane.

photons. The $2\pi^0$ invariant mass was given by

$$\begin{aligned} m^2_{\pi^0\pi^0} &= (\textstyle\sum_{i=1}^4 E_i)^2 \\ &- (\textstyle\sum_{i=1}^4 \frac{E_i}{\sqrt{\overline{d_{\pi^0}}^2+(x_i-x_K)^2+(y_i-y_K)^2}} \cdot \overline{d_{\pi^0}})^2 \\ &- (\textstyle\sum_{i=1}^4 \frac{E_i}{\sqrt{\overline{d_{\pi^0}}^2+(x_i-x_K)^2+(y_i-y_K)^2}} \cdot (x_i - x_K))^2 \\ &- (\textstyle\sum_{i=1}^4 \frac{E_i}{\sqrt{\overline{d_{\pi^0}}^2+(x_i-x_K)^2+(y_i-y_K)^2}} \cdot (y_i - y_K))^2, \end{aligned} \tag{7.3}$$

where E_i, x_i and y_i were the photon energies and cluster positions, respectively.

From Equations 7.2 and 7.3, we see that z_K is proportional to the neutral mode energy scale, while the kaon mass is insensitive to the neutral mode energy scale. Hence, a difference in the data-Monte Carlo z_K distributions could be due to an energy scale difference whereas a data-Monte Carlo difference in the mean kaon mass could not be reconciled with a simple energy scale correction but would involve either non-linear differences in the data-Monte Carlo photon energy and position reconstruction or

a variation in the energy and position reconstruction over the calorimeter. Possible causes for data-Monte Carlo reconstruction differences are discussed in detail in Appendix C.

7.3 Data-Monte Carlo Neutral Mode Energy Scale Difference

It was important to measure and correct for the neutral mode energy scale difference between the $K_{L,S} \to \pi^0\pi^0$ data and Monte Carlo because the the z-position of the reconstructed kaon vertex, z_K, was proportional to the energy scale. A data-Monte Carlo difference in the energy scale would lead to a difference in z_K distributions and this would mean that the acceptance along the length of the decay region would not be accurately determined. As discussed in Chapter 2, this would cause a first-order bias in $Re(\epsilon'/\epsilon)$. After correcting for the data-Monte Carlo neutral mode energy scale difference, the measured value of $Re(\epsilon'/\epsilon)$ increased by 2.1×10^{-4}.

Since the neutral mode energy scale was proportional to z_K, the data-Monte Carlo energy scale difference could be determined by comparing the data and Monte Carlo $z_{K\to\pi^0\pi^0}$ distributions. It was easiest to determine the difference between the data and Monte Carlo z_K distributions by comparing the z_K-distributions in a region in which the distribution was changing rapidly. The z_K distribution at the downstream edge of the regenerator was well-suited for comparing the data and Monte Carlo z_K distributions since the edge was well-defined and there was a large number of of $K_S \to 2\pi^0$ events to improve the statistical sensitivity of the comparison.

To measure the neutral mode energy scale difference using the z_K distribution at the downstream edge of the regenerator, we had to determine the data-Monte Carlo difference in the position of the effective regenerator edge. Since $K_{L,S} \to \pi^0\pi^0$ decays in the regenerator were not simulated in the Monte Carlo, the reconstructed downstream edge position of the regenerator was different for data and Monte Carlo $K_{L,S} \to \pi^0\pi^0$ decays. The position of the effective regenerator edge in the data was primarily defined by the 6 mm lead piece closest to the (downstream) physical edge of the regenerator (see Figure 3.5). Most photons from $K_L \to 2\pi^0$ decays in

the regenerator converted in the two lead pieces in the final regenerator module[7]. To determine the effective regenerator edge in data, a model which accounted for (a) K_L transmission, (b) K_S regeneration and decays within the regenerator, (c) the transmission of 4 photons through the regenerator and (d) the $2\pi^0$ z-vertex resolution was used. Using this model, the z-vertex distribution near the regenerator for events in which all four photons escaped the regenerator was determined and compared to the z_K-distribution of a model which did not allow decays in the regenerator and only accounted for the $2\pi^0$ z-vertex resolution. The regenerator edge in the model which allowed regenerator decays was (6.2±0.1) mm upstream of the edge in the latter model. Based on this, we concluded that the data-Monte Carlo difference in the effective regenerator downstream edge position was 6.2 mm (see Figure 3.5). As the kaon energy increased from 40 GeV to 160 GeV, the data-Monte Carlo effective regenerator edge difference decreased from 6.3 mm to 6.0 mm.

To correct for the data-Monte Carlo neutral mode energy scale difference, we first measured the energy scale correction required to match the data and Monte Carlo z_K distributions such that the distributions at the regenerator edge lay on top of each other as shown in Figure 7.7[8]. We then determined the energy scale correction needed to account for the difference in the data-Monte Carlo effective regenerator edges. The final energy scale correction applied to each hardware cluster in data was a product of the scale shift required to match the data and Monte Carlo $2\pi^0$ regenerator edges and the scale correction needed to shift the regenerator z-vertex distribution in data 6.2 mm upstream.

The data and Monte Carlo events were reconstructed with all clustering corrections in Equation 4.1 (except for $f^{Data}_{photons}(E_{Kaon})$), and all $K_{L,S} \to \pi^0\pi^0$ analysis cuts and background subtraction were applied. The data and Monte Carlo z_K distributions were matched in 10 GeV kaon energy bins[9] as shown in Figure 7.8. On average, the z_K

[7]There was some conversion in the upstream regenerator scintillator modules as well.

[8]The z_K distributions were matched using the Kolmogorov-Smirnov test.

[9]10 GeV kaon energy bins were used to be consistent with the fit that was used to determine $Re(\epsilon'/\epsilon)$ (see Chapter 10).

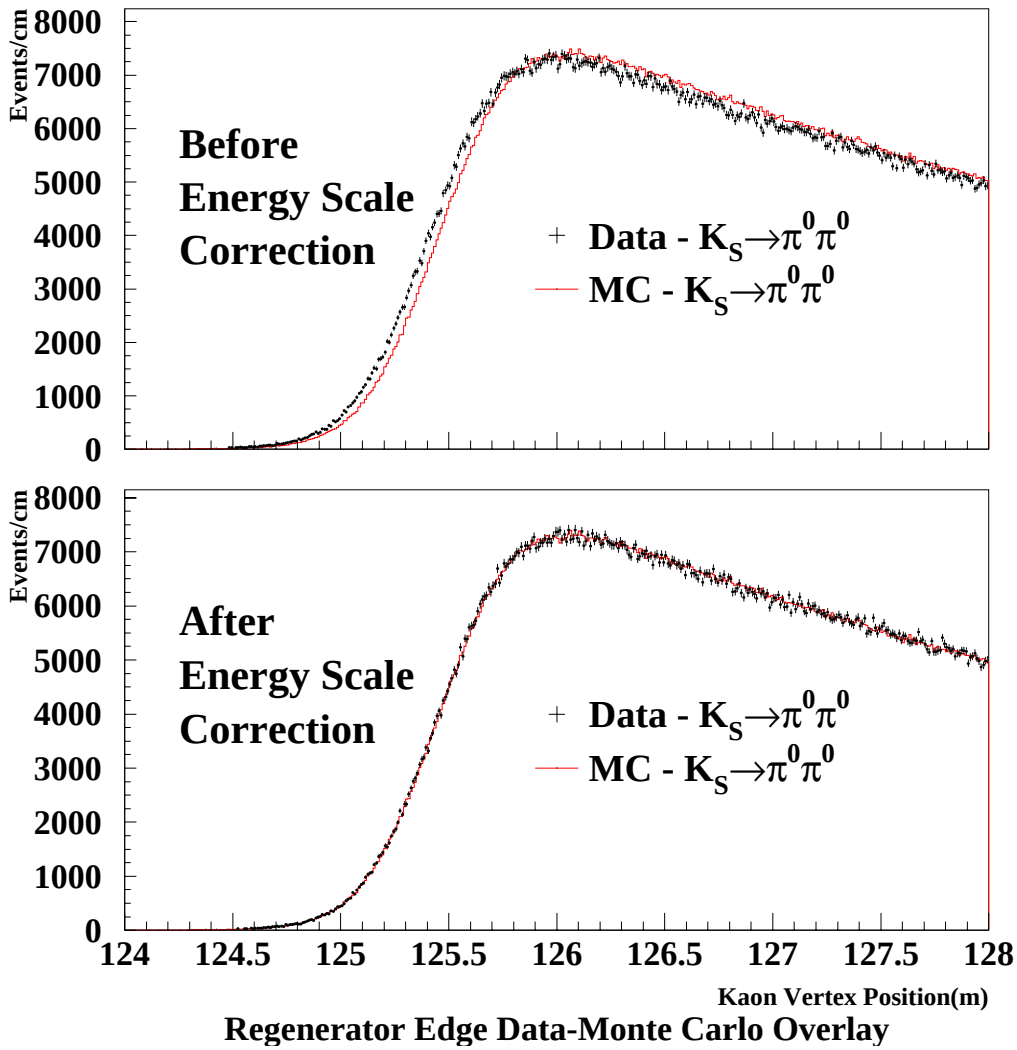

Figure 7.7: Data and Monte Carlo $K_{L,S} \to \pi^0\pi^0$ reconstructed z-vertex at the regenerator before(top) and after(bottom) applying the final neutral mode energy scale.

distribution at the regenerator edge in data was measured to be 4.9 cm upstream in data. The difference between the data and Monte Carlo z_K distributions varied with kaon energy, indicating that there were data-Monte Carlo reconstruction differences. In order that the energy scale correction that was applied to photons varied smoothly with kaon energy, we fit the energy scale that was needed to match the data and Monte Carlo z_K distributions at the regenerator edge (in 10 GeV kaon energy bins) to a fourth order polynomial. The polynomial used is shown in Figure 7.9. After accounting for the data-Monte Carlo difference in the effective regenerator edge, the average energy scale correction applied to photons in $K_{L,S} \to \pi^0\pi^0$ data events was

$$\begin{aligned} \overline{f^{Data}_{photons}} &= 1.0001 \times 0.9992 \\ &= 0.9993, \end{aligned} \tag{7.4}$$

where the energy scale required to shift the z_K distribution at the regenerator edge upstream by 6.2 mm is 1.0001 and the average energy scale required to match the data and Monte Carlo z_K distributions is 0.9992.

7.3.1 Effect of Neutral Mode Energy Scale on $Re(\epsilon'/\epsilon)$

The neutral mode energy scale affected the kaon energy, kaon vertex z-position, minimum photon energy and $\chi^2_{\pi^0}$ distributions. Since the effect of the nominal (kaon-energy dependent) energy scale correction on $Re(\epsilon'/\epsilon)$ was similar to the effect of the flat (energy-independent) scale correction. To understand how the neutral mode energy scale affected $Re(\epsilon'/\epsilon)$, we studied the effect of applying an energy scale shift, $\overline{f^{Data}_{photons}} = 0.9993$ (see Equation 7.5), to all photons in $K_{L,S} \to \pi^0\pi^0$ data events, independent of the kaon energy.

Applying an energy scale correction of 0.9993 resulted in an increase in $Re(\epsilon'/\epsilon)$ of 1.62×10^{-4} compared to an analysis where no energy scale correction was applied to the $2\pi^0$ data. This increase in $Re(\epsilon'/\epsilon)$ was mainly due to changes in the kaon energy and z_K distributions. Table 7.1 summarizes the contribution of changes in the kaon energy, z_K, minimum photon energy and $\chi^2_{\pi^0}$ distributions to the 1.62×10^{-4} increase

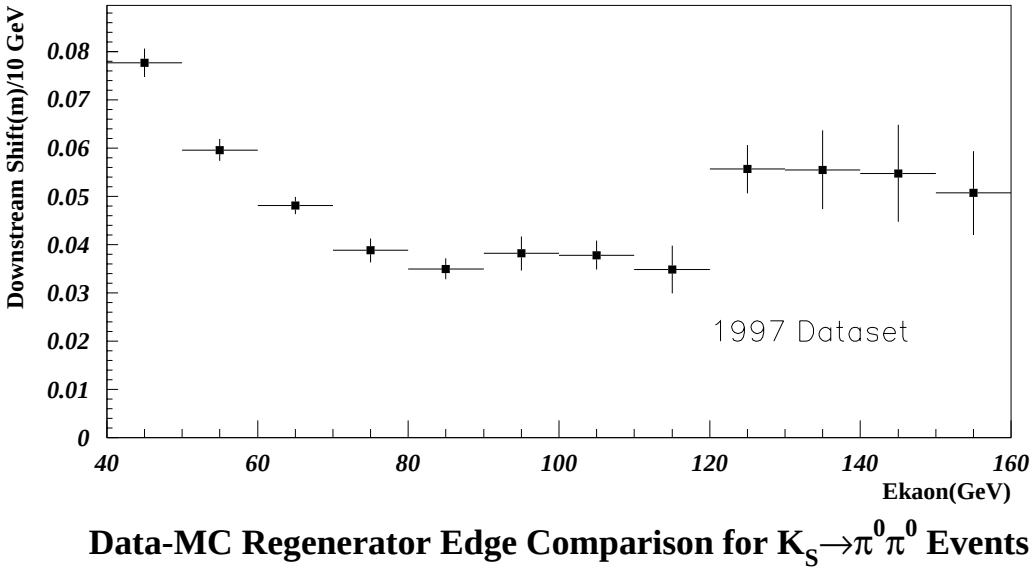

Figure 7.8: Kaon energy variation of data-Monte Carlo $K_{L,S} \to \pi^0\pi^0$ z_K difference at the the downstream regenerator edge before applying final energy scale. The y-axis shows how much upstream the z_K distribution in data is relative to the Monte Carlo.

in $Re(\epsilon'/\epsilon)$.

Of the 1.62×10^{-4} increase in $Re(\epsilon'/\epsilon)$ due to energy scale correction, an increase of 1.0×10^{-4} was due to the change in the kaon energy. There was a 0.32×10^{-4} increase in $Re(\epsilon'/\epsilon)$ due to events migrating into and out of the kaon energy cut bounds and a 0.68×10^{-4} increase in $Re(\epsilon'/\epsilon)$ due to migration within the kaon energy cut bounds. Both vacuum and regenerator beams were affected by the movement of events at the kaon energy cut limits, with more events being lost in the vacuum beam relative to the regenerator beam. Migration effects within the kaon energy cut limits that were the same for both regenerator and vacuum beams affected the energy variation of the kaon flux. The change in the kaon flux due to the flat energy scale led to an increase in $Re(\epsilon'/\epsilon)$ of 0.32×10^{-4}. The energy scale correction also resulted in the migration of events within the kaon energy cut limits that was different in both beams. Part of this relative change in the kaon energy distributions between regenerator and vacuum beams was accounted for by a modification of the regeneration power law. Changes in

Distribution	Effect	$\Delta Re(\epsilon'/\epsilon)$ ($\times 10^{-4}$)
Kaon Energy :	Migration into and out of cut limits	0.32
	Change in neutral flux vs kaon energy	0.32
	Change in regeneration parameters	0.19
	Non-power law changes in regenerator distribution	0.17
Z_K :	Migration into and out of cut limits	0.55
Minimum Photon : Energy	Migration into and out of cut limits	0.07
Pairing χ^2 :	Migration into and out of cut limits	<0.01
Total (Increase)		1.62

Table 7.1: The change in $Re(\epsilon'/\epsilon)$ due to an energy scale correction of 0.9993 applied to all photons in $K_{L,S} \rightarrow \pi^0\pi^0$ data. The change was compared to an analysis in which no final energy scale correction was applied.

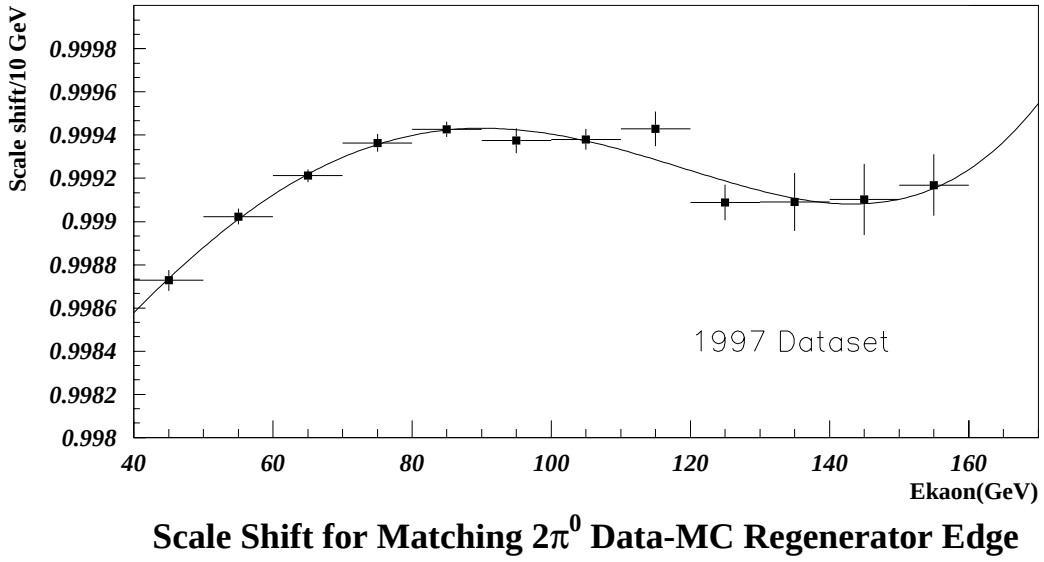

Figure 7.9: Energy scale required to match the data and Monte Carlo $K_{L,S} \to \pi^0\pi^0$ z_K distibutions. The fourth order polynomial used is indicated by the smooth curve. The energy-independent scale needed to shift the data distribution 6.2 mm upstream of the Monte Carlo has not been included.

the regeneration amplitude and power law exponent resulted in an increase in $Re(\epsilon'/\epsilon)$ of 0.19×10^{-4}. The kaon energy distribution in the regenerator beam also changed in such a way that a change in the power law could not account for the change in the energy spectrum. Such a change in the energy spectrum increased $Re(\epsilon'/\epsilon)$ by 0.17×10^{-4}.

The change in the energy scale affected the z_K, minimum photon energy and $\chi^2_{\pi^0}$ distributions by causing events to move into and out of the cut limits. The energy scale correction resulted in an increase in $Re(\epsilon'/\epsilon)$ of 0.55×10^{-4} due to the z_K analysis cut. The increase in $Re(\epsilon'/\epsilon)$ was mainly due to the loss of vacuum beam events at the downstream end of the decay region; the increase in the number of vacuum beam events upstream of the MA was small since the z_K-distribution fell off sharply at $z < 122m$ (Figure 7.18).

The effect of the energy scale correction the minimum photon energy cut was small causing an increase of 0.07×10^{-4}. The pairing χ^2 cut was least affected by the

Analysis Cut	Efficiency of Cut(%)				Purpose
	Signal		Background		
	Vac	Reg	Vac	Reg	
$\pi^0\pi^0$ invariant mass	99.8	99.9	43.7	94.9	Mis-ident. bkg.
Minimum Photon Energy	81.1	84.7	85.1	85.2	Level 2 sensitivity, Energy linearity
Ring Number	99.6	99.5	15.37	19.1	Scatter bkg.
Minimum Photon Separation	99.2	99.3	99.5	99.2	Energy, position Reconstruction
Pairing χ^2	98.9	98.7	65.1	98.1	Mis-recon bkg.
Shape χ^2	99.9	99.9	97.6	99.9	Mis-recon bkg.

Table 7.2: Neutral mode analysis cut efficiency for $K_{L,S} \to \pi^0\pi^0$ signal (after background subtraction) and total background in 1997. Efficiencies were measured with respect to a a sample in which all other $K_{L,S} \to \pi^0\pi^0$ analysis cuts, and Level 1, 2 and 3 triggers had been applied. The effectiveness of all the cuts (listed above) except for the $2\pi^0$ invariant mass cut was similar in 1996. The efficiency of the $2\pi^0$ invariant mass cut for background events in 1996 was 31.9% and 93.4% in the vacuum and regenerator beams, respetively, since the BA cut reduced the level of $3\pi^0$ background in 1997.

energy scale correction since the change in the energy scale affected the pairing χ^2 distribution in both beams almost equally.

7.4 Analysis Cuts

Analysis and event selection cuts were made to the $K_{L,S} \to \pi^0\pi^0$ data sample to reduce the number of poorly reconstructed events. Analysis cuts were important in suppressing the background to $K_{L,S} \to \pi^0\pi^0$ decays as well. Since understanding the acceptance of the final event sample was crucial to the KTeV measurement of $Re(\epsilon'/\epsilon)$, analysis cuts were chosen to minimize the sensitivity to a mis-understanding of the acceptance. This involved applying looser cuts in variables where the Monte Carlo simulation did not agree with the data as well as using cuts to define the detector apertures and decay region accurately. The effectiveness of some of the analysis cuts is presented in Table 7.2.

7.4.1 Common $K_{L,S} \to \pi^0\pi^0$ and $K_{L,S} \to \pi^+\pi^-$ Cuts

The kaon decay region was chosen to be between 110 m and 158 m from the target and the kaon energy range between 40 GeV and 160 GeV. The lower kaon energy bound was selected to reduce our sensitivity to the understanding of the Level 1 ET trigger which, in turn, was set based on the kaon production spectrum. The kaon energy range and decay region was the same in both modes.

Since inelastic regenerator scatters were the same in charged and neutral $K \to 2\pi$ decays, most of the cuts on the activity in the veto counters were common to both modes. Furthermore, since the simulation of regenerator scatters in the neutral mode was based on the high p_T^2 $\pi^+\pi^-$ events, applying common veto cuts also ensured that the regenerator scattering simulation was accurate in both modes.

We applied the same offline regenerator cuts as in the charged mode, rejecting events with any regenerator TDC activity in the early, late and in-time buckets, as well as vetoing events with more than 8 MeV (2 MIP energy equivalent) in any regenerator module or with more than 0.7 MIP[10] equivalent energy in the last module. Although the cut on the activity in the final module was used mainly to define the regenerator downstream edge in the charged mode, the same cut was applied in the neutral mode so that the simulation of inelastic kaon scattering in the regenerator which was derived from $K_{L,S} \to \pi^+\pi^-$ data could be applied to the neutral mode.

Rejecting events with significant event activity in the ring counters and SAs reduced inelastic background as well as suppressed $K_L \to \pi^0\pi^0\pi^0$ background to $2\pi^0$ decays where one or two photons escaped the decay volume and hit the veto counters. The veto cuts for the 1997 neutral mode analysis were the same as those in the 1997 charged mode analysis where events in which the RC trigger source fired were rejected. In the 1996 $2\pi^0$ analysis, the RC ADC was used to veto events with more energy than the equivalent energy of a 300 MeV photon. The SA veto cut was the same for both years.

[10] The online regenerator veto cut on the final module might have been slightly tighter (0.6±0.1 MIP).

7.4.2 Kinematic and Event Quality Cuts

To improve the reconstruction of events in the final data sample, several selection cuts were applied to the $2\pi^0$ data set. To ensure that we did not accept events which would have failed the $K_{L,S} \to \pi^0\pi^0$ Level 1 trigger, only events that fired the ET trigger source were accepted. To be less sensitive to the Level 2 HCC trigger as well as to avoid the energy and position mis-reconstruction of low-energy photons, each photon was required to have at least 3 GeV of energy. Approximately 20% of events were removed by the minimum photon energy cut. Loosening the cut to 2 GeV would increase the number of data events by ~15%. The viability of changing the minimum photon energy requirement is discussed in Chapter 9. Since clusters that were very close together were not well-reconstructed, we required photons to be separated by at least 7.5 cm. As seen in Table 7.2, the minimum photon separation cut rejected less than 1% of events after all other cuts. This is because most of the photons that are less than 7.5 cm apart come from different π^0. Since this event topology does not occur very often, the minimum photon separation cut accepts most events.

7.4.3 Background-suppression Cuts

To reduce $K_L \to \pi^0\pi^0\pi^0$ background, a $\chi^2_{\pi^0}$ cut was applied. The $\chi^2_{\pi^0}$ cut reduced contamination from $3\pi^0$ events where two photons from different π^0 were not detected. Although the $\chi^2_{\pi^0}$ distribution (see Figure 7.10) was very narrowly peaked close to zero, we applied a loose cut of 12 because the data-Monte Carlo agreement was poor in this variable. There was also a strong kaon energy dependance on the pairing χ^2 distribution which was not well-understood.

A shower quality cut based on the transverse energy distribution of the photon shower was applied to reduce the background due to $K_L \to \pi^0\pi^0\pi^0$ events where two photons were on top of each other or could not be distinguished. For each photon, we calculated a quality factor, χ^2_{shape}, that compared the energy distribution within each cluster to the transverse energy lookup (see Chapter 4 and Appendix A). We required the maximum χ^2_{shape} in each event to be less than 48. Although the maximum photon χ^2_{shape} was less than 10 in more than 99% of the events, we applied a loose cut because

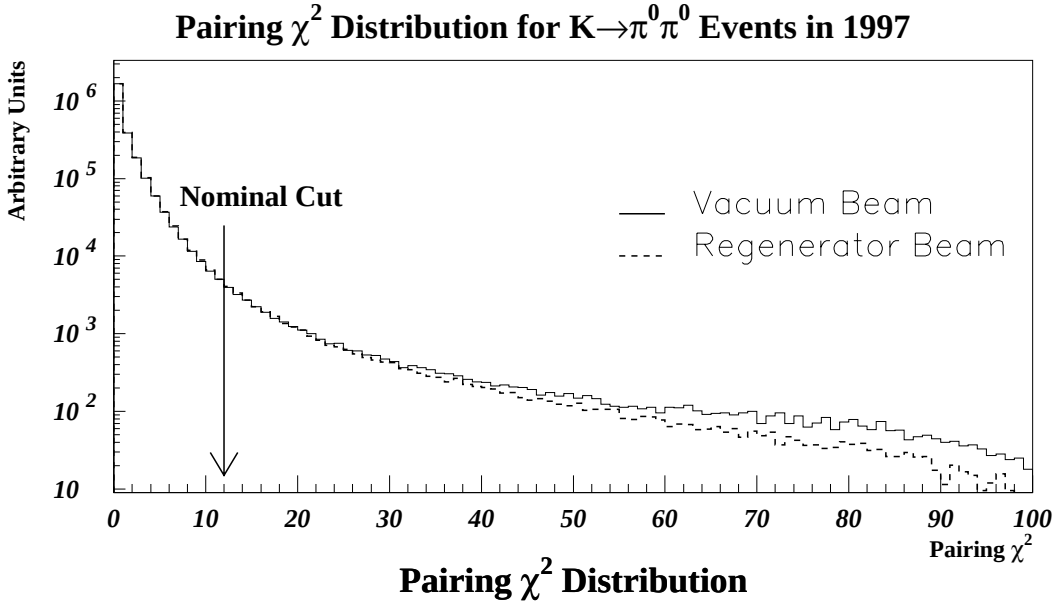

Figure 7.10: Pairing χ^2 distributions for $2\pi^0$ data in 1997 before background subtraction. The distributions have been normalized so that their areas are the same. The 1996 $2\pi^0$ distributions were similar.

the data-Monte Carlo agreement was different in the vacuum and regenerator beams. The maximum χ^2_{shape} cut was nevertheless useful in reducing some $K_L \rightarrow \pi^0\pi^0\pi^0$ background since the maximum χ^2_{shape} distribution for $3\pi^0$ background in the vacuum beam was much shallower than for $2\pi^0$ events as shown in Figure 7.11. Events with a very large amount of accidental activity were also removed by the χ^2_{shape} cut.

The BA was used to reject background events such as $3\pi^0$ where one or more photons escaped down the beam hole. Events with more energy than a photon equivalent of 5 GeV in the first section of the BA were removed. In 1997, a tighter offline analysis cut was applied by rejecting events in which the BA trigger source fired. The tighter cut in 1997 led to a decrease in the $3\pi^0$ background from 0.30% to 0.12% as seen in Table 7.4.

Background due to the mis-identification of events such as hadronic interactions in the regenerator and $K_L \rightarrow \pi^0\pi^0\pi^0$ decays were reduced by applying a cut requiring the

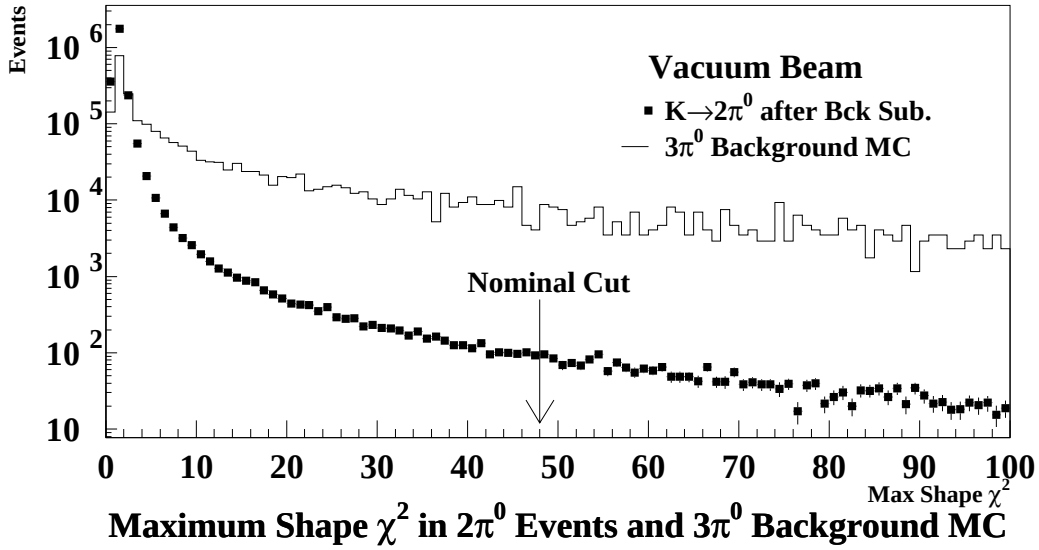

Figure 7.11: Comparison of maximum χ^2_{shape} distributions in vacuum beam $2\pi^0$ data after background subtraction and $K_L \to \pi^0\pi^0\pi^0$ background Monte Carlo in 1997. The distributions have been normalized such that the total area under the graphs are the same. The maximum χ^2_{shape} distributions for $K_{L,S} \to \pi^0\pi^0$ events in the vacuum and regenerator beams are very similar.

$2\pi^0$ invariant mass to be between 490 MeV/c^2 and 505 MeV/c^2. The $\pi^0\pi^0$ invariant mass distributions before background-subtraction are shown in Figure 7.12. From the figure, we see that the mass resolutions are the same for both beams. The kaon mass sidebands (see Figure 7.12) were lower in the regenerator beam because the K_L flux was attenuated.

By selecting events with only four hardware clusters, and without tracks or software clusters of more than 0.6 GeV, accidental events and background due to misidentified decays were reduced. We also applied cuts on the activity in the trigger counters and drift chambers to reduce background containing charged particles.

The inability to determine the kaon transverse momentum in the neutral mode meant that we were unable to apply a p_T^2 cut to reduce collimator and regenerator scatters. Instead, we reduced kaon scatter background by applying a cut on the position of the centre-of-energy of the four photons at the calorimeter. To apply a

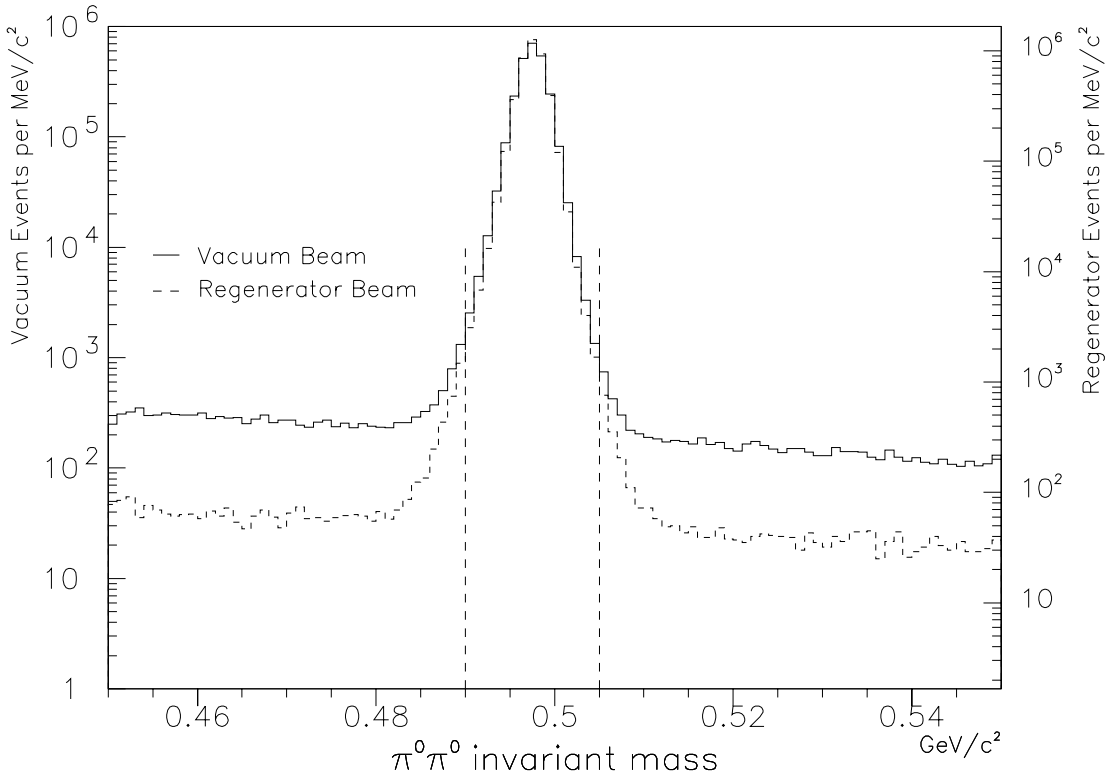

Figure 7.12: Vacuum (solid) and regenerator (dashed) beam $\pi^0\pi^0$ invariant mass distributions in 1997 $2\pi^0$ data before background subtraction. The kaon mass signal region is indicated by the area between the dashed vertical lines. The distributions in 1996 and 1997 were similar.

cut on the centre-of-energy, a "ring number", R, was defined. The "ring number" is defined by :

$$R \equiv 40000 \times (Max(x_{COE}, y_{COE}))^2 \tag{7.5}$$

where x_{COE} (y_{COE}) is the x-distance (y-distance) (in metres)[11] of the centre-of-energy from the centre of the closest calorimeter beam hole and $Max(x_{COE}, y_{COE})$ is the larger of x_{COE} and y_{COE}. Figure 7.13 shows the ring number distributions for $K_{L,S} \rightarrow \pi^0\pi^0$ events in data before background subtraction for both vacuum and regenerator beams.

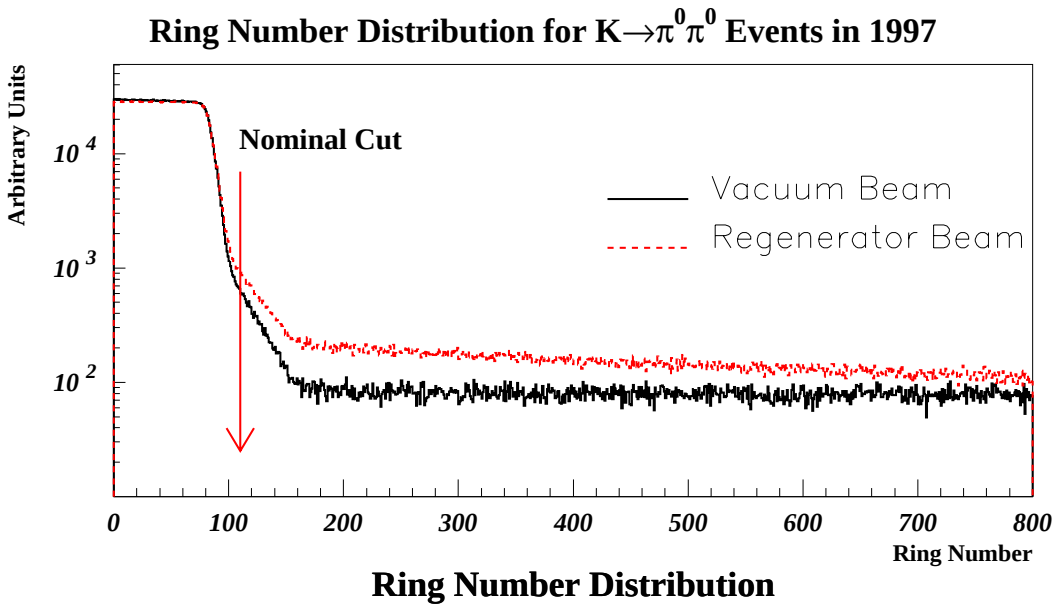

Figure 7.13: Ring number distributions for $2\pi^0$ data in 1997 before background subtraction. The distributions have been normalized so that their areas are the same. The ring number tail in the regenerator beam is larger than in the vacuum beam indicating that most of the regenerator scatters remain in the regenerator beam. The 1996 $2\pi^0$ distributions were similar.

A "ring number" cut of R≤110.0 was applied to ensure that only events where

[11] The factor, 40000, that was included in Equation 7.5 to convert distances measured in m^2 to cm^2.

the centre-of-energy of the four photons was well inside one of the neutral beams were chosen. In this way, kaon scattering backgrounds were reduced in the final $K_{L,S} \rightarrow \pi^0\pi^0$ sample. The "ring numbers" for points outside the beam hole are greater than 225. The ring number distribution above R=200 is dominated by kaon scatters as shown in Figure 7.15. We see from Figure 7.13 that the regenerator distribution had more events out in the ring number tail, indicating that most of the regenerator scatters remained in the regenerator beam.

7.4.4 Aperture Cuts

Analysis cuts were used to define the calorimeter apertures as well as the upstream decay region. The calorimeter inner aperture was defined by the Collar-Anti veto around the beam holes. Events with more than 1 GeV of equivalent photon energy in CA were rejected. The outer aperture was defined by the outermost "ring" (column or row) of large CsI blocks. For an event to have been accepted in the final event sample, all four photon cluster seeds had to be at least one block away from the outermost ring of blocks. To limit the number of kaons that scattered in the collimator from one beam into another, limit upstream decays and reduce upstream events with accidental activity and backgrounds due to radiative decays, we rejected events with more than 300 MeV of equivalent photon energy in the MA as well as events in which the MA trigger source fired. By limiting the number of upstream decays, the MA defined the upstream decay region in the vacuum beam.

7.5 Background Subtraction

As a result of good detector performance, tight analysis cuts and excellent veto efficiencies, the background levels in the charged and neutral modes were $\sim$0.1% and $\sim$1%, respectively. Despite the low background levels, it was important to understand and subtract the backgrounds accurately to achieve the desired precision in the measurement. If we did not subtract the background from the $K_{L,S} \rightarrow \pi^0\pi^0$ data samples, the measured value of $Re(\epsilon'/\epsilon)$ would change by 13×10^{-4}.

7.5.1 Sources of Background

As described in the previous chapter, the background to the 2π modes could be categorised as background due to mis-identified events and background due to kaon scatters.

The main source of background due to mis-identification in the neutral mode was $K_L \to \pi^0\pi^0\pi^0$ decays, where there were photons which did not deposit energy in the calorimeter or could not be distinguished from the other photons. As seen in Figure 7.14, the $K_L \to 3\pi^0$ background was more significant in the vacuum beam where K_L were not attenuated by the shadow absorber and regenerator. The $m_{\pi^0\pi^0}$ distribution for $K_L \to 3\pi^0$ background was almost flat (see Figure 7.16). The $3\pi^0$ background reconstructed vertex z-distribution was also peaked farther downstream than the $2\pi^0$ distribution since photons were not detected. As discussed in Chapter 3, the RCs, SAs and BA reduced the level of $3\pi^0$ background considerably. In addition, $m_{\pi^0\pi^0}$ and $\chi^2_{\pi^0}$ analysis cuts reduced the background further (see Table 7.2). To estimate the remaining $K_L \to 3\pi^0$ background, $K_L \to \pi^0\pi^0\pi^0$ events were simulated and analyzed using the same trigger and analysis conditions as was used in processing $K_{L,S} \to \pi^0\pi^0$ events.

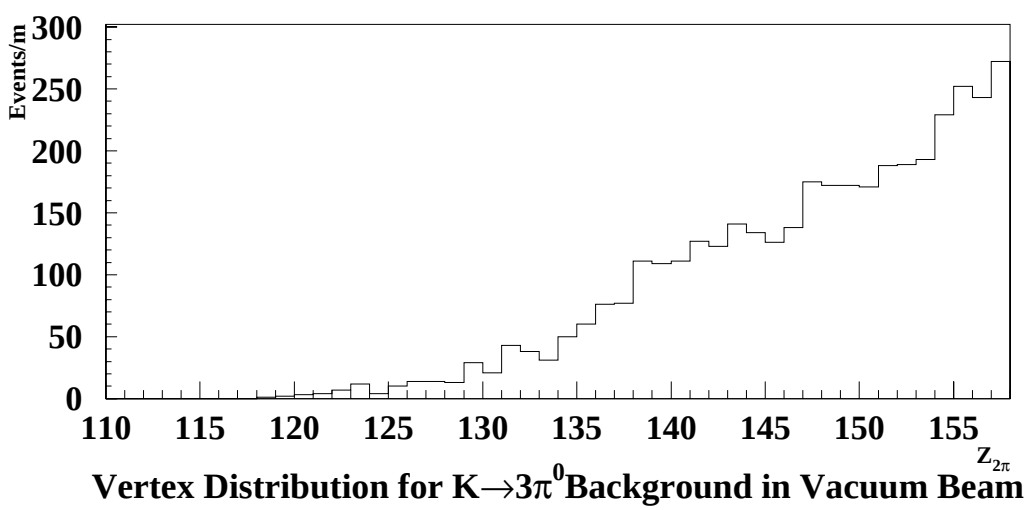

Figure 7.14: $2\pi^0$ vertex z-distribution for $K_L \to 3\pi^0$ background Monte Carlo.

Hadronic interactions in the regenerator could produce events with $2\pi^0$ in the final state. Background due to hadronic regenerator interactions was peaked at the downstream end of the regenerator and the $m_{\pi^0\pi^0}$ distribution was flat. Most of this background was reduced by the regenerator veto. To subtract any remaining background due to hadronic regenerator interactions, we simulated the production of $2\pi^0$ events at the end of the most downstream lead piece in the last regenerator module. The kinematics of the simulation were determined using regenerator beam events from the 1996 $2\pi^0$ data set where the $2\pi^0$ vertex was at the downstream end of the regenerator and the $m_{\pi^0\pi^0}$ was in the kaon mass-sidebands (i.e., outside the signal region).

There were sources of mis-identification background due to decays such as $K_L \to \pi^+\pi^-\pi^0$ which contained charged particles. As described earlier, analysis cuts reduced this background. Since the level of this background was small, we did not subtract the background explicitly from the $2\pi^0$ data sample[12].

Collimator and regenerator kaon scatters affected both $K_{L,S} \to \pi^+\pi^-$ and $K_{L,S} \to \pi^0\pi^0$ modes but were hard to identify and reduce in the $K_{L,S} \to \pi^0\pi^0$ channel. Kaons that scattered from one beam into the other and decayed to $2\pi^0$ could be assigned as coming from the wrong beam because the kaon beam was assigned by the x-position of the 4-photon centre-of-energy. The scattering background was the largest source of background in the neutral mode. A Monte Carlo simulation based on the $K_{L,S} \to \pi^+\pi^-$ mode was used to estimate and subtract the regenerator and collimator scattering background. The simulation is described in detail in Chapter 6.

$\sim$0.005% of the events in the final data sample contained mis-paired pions (π^0). Since this was a feature of the reconstruction, mis-paired pions were present in both the data and the $2\pi^0$ Monte Carlo. Hence, mis-paired photons were not treated as a background and subtracted. Although mis-paired π^0 were not subtracted from the final $2\pi^0$ data sample, events with mis-paired π^0 were subtracted from the data sample when determining the normalization for the background samples discussed

[12]Since the $K_L \to \pi^0\pi^0\pi^0$ and hadronic interaction backgrounds were normalized to the mass sidebands, we indirectly subtracted part of the mis-identification background due to decays such as $K_L \to \pi^+\pi^-\pi^0$.

Background process	1997 Normalization Factors		
	W_{Vac}	W_{Reg}	W_{Vac}/W_{Reg}
Kaon scattered in collimator	0.165±0.002	0.167±0.002	0.989±0.014
Kaon scattered **diffractively** in regenerator	0.201±0.001	0.203±0.001	0.990±0.005
Kaon scattered **inelastically** in regenerator	0.177±0.002	0.183±0.002	0.968±0.014
$K_L \to \pi^0\pi^0\pi^0$ with mis-identified or lost photons	0.701±0.017	0.656±0.059	1.069±0.099
Hadronic interactions producing $2\pi^0$ in regenerator	0.055±0.004	0.091±0.004	0.607±0.052

Table 7.3: Background normalization factors with respect to data for the $K_{L,S} \to \pi^0\pi^0$ events in 1997. Only the normalizations when the regenerator is in the left position are shown. The background normalizations for the regenerator "left" and "right" configurations are in statistical agreement with each other.

below since mis-paired pions (π^0) could reconstruct in the kaon mass sidebands.

7.5.2 Background Normalization and Subtraction

After simulating the background samples, the various sources of background needed to be normalized and subtracted from the data sample. The normalization of the background samples was performed separately for each beam and regenerator position to account for any differences in the beam configuration which could lead to different levels of background. All analysis cuts except for the ring number and kaon mass cuts were applied to the data and background samples before normalization. Mis-paired π^0 were first subtracted from the data before normalizing the background samples. The mis-paired photons were obtained from a sample of $K_{L,S} \to \pi^0\pi^0$ Monte-Carlo without any scattering.

The $K_L \to \pi^0\pi^0\pi^0$ background sample was normalized using events in the $m_{\pi^0\pi^0}$ sidebands (0.46 GeV/c^2< $m_{\pi^0\pi^0}$ <0.48 GeV/c^2 and 0.52 GeV/c^2< $m_{\pi^0\pi^0}$ <0.54 GeV/c^2) with a reconstructed $\pi^0\pi^0$-vertex between 140 m and 158 m from the target. To reduce the amount of scattering background in the normalization data sample, only events with a ring number in the signal region (R≤110) were selected.

Hadronic regenerator interactions were normalized to the data after subtracting

the normalized $K_L \to \pi^0\pi^0\pi^0$ background. Hadronic regenerator interactions were isolated by selecting events in the kaon-mass sidebands that had a $2\pi^0$-vertex at the downstream end of the regenerator between 125 m and 130 m from the target. To remove regenerator scatters from the normalization sample, the ring number had to lie in the signal region.

$K_{L,S} \to \pi^0\pi^0$ collimator scatters were normalized based on the fraction of $K_{L,S} \to \pi^+\pi^-$ and $K_L \to \pi^+\pi^-\pi^0$ vacuum beam data events that scattered in the collimators. The fraction of kaons that scattered in the collimator were the same in the charged and neutral modes. The normalization is described in Chapter 6.

The two components of regenerator scatters, inelastic scatters and diffractive scatters, were normalized separately. Since the fraction of kaons entering the regenerator that scattered diffractively had to be the same for both modes, diffractive regenerator scatters were normalized based on the number of $K_{L,S} \to \pi^+\pi^-$ events that had scattered diffractively in the regenerator relative to the number of coherent $K_{L,S} \to \pi^+\pi^-$ regenerator beam events. The normalization was determined from the fit that was used to obtain the regenerator scattering simulation (see Chapter 6). On the other hand, the fraction of inelastic regenerator scatters was expected to be different between the charged and neutral modes since the veto efficiencies were different. For example, in the neutral mode, the BA and HA were used to reject events whereas in the charged mode, the BA and HA were not used in the trigger or offline analysis. The inelastic scatters were normalized to the data sample after all other normalized background samples were subtracted. The normalization was performed using events in the kaon mass signal region with ring numbers between 300 and 800; the $2\pi^0$-vertex was also required to be between 125 m and 158 m from the target. In this region (see Figure 7.15), inelastic and diffractive regenerator scatters were the dominant background and only a small fraction of events were due to coherent $K_{L,S} \to \pi^0\pi^0$ decays.

Table 7.3 shows the normalization factors obtained for the 1997 $K_{L,S} \to \pi^0\pi^0$ data set. The normalization factors for inelastic regenerator scatters in the vacuum and regenerator beams are seen to agree well with each other indicating that the scattering simulation was accurate enough to describe both low-p_T^2 and high-p_T^2 re-

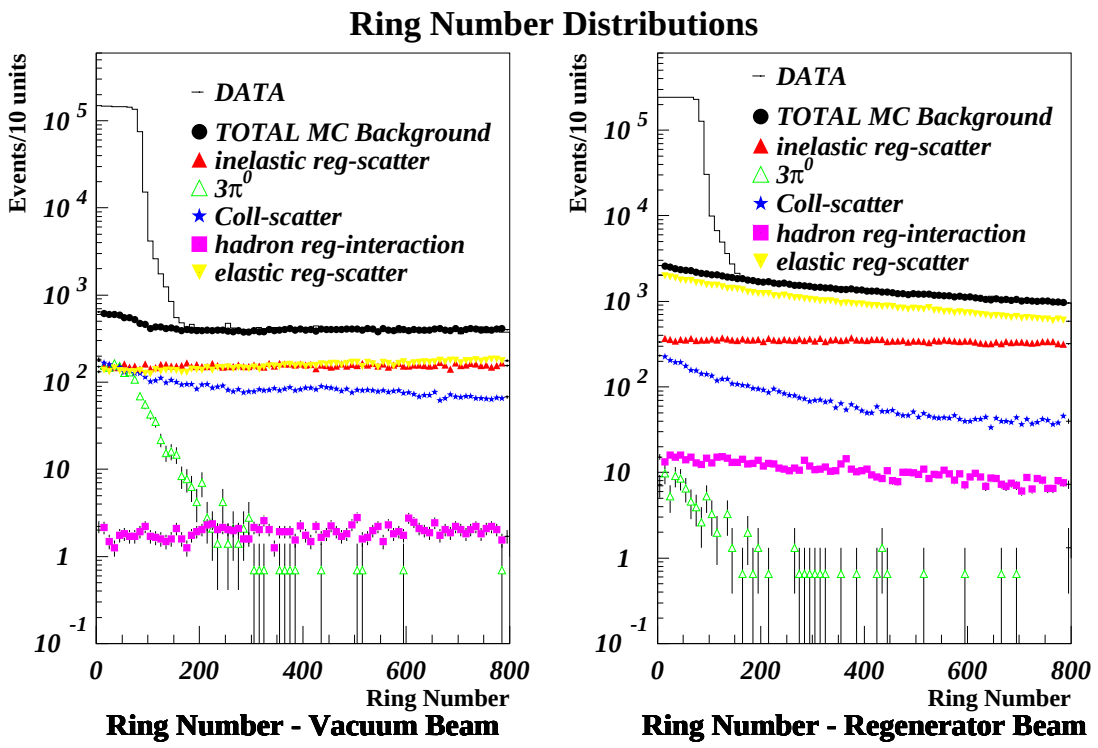

Figure 7.15: Vacuum and regenerator beam ring number distributions for $2\pi^0$ data and Monte Carlo background (after normalization) samples in 1997. Only the backgrounds shown in the plots are subtracted from the data distributions. Almost all of the events with ring number greater than 200 were due to collimator and regenerator scattering backgrounds. In the regenerator beam, the dominant background were elastic (diffractive) scatters whereas in the vacuum beam, the amount of collimator scatters and regenerator scatters are the same.

generator scatters. Kaons that scattered inelastically with low-p_T^2 tended to remain in the regenerator beam while most high-p_T^2 regenerator scatters crossed over into the vacuum beam. Although we generated both diffractive and inelastic regenerator scatters together, the normalization factors for inelastic regenerator scatters were lower than those for diffractive scatters. This shows that the level of inelastic scatters (relative to diffractive scatters) was lower in the neutral mode than in the charged mode. This is expected since the BA and HA were only used to reject events in the neutral mode. We also see that the vacuum and regenerator beam normalization factors for hadronic regenerator interaction background were significantly different. The disagreement between the vacuum and regenerator beam normalizations could be due to either the incomplete description of hadronic regenerator interactions, or the fact that other backgrounds due to mis-identification such as $K_L \to \pi^+\pi^-\pi^0$ decays were not simulated. Since the level of the hadronic regenerator background was low, the effect on $Re(\epsilon'/\epsilon)$ due to the disagreement in the vacuum and regenerator beam hadronic regnerator interaction normalizations was less than 0.05×10^{-4} (see Chapter 9).

7.5.3 Final $\pi^0\pi^0$ Background Levels

The background levels after normalization and all analysis cuts for 1996 and 1997 neutral mode data sets are presented in Table 7.4.

Figure 7.15 shows the ring number distributions for the $2\pi^0$ data and background samples in 1997. We see that in the regenerator beam, the dominant background was due to elastic (diffractive) regenerator scatters while in the vacuum beam, the level of collimator and regenerator (inelastic and diffractive) scatters was about the same. The ring number distribution for collimator scatters in the vacuum beam inreased under the signal region indicating that we would underestimate the level of the background if we were to extrapolate the distribution linearly at large ring numbers into the signal region. Hence, it was important to simulate the scattering background.

The 1997 $2\pi^0$ invariant mass distribution for the data and the various components

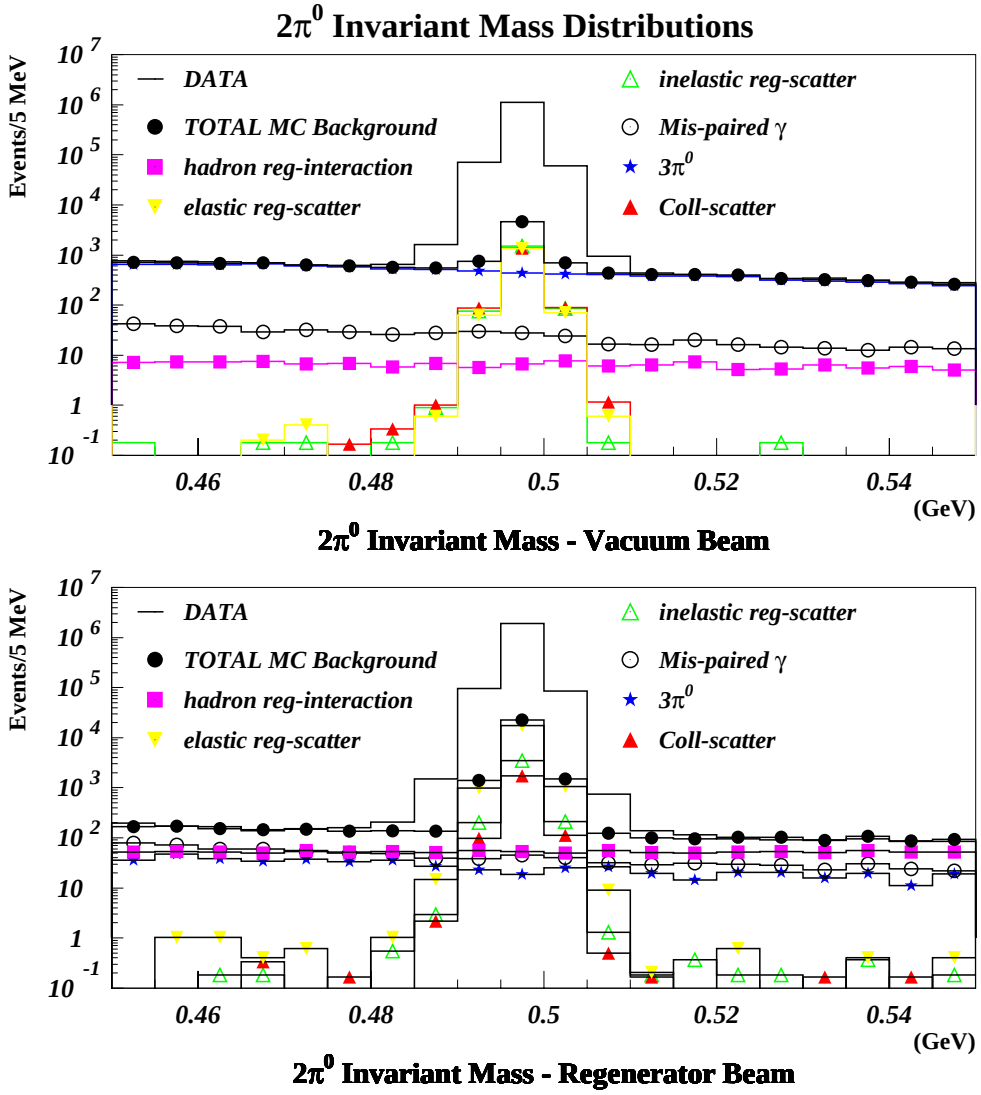

Figure 7.16: Vacuum and regenerator beam $\pi^0\pi^0$ invariant mass distributions for 1997 data, Monte Carlo background (after normalization) and mis-paired pions. Mis-paired π^0 are not subtracted from the data distributions when obtaining the final data sample.
The $2\pi^0$-mass of background due to scattering was peaked in the kaon mass signal region (490-505 MeV^2/c^2). The $2\pi^0$ mass distributions for $K_L \rightarrow \pi^0\pi^0\pi^0$ background and hadronic regenerator interactions were flat. The background in the kaon mass sidebands is dominated by $K_L \rightarrow \pi^0\pi^0\pi^0$ decays in the vacuum beam and hadronic regenerator interactions in the regenerator beam.

Background process	1996		1997	
	Vac (%)	Reg (%)	Vac (%)	Reg (%)
Kaon scattered in collimator	0.123	0.095	0.123	0.094
Kaon scattered **diffractively** in regenerator	0.123	0.937	0.118	0.941
Kaon scattered **inelastically** in regenerator	0.148	0.218	0.134	0.189
$K_L \to \pi^0\pi^0\pi^0$ with mis-identified or lost photons	0.233	0.009	0.107	0.003
Hadronic interactions producing $2\pi^0$ in regenerator	0.003	0.007	0.002	0.008
Total	0.630	1.267	0.484	1.235

Table 7.4: Background levels for the $K_{L,S} \to \pi^0\pi^0$ events in 1996 and 1997. The background levels are the same for both regenerator positions to within 0.007%. The effect of the tighter BA cut in 1997 is evident from the lower $3\pi^0$ background.

Data Sample	Vacuum Beam	Regenerator Beam
1996	858,191	1,425,397
1997	2,489,538	4,130,392
Total	3,347,729	5,555,789

Table 7.5: Number of background-subtracted $K_{L,S} \to \pi^0\pi^0$ events in the 1996 and 1996 dataset

of the background are shown in Figure 7.16. We see that the $2\pi^0$ invariant mass due to scattered kaons was in the kaon mass signal region while the background in the kaon mass sidebands is dominated by $K_L \to \pi^0\pi^0\pi^0$ decays and hadronic regenerator interactions in the vacuum and regenerator beams, respectively. We also see that the $2\pi^0$-mass distribution for mis-paired pions is flat.

7.6 Total Event Counts

The number of events in the final neutral mode data sample is presented in Table 7.5. After all event selection cuts and background subtraction, the final data sample contained 3,347,729 and 5,555,789 $K_{L,S} \to \pi^0\pi^0$ events in the vacuum and regenerator beams, respectively. The kaon energy and decay vertex z-position distributions in the 1997 $2\pi^0$ data sample after all analysis cuts are shown in Figures 7.17 and 7.18.

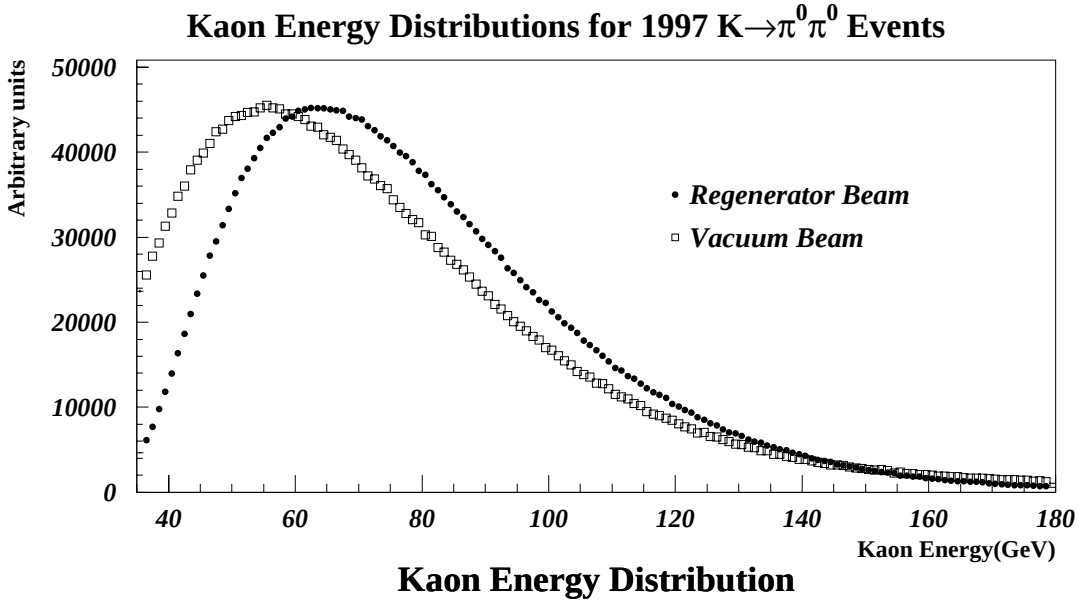

Figure 7.17: Vacuum and regenerator beam kaon energy distributions for 1997 $K_{L,S} \rightarrow \pi^0\pi^0$ data after all analysis cuts and background subtraction. The mean kaon energy for vacuum and regenerator beam events are ~70 GeV and ~80 GeV, respectively. The distributions have been normalized so that their areas are the same. The 1996 distributions were similar.

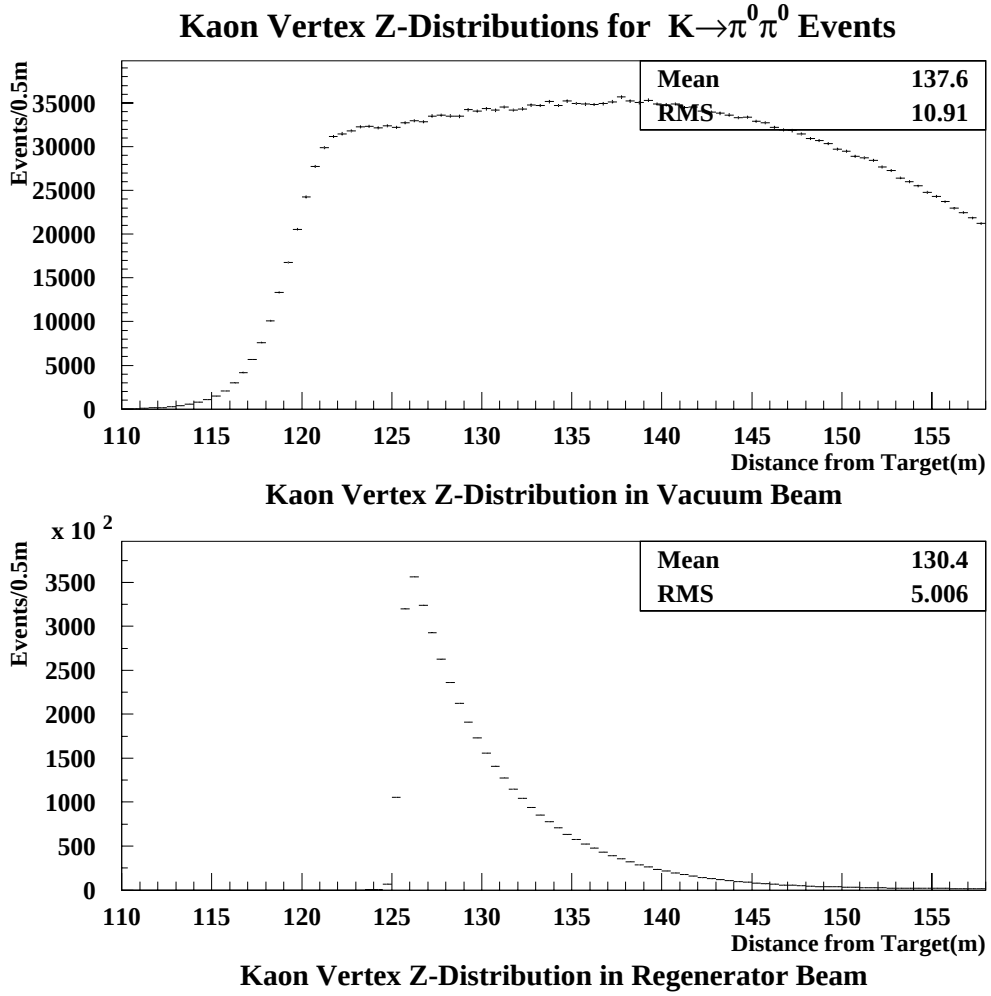

Figure 7.18: Vacuum and regenerator beam kaon vertex z-position distributions for 1997 $\pi^0\pi^0$ data after all analysis cuts and background subtraction.

CHAPTER 8
THE MONTE CARLO SIMULATION

This chapter describes the Monte Carlo simulation used in the $Re(\epsilon'/\epsilon)$ measurement. We begin by discussing the different types of Monte Carlo simulations that were employed in KTeV and then describe in detail the Monte Carlo that was used to determine the $K \to 2\pi$ acceptance in the nominal analysis.

8.1 Introduction to Monte Carlo in KTeV

Three kinds of Monte Carlo were used in the KTeV $Re(\epsilon'/\epsilon)$ measurement. These are:

- GEANT [65] Monte Carlo. The GEANT Monte Carlo was based on the CERN GEANT [65] package and was used to simulate the passage of particles through the detector. The GEANT Monte Carlo was important in determining the acceptance of the detector and was used to simulate multiple scattering in the spectrometer as well as the development of hadronic and electromagnetic showers in the calorimeter. The GEANT Monte Carlo was also used in the offline data analysis. In the neutral mode, the out-of-cone ($f_{out-of-cone}$) and the longitudinal uniformity $f_{longitudinal}$ corrections were based on the GEANT Monte Carlo. Finally, the GEANT Monte Carlo played a significant role in the design and construction of the KTeV detector. For example, in the preparation of the CsI crystals, the GEANT Monte Carlo was used to predict the energy resolutions. As described in Section 4.1, the longitudinal response of each crystal was tuned based on the GEANT predicted energy resolutions.

- Geometry Monte-Carlo. The Geometry Monte Carlo was used to determine the sensitivity of the acceptance to the geometry of the KTeV detector and to find

out the precision that was needed to understand the detector response. The Geometry Monte Carlo simulated the evolution, decay and passage of kaons and their decay products through the KTeV detector assuming a perfect detector response. The simulation did not include any resolution and scattering effects, and the decays were perfectly reconstructed (i.e., generated quantities were used in the analysis). All offline analysis cuts were applied when studying the effect of employing a Geometry Monte Carlo to measure the acceptance.

- KTEVMC. KTEVMC refers to the full KTeV Monte Carlo simulation. Like the Geometry Monte Carlo, KTEVMC included the evolution and decay of the kaons as they travelled through the KTeV detector, but in addition, KTEVMC accounted for the response of the detector by simulating detector inefficiencies, resolution effects and other performance features such as the response to accidentals were simulated, so that the data and Monte Carlo reconstructed distributions for $K_{L,S} \to \pi^0\pi^0$ and $K_{L,S} \to \pi^+\pi^-$ decays would agree. As described earlier, KTEVMC used the GEANT Monte Carlo to simulate showers in the calorimeter and multiple scattering in the spectrometer. Although the principle aim of KTEVMC was to determine the acceptance for $K_{L,S} \to \pi^0\pi^0$ and $K_{L,S} \to \pi^+\pi^-$ events, the Monte Carlo simulation was also used to optimize the online and offline reconstruction and analyses. The online Level 3 trigger and calibration code was initially tuned using the Monte Carlo simulation and both the online and offline analysis cuts were optimized based on Monte Carlo studies. KTEVMC was used to generate background samples. Finally, as discussed in the next chapter, KTEVMC was important in determining systematic uncertainties on $Re(\epsilon'/\epsilon)$.

The main purpose of KTEVMC was to measure the acceptance for $K \to 2\pi$ decays. The difference in $Re(\epsilon'/\epsilon)$ between an analysis which applied the nominal acceptance correction (using KTEVMC) and an analysis which did not correct for the acceptance at all was $\sim 80 \times 10^{-4}$. By comparing the $Re(\epsilon'/\epsilon)$ measurement using the Geometry Monte Carlo to the nominal measurement, we observed that $\sim$80% of the effect of the acceptance on $Re(\epsilon'/\epsilon)$ was due to the understanding of the geometrical

acceptance. Since the effect on $Re(\epsilon'/\epsilon)$ of simulating the full response of the detector was $\sim 10\times10^{-4}$, we had to understand the detector response to better than 10% of itself to measure $Re(\epsilon'/\epsilon)$ to a precision of 1×10^{-4}.

8.2 Kaon Production, Evolution, Decay and Transport

8.2.1 Kaon Production

The $K \to 2\pi$ Monte Carlo simulation began by selecting the beam (vacuum or regenerator) and the position of the regenerator; the position of the regenerator was chosen based on the accidental event which was overlaid (see Section 8.3). The primary particle was then selected to be either K^0 or $\overline{K^0}$. The vertical production angle was specified to be between 4.2 mrad and 5.5 mrad and was chosen from a distribution which optimized the data-Monte Carlo reconstructed beam profile agreement. The initial kaon energy was obtained from a distribution which resulted in the best possible E_K agreement between data and Monte Carlo $K_{L,S} \to \pi^+\pi^-$ decays in the vacuum beam[1]. As described in Section 8.2.4, only kaons that decayed within the decay volume were generated, so the initial energy and angular distributions were modified to ensure that the generated decay distributions were correct.

The initial position of the kaon in the target was based on the proton interaction length in Be and on the shape of the primary beam. The latter was used to determine the transverse position of the kaon in the target. The position and alignment of the target relative to the primary proton beam was determined using survey measurements.

8.2.2 Kaon Transport

Kaons that were produced at the target were traced down the KTeV beamline through the absorbers, collimators and regenerator (if the regenerator was in the path of the

[1]The kaon energy and angular distributions were obtained from the Malensek spectrum based on the K^+ and K^- production spectra but were modified to improve data-Monte Carlo agreement in reconstructed quantities.

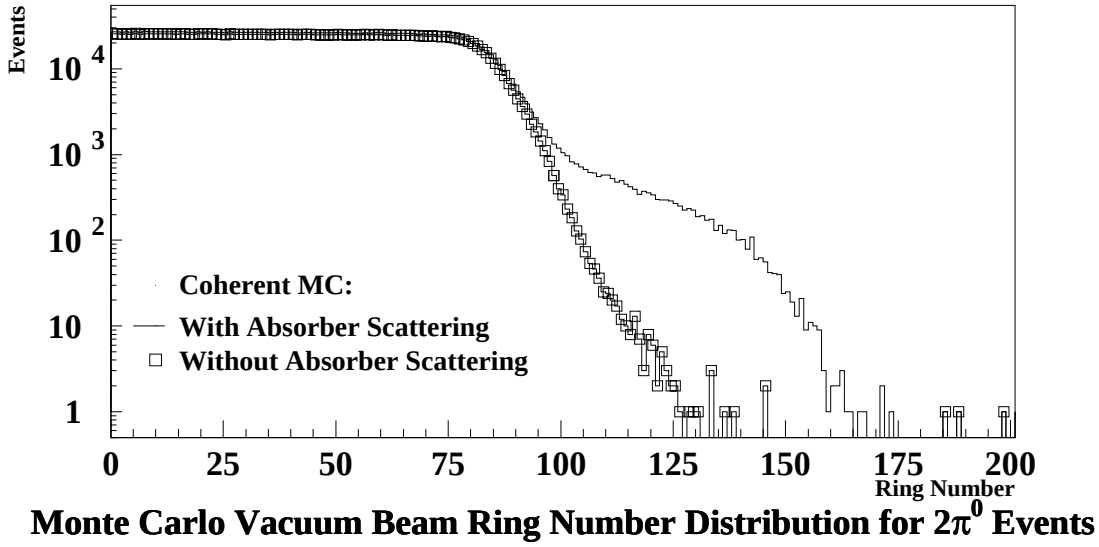

Figure 8.1: Vacuum beam ring number distribution for coherent $2\pi^0$ Monte Carlo with and without common absorber scatters.

kaon). The position and geometry of the absorbers and collimators were obtained from survey measurements[2]. The primary and slab collimators were treated as perfectly absorbing, since the collimation system (see Figure 3.2) was designed to minimize the number of kaons that scattered in the primary and slab collimators and decayed in the kaon decay volume. Both absorption and scattering in the absorbers were simulated. When a kaon scattered in the absorbers, the transverse momentum of the kaon was modified based on an exponential p_T^2 distribution. Both the neutral mode ring number and the charged mode p_T^2 distributions were sensitive to the common absorber scattering. The effect of absorber scattering in the neutral mode is seen in Figure 8.1. Scattering in the defining collimator was an important source of background in both charged and neutral modes, and a detailed simulation based on $K_L \to \pi^+\pi^-\pi^0$ and $K_{L,S} \to \pi^+\pi^-$ data was used. This simulation is described in Chapter 6.

[2]The alignment of the defining collimator in the 1996 Monte Carlo was modified to improve the data-Monte Carlo beam profile in the K_{e3} channel.

8.2.3 Kaon Evolution

The K^0 or $\overline{K^0}$ state was evolved through the KTeV beam line taking into account the attenuation and the regeneration within each element. A transformation matrix [64], which considered the geometry of the absorbers and regenerator, K^0 and $\overline{K^0}$ forward scattering amplitudes, and the composition of each beam line element, was applied to the intial kaon state. The basis states for the transformation matrix were the K_L and K_S states.

The transformation matrix only accounted for coherent transmission. Inelastic and incoherent scattering within the defining collimators and regenerator were treated as sources of background (see Chapter 6). The transformation matrix predicted a transmission of 7.38% over all energies through the shadow absorber and the regenerator. Since preliminary measurements based on $K_L \to \pi^+\pi^-\pi^0$ and $K_L \to \pi^0\pi^0\pi^0$ decays in the 1997a data set showed that the attenuation decreased linearly with kaon energy at a rate of 0.004%/GeV and the mean transmission was about 5% higher than the transmission predicted using the transformation matrix, the Monte Carlo attenuation in the regenerator beam was modified to agree with the measured attenuation (in the 1997a data set). Transmission measurements made using the complete 1997 data set showed that the mean transmission was actually higher by about 0.1%. A small transmission difference between the data and Monte Carlo could cause a mismatch between the data and Monte Carlo kaon energy distributions in the regenerator beam. The systematic uncertainty due to the attenuation in the shadow absorber and regenerator is described in Section 10.1.1.

8.2.4 Kaon Decay

Kaon decays were simulated by specifying the decay region and the kaon energy range at the start of the simulation. One way of simulating kaon decays was to evolve every kaon through the decay volume and then select the kaons that had decayed in the chosen kaon energy and decay region. This approach is extremely CPU-intensive since only a small fraction of K_L decay in the region of interest. To reduce the CPU-time, every kaon that was generated was forced to decay in the selected decay volume. To

ensure that the kaon scattering and decay distributions were still correct, we adjusted the kaon energy and angular distributions at the target.

The kaon decay products were traced through the detector region until they escaped the fiducial volume or were absorbed. The secondary particles were allowed to decay as well. Charged particles were bent at the final sweeping magnet and the analysis magnet[3]. The pair-production of photons was simulated throughout the spectrometer region and the trigger counters.

8.3 Accidentals

Primary particles (besides kaons) produced at the target and secondary products from their interactions and decays lead to extra ("accidental") activity in the detectors, uncorrelated with kaon interactions. Since the amount of accidental activity (or "accidentals") depends on the beam intensity as well as the beam elements such as the regenerator and absorbers, accidentals affected vacuum and regenerator beams differently. As mentioned in Chapter 2, the different amount of accidental activity in the two beams introduces bias in $Re(\epsilon'/\epsilon)$.

To account for accidental activity in the detectors, each KTEVMC event was overlaid with an "accidental" event. An "accidental trigger" was used to select accidental events during data-taking. The accidental trigger consisted of scintillation counters placed at 90° to target. The counters triggered on primary beam activity at the target. Since the rate of accidental triggers and the detector activity in events selected by the accidental trigger depended on the beam intensity but were uncorrelated with kaon decays, accidental trigger events accurately represented the underlying activity in the detectors.

To overlay an accidental event on a Monte Carlo kaon decay, detector information, such as the drift chamber hits and calorimeter energies, that was present in an accidental event was added to the information from the Monte Carlo simulated event. The accidental drift chamber and calorimeter information was needed to simulate the drift

[3]The momentum kick that was used to simulate the analysis magnet was the same one as was used in the analysis of the $K_{L,S} \to \pi^+\pi^-$ data sample.

chamber inefficiencies due to early hits (see Figure 8.3) and the neutral mode trigger, as discussed in the next section. The run and spill number for each Monte Carlo event was obtained from the accidental event header, so that the run-dependance of the accidental activity would be the same in data and Monte Carlo.

In the $K_{L,S} \to \pi^0\pi^0$ analysis, accidental activity resulted in a noticeable increase in the number of extra software clusters in an event. It also caused the total energy in the calorimeter to increase and changed the pairing and shape χ^2 distributions. On average, accidentals caused a $\sim$0.06% increase in the the kaon energy in $K \to \pi^0\pi^0$ events. The increase in kaon energy caused the regenerator edge to reconstruct farther upstream (away from the calorimeter). By matching the data and Monte Carlo z_K distributions at the regenerator edge, global neutral mode energy scale effects due to accidentals were accounted for. Residual effects due to accidentals showed up as a slope in the data-Monte Carlo vacuum beam z_K ratio vacuum beam because accidentals tended to cause a greater loss of events downstream where the kaon and photon energies were lower. As described in Chapter 9, the assigned uncertainties on $Re(\epsilon'/\epsilon)$ due to the acceptance and energy non-linearities accounted for the effect of accidentals.

8.4 Simulation of the Trigger and Detector

8.4.1 Drift Chambers

The simulation of the drift chamber involved calculating the distance from the closest wire as a charged particle passed close to it. The drift distance was converted to a drift time which was then digitized and stored in drift chamber TDC banks. In order to describe the behaviour of the drift chambers accurately, it was necessary to simulate effects that led to drift chamber inefficiencies and modified the drift times.

We simulated the drift chamber inefficiency which caused hits to be missed by determining the probability that a drift chamber wire did not detect any hits (the "missing hit" probability) using $K_{L,S} \to \pi^+\pi^-$ data for each wire. The inefficiency for each wire in a plane as well as the spatial variation of the inefficiency along the wire

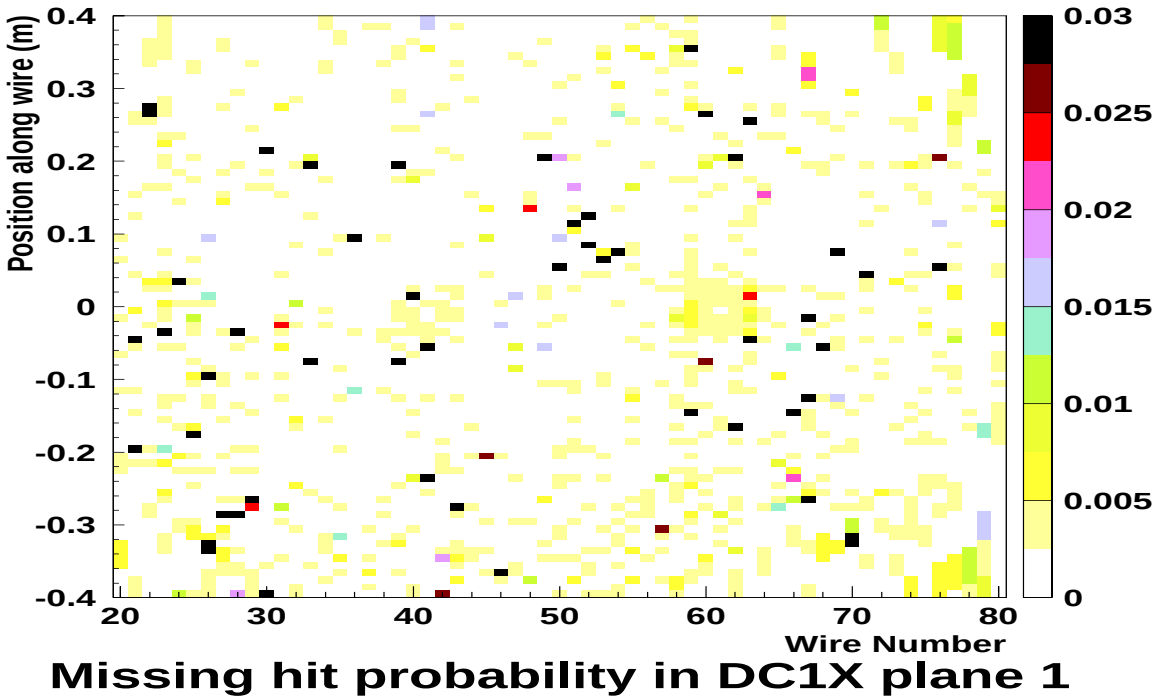

Figure 8.2: Missing hit probability for the first X-plane in the first drift chamber. The regenerator is on the left in this plot.

were simulated. The fact that the missing hit inefficiency increased farther away from the wire was also accounted for. The missing hit probability for the first plane in the DC1 x-view is shown in Figure 8.2. Although the average inefficiency due to missing hits along each wire was <1%, there were parts of a wire which exhibited inefficiencies of a few percent. The missing hit inefficiency also depended on the distance of the track from the wire, increasing farther away from the wire.

KTEVMC also simulated inefficiencies which led to high-SODs. The simulation was based on the pulse shape, the point of first ionization along the path of the track and the electronics threshold was used. Details of the simulation can be found in [39].

The modelling of the DC discriminator response was important as well since early hits could obscure later hits because of the discriminator dead-time. The discriminator dead-time of ∼50 ns resulted in a wire being 100% inefficient during this period.

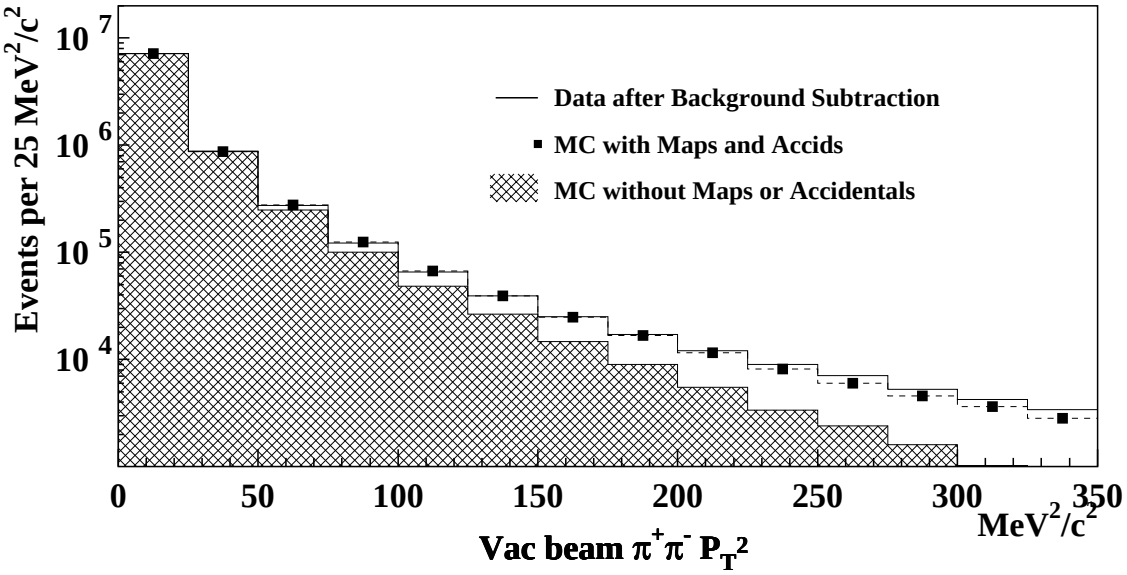

Figure 8.3: Vacuum beam p_T^2 distribution for $\pi^+\pi^-$ Events for background-subtracted data and Monte Carlo with (solid) and without (shaded) inefficiency maps and accidentals.

In addition, large analog pulses which remained above the discriminator threshold for a long time caused the discriminator not to re-trigger. We simulated these effects by making a wire 100% inefficient for about ∼50 ns after a hit and then modelling the inefficiency based on the pulse shape which was measured from data. The inefficiency due to large, long pulses was modelled using the pulse shape and the the path of the early track through the drift cell. The modelling of the response due to early hits was important in accounting for early accidentals which caused the drift chamber to be inefficient to in-time hits. The importance of accurately simulating the effect of accidentals and DC inefficiencies is seen in Figure 8.3 where there is a large improvement in the agreement between data and Monte Carlo vacuum beam p_T^2 distributions for $K_{L,S} \to \pi^+\pi^-$ events.

The drift chamber simulation also accounted for δ-rays above a minimum cutoff energy of 0.5 keV. δ-rays could arrive earlier than the primary drift electron leading to a low-SOD.

The drift distance was smeared so that the plane resolutions in the data and Monte Carlo matched. The smearing was based on the quadrature difference between the plane resolution in data and the resolution obtained from the Monte Carlo.

More details on the drift chamber simulation can be found in [39].

8.4.2 Calorimeter

The simulation of the calorimeter involved describing the deposition of energy within the calorimeter, converting the energy to a charge and subsequently digitizing the charge. The simulation of electrons and photons in the calorimeter required describing electromagnetic showers and was different from the treatment of pions and minimum ionizing particles.

Electromagnetic Showers

A library of 32.5 cm $\times$ 32.5 cm (13$\times$13 small blocks) GEANT-based[65] electron and photon showers was used to simulate the response of photon and electrons in the calorimeter. The 18.75 μm thick mylar wrapping of each of the 169 small crystals was simulated as well. By using a shower library, we were able to simulate the transverse and longitudinal development of showers in the CsI based on well-understood photon and electron interactions, accounting for energy leakage (e.g. at the rear end of the crystal) and absorption effects due to the wrapping material, while at the same time, reducing the processing time compared to a full GEANT simulation for each shower. The showers were generated at six different energies (2 GeV, 4 GeV, 8 GeV, 16 GeV, 32 GeV and 64 GeV) and in 325 500$\times$500 μm^2 position bins spread over one octant of the central crystal (see Figure 8.4). There were five showers in each position and energy bin with a total of $9,750$ showers in the library. The energy cutoffs in the GEANT simulation for electrons and photons in the shower were 600 keV and 50 keV, respectively. The showers were generated at a polar angle of 8 mrad with azimuthal isotropy. The effect of using showers at a fixed polar angle was one cause for differences in the photon energy reconstruction between the data and Monte Carlo. Since we did not correct for the angle of incidence of an electron or photon in the

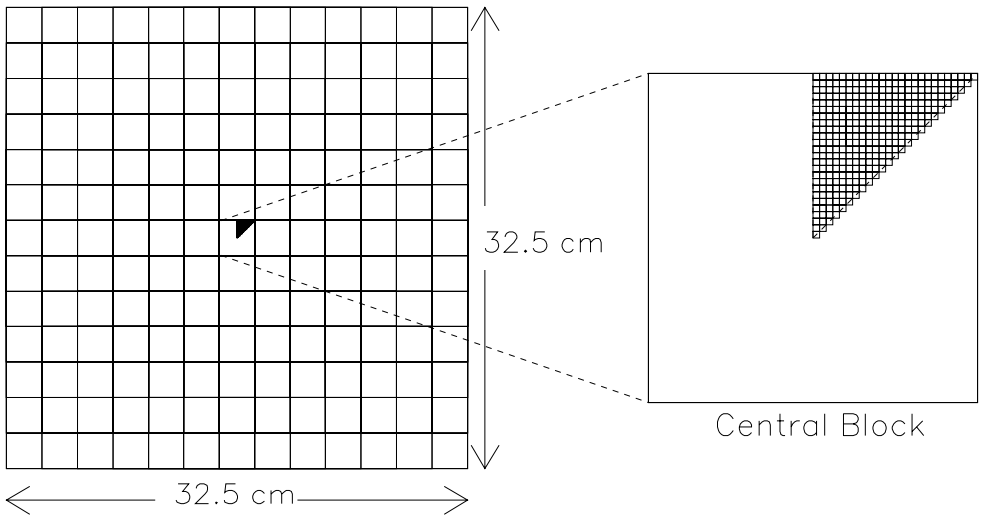

Figure 8.4: Monte Carlo electromagnetic shower position bins.

reconstruction, reconstruction features related to the incident angle would not be the same in data and Monte Carlo, potentially causing a bias in the acceptance-corrected double ratio.

In an effort to pack information efficiently, the shower packing scheme that was used in the analysis of the 1996 and 1997 Monte Carlo only stored selected shower information. The GEANT showers were segmented in the longitudinal (z) direction. The z-segmentation was important in simulating the effect of longitudinal response non-uniformities which were present in the data. For the central block and the three other blocks closest to the shower position, the shower was segmented in 25 bins along the longitudinal direction. For the remaining 45 blocks in the central 7×7 region, the longitudinal shower profile that was stored was obtained by averaging the longitudinal profiles of the 45 blocks. There was no z-segmentation of energy for the outer 120 blocks.[4]

Before a shower was selected, the energy of the incident particle was smeared be-

[4]By averaging the longitudinal response over 45 blocks, the data and Monte Carlo fractions of energy in each block did not agree. Instead of storing 25 bins of longitudinal information, it would have been much wiser to use coarser z-segmentation within a block and more blocks with longitudinal energy profile information.

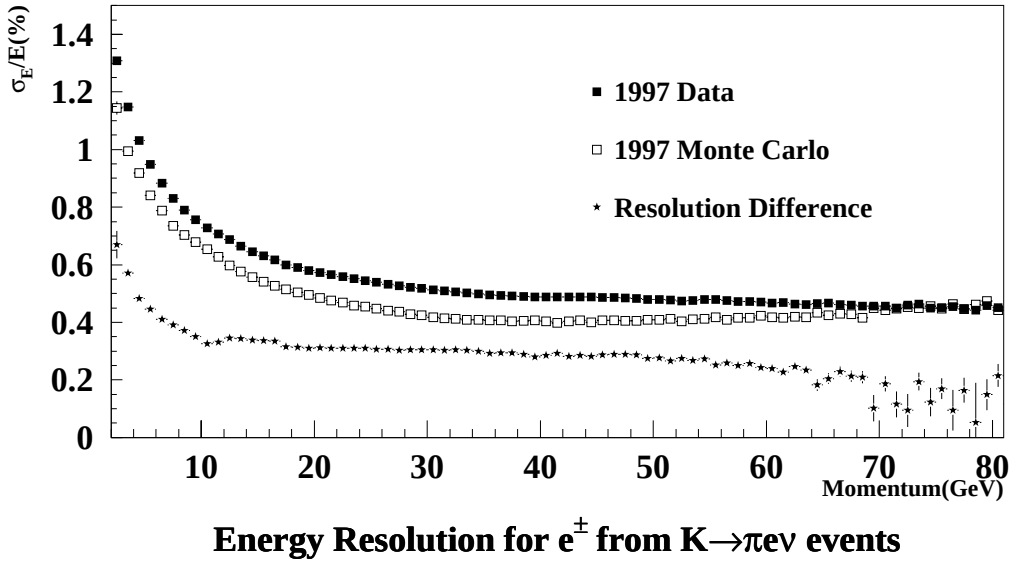

Figure 8.5: Energy resolutions for K_{e3} electrons in 1997 data and Monte Carlo before energy smearing. In the final analysis, the Monte Carlo was smeared so that the data and Monte Carlo energy resolutions would agree.

cause there were some resolution effects in the data that were not simulated in the Monte Carlo. The smearing was tuned such that the data and Monte Carlo reconstructed electron resolutions agreed. The energy smearing depended on the energy of the incident particle as well as the size of the central block. For shower energies less than 2 GeV, the smearing also accounted for the difference between the shower fluctuations at the GEANT shower energy, 2 GeV, and those at the particle energy. For showers higher than 2 GeV, shower fluctuations were simulated by choosing showers from the two closest energy bins. The data and Monte Carlo resolutions before energy smearing are shown in Figure 8.5.

Since the showers were only generated at fixed energies, a shower was chosen from one of the two closest energy bins if the shower energy was greater than 2 GeV[5]. The probability of selecting a shower from an energy bin varied logarithmically with the smeared shower energy. The energy of a shower was normalized using the

[5]For shower energies less than 2 GeV, showers are selected from 2 GeV GEANT showers.

smeared incident energy of the particle. Although this approach of selecting showers obtained the correct mean shower energy distribution at the incident particle energy, by selecting showers from two energy bins the energy fluctuations were more than the fluctuations that one would have expected if we generated showers at the incident particle energy. The effect of this was most evident in the blocks farthest away from the cluster centre. The energy fluctuations in the outer blocks can affect the energy resolution of overlapping showers and clusters with blocks under threshold. Although the shower fluctuations in Monte Carlo were expected to be larger than the data, Figure 8.5 shows that before any extra smearing, the Monte Carlo energy resolutions were lower than the data. This meant that there were resolution effects in the data that were not simulated in the Monte Carlo.

The choice of showers also depended on the position of the particle within the central block. The shower position was chosen by first extrapolating the position of the particle to its maximum shower depth position z_{shmax}, and then applying a correction based on the observed differences in the electron track and cluster positions at the cesium iodide shower maximum in data[6]. The track-cluster mis-match corresponded to a shift in z_{shmax} of ~3 cm and ~5 cm for small and large channels, respectively. Once the position of the shower had been established, the shower was selected from the shower library by mapping of the corrected shower position within the block to a position within the first octant (see Figure 8.4). In KTEVMC, z_{shmax} was given by:

$$\begin{aligned} z_{shmax} &= 0.11 + 0.18 \log E_{incident} \quad : electrons \\ z_{shmax} &= 0.12 + 0.18 \log E_{incident} \quad : photons, \end{aligned} \tag{8.1}$$

where $E_{incident}$ was the incident particle's energy. Although the Equation 8.1 indicates that the maximum shower depth for photons was 1.0 cm further into the cesium iodide than for electrons of the same energy, GEANT [65] and EGS4 [66] simulations showed that a shower maximum position difference of one radiation length, 1.85 cm, should have been used. The systematic uncertainty due to variations in the shower

[6]The track-cluster position-based correction attempted to account for variations in the cluster energy due to the angle and position of incidence.

maximum as well as electron track-cluster position differences within the seed block are addressed in Appendix C.

In order to simulate energy non-linearities due to the crystal response, the energy deposited in the CsI was convolved with the longitudinal (z) response of the crystals (see Section 4.5.1). The variation in light output for each crystal was measured in 5 cm z-bins using cosmic rays and normalized with 8 GeV GEANT showers. Figure 8.6 shows the effect of including longitudinal non-uniformities in the Monte Carlo simulation. The energy linearity in both small and large channel clusters was affected at $< 0.1\%/100GeV$ while the energy resolution was only affected in large block clusters.

Simulating the longitudinal uniformity of each crystal affected the transverse energy distribution of a cluster as shown in Figure 8.7, which compares the fraction of cluster energy in the central block for the standard K_{e3} Monte Carlo (KTEVMC) with a Monte Carlo simulation which did not convolve the shower profile with the longitudinal uniformity. The transverse energy distribution changed because a crystal's length-wise non-uniformity affected the channel's energy scale as well as its energy linearity. In order to determine the energy scale for each channel, each channel must be calibrated individually and the calibration must be applied to each block before determining the transverse energy profile. This was done in the data but not in the Monte Carlo. Averaging the longitudinal energy distribution for certain blocks in a cluster (as was done in the Monte Carlo) also affected the transverse energy distribution. As a result of these calibration and reconstruction differences between the data and Monte Carlo, it was not surprising that the transverse energy distributions in data and Monte Carlo were different. Having different data and Monte Carlo transverse distributions could affect the measurement of the $K_{L,S} \to \pi^0\pi^0$ Level 2 trigger acceptance as well as the cluster energy reconstruction (e.g., the separation of close clusters). To correct for data-Monte Carlo differences in the transverse profile of photon showers, the Monte Carlo energy distribution within the central 7.5 cm $\times$ 7.5 cm region was adjusted after the longitudinal non-uniformity convolution. The energies were adjusted to match the shower profiles of photons in the 5.7 GeV to 11.3 GeV range in $2\pi^0$ data events.

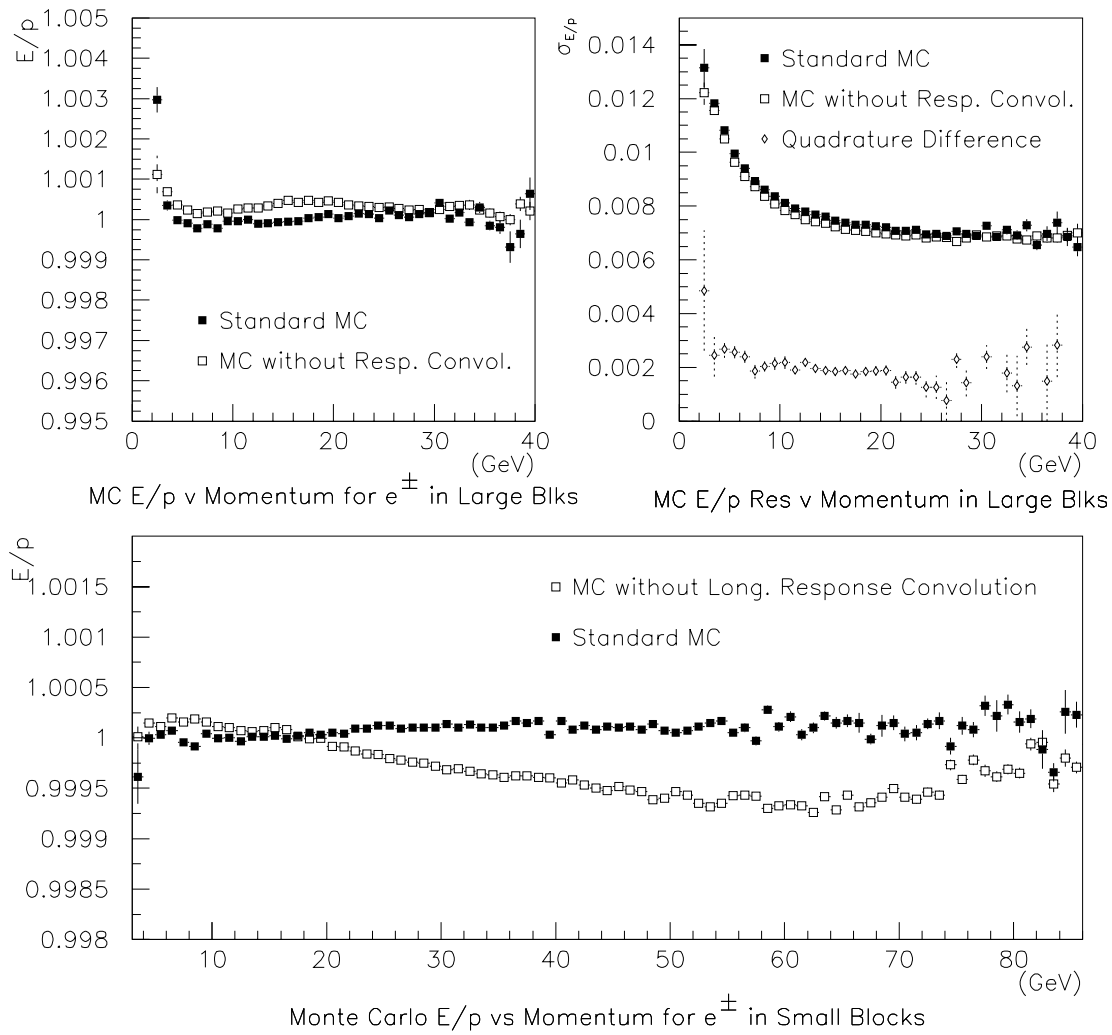

Figure 8.6: Monte Carlo K_{e3} electron energy resolution and linearity with and without CsI longitudinal response simulation. Energy calibration which was applied to both Monte Carlo samples was based on the standard Monte Carlo. The energy resolution is not affected for clusters in the small-region.

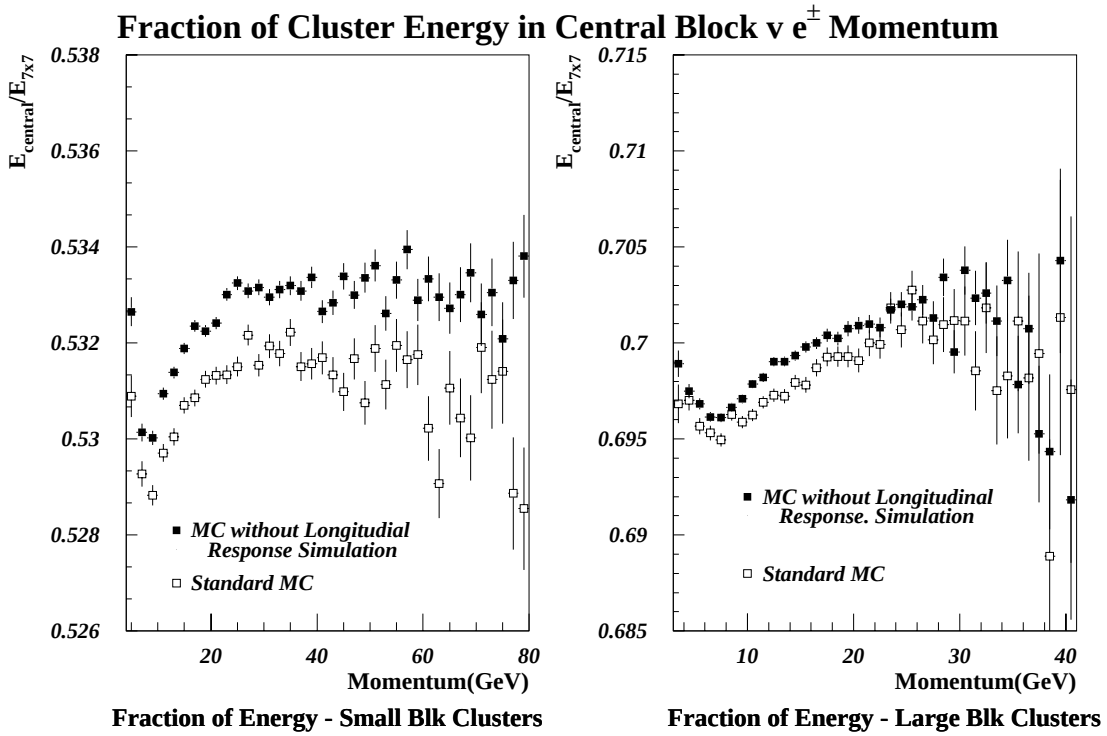

Figure 8.7: Fraction of cluster energy in central block in Monte Carlo K_{e3} electrons with and without the CsI longitudinal response simulation. The cluster energy is the sum of the block energies without any scale corrections.

For showers near the CsI calorimeter beam holes, the energy distribution was modified to account for energy leakage across the hole (E_{sneaky}). Since this modification was based on the leakage across the hole observed in electrons from K_{e3} data events, data distributions were used to correct for energy leakage across the hole from one shower into another (see Section 4.5.1).

Since electromagnetic showers were larger than the size of showers in the GEANT library, energy was added to blocks which were outside the nominal GEANT shower limits but were within a 27×27 small block region. The amount of energy that was added to each block was based on a GEANT Monte Carlo simulation of 31×31 2.5 cm crystals, and depended on the energy of the incident particle and the distance of the block from the shower center. Although the amount of energy was small, it was important in simulating photons with overlapping showers.

Simulation of other particles

Besides electromagnetic showers, the Monte Carlo simulation also treated the interaction of other particles in the calorimeter. The energy loss of muons in the calorimeter was confined to a single channel and was calculated using the Bethe-Bloch energy loss mechanism with fluctuations. Other minimum ionizing particles deposited 320 MeV in a single CsI channel. For pions that showered, a GEANT shower simulation was used. To describe the pion shower accurately, the stored shower size was 102.5×102.5 cm^2 (41×41 small blocks).

Digitization and Readout

The total energy deposited in each crystal was determined by summing the energy deposited by each particle and the energy from accidental events. The energy in each block was then converted to a charge by applying the Q/E calibration constants obtained in the K_{e3} data calibration. The total charge in each block was divided into time-slices using the RF-phase-dependent pulse time profiles obtained from $K \to \pi^0\pi^0$ data. The charge within a time slice was smeared based on photostatistics and digitized by applying the same DPMT calibration constants used in reconstructing data events. The digitized information in each block was only written out if the energy in that block exceeded the readout threshold. By only writing out the data from channels which exceeded the readout threshold, we modelled the acceptance of clusters with blocks below the readout threshold. The effect of baseline (pedestal) fluctuations were not considered during digitization. Since pedestal fluctuations degraded the reconstructed energy resolution at lower energies but were not simulated, it was important to determine the uncertainty on $Re(\epsilon'/\epsilon)$ due to pedestal fluctuations in the data. This systematic uncertainty is discussed in Appendix C.

Calibration

The Monte Carlo was calibrated by determining a linearity correction ($f_{linearity}$) for each channel using electrons from simulated K_{e3} events. Since DPMT non-linearities,

gain fluctuations and transverse response variations were not simulated, no corrections were made for them when calibrating and analyzing the Monte Carlo. However, other clustering corrections due to close clusters ($E_{overlap}$), "out-of-cone" energy ($f_{out-of-cone}$), clusters near the hole and edges ($E_{missing}$), blocks below threshold ($E_{sub-thresh}$) and non-uniformities in longitudinal response ($f_{longitudinal}$) were applied in the Monte Carlo event reconstruction. Although the fraction of energy within the 3×3 or 7×7 crystal region depended on the incident position in the central block, in the Monte Carlo analysis, no correction was made to account for the variation in the reconstructed cluster energy.across the face of the seed block ($f_{transverse}$). The effect on $Re(\epsilon'/\epsilon)$ of not applying a transverse response correction was estimated to be $< 0.31 \times 10^{-4}$.

The magnitude of the Monte Carlo energy linearity correction is indicated by the Monte Carlo electron E/p linearity before calibration shown in Figure 8.8. It is important to realise that since the Monte Carlo was calibrated by using a cluster-level energy linearity correction, the energy scale of each individual block was not determined. Based on Figure 8.8, we estimated that, on average, the energy scale in each block was correct at the 0.1% level. Since the Monte Carlo calibration was cluster-energy-based, differences between photon and electron transverse shower shapes affected the Monte Carlo energy scale in $2\pi^0$ events to first-order [7].

8.4.3 Trigger

The charged mode Level 1 and 2 trigger elements were simulated by modelling the hit-counting and track-finding performed by the YTF and Banana/Kumquat modules. The simulations of the YTF and the Banana/Kumquat modules were simplified because they only used the digitized drift chamber information.

The Level 1 and Level 2 triggers for $K_{L,S} \to \pi^0\pi^0$ and $K_L \to \pi^0\pi^0\pi^0$ events used the calorimeter and hence, the simulation of these triggers was closely related to the

[7] The effect of the Monte Carlo CsI blocks not being calibrated individually on the HCC simulation was negligible.

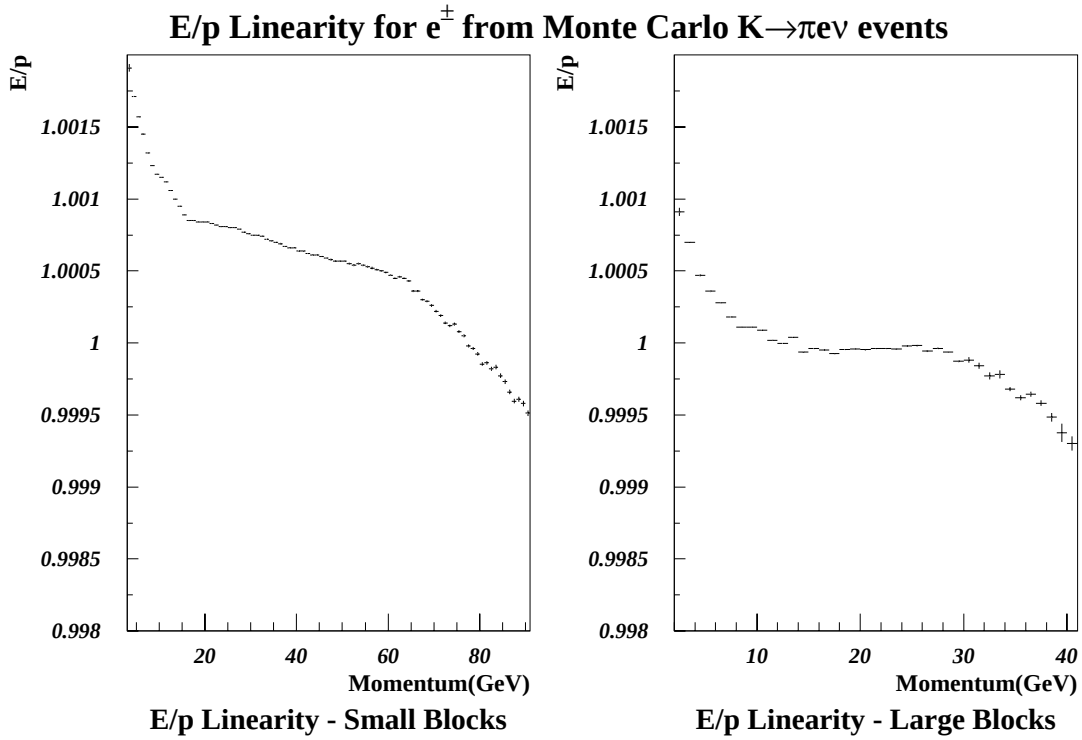

Figure 8.8: Monte Carlo K_{e3} E/p Linearity in 1997 for small (left) and large-seed (right) clusters before applying the energy linearity correction.

simulation of the calorimeter. The E-Total trigger threshold and "turn-on width"[8] (see Figure 7.2) were carefully measured and simulated using a minimum-bias ECAL trigger that did not require the sum of calorimeter energy. In 1997, the thresholds were simulated based on the energy in the in-time slice, since this was what the online trigger decision was based on. Due to the larger time slewing of DPMT pulses and greater susceptibility to out-of-RF-phase accidentals, the simulation in 1996 was based on the total 4-slice (228 ns) energy sum.

To simulate the trigger accurately, the ET contribution of each channel had to be understood. Corrections for channel-to-channel differences in the analog pulses were made. We also simulated the effect of channels that did not contribute to the online ET trigger during part of the data-taking because the dynodes leading to the ET-

[8]The threshold was defined to be the energy at which the system was 50% efficient, while the "turn-on width" was the energy range in which the efficiency was between 10% and 90%.

system were broken. Trigger inefficiencies due to early accidentals which did not allow re-triggering of the ET discriminator as well as the contribution of in-time accidentals were considered too. The ET constants were determined during several periods in the 1996 and 1997 run, so time variations in the ET efficiency were accounted for. As a result of the detailed simulation, the data and Monte Carlo ET trigger thresholds agreed to within 250 MeV.

The KTEVMC simulation of the Level 2 neutral mode trigger involved modelling the HCC bit inefficiencies and the HCC trigger logic. As described below, the HCC bit efficiencies for each channel had to be individually measured and simulated. The HCC trigger logic in the simulation was exactly the same as that used online in the programmable hardware(HCC) trigger.

Essential to simulating the Level 2 HCC system was the description of the HCC bit efficiencies close to the threshold for each channel. Figure 8.9 shows the HCC bit efficiency and the fit used in the simulation for a typical channel. The thresholds were based on the total energy in each channel, although the online trigger was based only on the charge in the in-time slice. Since out-of-time accidentals affected the total energy in the calorimeter but not the HCC bit efficiency, when determining the thresholds, we rejected out-of-time accidental activity based on the pulse profile (i.e., fraction of total energy in each QIE slice). The contribution of in-time accidentals was also included in the HCC trigger simulation. The HCC bit thresholds were determined over several run periods since the HCC system depended on the timing of the beam with respect to the RF. The data and Monte Carlo Level 2 trigger "turn-on" thresholds agreed to within 30 MeV for most channels.

As described in Section 7.1.2, the HCC bit efficiency was very sensitive to the timing of the dynode signal. High-energy pulses (>3 GeV) which arrived too early resulted in an HCC inefficiency (see Figure 7.4). In 1996, there were up to ~30 channels with HCC bits which were more than 10% inefficient above 3 GeV. High-energy HCC bit inefficiencies in 1996 were simulated by using a "turn-off" curve as shown in Figure 8.10. Since effort was made during data-taking to minimize high-energy HCC bit inefficiencies in 1997, every channel was more than 99.5% HCC-efficient at energies above 3 GeV. Besides HCC bit inefficiencies due to pulse timing,

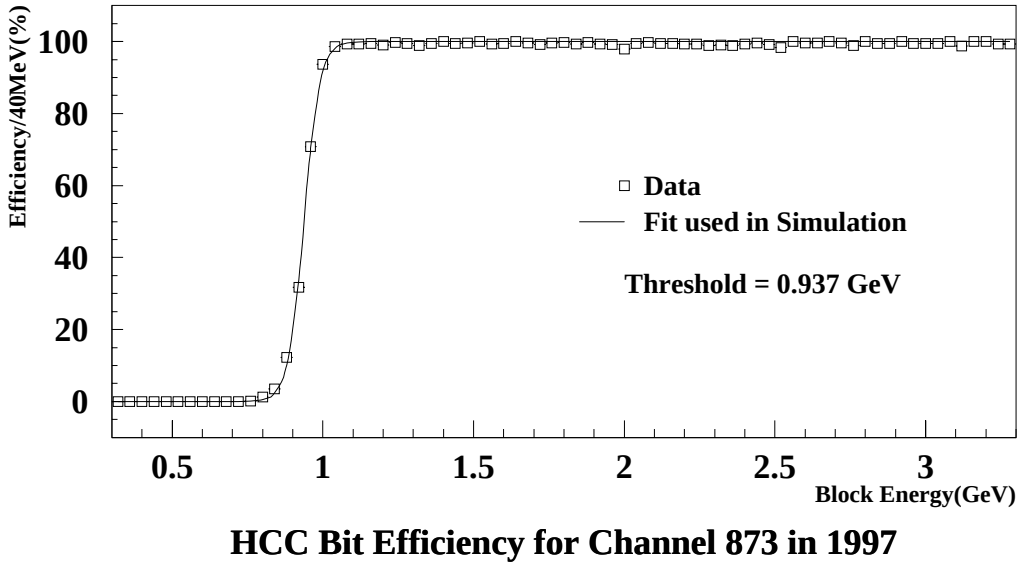

Figure 8.9: The HCC bit efficiency (%) for channel 873 in 1997 indicating the efficiency measured using ECAL events (open) and the function (smooth curve) used in the HCC bit efficiency simulation.

the effect of channels with dynode failures as well as other HCC failure modes were simulated.

8.4.4 Veto, Trigger and Aperture Elements

Photons and electrons which hit the RCs and SAs were not traced any farther. Instead, they deposited all their energy in the veto counters. The energy that was deposited in the veto elements by photons and electrons was smeared using a Gaussian distribution with an energy-dependent resolution. On the other hand, minimum ionizing particles deposited a mean energy of 130 MeV in the RC counters and 195 MeV in the SAs, and the energy deposited was smeared using a Gaussian distribution of fixed resolution. The resolutions used in KTEVMC were 35% and 30% for the RCs and SAs, respectively.

The MA and CA simulations were important to the neutral mode since they defined the upstream decay region and calorimeter inner aperture. The MA and CA

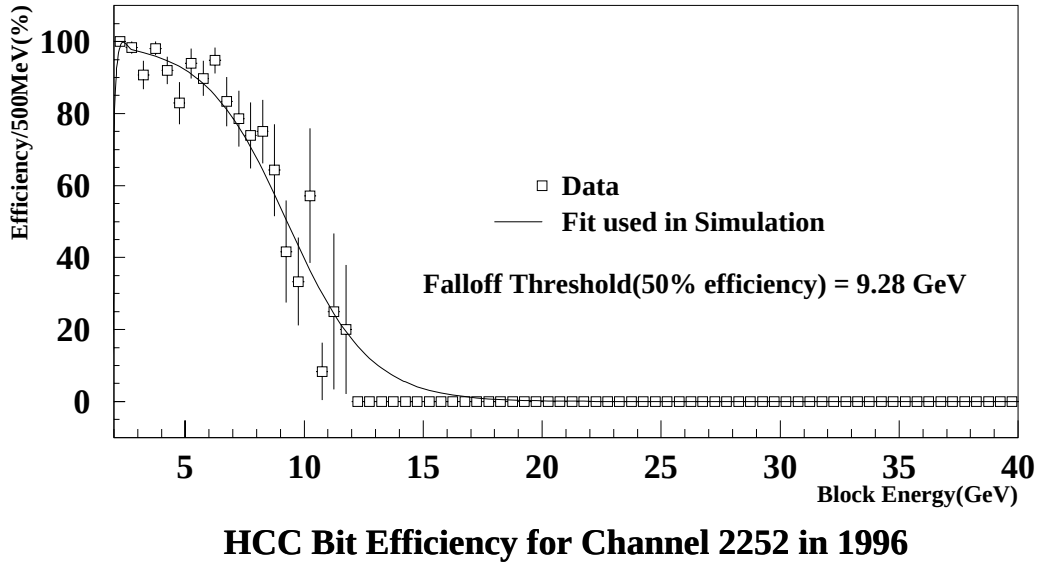

Figure 8.10: The HCC bit efficiency (%) at energies greater than 2 GeV for channel 2252 in 1996. The channel is 100% efficient between 1.1 GeV and 2.25 GeV. The data (open) and the "turn-off" function (smooth curve) used in the HCC high-energy inefficiency simulation are shown.

apertures were obtained using electrons from K_{e3} data events. However, photon-electron differences in scattering and absorption led to an "effective" aperture for photons that was different from that measured using K_{e3} electrons. The difference was more significant for the MA aperture than the CA aperture. In order to account for the difference, $\sim$200 μm larger, in the effective MA size, photons that were close to the edge of the MA holes could travel through the MA. The "punch-through" probability depended on the distance travelled through the MA. Simulating photon punch-through in the MA improved the data-Monte Carlo z_K agreement for $K_{L,S} \rightarrow \pi^0\pi^0$ events upstream of the MA (z <120 m). Understanding the acceptance in the z >120 m region was important since the acceptance varied rapidly in this region. $Re(\epsilon'/\epsilon)$ increased by 0.45×10^{-4} when we included photon punch-throughs in the MA Monte Carlo. In the simulation, photons which passed through the MA did not deposit energy in it whereas those that were stopped in the MA deposited all their energy. Electrons and pions that showered deposited all their energy in the MA. The

energy deposited was smeared using an energy-dependent Gaussian distribution. For minimum-ionizing particles, both the energy that was deposited and the scattering in the MA were simulated.

Since the effect on $Re(\epsilon'/\epsilon)$ of photon-electron differences in the apparent CA size was negligible, the CA simulation did not allow photon punch-throughs and instead, electrons and photons that were incident on the CA were stopped with all their energy being deposited in the CA. Each CA (left and right) was treated separately. MIPs deposited a fixed amount of energy (which was smeared to simulate the resolution of the CA) and were traced through to the CsI.

Scattering in the (VV‘) trigger counters, the trigger counter performance and the digitization of trigger counter hit information were carefully simulated since the TDC hit information from the trigger counters was used when modelling the charged mode Level 1 trigger. Trigger counter inefficiencies were also reproduced in KTEVMC. In this regard, it was important that the geometry of the VV‘ counters that was used in KTEVMC accurately described the dead spaces in the system.

The simulation of energy deposition in the muon counters was based on the Bethe-Bloch ionization loss mechanism that included Landau fluctuations from a parametrization based on GEANT.

8.5 Generation of Monte Carlo Samples

In the $Re(\epsilon'/\epsilon)$ analysis, coherent $K \to 2\pi$ Monte Carlo was used to determine the acceptance. KTEVMC was also used to generate non-coherently scattered kaons as well as other sources of background. In addition, Monte Carlo samples of other decay channels such as $K_L \to \pi^0\pi^0\pi^0$ and $K_L \to \pi^\pm e^\mp \nu$ were generated.

The run-to-run event fractions were tuned such that the number of events passing all cuts per run were the same in data and $K \to 2\pi$ Monte Carlo. In this way, run-dependent trigger and analysis features that were present in the data were reproduced in the Monte Carlo. No Level 3 filtering was performed on the Monte Carlo signal and background samples since the Level 3 cuts were considered to be loose enough that they were superseded by the tighter offline analysis. Instead of simulating the Level 3

filter, the Level 3 inefficiency in the data was measured and a systematic uncertainty was assigned. This is described in the next chapter. In the generation of $K_{L,S} \to \pi^0\pi^0$ and $K_{L,S} \to \pi^+\pi^-$ Monte Carlo samples, secondary particles were allowed to be 'lost' and not be detected. For such an event to pass the final offline analysis cuts, particles from accidental events had to mimic the presence of the "lost" particle. For example, a $K_{L,S} \to \pi^0\pi^0$ event with a photon that went down the beam hole could appear to have four photons if there was an accidental cluster in the calorimeter. Since most such events failed the kinematic cuts, allowing for "lost" photons in the neutral mode Monte Carlo had a negligible effect on the double ratio. Besides allowing secondary particles to be lost in the simulation, bremsstrahlung $K \to \pi^+\pi^-\gamma$ decays were also generated as part of the $K_{L,S} \to \pi^+\pi^-$ Monte Carlo.

The Monte Carlo events were written out in the same format as the data. In this way, the charged and neutral mode Monte Carlo analyses could be made as similar as possible to the analyses of the data samples, and biases due to reconstruction and analysis inefficiencies reduced. Runs and spills with detector, trigger and data-taking problems that were eliminated in the data analysis were also removed in the Monte Carlo analysis.

The $K_{L,S} \to \pi^+\pi^-$ signal and background Monte Carlo samples were reconstructed using the Monte Carlo-based DC and CsI calibration constants. The charged mode Monte Carlo reconstruction was almost the same as that of the $K_{L,S} \to \pi^+\pi^-$ data. Effects that were not simulated, such as the analysis magnet fringe field, were not corrected for in the Monte Carlo reconstruction. The analysis cuts were the same as those used in the data.

The $K_{L,S} \to \pi^0\pi^0$ Monte Carlo signal and background samples were reconstructed using the same DPMT and energy calibration constants as the data but as mentioned previously, the channel-by-channel linearity corrections were obtained from the KTEVMC K_{e3} electron calibration. Position lookups, which were used to determine cluster positions, and transverse energy distributions, which were used to correct for energy losses at the holes and edges ($E_{missing}$), were made using coherent $K_{L,S} \to \pi^0\pi^0$ Monte Carlo. Since the simulation of clusters near the hole relied partly on $K_L \to \pi^\pm e^\mp \nu$ data showers, the correction for overlapping energy near the beam

Monte Carlo Statistics	$K \to \pi^0\pi^0$		$K \to \pi^+\pi^-$	
	1996	1997	1997a	1997b
Number of data sets	19.9	9.0	4.75	4.07
Statistical Error ($\times 10^{-4}$)	0.49	0.55	0.48	0.33
Total Statistical Error ($\times 10^{-4}$)	0.37		0.27	

Table 8.1: Statistics for coherent $K \to \pi^0\pi^0$ and $K \to \pi^+\pi^-$ Monte Carlo samples. In this table, a "data set" refers to the statistics in the $K \to 2\pi$ data sample.

holes used the same maps in data and Monte Carlo. The analysis cuts that were applied to the coherent $K_{L,S} \to \pi^0\pi^0$ and background Monte Carlo samples were the same as those used in the $K \to \pi^0\pi^0$ data analysis.

$K_L \to \pi^\pm e^\mp \nu$ and $K_L \to \pi^0\pi^0\pi^0$ Monte Carlo samples were generated to cross-check the charged and neutral mode analyses, respectively. As discussed in the next chapter, both these decay channels were also important in determining the systematic uncertainties due to the event reconstruction. As far as possible, the reconstruction of $K_L \to \pi^\pm e^\mp \nu$ and $K_L \to 3\pi^0$ samples used the same corrections and calibration as the $K \to \pi^+\pi^-$ and $K \to \pi^0\pi^0$ modes.

8.6 Monte Carlo Samples

Table 8.1 presents the statistics for the coherent $K \to \pi^0\pi^0$ and $K \to \pi^+\pi^-$ Monte Carlo samples. We generated 4.75 times more coherent $K_{L,S} \to \pi^+\pi^-$ Monte Carlo than data in 1997a, and 4.07 times more coherent $K_{L,S} \to \pi^+\pi^-$ Monte Carlo than data in 1997b. The total statistical error for the full 1997 $K \to \pi^+\pi^-$ Monte Carlo sample was 0.27×10^{-4}. In the $K_{L,S} \to \pi^0\pi^0$ mode, we also generated 19.9 times more coherent $K \to 2\pi$ Monte Carlo than data in 1996 and 9 times more coherent $K \to 2\pi$ Monte Carlo than data in 1997. This led to a total statistical uncertainty of 0.37×10^{-4} for the combined 1996 and 1997 $K \to \pi^0\pi^0$ Monte Carlo samples.

CHAPTER 9
SYSTEMATIC UNCERTAINTIES IN $K_{L,S} \to \pi^0\pi^0$ AND $K_{L,S} \to \pi^+\pi^-$ DECAYS

This chapter discusses the systematic uncertainties in the $Re(\epsilon'/\epsilon)$ measurement due to the neutral and charged mode reconstruction and analysis. Since the analysis and reconstruction of the two modes can, for the most part, be treated separately, the systematics in each mode will be described in separate sections. Uncertainties which affect both modes will be described in the next chapter. Examples of common systematics include the behaviour of the regenerator and the assumptions applied in the fit used to extract $Re(\epsilon'/\epsilon)$ from the acceptance-corrected double ratio.

9.1 General Comments

Although the sources of the systematic uncertainties in the charged and neutral modes were different, we tried to adopt a consistent approach in assigning systematic errors. In many cases, our approach to determining systematic errors was to measure the potential bias on $Re(\epsilon'/\epsilon)$ and then convert the measured bias, B, and statistical error on the bias, σ_B, to an uncertainty. We chose to assign symmetric systematic errors, ΔB, such that the ~68% of the area of a Gaussian with mean B and standard deviation σ_B was included in the range $[-\Delta B, \Delta B]$. Using this convention, if the statistical error on the bias was much larger than the bias itself, the assigned systematic uncertainty would be given by the statistical error on the bias.

Often a certain feature of the reconstruction or analysis would affect more than one parameter which was used to assign a systematic error. In such a case, we tried to account for the effect only once. For example, if an analysis cut affected the acceptance, we "subtracted" the effect on $Re(\epsilon'/\epsilon)$ due to the acceptance change before assigning an uncertainty due to the analysis cut. This was done since a separate uncertainty had already been assigned for the acceptance,

9.2 Neutral Mode Systematic Studies

Studies of systematic issues in the $K_{L,S} \to \pi^0\pi^0$ mode were broadly divided into several categories. These categories included the efficiency of the online triggers, the neutral mode energy scale, cluster energy and position reconstruction, the $K_{S,L} \to 2\pi^0$ analysis cuts and the $K_{S,L} \to 2\pi^0$ background. For each of these categories, we discuss the systematic uncertainty in the 1997 data set and then describe any differences in the uncertainty in the 1996 data set.

9.2.1 Triggers

The intrinsic ET inefficiency[1] above the E_K lower limit of 40 GeV was measured to be 0.6×10^{-4} using $K_L \to \pi^+\pi^-\pi^0$ events from the full 1997 E832 data set. The ET inefficiency was cross-checked using $K_L \to \pi^\pm e^\mp \nu$ events and found to be between 0.4×10^{-4} and 1.0×10^{-4}. There was a wide range in the measured ET inefficiency because only a few runs in the 1997 E832 data set were used. Since the $K_L \to \pi^+\pi^-\pi^0$ event analysis covered the full 1997 E832 run range and the $K_L \to \pi^\pm e^\mp \nu$ determined ET inefficiencies bounded the $K_L \to \pi^+\pi^-\pi^0$ result, we assigned the systematic error on $Re(\epsilon'/\epsilon)$ due to the Level 1 neutral mode trigger using the ET inefficiency from $K_L \to \pi^+\pi^-\pi^0$ events. The systematic uncertainty on $Re(\epsilon'/\epsilon)$ assigned was $(0.6 \times 10^{-4})/6 = 0.1 \times 10^{-4}$; this assumed a maximum bias due to the ET inefficiency. The systematic uncertainty due to the Level 1 trigger in 1996, 0.07×10^{-4}, was determined using the average of the inefficiencies measured with $K_L \to \pi^\pm e^\mp \nu$ and $K_L \to \pi^+\pi^-\pi^0$ decays.

The uncertainty due to the Level 2 trigger was based on the comparison of data and Monte Carlo HCC bit thresholds as well as the Level 2 inefficiency when requiring a minimum photon energy of 3 GeV. A comparison of data and Monte Carlo Level 2 efficiencies using $K_L \to \pi^0\pi^0\pi^0$ decays from a trigger which only applied the ET requirement indicated that the data-Monte Carlo HCC bit threshold agreement was good to $\sim$26 MeV in 1997. To determine the effect of a $\sim$30 MeV change in the HCC

[1]The Monte Carlo only simulated the ET inefficiencies due to accidentals which arrived early and did not simulate the intrinsic ET inefficiency.

thresholds, we measured the change in the $Re(\epsilon'/\epsilon)$ bias when we raised the HCC thresholds by 30 MeV. As seen in Figure 9.1, if we raised the HCC thresholds by 30 MeV, the $Re(\epsilon'/\epsilon)$ bias using the nominal minimum photon energy cut of 3 GeV, changed by 0.12×10^{-4} with respect to $Re(\epsilon'/\epsilon)$ bias expected with the nominal HCC thresholds. Based on the data-Monte Carlo HCC threshold agreement and the change in $Re(\epsilon'/\epsilon)$ bias shown in Figure 9.1, we assigned the uncertainty due to the HCC bit threshold simulation to be 0.12×10^{-4}. HCC inefficiencies also caused a bias in $Re(\epsilon'/\epsilon)$ which varied with the minimum photon energy cut. The uncertainty due to HCC inefficiencies was assigned by estimating the difference between the data and Monte Carlo $Re(\epsilon'/\epsilon)$ biases due to HCC inefficiencies at the nominal minimum photon energy cut of 3.0 GeV. We assigned an uncertainty on $Re(\epsilon'/\epsilon)$ of 0.03×10^{-4} due to HCC inefficiencies. In 1996, besides including the uncertainty due to the HCC thresholds and HCC inefficiencies, the bias due to 'hot bits' was also considered as part of the Level 2 uncertainty. The total Level 2 uncertainty in 1996 was 0.20×10^{-4}.

The uncertainty due to the online level 3 trigger was determined using triggers which only applied the Level 1 and 2 requirements. The $Re(\epsilon'/\epsilon)$ bias due to events which passed all offline $K_{L,S} \to \pi^0\pi^0$ cuts but did not pass Level 3 was $(-0.004 \pm 0.04)\times10^{-4}$. We set an uncertainty on $Re(\epsilon'/\epsilon)$ of 0.05×10^{-4} due to the neutral mode Level 3 trigger. There was no observable effect due to "hot HCC bits" (see Section 7.1.2) on our software filter because most of the spills with ET problems were eliminated in the offline analysis. In the 1996 analysis, the systematic uncertainty on $Re(\epsilon'/\epsilon)$ due to the Level 3 trigger was 0.20×10^{-4}.

9.2.2 Analysis Cuts

To determine the systematic uncertainty due to cuts applied in the neutral mode analysis, we studied the change in $Re(\epsilon'/\epsilon)$ as we varied cuts on the following variables: the minimum photon energy, minimum separation between photons, $\chi^2_{\pi^0}$, χ^2_{shape} and ring number. Each time a cut was changed, the data, Monte Carlo and background samples were re-analyzed and the background subtraction was repeated.

We varied the minimum photon energy cut between 2.0 GeV and 4.0 GeV and

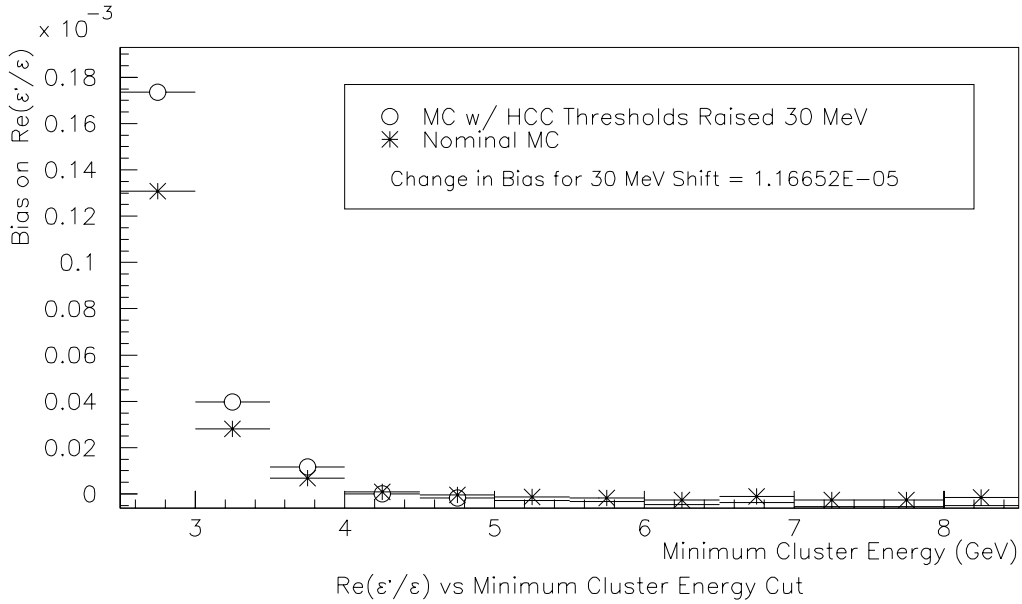

Figure 9.1: $Re(\epsilon'/\epsilon)$ bias as a function of minimum photon energy cut (GeV). The variation in the $Re(\epsilon'/\epsilon)$ bias arises from the sensitivity to the HCC thresholds. The "starry" points show the $Re(\epsilon'/\epsilon)$ bias using the nominal Monte Carlo while the open circles show the $Re(\epsilon'/\epsilon)$ bias when we raised the HCC thresholds for each channel by 30 MeV.

Cut Variable	Cut Value	$\Delta Re(\epsilon'/\epsilon)$ ($\times 10^{-4}$) wrt nominal value	Expected Statistical Error on $\Delta Re(\epsilon'/\epsilon)$ ($\times 10^{-4}$)
Minimum Photon Energy	3.0 GeV (default)	—	—
	2.0 GeV	-0.57	0.58
	2.5 GeV	-0.86	0.43
	3.5 GeV	0.33	0.48
	4.0 GeV	0.46	0.72

Table 9.1: Dependance of $Re(\epsilon'/\epsilon)$ on minimum photon energy cut. The nominal cut value was 3.0 GeV.

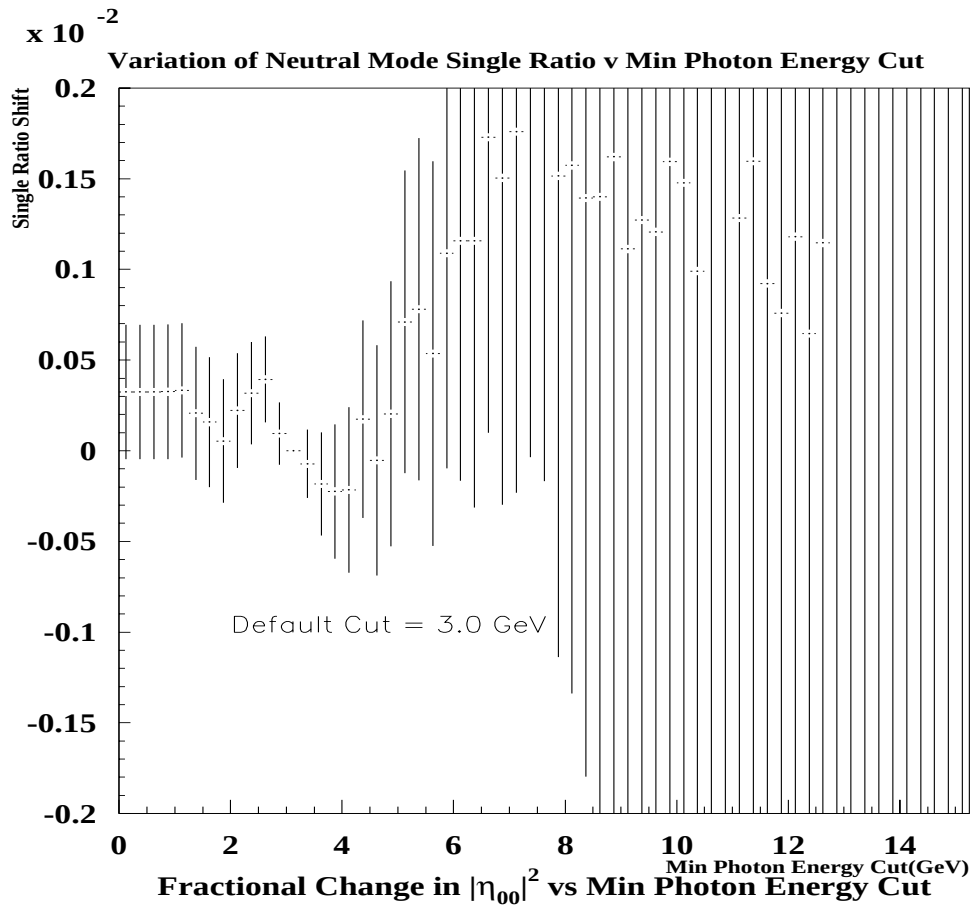

Figure 9.2: Variation of the neutral mode single ratio versus the minimum photon energy cut in 1997. The variation is shown with respect to the single ratio at the nominal cut value of 3.0 GeV.

measured the fractional change in the single ratio, $|\eta_{00}|^2$, to be $\sim 3 \times 10^{-4}$ as shown in Figure 9.2. The change in $Re(\epsilon'/\epsilon)$ as we varied the cut is presented in Table 9.1. The change in $Re(\epsilon'/\epsilon)$ was consistent with the expected statistical fluctuation, so we did not assign a systematic uncertainty due to the minimum photon energy cut.

The minimum photon separation cut was varied between 5 cm and 20 cm and the maximum change in $Re(\epsilon'/\epsilon)$ with respect to the nominal cut of 7.5 cm was $(0.59 \pm 0.68) \times 10^{-4}$. The bias in $Re(\epsilon'/\epsilon)$ due to this cut was very sensitive to the reconstruction of clusters which were close together. As described in Appendix C, we studied the reconstruction of close clusters in $K_{S,L} \to 2\pi^0$ data and Monte Carlo, and assigned a systematic uncertainty on $Re(\epsilon'/\epsilon)$ of 0.58×10^{-4} due to the reconstruction

of close clusters[2]. Since the maximum change in $Re(\epsilon'/\epsilon)$ due to variations of the minimum photon separation cut was consistent with the systematic error due to close clusters, we did not assign any additional systematic uncertainty on $Re(\epsilon'/\epsilon)$ for the minimum photon separation cut.

The ring number cut was varied between 100 and 150. In this region, the ring number distribution was sensitive to scattering in the regenerator, collmator and absorber. Although the data and Monte Carlo did not agree well for ring numbers between 100 and 150 as shown in Figure 9.3, the data-Monte Carlo differences were almost the same in both beams. Hence the largest change in $Re(\epsilon'/\epsilon)$ with respect to the nominal cut of 110 was only 0.24×10^{-4} as the ring number cut was varied. We assigned an uncertainty on $Re(\epsilon'/\epsilon)$ of 0.24×10^{-4} due to the ring number cut.

We varied the χ^2_{shape} cut by tightening the nominal cut, 48, to 25 as well as removing the cut completely. Based on this range of variations, the systematic uncertainty on $Re(\epsilon'/\epsilon)$ due to the χ^2_{shape} cut was 0.20×10^{-4}.

The largest variation of $Re(\epsilon'/\epsilon)$ as we varied the $\chi^2_{\pi^0}$ cut between 10 and 24 was 0.20×10^{-4} as shown in Table 9.2. Although the variation in $Re(\epsilon'/\epsilon)$ as we changed the $\chi^2_{\pi^0}$ cut to be between 10 and 24 was small, we see in Table 9.2 that $Re(\epsilon'/\epsilon)$ decreased by 1.47×10^{-4} with respect to the nominal analysis when we tightened the $\chi^2_{\pi^0}$ cut to 6. The large change in $Re(\epsilon'/\epsilon)$ when we varied the cut from 12 to 6 was partly due to a change in the acceptance which caused the data-Monte Carlo z_K slope to increase by 0.77×10^{-4}. We also observed that the data and Monte Carlo kaon energy distributions in the $K_{L,S} \to \pi^0\pi^0$ and $K_L \to \pi^0\pi^0\pi^0$ modes were very sensitive to the $\chi^2_{\pi^0}$ cut. Although the dependance of the acceptance on the $\chi^2_{\pi^0}$ cut is still not understood, since $Re(\epsilon'/\epsilon)$ is stable in the vicinity of the nominal cut, we assigned a systematic uncertainty on $Re(\epsilon'/\epsilon)$ of 0.20×10^{-4} due to the $\chi^2_{\pi^0}$ cut.

We summed the uncertainty contributions from the χ^2_{shape}, $\chi^2_{\pi^0}$ and ring number cuts in quadrature to obtain a total systematic error on $Re(\epsilon'/\epsilon)$ of 0.37×10^{-4} for analysis cuts in 1997. For the 1996 data set, the uncertainty on $Re(\epsilon'/\epsilon)$ due to analysis cuts was 0.33×10^{-4}.

---

[2]The uncertainty was included as part of the error due to CsI energy and position non-linearities.

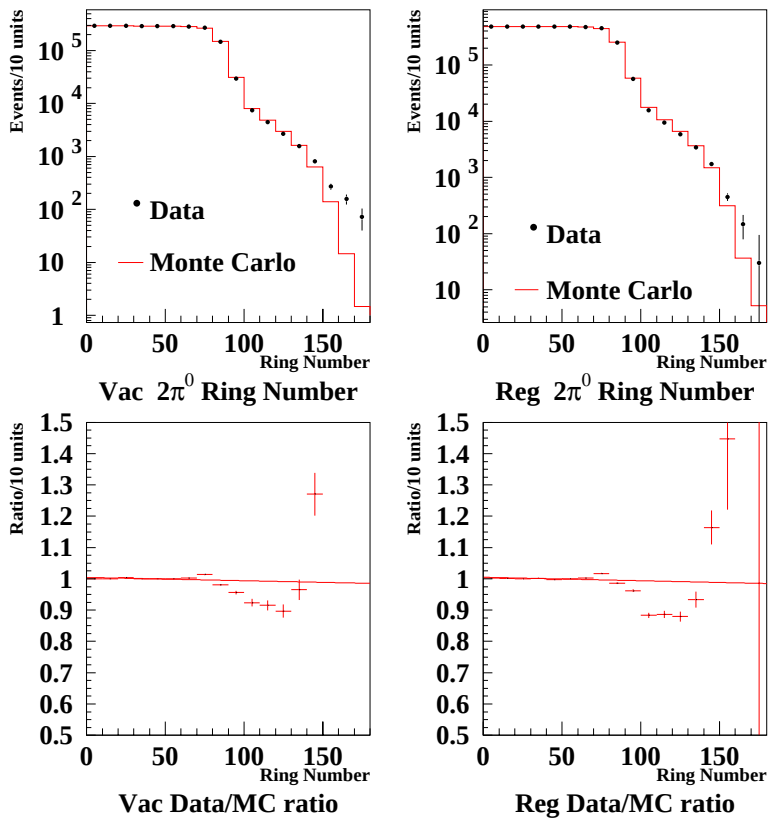

Figure 9.3: Data-Monte Carlo comparison of ring number in $K_{L,S} \to \pi^0\pi^0$ events in 1997. Although the data is background-subtracted, at ring numbers >150, there is hint of residual background.

$\chi^2_{\pi^0}$ Cut Value	$\Delta Re(\epsilon'/\epsilon)$ ($\times 10^{-4}$) wrt nominal value	Expected Statistical Error on $\Delta Re(\epsilon'/\epsilon)$ ($\times 10^{-4}$)	$\Delta Re(\epsilon'/\epsilon)$ ($\times 10^{-4}$) due to change in acceptance slope
12.0 (default)	—	—	—
6.0	-1.47	0.29	-0.92
10.0	-0.07	0.12	-0.13
14.0	0.21	0.06	0.02
24.0	0.20	0.14	0.12

Table 9.2: Dependance of $Re(\epsilon'/\epsilon)$ on $\chi^2_{\pi^0}$. The nominal cut value was 12.

9.2.3 Energy Scale

Energy scale differences along the decay region affected regenerator and vacuum beam events differently thereby causing a bias in $Re(\epsilon'/\epsilon)$. In order to assign an uncertainty on $Re(\epsilon'/\epsilon)$ due to the neutral mode energy scale, the variation of the energy scale over the decay region was determined by studying the effect of the energy scale correction on various decay modes that were sensitive to the neutral mode reconstruction. The data-Monte Carlo energy scale agreement in the $K_{L,S} \to \pi^0\pi^0$ mode was not considered because it was used to set the final energy scale as described in Section 7.3. To check the neutral mode energy scale at the regenerator, we compared the data and Monte Carlo $z_{2\pi^0}$ distributions at the downstream end of the regenerator using hadronic regenerator interactions, $K_L \to \pi^0\pi^0\pi^0$ and $K^* \to \pi^0 + K_S$ decays. At the downstream end of the decay region, the data-Monte Carlo energy scale agreement was studied using the $2\pi^0$ vertex from hadronic interactions in the vacuum window region, and the $\eta \to 3\pi^0$ vertex due to η produced in the vacuum window. $K_L \to \pi^+\pi^-\pi^0$ decays were used to study the variation of the energy scale over the entire decay volume. There was also a small data sample of $2\pi^0$ Dalitz decays which we used to check the energy scale at $z_K \sim$130 m.

The data-Monte Carlo $z_{2\pi^0}$ vertex agreement for the various decay modes is shown in Figure 9.4. After accounting for systematic uncertainties due to the production mechanisms of the different decay modes, we found that the data and Monte Carlo $z_{2\pi^0}$ distributions in the various decay modes agreed at the regenerator downstream edge. At the vacuum window, the data-Monte Carlo $z_{2\pi^0}$ agreement was not as good, with the largest data-Monte Carlo discrepancy being due to hadronic interactions in the vacuum window. The data-Monte Carlo $z_{2\pi^0}$ vertex difference due to hadronic interactions at the vacuum window was (1.89±0.41) cm and (2.46±0.37) cm for the 1996 and 1997 data sets, respectively. (See Figure 9.5.) In both data sets, the data reconstructed farther downstream than the Monte Carlo.

The systematic uncertainty due to the neutral mode energy scale was determined by considering the effect on $Re(\epsilon'/\epsilon)$ of an energy scale which varied linearly along the decay region as shown in Figure 9.4. The linear energy scale variation was chosen

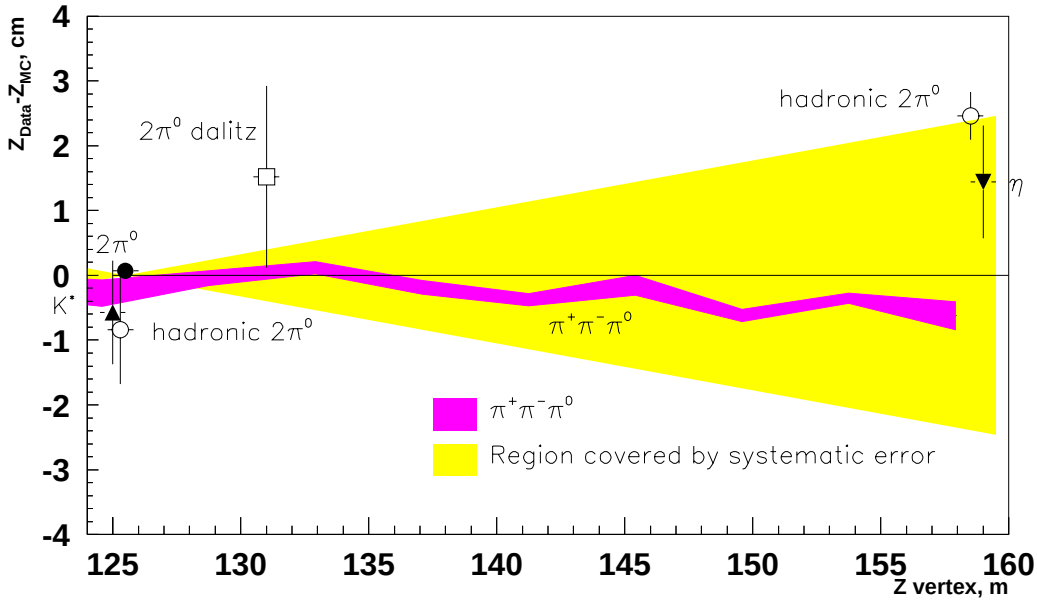

Figure 9.4: Data-Monte Carlo difference in the reconstructed vertex z-position for various modes as a function of vertex z-position. The error bars for $K_L \to \pi^+\pi^-\pi^0$ events are indicated by the width of the dark band. The region covered by the uncertainty on $Re(\epsilon'/\epsilon)$ due to the neutral mode energy scale is shown by the wide triangular band.

so that the data and Monte Carlo $z_{2\pi^0}$ distributions would be matched for hadronic vacuum window interactions while continuing to agree at the regenerator edge. Figure 9.5 shows the data-Monte Carlo $z_{2\pi^0}$ agreement for vacuum window hadronic interactions before and after the the linearly varying energy scale was applied.

After subtracting the effect of a small acceptance change, the change in $Re(\epsilon'/\epsilon)$ due to the linearly varying energy scale was 1.08×10^{-4} and 1.37×10^{-4} for the 1996 and 1997 data sets, respectively. We used this change in $Re(\epsilon'/\epsilon)$ as the systematic uncertainty due to the neutral mode energy scale. An extensive discussion of the neutral mode energy scale systematic error is presented in Appendix B.

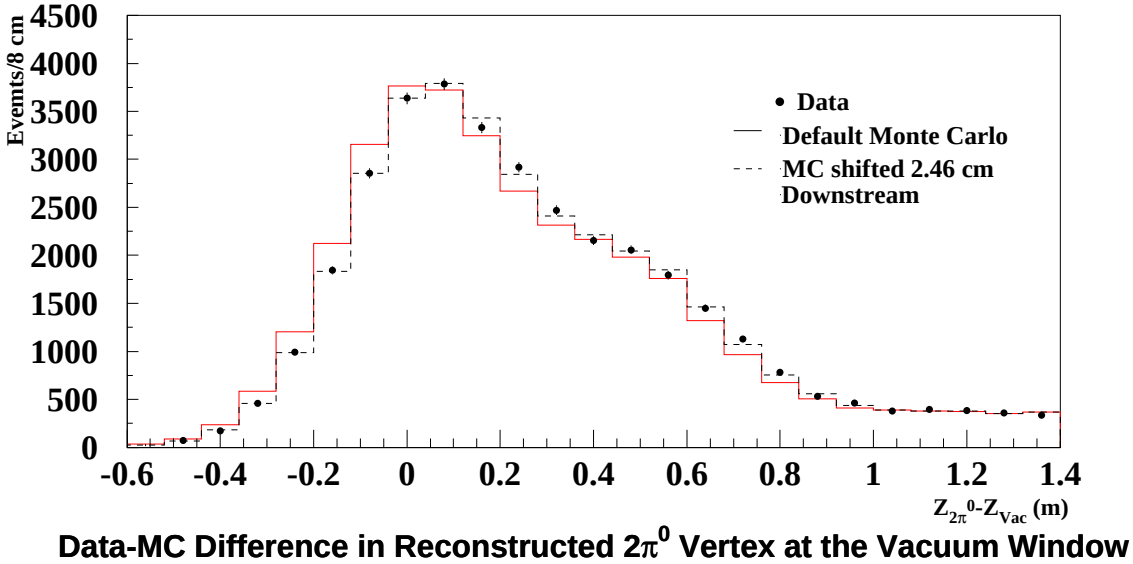

Figure 9.5: 1997 data (dark circles) and Monte Carlo $z_{2\pi^0}$ distributions for hadronic interactions at the vacuum window before (solid) and after (dashed) applying an energy scale which shifts the Monte Carlo $z_{2\pi^0}$ distribution at the vacuum window 2.46 cm downstream.

9.2.4 CsI Reconstruction and Energy Resolution

Based on hadronic interactions at the regenerator which produced $2\pi^0$, the photon energy resolutions in data and Monte Carlo were found to agree to better than 0.2% in quadrature. We smeared the Monte Carlo energy by 0.2% and observed a shift in $Re(\epsilon'/\epsilon)$ of 0.08×10^{-4}. We assigned this shift in $Re(\epsilon'/\epsilon)$ as the uncertainty due to the energy resolution in the $K \to \pi^0\pi^0$ mode.

To assign an uncertainty on $Re(\epsilon'/\epsilon)$ due to the photon energy and position reconstruction, we studied the effect on $Re(\epsilon'/\epsilon)$ of several energy and position-dependent reconstruction modifications which improved the $K_{L,S} \to \pi^0\pi^0$ data-Monte Carlo agreement in variables such as the kaon mass. These variables were very sensitive to the reconstruction of photon energies and positions. Based on the quadrature sum of the changes in $Re(\epsilon'/\epsilon)$ due to the different reconstruction modifications, we assigned a systematic uncertainty on $Re(\epsilon'/\epsilon)$ of 0.66×10^{-4}. The systematic uncertainty on

$Re(\epsilon'/\epsilon)$ due to the position and energy reconstruction was the same for the 1996 and 1997 data sets.

A detailed discussion of the energy and position nonlinearities in the reconstruction is presented Appendix C. The determination of the systematic error due to the nonlinearities in the neutral mode reconstruction is also described.

9.2.5 Acceptance

We determined the systematic error due to the neutral mode acceptance by comparing the data and Monte Carlo z_K distributions in the vacuum beam for $K_{L,S} \to \pi^0\pi^0$ and $K_L \to \pi^0\pi^0\pi^0$ events after applying all analysis cuts. Since the fit that was used to determine $Re(\epsilon'/\epsilon)$ (see Chapter 10) was performed in 10 GeV kaon energy bins, the z_K-distributions were weighted ("energy-reweighting") before comparing the data and Monte Carlo z_K distributions so that the data and Monte Carlo kaon energy distributions had the same shape when they were binned in 10 GeV bins.

The data-Monte Carlo z_K-comparisons after "energy-reweighting" of vacuum beam $K_{L,S} \to \pi^0\pi^0$ and $K_L \to 3\pi^0$ events in the combined 1996 and 1997 data sets are shown in Figure 9.6. There was a slope of $(0.60\pm0.53)\times10^{-4}$/m in the $2\pi^0$ channel and $(0.23\pm0.19)\times10^{-4}$/m in the $3\pi^0$ channel. Although the slopes were not significant, there was a small $K \to \pi^0\pi^0$ data-Monte Carlo discrepancy for $z_K < 122$ m, where the reconstruction was very sensitive to the MA aperture (see Figure 3.7) and the neutral mode energy scale. We did not assign a separate uncertainty due to the data-Monte Carlo z_K difference at $z_K < 122$ m because the systematic uncertainties assigned due to the size of the MA aperture and the energy scale accounted for this difference.

The systematic uncertainty in the neutral mode acceptance was assigned using the vacuum beam $K_L \to 3\pi^0$ z_K-slope because $K_L \to 3\pi^0$ decays were more sensitive than $K_{S,L} \to 2\pi^0$ events to most data-Monte Carlo acceptance differences. Since the mean z_K positions for the vacuum and regenerator beam $K_{L,S} \to \pi^0\pi^0$ distributions differed by 7.2 m (see Figure 7.18), a data-Monte Carlo z_K slope of $(0.23\pm0.19)\times10^{-4}$/m lead to an $Re(\epsilon'/\epsilon)$ bias of $(7.2\text{ m} \times (0.23\pm0.19)\times10^{-4}/\text{m})/6 = (0.28\pm0.23)\times10^{-4}$.

Based on this $Re(\epsilon'/\epsilon)$ bias, the systematic error on $Re(\epsilon'/\epsilon)$ due to the neutral mode acceptance for the combined 1996 and 1997 neutral datasets was assigned to be 0.39×10^{-4}.

Vacuum beam events were used to determine the systematic error due to the acceptance since the parameters such as the K_L lifetime which described the decay distribution were known with sufficient precision from previous experiments. Furthermore, unlike the regenerator beam, the vacuum beam decay distribution was almost flat over the decay volume. The regenerator beam z_K distribution was not suitable for studying the acceptance since the regenerator beam distribution depended on a precise knowledge of the regeneration and kaon parameters such as the K_S lifetime. By using the vacuum beam z_K distributions to determine the acceptance uncertainty, we have implicitly assumed that the data-Monte Carlo z_K differences were the same in both beams. Since the acceptance was essentially described by the detector geometry and the kinematics of the decay, this assumption was reasonable.

By using $K_L \to 3\pi^0$ decays, we assumed that the data-Monte Carlo acceptance differences in $K_L \to 3\pi^0$ and $K_{S,L} \to 2\pi^0$ analyses were the same. However, since the energy scale correction in the nominal analysis that was applied to $K_L \to 3\pi^0$ data events, $f^{Data}_{photons}(E_K))$, was based on the kaon energy, E_K, and derived using $K_{L,S} \to \pi^0\pi^0$ events, it was possible that the data-Monte Carlo acceptance agreement was different for $K_{S,L} \to 2\pi^0$ and $K_L \to 3\pi^0$ events. To study the effect of applying an energy scale correction that was E_K-dependent on the $K_L \to \pi^0\pi^0\pi^0$ data-Monte Carlo acceptance, we compared the 1997 $K_L \to \pi^0\pi^0\pi^0$ data-Monte Carlo z_K slope obtained using an E_K-independent ("flat") energy scale correction with the data-Monte Carlo z_K slope from the nominal $K_L \to 3\pi^0$ analysis. The difference between the $3\pi^0$ data-Monte Carlo z_K-slope, $(0.21\pm0.23)\times10^{-4}$/m, using a flat energy scale correction and the z_K-slope, $(0.01\pm0.22)\times10^{-4}$/m, obtained with the nominal $K_L \to 3\pi^0$ analysis was covered by the systematic error assigned due to acceptance; the quality (χ^2) of the data-Monte Carlo z_K agreements were consistent as well. Since the energy dependance of the scale correction did not affect the $K_L \to \pi^0\pi^0\pi^0$ data-Monte Carlo z_K agreement noticeably, we concluded that there was no significant acceptance difference between $K_L \to 3\pi^0$ and $K_{S,L} \to 2\pi^0$ events due to the energy

scale correction.

9.2.6 Calorimeter Size and CsI Position Bias

To determine the uncertainty in the size of the CsI calorimeter, we compared the positions of extrapolated electron and muon tracks with the electron and muon positions determined using the calorimeter. Electron tracks from the 1996 K_{e3} sample were extrapolated to the mean (energy-dependent) shower depth in the calorimeter, and compared to the electron cluster positions which depended on the calorimeter survey measurement as well as the cluster reconstruction. To determine the uncertainty in the CsI size with muons, we used muons from special runs that had the analysis magnet turned off. The track positions of muons that were at crystal boundaries were compared to the crystal positions which were based on the survey. From these studies of the CsI size, we found that the uncertainty in the calorimeter size was 0.5 mm in the horizontal dimension and $\sim$1 mm in the vertical dimension.

To assign an error on $Re(\epsilon'/\epsilon)$ due to the CsI size uncertainty, we studied the effect on $Re(\epsilon'/\epsilon)$ of a change in the the calorimeter size using the Monte Carlo simulation. Based on the change in $Re(\epsilon'/\epsilon)$ due to a 1 mm change in both the horizontal and vertical dimensions of the calorimeter, we assigned a systematic error of 0.15×10^{-4} due to the CsI size.

Although there were systematic errors assigned for cluster position and energy nonlinearities, we assigned an additional error due to the cluster position determination within a seed block. The local position bias was determined from the electron track-cluster mismatch seen in data $K_L \to \pi^{\pm}e^{\mp}\nu$ events. Although we attempted to account for track-cluster mis-matches in the Monte Carlo fully, there was still a residual position bias. The uncertainty on $Re(\epsilon'/\epsilon)$ due to this bias was 0.35×10^{-4}.

9.2.7 Apertures

The sizes of the CA and MA apertures were determined using K_{e3} and $K_L \to \pi^0\pi^0\pi^0$ events in 1996. Using K_{e3} events, the average data-Monte Carlo difference in the (total) sizes of the CA and MA apertures were (26$\pm$106) μm and (2$\pm$86) μm, re-

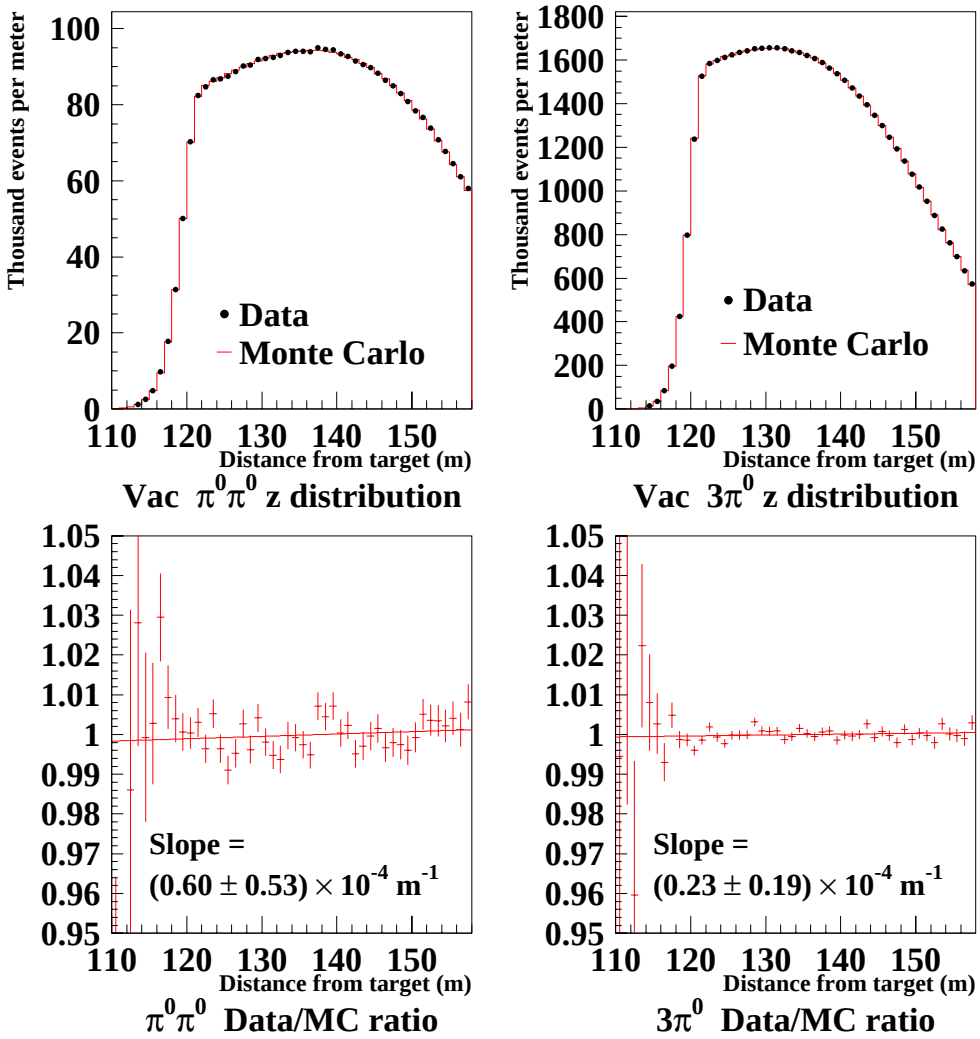

Figure 9.6: Data-Monte Carlo comparison of kaon vertex z-distributions after energy reweighting in $K_{L,S} \to \pi^0\pi^0$ and $K_L \to \pi^0\pi^0\pi^0$ vacuum beam events. Both 1996 and 1997 data sets have been combined. Background has been subtracted from the $K_{L,S} \to \pi^0\pi^0$ data sample.

spectively. From the studies of $K_L \to 3\pi^0$ z_K distributions upstream of the MA, the data-Monte Carlo difference in the MA size was (12±50) μm.

The effect on $Re(\epsilon'/\epsilon)$ of changing the MA and CA aperture sizes was investigated using Monte Carlo $2\pi^0$ events. A 50 μm change in the total size of each CA aperture caused a change in $Re(\epsilon'/\epsilon)$ of $(0.15\pm0.03)\times10^{-4}$ and a 200 μm change in the MA aperture resulted in a $(0.58\pm0.02)\times10^{-4}$ change in $Re(\epsilon'/\epsilon)$. Based on the effect of a 132μm (=26+106 μm) change in each CA aperture, we assigned an uncertainty of 0.42×10^{-4} due to the CA size. The systematic uncertainty on $Re(\epsilon'/\epsilon)$ due to the size of the MA aperture was assigned to be 0.18×10^{-4} based on a 62 μm (=12+50 μm) change in the size of each MA aperture.

The effect on $Re(\epsilon'/\epsilon)$ of a shift in the CA and MA positions was negligible.

9.2.8 Background

The total systematic error on $Re(\epsilon'/\epsilon)$ due to the neutral mode background was 1.14×10^{-4} and 1.06×10^{-4} in the 1996 and 1997 data sets, respectively. The systematic error was dominated by the uncertainty on $Re(\epsilon'/\epsilon)$ due to regenerator scatters. The different contributions to the uncertainty are presented in Table 9.3.

We will describe the systematic uncertainty on $Re(\epsilon'/\epsilon)$ due to regenerator scatters in the following section and then discuss the systematic error due to the other background sources in a separate section.

Regenerator Scatters

Since the regenerator scattering simulation was derived from the the distribution of $K_{L,S} \to \pi^+\pi^-$ decays with large p_T^2 (p_T^2 >2000 MeV^2/c^2), the uncertainty due to the regenerator scattering background depended on the p_T^2 acceptance, the charged mode analysis and reconstruction, the agreement between the p_T^2 fit and the $K_{L,S} \to \pi^+\pi^-$ data distributions at large transverse momentum, and differences between the charged and neutral mode analyses that affect the regenerator scattering background.

To determine the systematic error due to the p_T^2 acceptance, we compared the data and Monte Carlo $\pi^+\pi^-$ track p_T^2 distributions using $K_L \to \pi^+\pi^-\pi^0$ events. We

Background Source	Systematic Uncertainty($\times 10^{-4}$) 1996	1997
Regenerator Scatters:		
p_T^2 Acceptance	0.40	0.40
Charged Mode Backgrounds	0.20	0.20
$\pi^+\pi^-$ Reconstruction	0.75	0.75
Fit Procedure	0.30	0.30
Fit Quality	0.40	0.40
Veto Efficiency Differences	0.50	0.30
Collimator Scatters	0.10	0.10
$K_L \to \pi^0\pi^0\pi^0$ Background	0.10	0.06
Hadronic Regenerator Interactions	0.05	0.05
Other Mis-reconstructed Backgrounds	0.10	0.10
Total	1.14	1.06

Table 9.3: Systematic Errors due to Background in the $K_{L,S} \to \pi^0\pi^0$ Analysis.

found that the data-Monte Carlo agreement was good to 0.49 GeV^{-2}, corresponding to an uncertainty in $Re(\epsilon'/\epsilon)$ of 0.4×10^{-4}.

The charged mode analysis cuts affected the p_T^2 distribution and this, in turn, affected the regenerator scattering simulation and hence, $Re(\epsilon'/\epsilon)$. To study the effect of the $K_{L,S} \to \pi^+\pi^-$ analysis cuts on the p_T^2 distribution, we varied the cuts about their nominal values. The variation in the regenerator ADC cut between 12 MeV and 20 MeV was seen to cause the largest change in $Re(\epsilon'/\epsilon)$. (The nominal regenerator ADC cut corresponded to 8 MeV energy.) Based on the largest change in $Re(\epsilon'/\epsilon)$ seen in the cut variations, we assigned an uncertainty on $Re(\epsilon'/\epsilon)$ of 0.75×10^{-4} due to the dependance of regenerator scatter simulation on the p_T^2 reconstruction.

The effect of semi-leptonic background, collimator scatters and the coherent $K_{L,S} \to \pi^+\pi^-$ tail on the $\pi^+\pi^-$ data sample at large p_T^2 was determined by varying the amount of collimator scatters, semi-leptonic background and coherent tail by 15%, 20% and 50%, respectively. The total change in $Re(\epsilon'/\epsilon)$, 0.20×10^{-4}, was obtained by summing in quadrature the effect of changing each background level individually.

The systematic effects on $Re(\epsilon'/\epsilon)$ due to the p_T^2 fitting procedure (see Sec-

tion 6.4.1) used to determine the regenerator scattering simulation was determined by varying fitting parameters such as the bin size and kinematic region of the fit. The fitting procedure was stable to most variations. The largest variation was due to changing the p_T^2 binning; this led to an uncertainty on $Re(\epsilon'/\epsilon)$ of 0.3×10^{-4} which we assigned as the systematic error due to the fitting procedure.

The agreement between the $K_{L,S} \to \pi^+\pi^-$ data and the p_T^2 fit was good to 2.5% over the 40 GeV to 160 GeV kaon energy range as shown in Figure 9.7. Based on the effect on $Re(\epsilon'/\epsilon)$ of a 2.5% variation in the overall normalization for the regenerator scattering background, we assigned an uncertainty in $Re(\epsilon'/\epsilon)$ of 0.4×10^{-4} due to the agreement between the $\pi^+\pi^-$ data and p_T^2 fit.

The charged and neutral mode analyses had different efficiencies for rejecting inelastic regenerator scatters since the BA and HA were only used in the neutral mode analysis. The BA and HA affected the amount of inelastic regenerator scatters but had no effect on diffractive scatters, so the level of diffractive regenerator scatters was the same in charged and neutral modes. To account for this charged-neutral mode difference in veto efficiencies, we studied the effect on $Re(\epsilon'/\epsilon)$ due to a neutral mode background subtraction scheme in which both inelastic and diffractive backgrounds were normalized together using the ring number sidebands. We found that the $Re(\epsilon'/\epsilon)$ changed by 0.3×10^{-4} with respect to the nominal analysis, where the normalization for diffractive scatters was obtained from the p_T^2 fit and inelastic scatters were normalized based on the neutral mode ring number sidebands. We assigned an uncertainty on $Re(\epsilon'/\epsilon)$ of 0.3×10^{-4} due to the veto efficiency differences in 1997. In the 1996 analysis, the larger difference between the charged and neutral mode veto efficiencies led to a correspondingly greater uncertainty in $Re(\epsilon'/\epsilon)$ of 0.5×10^{-4}.

The total systematic error on $Re(\epsilon'/\epsilon)$ due to the regenerator scattering background was obtained by adding in quadrature the uncertainties due to the various contributions shown in Table 9.3. The uncertainty on $Re(\epsilon'/\epsilon)$ due to regenerator scatters was 1.12×10^{-4} and 1.05×10^{-4} in the 1996 and 1997 neutral mode analyses, respectively.

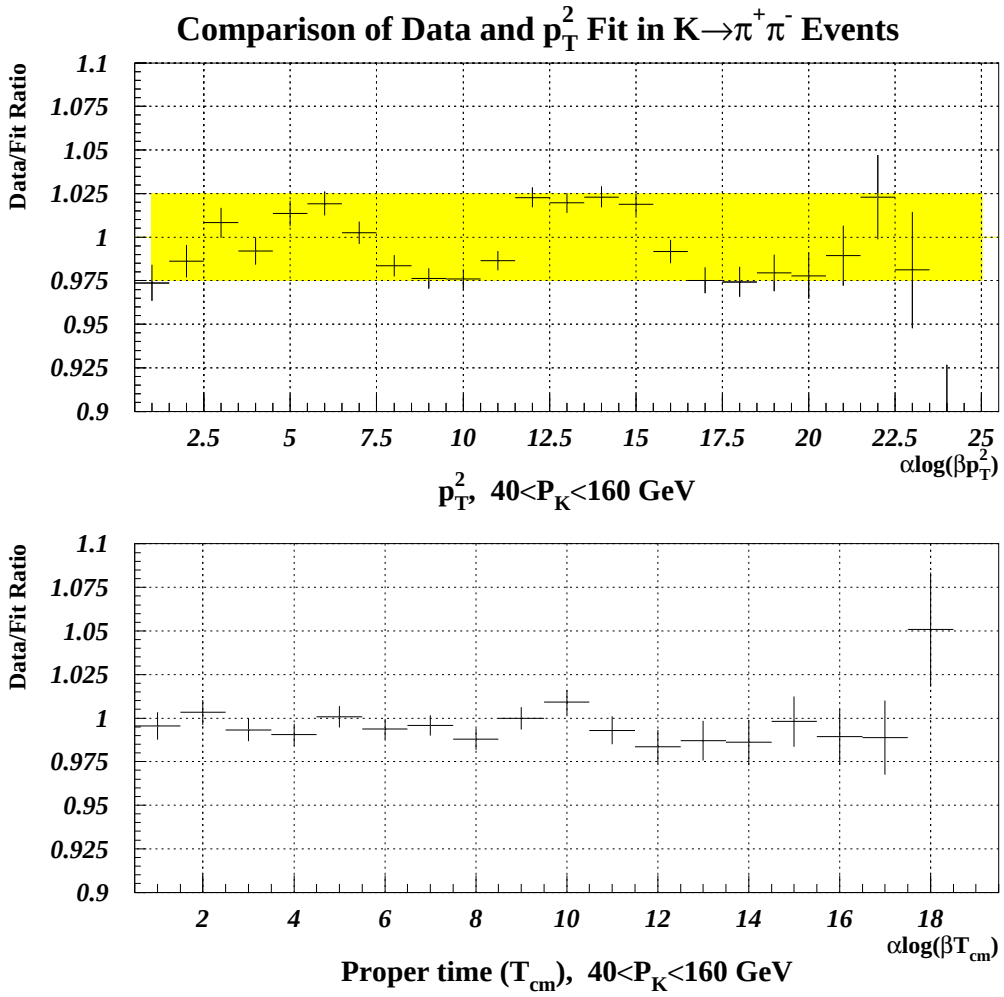

Figure 9.7: Comparison of $K_{L,S} \to \pi^+\pi^-$ and p_T^2 fit used in the regenerator scattering simulation. Top:The ratio of the data and fit p_T^2 distributions for kaons with momentum between 40 GeV and 160 GeV. The horizontal axis is a logarithmic function of the $\pi^+\pi^-$ p_T^2 with bins 6 and 16 corresponding to p_T^2 of 0.01 and 0.1 GeV$^2/c^2$, respectively. The dark band indicates the $\pm 2.5\%$ variation in the data/fit ratio which was used to assign the systematic uncertainty on $Re(\epsilon'/\epsilon)$ due to the agreement between the data and the fit. Bottom: The variation in the ratio of the data and p_T^2 fit distribution as a function of the kaon proper time, T_{cm}. The horizontal axis is a logarithmic function of T_{cm} with bin 7 corresponding to one K_S lifetime.

Other Backgrounds

The systematic uncertainty due to the collimator scatters was based on the uncertainty in the normalization with respect to coherent scatters. We conservatively assigned 15% as the normalization uncertainty. This corresponded to a systematic error of 0.1×10^{-4} on $Re(\epsilon'/\epsilon)$.

In the analysis of the 1997 $K_{L,S} \to \pi^0\pi^0$ data set, the systematic uncertainty on $Re(\epsilon'/\epsilon)$ due to $K_L \to \pi^0\pi^0\pi^0$ background was determined by comparing the nominal background subtraction method, which simulated the $K_L \to \pi^0\pi^0\pi^0$ and hadronic regenerator interaction backgrounds, to a background subtraction scheme that estimated the backgrounds due to mis-identified events by averaging the distributions in the $2\pi^0$-mass sidebands. The change in $Re(\epsilon'/\epsilon)$, 0.06×10^{-4}, was used as the uncertainty in $Re(\epsilon'/\epsilon)$ due to the $K_L \to \pi^0\pi^0\pi^0$ background. In the analysis of the 1996 data set, the assigned uncertainty on $Re(\epsilon'/\epsilon)$ due to $K_L \to 3\pi^0$ background was 0.10×10^{-4} and it was based on the effect of varying the veto cuts on $Re(\epsilon'/\epsilon)$.

The effect on $Re(\epsilon'/\epsilon)$ of not subtracting the background due to hadronic interactions in the regenerator was 0.05×10^{-4}. We assigned this value as the uncertainty on $Re(\epsilon'/\epsilon)$ due to the hadronic regenerator interaction background. The systematic uncertainty due to other mis-reconstructed decays such as $K \to \pi^0\gamma\gamma$ and $\Xi \to \Lambda\pi^0$, where Λ decays to $n\pi^0$, was determined using the bias on $Re(\epsilon'/\epsilon)$ due to these decays. The systematic error on $Re(\epsilon'/\epsilon)$ was 0.10×10^{-4}.

9.2.9 Accidentals

There was good agreement between the Monte Carlo with accidental events and the data in quantities which were sensitive to underlying event activity such as the number of software clusters. Based on studies of Monte Carlo samples with and without accidental events, the Monte Carlo predicted a small bias due to accidental events, $\Delta Re(\epsilon'/\epsilon) = (0.51\pm0.14)\times10^{-4}$. This bias was consistent with the acceptance change and energy nonlinearity caused by accidental activity. Since we have already assigned uncertainties due to the acceptance and energy nonlinearities, no additional systematic error was included for accidental activity in neutral mode events.

9.2.10 Summary of Neutral Mode Systematic Errors

The total uncertainty on $Re(\epsilon'/\epsilon)$ due to the $K_{L,S} \rightarrow \pi^0\pi^0$ trigger, reconstruction and analysis was 2.13×10^{-4} and 2.01×10^{-4} for the 1996 and 1997 data sets, respectively. Table 9.4 presents the systematic errors for the 1996 and 1997 data sets as well as for the combined data set. The statistical error due to the Monte Carlo is presented as well. In most cases, the systematic errors were combined by taking the weighted mean of the errors from both years. For the systematic uncertainty due to the acceptance and neutral mode energy scale, we calculated the weighted average of the data-Monte Carlo z_K-slopes and discrepancies at the vacuum window, respectively, before determining the systematic error for the combined data set. The total systematic uncertainty on $Re(\epsilon'/\epsilon)$ due to the combined 1996 and 1997 $K_{L,S} \rightarrow \pi^0\pi^0$ analysis was 1.97×10^{-4}; this led to a total error of 2.00×10^{-4} when we included the error due to the $K_{L,S} \rightarrow \pi^0\pi^0$ Monte Carlo statistics.

9.3 Charged Mode Systematic Studies

The systematic uncertainties in the charged mode will be described briefly. A detailed discussion can be found in [39]. As in the neutral mode, the systematic errors were divided into several broad categories.

9.3.1 Triggers

The systematic uncertainty for the Level 1 and 2 charged mode triggers were determined from the trigger inefficiencies measured using K_{e3} events[3]. Based the $Re(\epsilon'/\epsilon)$ bias that was expected due to the trigger inefficiencies, the systematic errors on $Re(\epsilon'/\epsilon)$ were assigned to be 0.33×10^{-4} and 0.22×10^{-4} in the 1997a and 1997b data sets, respectively.

The Level 3 uncertainty was determined from a sample of events in which the Level 3 requirement was not applied. From the vacuum to regenerator beam ratio of

[3] K_{e3} events were used instead of $K_{L,S} \rightarrow \pi^+\pi^-$ events to reduce the statistical error on the trigger inefficiencies.

events that passed all offline cuts but failed Level 3, the systematic error on $Re(\epsilon'/\epsilon)$ was measured to be 0.42×10^{-4} in 1997a and 0.58×10^{-4} in 1997b.

9.3.2 Drift Chamber Simulation

The systematic error due to the drift chamber simulation was divided into two categories: uncertainties due to the simulation of inherent drift chamber inefficiencies and uncertainties due to the simulation of inefficiencies due to accidental events. By comparing the "high-SOD" and missing hit inefficiency rates in data and Monte Carlo, we assigned an uncertainty of 0.21×10^{-4} on $Re(\epsilon'/\epsilon)$ due to inherent drift chamber inefficiencies.

To determine the uncertainty due to accidental effects, correlated Monte Carlo samples were used to study the effect of extra hits in the drift chambers. The systematic error on $Re(\epsilon'/\epsilon)$ due to accidental effects was 0.3×10^{-4}.

The total systematic uncertainty on $Re(\epsilon'/\epsilon)$ due to the drift chamber simulation, 0.37×10^{-4}, was determined by adding the two contributions in quadrature. The systematic error was the same in both 1997a and 1997b samples.

9.3.3 DC Resolution

The data and Monte Carlo drift chamber resolutions agreed to within 5% of themselves. This led to a systematic uncertainty on $Re(\epsilon'/\epsilon)$ of 0.15×10^{-4} which was common to both 1997a and 1997b data sets.

9.3.4 Momentum Scale

The charged mode momentum scale was set by the analysis magnet kick and tuned to the kaon mass using $K \to \pi^+\pi^-$ events. The uncertainty due to the momentum scale was assigned based on the kaon mass resolution and the comparison of the kaon mass in data, Monte Carlo and the nominal Particle Data Group value. The systematic error was 0.16×10^{-4} and was common to both 1997a and 1997b samples.

9.3.5 Acceptance

The systematic error due to the charged mode acceptance was based on the data-Monte Carlo agreement in the reconstructed z_K distribution of vacuum beam $K_{L,S} \to \pi^+\pi^-$ decays. Figure 9.8 shows the comparison of the data and Monte Carlo $K_{L,S} \to \pi^+\pi^-$ z_K distributions for the full 1997 dataset. There was a slope in the ratio of data and Monte Carlo z_K distributions of (-0.82±0.30)×10^{-4}/m. The data-Monte Carlo z_K agreement in the $K_{L,S} \to \pi^+\pi^-$ channel was cross-checked using $K_L \to \pi^\pm e^\mp \nu$ decays. $K_L \to \pi^\pm e^\mp \nu$ decays were not used to set the systematic error due to the acceptance because of the different particle types in the final state. As shown in Figure 9.8, the data and Monte Carlo z_K distributions agreed very well in the K_{e3} channel.

Since the difference in the average $K_{L,S} \to \pi^+\pi^-$ vertex positions between the vacuum and regenerator beams was 5.6 m, the bias in $Re(\epsilon'/\epsilon)$ due to the z_K-slope was (5.6 m × (-0.82±0.30)×10^{-4}/m)/6 = (-0.77±0.28)×10^{-4}. Based on the bias in $Re(\epsilon'/\epsilon)$ due to the $K_{L,S} \to \pi^+\pi^-$ data-Monte Carlo z_K-slope, the uncertainty on $Re(\epsilon'/\epsilon)$ due to the acceptance was 0.90×10^{-4} for the combined 1997 charged mode data set. The systematic uncertainty on $Re(\epsilon'/\epsilon)$ was 0.53×10^{-4} in the 1997b sample compared to 2.22×10^{-4} in the 1997a sample since the data-Monte Carlo z_K agreement was much better in the 1997b sample.

The z_K distribution for vacuum beam $K_{L,S} \to \pi^+\pi^-$ events was sensitive to K_S produced in the target. Floating the level of primary K_S in the $Re(\epsilon'/\epsilon)$ fit (see Chapter 10) suggested that the Monte Carlo simulation generated too few primary K_S. Since increasing the amount of primary K_S improved the data-Monte Carlo z_K agreement, the systematic error due to the charged mode acceptance that was assigned accounted for the uncertainty in the level of primary K_S.

9.3.6 Analysis Cuts

We studied the effect on $Re(\epsilon'/\epsilon)$ of p_T^2 and invariant $\pi^+\pi^-$-mass cut variations in the data and Monte Carlo after accounting for changes in the data-Monte Carlo z_K-ratio. Systematic errors on $Re(\epsilon'/\epsilon)$ of 0.19×10^{-4} and 0.25×10^{-4} were assigned to the 1997a

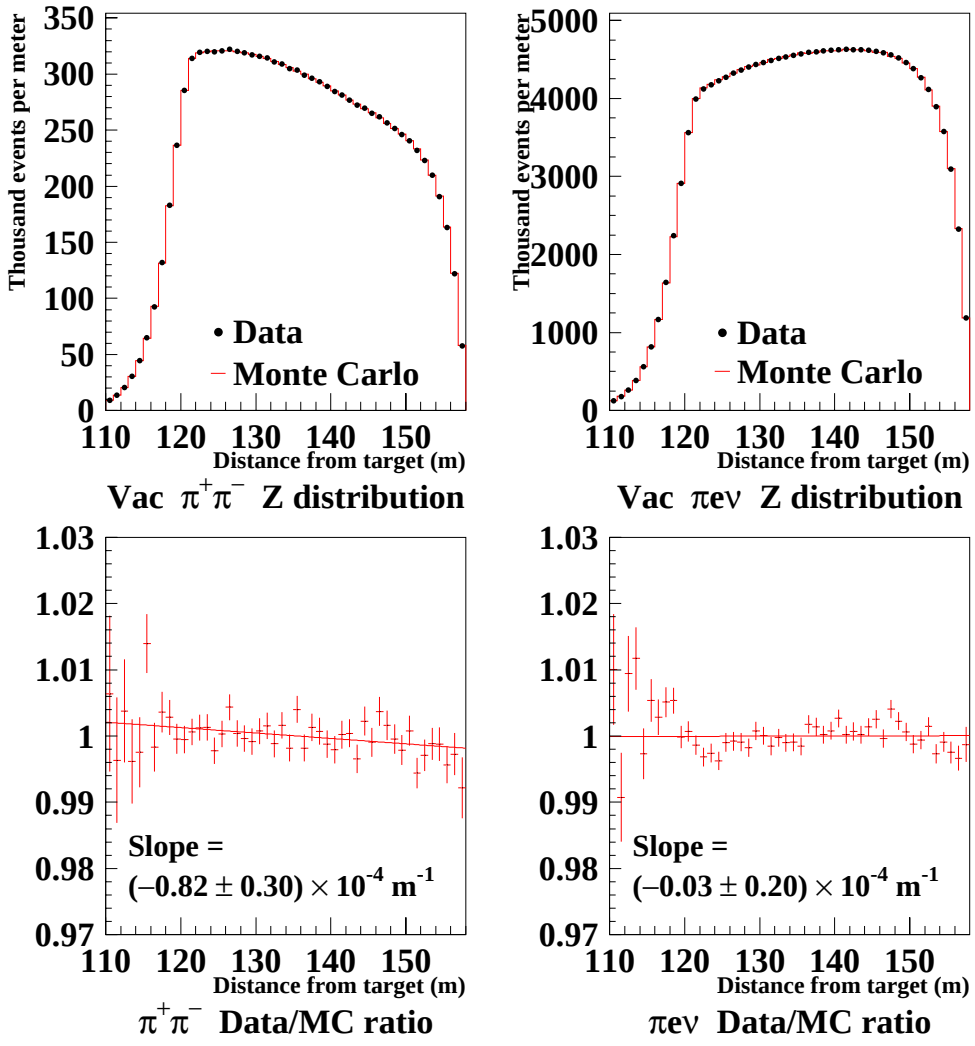

Figure 9.8: Data-Monte Carlo comparison of kaon vertex z-distributions after energy reweighting in $K_{L,S} \to \pi^+\pi^-$ and $K_L \to \pi^\pm e^\mp \nu$ vacuum beam events. The 1997a and 1997b data sets have been combined and background has been subtracted.

and 1997b charged mode analyses, respectively.

9.3.7 Detector Alignment and Calibration

The systematic error on $Re(\epsilon'/\epsilon)$ due to the the spectrometer alignment and calibration was based on the uncertainty in the drift chamber positions and the data-Monte Carlo difference in the drift chamber cell size (see Figure 3.6). The data-Monte Carlo difference in the cell size measurement affected $Re(\epsilon'/\epsilon)$ via the track separation cut. The uncertainty on $Re(\epsilon'/\epsilon)$ due to the relative data-Monte Carlo cell size was 0.22×10^{-4}. The error on $Re(\epsilon'/\epsilon)$ due to the uncertainty in the drift chamber position and alignment was assigned to be 0.18×10^{-4}, The total error on $Re(\epsilon'/\epsilon)$ due to the spectrometer alignment and calibration was 0.28×10^{-4}. The error was the same for both 1997a and 1997b data samples.

9.3.8 Limiting Apertures

The total systematic uncertainty on $Re(\epsilon'/\epsilon)$ due to apertures in the charged mode analysis was the quadrature sum of the uncertainty due to close track inefficiences and the uncertainty due to the position of the effective regenerator edge.

Inefficiencies caused by the reconstruction of close tracks affected the track separation cut. Hence, to determine the effect of close track reconstruction inefficiencies, we measured the bias on $Re(\epsilon'/\epsilon)$ when we varied the track separation cut. We found that there was no significant change in $Re(\epsilon'/\epsilon)$ if we required tracks to be more than three cells apart. As a result, the systematic error due to close tracks was assigned based on the statistical precision of measuring the bias on $Re(\epsilon'/\epsilon)$. The uncertainty on $Re(\epsilon'/\epsilon)$ due to the reconstruction of close tracks was 0.40×10^{-4} in 1997a, 0.26×10^{-4} in 1997b and 0.22×10^{-4} for the full 1997 data set.

The effective regenerator edge for $K_{L,S} \to \pi^+\pi^-$ decays was determined to be (1.65 ± 0.45) mm upstream of the downstream physical edge of the regenerator. The error on $Re(\epsilon'/\epsilon)$ due to the 0.45 mm uncertainty in the effective regenerator edge position was 0.20×10^{-4}.

The total systematic uncertainty on $Re(\epsilon'/\epsilon)$ due to charged mode apertures was 0.45×10^{-4} and 0.33×10^{-4} in the 1997a and 1997b data samples, respectively.

9.3.9 Background Subtraction

The background levels were varied by $\pm10\%$ and the background subtraction procedure was tested. We assigned a systematic error on $Re(\epsilon'/\epsilon)$ of 0.20×10^{-4} which was the same in 1997a and 1997b.

9.3.10 Summary of Charged Mode Systematic Errors

The systematic errors for the 1997a and 1997b data sets, as well as the combined 1997 data set are presented in Table 9.5. The total systematic errors due to the $K_{L,S} \to \pi^+\pi^-$ analysis of the 1997a and 1997b data sets were 2.40×10^{-4} and 1.07×10^{-4}, respectively. Including the statistical error due to the Monte Carlo, the total error on $Re(\epsilon'/\epsilon)$ due to the charged mode in 1997 was 1.28×10^{-4}.

Source	$\Delta Re(\epsilon'/\epsilon)$ $(\times 10^{-4})$			Comments
	1996	1997	Combined	
L1 trigger	0.07	0.19	0.10	Weighted Mean
L2 trigger	0.20	0.12	0.13	Weighted Mean
L3 filter	0.20	0.05	0.08	Weighted Mean
Energy Scale	1.08	1.37	1.27	Weight Vacuum Window Shifts
CsI Resolution and Reconstruction	0.66	0.66	0.66	Weighted Mean
Analysis Cuts	0.33	0.37	0.37	Weighted Mean
Background	1.14	1.06	1.07	Weighted Mean
z-slope	1.04	0.26	0.39	Weighted Z-slope
CA aperture	0.42	0.42	0.42	Common
MA aperture	0.18	0.18	0.18	Common
CsI size	0.15	0.15	0.15	Common
CsI position	0.35	0.35	0.35	Common
TOTAL	2.13	2.01	1.97	
MC Statistics	0.55	0.49	0.37	
TOTAL with MC Statistics	2.20	2.07	2.00	

Table 9.4: Summary of $Re(\epsilon'/\epsilon)$ systematic uncertainties from the 1996, 1997 and combined neutral mode datasets. The rightmost column indicates how the 1996 and 1997 systematic errors were combined for the full neutral mode data set. Errors which were the same in the 1996 and 1997 neutral mode analyses were indicated by the term, "common", in the "Comments" column.

Source of uncertainty	Uncertainty on $Re(\epsilon'/\epsilon)$ ($\times 10^{-4}$) due to $K_{L,S} \to \pi^+\pi^-$ mode		
	1997a	1997b	Full 1997
Level 1,2,3 Trigger	0.53	0.62	0.56
Drift Chamber Simulation	0.37	0.37	0.37
Drift Chamber Resolution	0.15	0.15	0.15
Momentum Scale	0.16	0.16	0.16
Analysis Cuts	0.19	0.25	0.23
z_K-slope	2.22	0.53	0.90
Detector Calibration, Alignment	0.28	0.28	0.28
Limiting Apertures	0.45	0.33	0.30
Background Subtraction	0.20	0.20	0.20
Total Systematic Error	2.40	1.07	1.25
Monte Carlo Statistics	0.48	0.33	0.27
Total Error	2.45	1.12	1.28

Table 9.5: Table of systematic errors and Monte Carlo statistical errors on $Re(\epsilon'/\epsilon)$ in the 1997a, 1997b and combined 1997 $K_{L,S} \to \pi^+\pi^-$ data samples.

CHAPTER 10
DETERMINATION OF $RE(\epsilon'/\epsilon)$

This chapter describes how $Re(\epsilon'/\epsilon)$ was determined from the acceptance-corrected $K \to 2\pi$ data. The measured value of $Re(\epsilon'/\epsilon)$ and various cross-checks of the measurement will be presented. We will also discuss the measurement of other important kaon parameters such as Δm, τ_S and $\Delta\phi$.

10.1 Extracting $Re(\epsilon'/\epsilon)$

Once the $K \to 2\pi$ background-subtracted data samples had been obtained and the acceptance has been determined using the Monte Carlo simulation, we were ready to measure $Re(\epsilon'/\epsilon)$. We could determine the ratio of $K_{L,S} \to \pi^+\pi^-$ and $K_{L,S} \to \pi^0\pi^0$ decays in the vacuum and regenerator beams,

$$R = \frac{(N_{vac}(K_L \to \pi^+\pi^-)/A_{vac}(K_S \to \pi^+\pi^-)) \,/\, (N_{reg}(K_L \to \pi^+\pi^-)/A_{reg}(K_S \to \pi^+\pi^-))}{(N_{vac}(K_L \to \pi^0\pi^0)/A_{vac}(K_S \to \pi^0\pi^0)) \,/\, (N_{reg}(K_L \to \pi^0\pi^0)/A_{reg}(K_S \to \pi^0\pi^0))}, \tag{10.1}$$

where N and A represent the number of data events and acceptance, respectively and use R to extract $Re(\epsilon'/\epsilon)$ based on Equation 1.26, with $Re(\epsilon'/\epsilon) \approx \frac{1}{6}R - 1$. Such an approach assumed that the regenerator beam only contained K_S. However, in reality, the regenerator beam contained both K_S and K_L decays, so not only was there a small amount of $K_L \to 2\pi$ decays but there was an interference between the amplitudes. The effect of the interference is clearly seen in Figure 10.1, which shows the regenerator beam $K_{L,S} \to \pi^+\pi^-$ z_K distribution in data and the z_K distribution that would have been expected in the absence of interference.

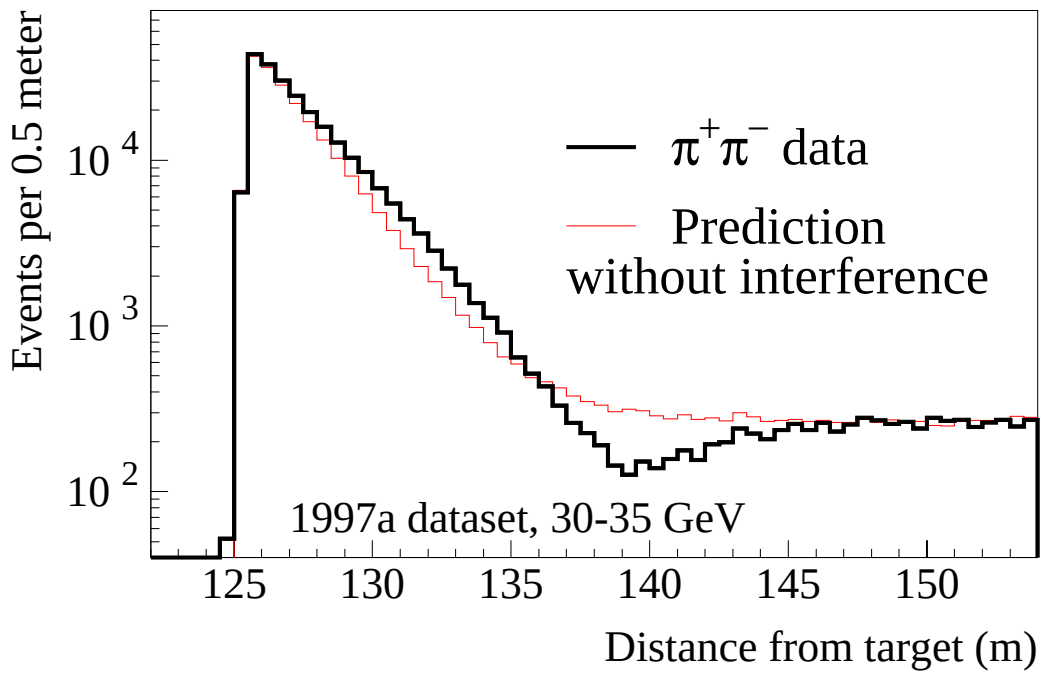

Figure 10.1: Kaon decay vertex z-distributions of $K_{L,S} \to \pi^+\pi^-$ data in the regenerator beam and the distribution expected in the absence of the intereference of amplitudes.

10.1.1 The Prediction Function

To account for the interference in amplitudes, $K_L \to 2\pi$ decays in the regenerator beam, and the small amount of high-energy K_S in the vacuum beam, the data were fitted to a prediction function which evolved the kaon states from the target. The prediction function determined the relative production of K^0 and $\overline{K^0}$ based on the production cross-sections of K^+ and K^-. To generate the energy spectra for K^0 and $\overline{K^0}$, a Malensek spectrum [63] for a 4.8 mrad targetting angle was used; the Malensek spectrum was different for K^0 and $\overline{K^0}$. The kaon energy spectra were also modifed by the same polynomial correction which was used in the Monte Carlo simulation. The kaon states were evolved as they passed through the beam line and decay region. Coherent propagation through the regenerator and absorbers was performed using a full matrix transformation of the incoming states. Noncoherent transmission was treated as a background and was removed from the final background-subtracted data

sample.

The evolution of kaons through the regenerator accounted for the transport through the plastic scintillator section as well as the lead-scintillator sandwich at the downstream end. Regeneration in the lead obeyed a power law whose parameters were obtained from other experiments. The regeneration parameters that were used for lead were the same in the absorbers and regenerator. For propagation through the plastic scintillator, the difference in the forward scattering amplitudes, $(f(0)-\overline{f}(0))/k$, was calculated by adding the hydrogen and carbon contributions in the ratio 1.1:1. The difference in the forward scattering amplitudes for hydrogen followed a power law whose parameters were fixed. Although $(f(0)-\overline{f}(0))/k$ for carbon was also governed by a power law, both the amplitude of $(f(0)-\overline{f}(0))/k$ at 70 GeV and the power law exponent, α, for carbon were free parameters in the fit. The phase of $(f(0)-\overline{f}(0))/k$ was related to the power law exponent by constraining the forward scattering functions to be analytic. The power law treatment of carbon regeneration is not exact due to nuclear screening effects, with deviations getting larger at lower kaon momenta (<40 GeV) [68]. To account for this behaviour, we allowed for deviations from the power law. After accounting for the power law behaviour and deviations, $(f(0)-\overline{f}(0))/k$ for carbon was given by

$$|(\frac{f(0)-\overline{f}(0)}{k})(p)| = |(\frac{f(0)-\overline{f}(0)}{k})(70GeV)|(\frac{p}{70GeV})^{\alpha} + A_{Screening}, \tag{10.2}$$

and

$$\phi_{\frac{f(0)-\overline{f}(0)}{k}} = -\frac{\pi}{2}(2+\alpha) + \phi_{Screening}, \tag{10.3}$$

where $A_{Screening}$ and $\phi_{Screening}$ were the amplitude and phase due to deviations from the power law, and p was the kaon momentum.

It was important to know the kaon momentum dependance of the transmission in the regenerator beam, since the transmission affected the measurement of the carbon regeneration parameters and hence, affected our measurement of $Re(\epsilon'/\epsilon)$. Based on the kaon evolution through the shadow absorber and regenerator, the predicted transmission in the regenerator beam was 7.38%. However, using $K_L \rightarrow \pi^+\pi^-\pi^0$

decays in 1997, the transmission, $T(p)$, was found to be

$$T(p) = (8.02 \pm 0.03)\% - (0.00451 \pm 0.00048)\%/GeV \times p, \tag{10.4}$$

where p was the kaon momentum[1]. To account for the momentum-dependence of the regenerator beam transmission, the prediction function was modified so that the regenerator beam transmission was given by Equation 10.4. The systematic uncertainty on $Re(\epsilon'/\epsilon)$ due to the regenerator beam transmission is discussed in Section 10.2.

The transmission modification accounted for flux differences between the vacuum and regenerator beams, that affected both charged and neutral modes in the same way. To allow for differences between the momentum spectrum of the vacuum beam data and the flux determined by the predicted function, we floated the flux normalization in each 10 GeV kaon energy bin. To allow for differences in the flux between charged and neutral modes, the flux normalizations for the two modes were floated independently. Since the charged and neutral mode data were collected at different times, the fluxes could be different in the two modes.

Having evolved the kaon states through the beam line, the prediction function determined the rate of $K \to 2\pi$ decays in the vacuum and regenerator beams. The prediction function determined the distribution of decays that occurred in the specified decay volume without accounting for any smearing or resolution effects. Smearing and resolution effects were dealt with by the acceptance calculation.

10.1.2 The Acceptance and Fit to Data

The fit for $Re(\epsilon'/\epsilon)$ used distributions of kaon energies and decay vertex z-positions (i.e., p-z tables). Although there were separate data p-z tables for both regenerator beam positions, the p-z tables were added together (using an arithmetic mean) since the left and right beams were very similar (see Figure 10.3).

Before the p-z tables of the prediction function could be compared to the data, the

[1]The regenerator beam transmission was measured after accounting for scattering in the shadow absorber.

p-z tables of the prediction function had to account for the acceptance of the detector. The acceptance was determined by dividing the number of coherent Monte Carlo $K \to 2\pi$ decays that were accepted after all analysis cuts by the number of generated $K \to 2\pi$ decays. The acceptance was measured in 120 1 GeV kaon energy (E_K) bins between 40 GeV and 160 GeV over the whole decay region. It was important to measure the acceptance using fine E_K bins because if we had used only one E_K-bin, the measurement would become more sensitive to an accurate understanding of overall data-Monte Carlo kaon energy agreement.

To determine $Re(\epsilon'/\epsilon)$, the $K \to 2\pi$ decays in the acceptance-corrected fit prediction and the data were integrated in 12 10-GeV kaon energy bins from 40 GeV to 160 GeV over a z_K-region of 110 m to 158 m in the vacuum beam and 124 m to 158 m in the regenerator beam. There were a total of 48 fit bins corresponding to 12 kaon energy bins for each beam (vacuum and regenerator) in each mode (charged and neutral). By only using one z-bin, the $Re(\epsilon'/\epsilon)$ measurement was less sensitive to data-Monte Carlo differences in the z_K resolution. The data and prediction were compared by calculating a χ^2 for each 10-GeV kaon energy bin. The χ^2 within an energy bin was given by

$$\Delta\chi^2 = \frac{(N_{Data} - N_{Prediction})^2}{\sigma^2_{Data} + \sigma^2_{Pred}}, \tag{10.5}$$

where N_{Data} and $N_{Prediction}$ were the number of data and acceptance-corrected predicted decays, respectively, and σ_{Data} and σ_{Pred} their respective errors. σ_{Pred} was determined by the Monte Carlo statistics and was calculated binomially using the ratio of accepted to generated decays. Since σ_{Pred} was smaller than $\sqrt{N_{Prediction}}$, we were able to estimate σ_{Data} by $\sqrt{N_{Prediction}}$, thereby avoiding mis-calculating the errors in fit bins with low statistics. The χ^2 over all 48 fit bins were summed and then minimized using the MINUIT package [69].

10.1.3 Fitting Parameters

Information about $Re(\epsilon'/\epsilon)$ was contained in the decay rates determined by the prediction function. In order to calculate the decay rates, the prediction function had to

determine η_{00} and η_{+-} from the relation 1.24. To reconstruct the 2 complex numbers, η_{+-} and η_{00}, four parameters were required. In the nominal $Re(\epsilon'/\epsilon)$ fit, $|\epsilon|$, ϕ_{+-} and $\Delta\phi$ were fixed while $|\frac{\epsilon'}{\epsilon}|$ was floated. $|\epsilon|$ was fixed to the average Particle Data Group value, 2.28×10^{-3} [45]. CPT conservation was assumed by setting the phase, ϕ_{+-}, to the superweak phase, ϕ_{SW}, and fixing $\Delta\phi$ to be zero. Although $Re(\epsilon'/\epsilon)$ could be derived from the four parameters, $|\epsilon|$, $|\frac{\epsilon'}{\epsilon}|$, ϕ_{+-} and $\Delta\phi$, the nominal "$Re(\epsilon'/\epsilon)$" fit assumed that $Im(\epsilon'/\epsilon) = 0$, so $Re(\epsilon'/\epsilon)$ was equal to $|\frac{\epsilon'}{\epsilon}|$. In reality, even with CPT conservation, $Im(\epsilon'/\epsilon)$ can be slightly different from zero due to the phase of the final state interactions. The effect of assuming $Im(\epsilon'/\epsilon) = 0$ is an overestimate of $Re(\epsilon'/\epsilon)$ by 0.1×10^{-4} for $Re(\epsilon'/\epsilon) \sim 20 \times 10^{-4}$.

The decay rate distributions were sensitive to η, the regeneration parameters and the kaon parameters, Δm and τ_S. In addition to their direct effect on the regenerator beam decay rate (Equation 2.1), Δm and τ_S affected the phase, ϕ_η, because the CPT assumption meant that $\phi_{00} = \phi_{+-} = \phi_{SW}$, and ϕ_{SW} depended on Δm and τ_S. In the $Re(\epsilon'/\epsilon)$ fit, Δm and τ_S were fixed to be 0.5262×10^{10} $\hbar$s^{-1} and 0.89645×10^{-10} s, respectively; as described in Section 10.6, these values were obtained by averaging the KTeV charged and neutral mode Δm and τ_S measurements.

10.2 Systematic Errors due to the Fit

To determine the systematic uncertainty on $Re(\epsilon'/\epsilon)$ due to imperfections in the prediction function and the $Re(\epsilon'/\epsilon)$ fit, we studied the effect of the attenuation parametrization and the dependance on the kaon parameters, Δm and τ_S. The sensitivity of the $Re(\epsilon'/\epsilon)$ measurement to the power law assumption was also investigated. The systematic errors due to the fit were the same for the 1996/1997a and 1997/1997b measurements.

By varying the momentum-dependance and mean of the attenuation by one standard deviation about its measured value and determining the effect on $Re(\epsilon'/\epsilon)$, we assigned a systematic uncertainty on $Re(\epsilon'/\epsilon)$ of 0.19×10^{-4} due to the regenerator beam attenuation.

The $Re(\epsilon'/\epsilon)$ fit was sensitive to the Δm and τ_S input values since they affected

the interference term as well as the measurement of the regeneration parameters (which, in turn, affected the measurement of $Re(\epsilon'/\epsilon)$). By varying the Δm and τ_S values used in the fit by one standard deviations about their KTeV measured values (Equation 10.11) and observing the maximum change in $Re(\epsilon'/\epsilon)$, a systematic uncertainty on $Re(\epsilon'/\epsilon)$ of 0.12×10^{-4} was assigned due to the dependance on Δm and τ_S.

The assumption of analyticity was tested by allowing the regeneration phase to deviate by $\pm0.25°$ from the value determined by analyticity. Based on regeneration phase and amplitude comparisons between experimental data and predictions that assumed analyticity over a kaon momentum range of 20-160 GeV/c, Briere [67] estimated a $\pm0.35°$ error on the regeneration phase. Since the deviations from analyticity decrease at higher kaon energies, we assumed a $\pm0.25°$ deviation from analyticity. The effect of this (0.25°) deviation on $Re(\epsilon'/\epsilon)$ was 0.07×10^{-4}.

Deviations from the power law affect the regeneration amplitude and hence the predicted number of regenerator beam decays. The systematic error due to the power law assumption used in the nominal $Re(\epsilon'/\epsilon)$ fit was determined by comparing the value of $Re(\epsilon'/\epsilon)$ obtained from a prediction function which assumed pure power law-dependent regeneration for carbon, with the nominal measurement of $Re(\epsilon'/\epsilon)$ which allowed for power law deviations due to nuclear screening effects. The systematic error due to the power law assumption was 0.30×10^{-4}.

The total systematic error on $Re(\epsilon'/\epsilon)$ due to its dependance on Δm, τ_S and the carbon regeneration parameters was 0.33×10^{-4}.

10.3 Total Systematic Error

The total systematic error for the combined 1996 and 1997 neutral mode and the full 1997 charged mode $Re(\epsilon'/\epsilon)$ analyses was 2.41×10^{-4}. The charged and neutral mode contributions to the systematic error as well as the error due to the extraction of $Re(\epsilon'/\epsilon)$ are presented in Table 10.1.

The total systematic error for the 1997a charged and 1996 neutral mode $Re(\epsilon'/\epsilon)$ analysis are shown in Table 10.2 while the breakdown of uncertainties on $Re(\epsilon'/\epsilon)$

Source of uncertainty	Uncertainty on $Re(\epsilon'/\epsilon)$ ($\times 10^{-4}$) from $\pi^+\pi^-$	from $\pi^0\pi^0$
Class 1: Data collection		
Trigger and level 3 filter	0.56	0.18
Class 2: Event reconstruction, selection, backgrounds		
Energy/Momentum scale	0.16	1.27
Calorimeter nonlinearity	—	0.66
Detector calibration, alignment	0.28	0.38
Analysis cut variations,	0.23	0.37
Background subtraction	0.20	1.07
Class 3: Detector acceptance		
Limiting apertures	0.30	0.46
Detector resolution	0.15	0.08
Drift chamber simulation	0.37	—
z dependence	0.90	0.39
Monte Carlo statistics	0.27	0.37
Class 4: Kaon flux and physics parameters		
Regenerator-beam attenuation:		
Energy dependence	0.19	
Δm, τ_S, regeneration phase	0.33	
TOTAL	2.41	

Table 10.1: Table of systematic errors on $Re(\epsilon'/\epsilon)$ for the COMBINED 1996 and 1997 analyses.

Source of uncertainty	Uncertainty on $Re(\epsilon'/\epsilon)$ ($\times 10^{-4}$) from $\pi^+\pi^-$	from $\pi^0\pi^0$
Class 1: Data collection		
Trigger and level 3 filter	0.53	0.29
Class 2: Event reconstruction, selection, backgrounds		
Energy/Momentum scale	0.16	1.08
Calorimeter nonlinearity	—	0.66
Detector calibration, alignment	0.28	0.38
Analysis cut variations,	0.19	0.33
Background subtraction	0.20	1.14
Class 3: Detector acceptance		
Limiting apertures	0.45	0.46
Detector resolution	0.15	0.08
Drift chamber simulation	0.37	—
z dependence	2.22	1.02
Monte Carlo statistics	0.48	0.55
Class 4: Kaon flux and physics parameters		
Regenerator-beam attenuation:		
Energy dependence	0.19	
Δm, τ_S, regeneration phase	0.33	
TOTAL	3.30	

Table 10.2: Table of systematic errors on $Re(\epsilon'/\epsilon)$ for the 1996 neutral and 1997a charged mode analyses.

due to the 1997b charged and 1997 neutral modes are found in Table 10.3.

10.4 $Re(\epsilon'/\epsilon)$ Fit Result

The measurement of $Re(\epsilon'/\epsilon)$ for the full charged and neutral mode samples discussed in this dissertation were obtained by fitting for $|\epsilon'/\epsilon|$ using two statistically independent samples of charged and neutral mode data: the 1996 neutral mode and 1997a charged mode data sets, and the 1997 neutral mode and 1997b charged mode data sets. The results for $|\epsilon'/\epsilon|$ in the two statistically independent samples were then averaged by weighting the samples based on their total (data + Monte Carlo) statistical errors. As described in the previous section, the fit for $|\epsilon'/\epsilon|$ also floated the amplitude and phase of $(f(0) - \overline{f}(0))/k$ for carbon, and the 24 10-GeV bin flux normalizations (12 in each mode).

Source of uncertainty	Uncertainty on $Re(\epsilon'/\epsilon)$ ($\times 10^{-4}$) from $\pi^+\pi^-$	from $\pi^0\pi^0$
Class 1: Data collection		
Trigger and level 3 filter	0.62	0.16
Class 2: Event reconstruction, selection, backgrounds		
Energy/Momentum scale	0.16	1.37
Calorimeter nonlinearity	—	0.66
Detector calibration, alignment	0.28	0.38
Analysis cut variations,	0.25	0.37
Background subtraction	0.20	1.06
Class 3: Detector acceptance		
Limiting apertures	0.33	0.46
Detector resolution	0.15	0.08
Drift chamber simulation	0.37	—
z dependence	0.53	0.26
Monte Carlo statistics	0.33	0.49
Class 4: Kaon flux and physics parameters		
Regenerator-beam attenuation:		
Energy dependence	0.19	
Δm, τ_S, regeneration phase	0.33	
TOTAL	2.38	

Table 10.3: Table of systematic errors on $Re(\epsilon'/\epsilon)$ for the neutral mode 1997 and charged mode 1997b analyses.

Data Set	$Re(\epsilon'/\epsilon)$ ($\approx \lvert\epsilon'/\epsilon\rvert$) ($\times 10^{-4}$)	Power Law Exponent, α	Fit χ^2 (per 21 $d.o.f.$)
1996 $K_{L,S} \to \pi^0\pi^0$, 1997a $K_{L,S} \to \pi^+\pi^-$	23.24±2.94	-0.5419±0.0015	18.7
1997 $K_{L,S} \to \pi^0\pi^0$, 1997b $K_{L,S} \to \pi^+\pi^-$	19.82±1.73	-0.5429±0.0009	31.5
1996+1997 $K_{L,S} \to \pi^0\pi^0$, 1997 $K_{L,S} \to \pi^+\pi^-$	20.74±1.50	-0.5426±0.0008	—

Table 10.4: $Re(\epsilon'/\epsilon)$ Fit Results. Only the statistical errors are presented. The errors on $Re(\epsilon'/\epsilon)$ measurements shown were due to the statistical uncertainty of the data sample.

The results of the fits are presented in Table 10.4. For the 1996 neutral and 1997a charged mode samples, $Re(\epsilon'/\epsilon)$ was measured to be $(23.24\pm2.94)\times10^{-4}$, while for the 1997 neutral and 1997b charged mode samples, $Re(\epsilon'/\epsilon)$ was determined to be $(19.82\pm1.73)\times10^{-4}$, where the errors quoted for both measurements were only due to the statistics in the data sample. The power law exponents in both fits were in good agreement with each other as well. The two $Re(\epsilon'/\epsilon)$ measurements were averaged to yield $(20.74\pm1.50(stat))\times10^{-4}$ for the combined data set, where the 1.50×10^{-4} uncertainty on $Re(\epsilon'/\epsilon)$ does not include the statistical error due to the Monte Carlo.

10.5 Cross-checks of $Re(\epsilon'/\epsilon)$ Measurement

The nominal $Re(\epsilon'/\epsilon)$ measurement was checked in many ways. Most cross-checks were made using the 1997 neutral and 1997b charged mode data sets. We also compared $Re(\epsilon'/\epsilon)$ from the 1996 neutral-1997a charged data sets, used for our first publication, with that from statistically independent samples in 1997.

As shown in Figure 10.2, $Re(\epsilon'/\epsilon)$ was measured in separate 10 GeV kaon energy bins using the 1997 neutral and 1997b charged mode data samples. In order to determine $Re(\epsilon'/\epsilon)$ in each 10-GeV kaon energy bin, the power law constraint on $|f(0) - \overline{f}(0)|/k$ was removed and the amplitude, $|f(0) - \overline{f}(0)|/k$, was determined

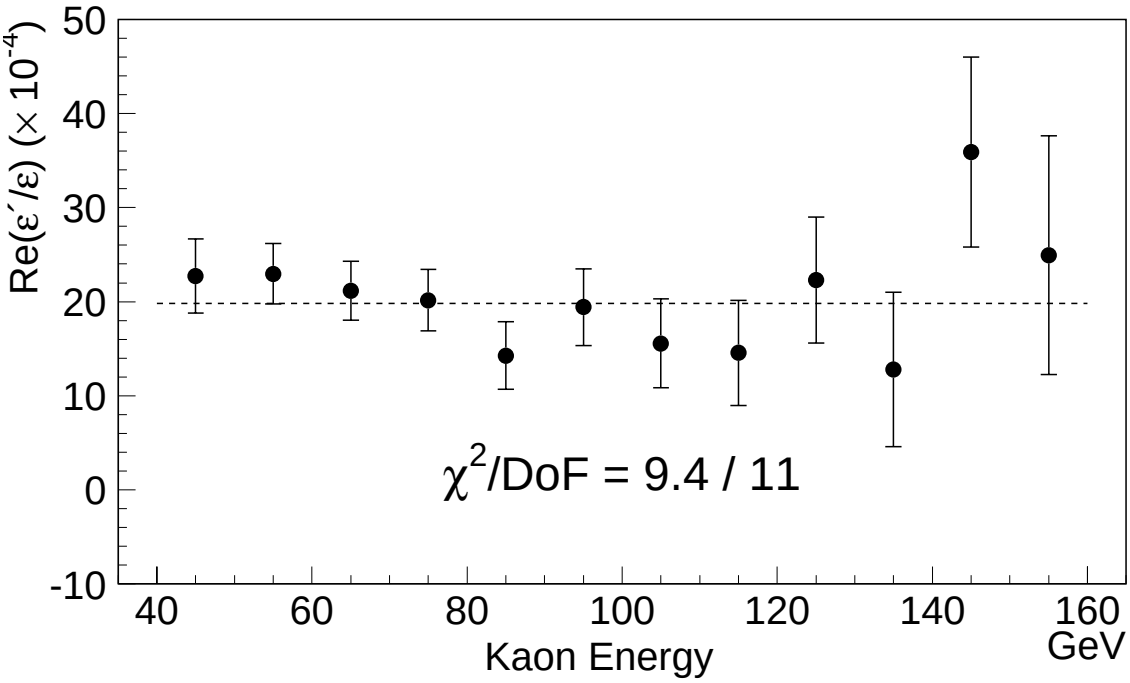

Figure 10.2: Variation of $Re(\epsilon'/\epsilon)$ as a function of kaon energy for the 1997 neutral and 1997b charged data sets.

separately in each 10-GeV bin. Within each kaon energy bin, we required that the regeneration amplitude follow a power law, with the regeneration phase from the nominal fit. The average value of $Re(\epsilon'/\epsilon)$ was 20.0×10^{-4} with a χ^2 of 9.4 for 11 degrees of freedom indicating that the variation in $Re(\epsilon'/\epsilon)$ as a function of kaon energy was consistent with the expected statistical fluctuation..

Instead of combining both left and right beam regenerator configurations, we determined $Re(\epsilon'/\epsilon)$ for the 2 regenerator configurations separately. $Re(\epsilon'/\epsilon)$ was found to be $(19.27\pm2.58)\times10^{-4}$ and $(20.01\pm2.59)\times10^{-4}$ when the regenerator was in the left and right positions, respectively. The comparison is shown graphically in Figure 10.3. The good agreement between the two regenerator configurations was due to the fact that left-right differences in the beamline and detector were small and well-understood.

The 1997 neutral and 1997b charged mode data sets were divided into four independent time periods, each containing about the same amount of data as the

1996 neutral-1997a charged mode data sample. $Re(\epsilon'/\epsilon)$ was measured in each of the four time periods as well as in the 1996/1997a data sample. As shown in Figure 10.3, the agreement between the five statistically-independent data samples was very good, showing that the difference in $Re(\epsilon'/\epsilon)$ between the 1996/97a sample and the 1997/1997b sample was consistent with statistal fluctuations. Figure 10.3 also shows that the measurement of $Re(\epsilon'/\epsilon)$ using charged and neutral mode data collected in different years was consistent with the measurement using charged and neutral mode data from the same period.

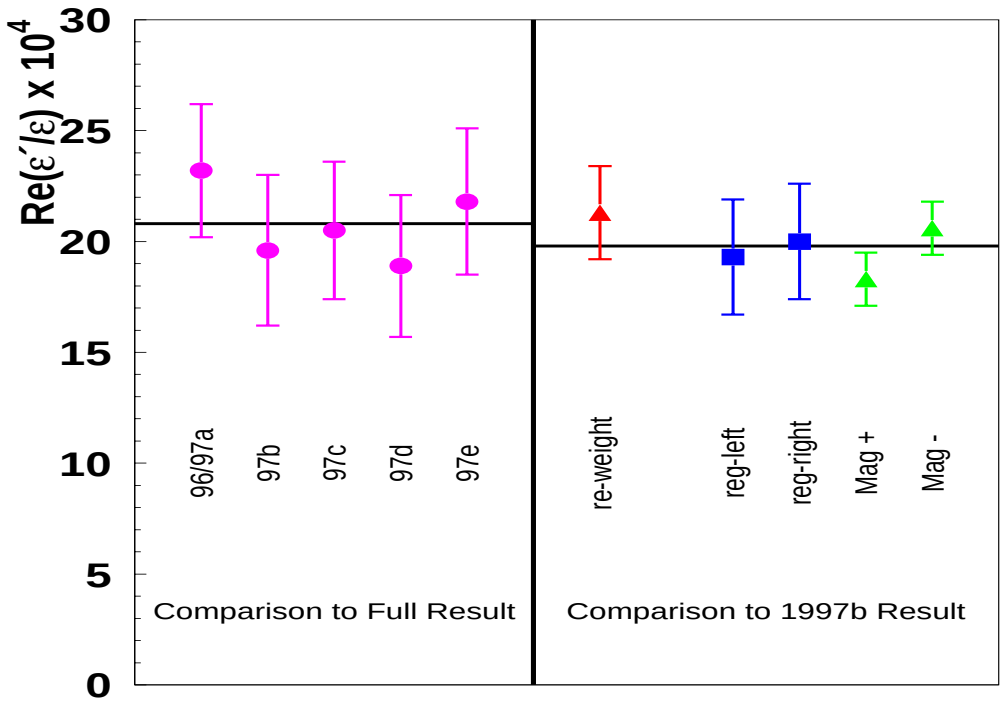

Figure 10.3: Cross-checks of $Re(\epsilon'/\epsilon)$ measurement. Cross-checks which were compared to the nominal 1997b result only used the 1997 neutral and 1997b charged mode datasets. 97b-e are data sub-samples within the 1997 neutral mode and 1997b charged mode samples.

To ensure that the $Re(\epsilon'/\epsilon)$ measurement was consistent between both analysis magnet polarities, we divided the 1997b charged mode data based on the analysis

magnet polarity. The neutral mode data in 1997 was not divided. As shown in Figure 10.3, there was no bias in $Re(\epsilon'/\epsilon)$ due to the analysis magnet polarity.

10.5.1 Reweighting Analysis

As described in Section 2.2, to reduce the sensitivity of the $Re(\epsilon'/\epsilon)$ measurement on the understanding of the acceptance, the events in the vacuum beam could be weighted such that the distributions in the vacuum and regenerator beams looked similar. By doing this, geometrical and kinematic effects which depended on the z-position of the kaon decay would be the same in both beams. Although the "reweighting approach" to measuring $Re(\epsilon'/\epsilon)$ was statistically weaker than the nominal KTeV technique, it was a useful cross-check of the nominal $Re(\epsilon'/\epsilon)$ analysis and in particular, it tested the dependance of the nominal KteV $Re(\epsilon'/\epsilon)$ measurement on the Monte Carlo acceptance determination. As mentioned in Section 2.2, the NA48 experiment at CERN uses the "reweighting approach" to measure $Re(\epsilon'/\epsilon)$.

The systematic issues were different from the nominal KTeV technique as well since there was less dependance on the Monte Carlo simulation[2]. The reweighting approach to determining $Re(\epsilon'/\epsilon)$ was applied to the 1997 neutral and 1997b charged mode data sets. The weighting function that was applied to both charged and neutral mode vacuum beam events was the same. The vacuum and regenerator beam $K_{L,S} \rightarrow \pi^0\pi^0$ z_K distributions before and after reweighting are shown in Figure 10.4. The difference in the measured value of $Re(\epsilon'/\epsilon)$, $\Delta Re(\epsilon'/\epsilon)$, between the "reweighting approach" and the nominal $Re(\epsilon'/\epsilon)$ fit was

$$\Delta Re(\epsilon'/\epsilon) = (1.5 \pm 2.1(stat) \pm 3(syst)) \times 10^{-4}, \tag{10.6}$$

where the statistical and systematic errors were the uncorrelated errors between the two measurement techniques. The "reweighting approach" yielded a slightly higher $Re(\epsilon'/\epsilon)$ result. The consistency between the two approaches indicated that the re-

[2]The Monte Carlo simulation was still important in the "reweighting technique" in subtracting the background and studying the systematics.

liance on the Monte Carlo in the nominal fit was not causing a large systematic shift in $Re(\epsilon'/\epsilon)$.

10.6 Measurement of Other Physics Parameters

As discussed in Section 2.1.3, the K_L-K_S interference (see Equation 2.1) in the regenerator beam $K \to 2\pi$ decay distributions could be used to determine Δm, τ_S and the phases of η, ϕ_η. The measurements of these kaon parameters were important both as tests of CPT-symmetry as well as cross-checks of the consistency between the charged and neutral mode analyses.

While the $Re(\epsilon'/\epsilon)$ fit was performed in one z_K-bin over the whole decay region in order to be less sensitive to the shape of the $K \to 2\pi$ decay distribution, we performed a fit in several z_K-bins to measure Δm, τ_S and ϕ_η. The information regarding the shape of the decay distribution in the regenerator beam was needed to extract the value of these kaon sector parameters from the regenerator beam decay distributions. As described below, fits with different assumptions were used to measure different combinations of parameters.

10.6.1 Measurement of Δm and τ_S in the Neutral Mode

The prediction function used to measure Δm and τ_S in the neutral mode assumed CPT by setting $\Delta\phi$ to be zero and requiring ϕ_{+-} to be equal to the superweak phase, ϕ_{SW}. ϕ_{SW} was determined dynamically since it depended on Δm and the kaon lifetimes. As in the $Re(\epsilon'/\epsilon)$ fit, the regeneration in carbon was described by a power law with small deviations due to nuclear screening effects. The power law exponent and regeneration amplitude at 70 GeV kaon energy for carbon were floated in the fit. Analyticity was assumed in order to determine the regeneration phase of carbon.

Before fitting the predicted distribution of decays to the data, the prediction function was first multiplied by the acceptance which was determined in 1 GeV$\times$2 m p-z bins. The Δm and τ_S fits were performed using one z_K-bin extending between

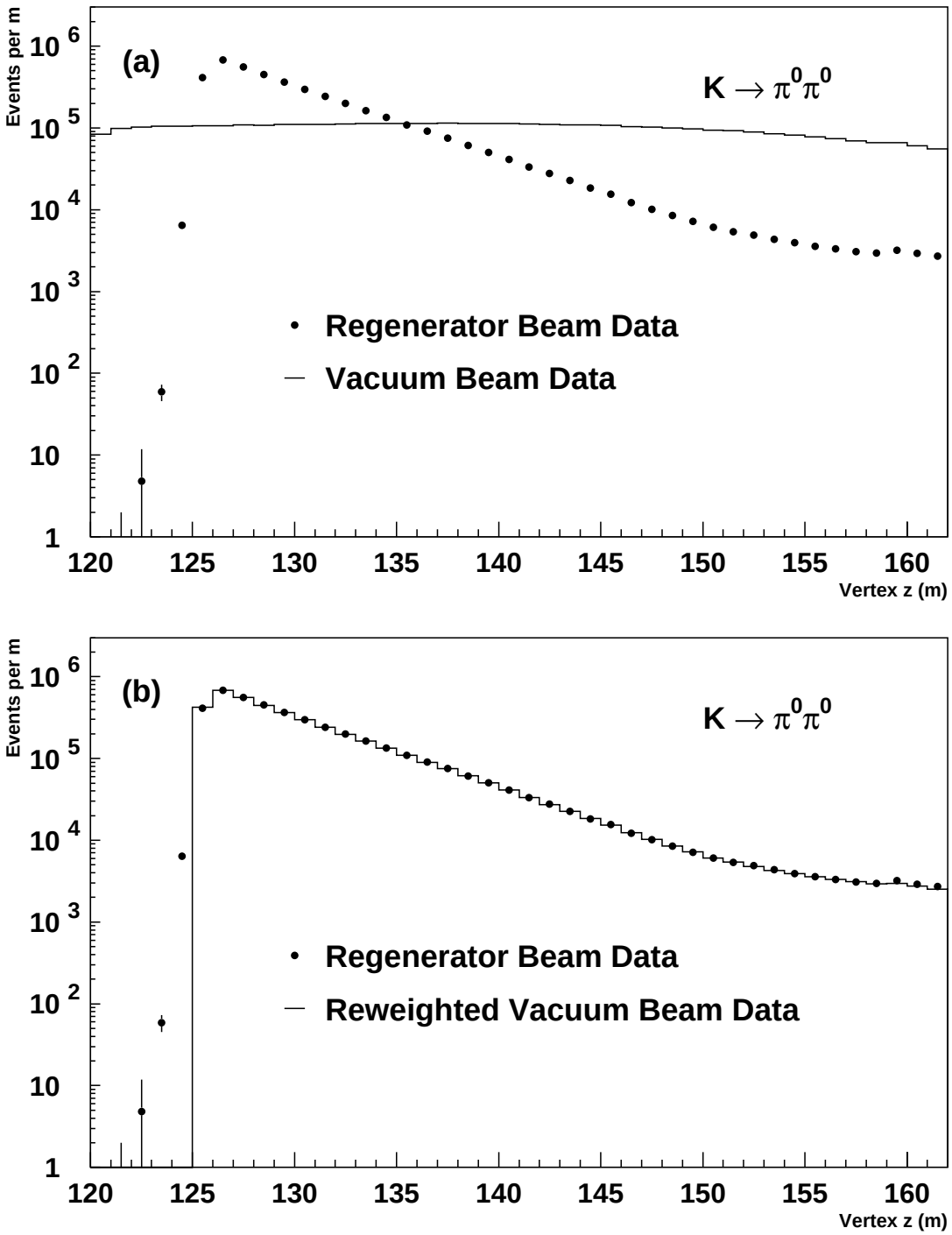

Figure 10.4: Vacuum and regenerator beam $K_{L,S} \to \pi^0\pi^0$ events in 1997 before(top) and after(bottom) the vacuum beam events have been reweighted.

110 m and 158 m from the target for vacuum beam decays[3] and seventeen 2 m-wide z_K bins from 124 m to 158 m from the target in the regenerator beam. 10-GeV kaon energy bins between 40 GeV and 160 GeV were used in the fit. Besides floating Δm, τ_S and the carbon regeneration parameters, the flux normalizations in 10 GeV bins and the effective regenerator edge position were free parameters. The effective regenerator edge position was floated to allow for z_K-resolution effects in the data that could affect the reconstructed z_K distribution close to the downstream regenerator edge. Since the position of the effective regenerator edge affected the z_K-distribution, τ_S and Δm were both sensitive to the effective regenerator edge position at the 0.0003×10^{-10} s and 0.0003×10^{10} $\hbar\mathrm{s}^{-1}$ level, respectively.

Δm and τ_S were measured using $K_{L,S} \to \pi^0\pi^0$ decays from the 1996 and 1997 data sets separately. For the 1996 neutral mode data set, we measured

$$\begin{aligned} \Delta m &= (0.5268 \pm 0.0022)\times10^{10}\ \hbar\mathrm{s}^{-1} \\ \tau_S &= (0.8948 \pm 0.0010)\times10^{-10}\ \mathrm{s}, \end{aligned} \tag{10.7}$$

while in the 1997 data set, Δm and τ_S were found to be

$$\begin{aligned} \Delta m &= (0.5225 \pm 0.0013)\times10^{10}\ \hbar\mathrm{s}^{-1} \\ \tau_S &= (0.8970 \pm 0.0006)\times10^{-10}\ \mathrm{s}, \end{aligned} \tag{10.8}$$

where the quoted errors are statistical in both measurements.

The systematic uncertainties on the Δm and τ_S measurement were divided into two large categories: systematics specific to the neutral mode and systematics which were common to the both charged and neutral modes. The systematic errors which were specific to the neutral mode were determined in a similar way to the $Re(\epsilon'/\epsilon)$ systematics. Assigning the systematic uncertainties which were common to both modes included studying how Δm and τ_S were affected by the size of the fit and

[3]In the fit to measure Δm and τ_S, the vacuum beam distribution was used obtain the normalization of the kaon flux. To reduce the sensitivity to the z_K-variation of the acceptance in the vacuum beam, only one z_K-bin was used in the fit.

Source of Uncertainty	$\delta(\Delta m)$ ($\times 10^{10}$ $\hbar$s^{-1})	$\delta(\tau_S)$ ($\times 10^{-10}$ s)
Analysis Cuts	0.0008	0.0004
Energy and Position Linearity	0.0002	0.0006
Energy Resolution	0.0002	0.0001
Energy Scale	0.0006	0.0008
Backgrounds	0.0007	0.0003
Apertures	0.0002	0.0004
Reconstruction	0.0003	0.0004
Acceptance Slope 1×10^{-4}	0.0002	0.0003
Total Systematic (neutral mode-specific)	0.0013	0.0013
Fitting Procedure (common to both modes)	0.0013	0.0004

Table 10.5: Summary of systematic uncertainties on Δm and τ_S in the $K_{L,S} \to \pi^0\pi^0$ mode

acceptance bins. We also determined the effect of the fit conditions such as the analyticity assumption and the regenerator beam attenuation on $Re(\epsilon'/\epsilon)$. Δm was very sensitive to the analyticity assumption and the regenerator beam attenuation. Since the momentum-dependance of the regenerator attenuation affected the measurement of the power law exponent, α, due to the analyticity assumption, ϕ_ρ was affected as well. Since ϕ_ρ and Δm were measured from the inteference term in the decay rate (Equation 2.1), Δm was sensitive to the attenuation and analyticity assumption.

The systematic errors on Δm and τ_S are presented in Table 10.5. The total systematic errors on Δm and τ_S were 0.0018×10^{10} $\hbar$s^{-1} and 0.0014×10^{-10} s, respectively. The systematic errors were the same for the 1996 and 1997 data sets.

The 1996 and 1997 neutral mode Δm and τ_S measurements were averaged to give

$$\Delta m \;=\; (0.5237 \pm 0.0011(stat) \pm 0.0018(syst))\times 10^{10}\ \hbar\mathrm{s}^{-1}$$

$$\tau_S = (0.8964 \pm 0.0005(stat) \pm 0.0014(syst)) \times 10^{-10} \text{ s.} \quad (10.9)$$

The charged mode measurements, which are discussed in [39], were

$$\Delta m = (0.5267 \pm 0.0006(stat) \pm 0.0014(syst)) \times 10^{10} \ \hbar \text{s}^{-1}$$
$$\tau_S = (0.8965 \pm 0.0003(stat) \pm 0.0005(syst)) \times 10^{-10} \text{ s.} \quad (10.10)$$

The charged and neutral mode τ_S and Δm measurements are in good agreement with each other.

The charged and neutral mode results were combined by taking a weighted averaged based on the statistical and mode-specific systematic errors. From the full charged and neutral mode data sets discussed in this dissertation, Δm and τ_S were measured to be

$$\Delta m = (0.5262 \pm 0.0007(stat + syst) \pm 0.0013(comm.syst)) \times 10^{10} \ \hbar \text{s}^{-1}$$
$$\tau_S = (0.8965 \pm 0.0004(stat + syst) \pm 0.0004(comm.syst)) \times 10^{-10} \text{ s}, \quad (10.11)$$

where the statistical and mode-specific systematic errors have been separated from the systematic errors which were common to both modes.

10.6.2 Measurement of $\Delta\phi$

We measured $\Delta\phi$ by fitting for $Im(\epsilon'/\epsilon)$ and then extracting $\Delta\phi$ from Equation 1.36. In the nominal $Im(\epsilon'/\epsilon)$ fit, η_{+-} and η_{00} were reconstructed from $|\epsilon|$, $arg(\epsilon)$, $Re(\epsilon'/\epsilon)$ and $Im(\epsilon'/\epsilon)$. When measuring $Im(\epsilon'/\epsilon)$, we floated the carbon regeneration parameters, Δm, τ_S, $Re(\epsilon'/\epsilon)$, $(arg(\epsilon) - \phi_{SW})$, the neutral mode effective regenerator edge, a stretch in the charged mode decay region and the flux normalizations for the charged and neutral modes.

Based on the 1997 neutral mode and 1997b charged mode data sets, $\Delta\phi$ was measured to be

$$\Delta\phi = (0.74 \pm 0.27(stat))^\circ. \quad (10.12)$$

Combining the full 1996 and 1997 KTeV data sets, $\Delta\phi$ was

$$\Delta\phi = (0.41 \pm 0.22(stat))^{\circ}. \tag{10.13}$$

Floating the regenerator beam transmission or fixing Δm, τ_S, $(arg(\epsilon) - \phi_{SW})$ or the effective regenerator edge positions did not have a significant effect on $Im(\epsilon'/\epsilon)$. There was, however, a large correlation between $Re(\epsilon'/\epsilon)$ and $Im(\epsilon'/\epsilon)$. This was also reflected in the fit for $Re(\epsilon'/\epsilon)$, if we did not assume $Im(\epsilon'/\epsilon)$ to be zero but instead, allowed it to be a free parameter in the fit. In such a fit, the statistical error increased considerably and the value of $Re(\epsilon'/\epsilon)$ changed by $\sim 3 \times 10^{-4}$ with respect to the nominal $Re(\epsilon'/\epsilon)$ fit. There was a large change in $Re(\epsilon'/\epsilon)$ because the data were consistent with a non-zero $Im(\epsilon'/\epsilon)$.

The measurement of $\Delta\phi$ was sensitive to both the charged and neutral mode analyses. Therefore, systematic effects due to both modes needed to be considered. The systematic uncertainties on $\Delta\phi$ are presented in Table 10.6.

The largest contributions to the error on $\Delta\phi$ due to the charged mode was the sensitivity to the track separation cuts at the drift chambers and calorimeter, and the charged mode acceptance.

The systematic error on $\Delta\phi$ due to the neutral mode reconstruction and analysis was dominated by the uncertainty in the energy reconstruction. Since the energy reconstruction in the neutral mode affected the z_K distribution directly, the $\Delta\phi$ measurement was very sensitive to the determination of the energy scale and non-linearities in the energy reconstruction. The measurement of $\Delta\phi$ was also sensitive to the reconstruction of clusters near the hole since the effect of the K_L-K_S interference term on the regenerator beam $K \to 2\pi$ decay distribution was largest at $z_K > 140$ m, where decays caused a higher illumination at the centre of the calorimeter. We also investigated the effect on $\Delta\phi$ of a 1 mm increase in the transverse dimensions of the calorimeter, and observed a 0.14° change relative to the nominal measurement. The large change in $\Delta\phi$ was due to changes in the photon separations that affected the z_K distribution. The systematic error due to the regenerator scattering background in the neutral mode was determined in the same way as in the $Re(\epsilon'/\epsilon)$ measurement.

Source of Uncertainty	Uncertainty on $\Delta\phi$ (degrees)
Charged Mode :	
Charged Mode Analysis Cuts	0.09
Drift Chamber Resolutions	0.02
Drift Chamber Simulation	0.04
Acceptance	0.06
Accidental Effects	0.04
Background	–
Neutral Mode :	
Energy Scale	0.33
Energy Nonlinearities and Resolutions	0.17
Analysis Cuts and Reconstruction	0.19
Apertures and Calorimeter Size	0.14
Acceptance	0.05
Background	0.14
Fitting parameters	0.06
Total	0.48

Table 10.6: Systematic Errors on $\Delta\phi$

The total systematic error due to the neutral mode background was 0.14°.

We measured the sensitivity of the $\Delta\phi$ measurement to the power law assumption by comparing the measurement with and without power law deviations due to screening corrections. Based on the sensitivity to the power law assumption, we assigned an uncertainty on $\Delta\phi$ of 0.05°. We also studied the dependance of $\Delta\phi$ on the E_K and z_K binning used in the fit and found that $\Delta\phi$ was sensitive to the E_K binning. We assigned an error of 0.035° due to binning effects.

The total systematic error on $\Delta\phi$ was 0.48°. The systematic uncertainty was the same for both 1996-1997a and 1997-1997b data sets. Based on the data sets discussed in this dissertation, $\Delta\phi$ was measured to be $(0.41\pm0.53)^\circ$, where the statistical and systematic errors have been combined.

CHAPTER 11
CONCLUSION

This chapter summarizes the results of the measurement of $Re(\epsilon'/\epsilon)$, $\Delta\phi$, Δm and τ_S using the KTeV data sets discussed in this thesis.

11.1 Measurement of $Re(\epsilon'/\epsilon)$

$Re(\epsilon'/\epsilon)$ was measured using the 1996 and 1997 $K_{L,S} \to \pi^0\pi^0$ and the 1997 $K_{L,S} \to \pi^+\pi^-$ data sets to be[1]

$$Re(\epsilon'/\epsilon) = (20.74 \pm 1.50(stat) \pm 2.41(syst)) \times 10^{-4}. \tag{11.1}$$

Using only the 1997 $K_{L,S} \to \pi^0\pi^0$ and 1997b $K_{L,S} \to \pi^+\pi^-$ data sets yielded a measurement of $Re(\epsilon'/\epsilon)$ of

$$Re(\epsilon'/\epsilon) = (19.82 \pm 1.73(stat) \pm 2.38(syst)) \times 10^{-4}. \tag{11.2}$$

The 1997 neutral mode and 1997b charged mode data sets were statistically-independent from the data sets that were used to obtain the KTeV $Re(\epsilon'/\epsilon)$ result published in [34]. The KTeV published sample, which was based on the 1996 $K_{L,S} \to \pi^0\pi^0$ and 1997a $K_{L,S} \to \pi^+\pi^-$ data sets, was re-analyzed in the same way as the 1997 neutral mode-1997b charged mode sample. Based on the re-analysis, $Re(\epsilon'/\epsilon)$ was found to be

$$Re(\epsilon'/\epsilon) = (23.24 \pm 2.94(stat) \pm 3.30(syst)) \times 10^{-4}. \tag{11.3}$$

[1]The statistical errors on $Re(\epsilon'/\epsilon)$ presented in Equations 11.1, 11.2 and 11.3 refer to the statistical uncertainty of the data sample alone while the systematic error includes the error due to Monte Carlo statistics (see Tables 10.1), 10.2 and 10.3).

11.1.1 Re-analysis of KTeV Published $Re(\epsilon'/\epsilon)$ Result

In the re-analysis of the 1996 neutral mode-1997a charged mode data, $Re(\epsilon'/\epsilon)$ decreased by 4.8×10^{-4} with respect to the published $Re(\epsilon'/\epsilon)$ result, $(28.0\pm3.0(\text{stat})\pm2.8(\text{syst}))\times10^{-4}$ [34]. The main contributions to the change in the published result were modifications to the background simulation, changes to the assumptions and parameters used in extracting $Re(\epsilon'/\epsilon)$ from the $K \to 2\pi$ decay distributions (see Chapter 10), and the statistical change expected from the different Monte Carlo samples used in the published and re-analyzed results. We now discuss these changes.

The largest change in the KTeV published value of $Re(\epsilon'/\epsilon)$ was due to a mistake in the treatment of regenerator scatter background. Besides correcting the mistake, we also made improvements to the simulation of both regenerator and collimator scatter background. These changes mainly affected the $K_{L,S} \to \pi^0\pi^0$ analysis. The total change due to the modifications to the background simulation was -1.9×10^{-4}.

The effect of the change in $Re(\epsilon'/\epsilon)$ due to the assumptions and parameters used in extracting $Re(\epsilon'/\epsilon)$ from $K \to 2\pi$ decays was -1.1×10^{-4}. The assumptions and parameters were changed by allowing deviations from the regeneration power law and by using a statistically improved measurement of the regenerator beam transmission. In addition, unlike the KTeV published analysis, where PDG [45] values of Δm and τ_S were used, in the current analysis, the values of Δm and τ_S that were determined at KTeV were used in the $Re(\epsilon'/\epsilon)$ measurement.

The systematic error on $Re(\epsilon'/\epsilon)$ (excluding any Monte Carlo statistical contribution) increased by 1.7×10^{-4} in quadrature after the re-analysis of the published data sample. The change in the systematic uncertainty was mainly due to the increase in the systematic uncertainty due to the $K_{L,S} \to \pi^+\pi^-$ acceptance. The systematic uncertainty on $Re(\epsilon'/\epsilon)$ due to the charged mode acceptance increased because the slope in the z_K overlay of data and Monte Carlo $K_{L,S} \to \pi^+\pi^-$ vacuum beam events changed from $(-1.60\pm0.63)\times10^{-4}$ to $(-2.10\pm0.60)\times10^{-4}$ after re-analyzing the published data sample. Furthermore, the assigned uncertainty on the acceptance now considered the statistical error on the z_K slope, as discussed in Section 9.1.

11.1.2 Discussion of $Re(\epsilon'/\epsilon)$ Measurements and Theoretical Predictions

The KTeV result for the 1996 and 1997 data sets(Equation 11.2) is compared to the three most recent measurements of $Re(\epsilon'/\epsilon)$ in Figure 11.1. The world average of the four measurements shown in Figure 11.1 is $(17.3\pm1.7)\times10^{-4}$ with a χ^2 of 5.7 for 3 degrees of freedom corresponding to a confidence level of 13%. The large spread in the experimental measurements seen in Figure 1.1 before the analysis of the KTeV 1997 dataset has been reduced, with especially good agreement between the two most recent $Re(\epsilon'/\epsilon)$ results from CERN [33] and Fermilab. The experimental results not only show definitively that the direct CP-violation is present in the kaon sector but that $Re(\epsilon'/\epsilon)$ is now known to $\sim$10% of itself.

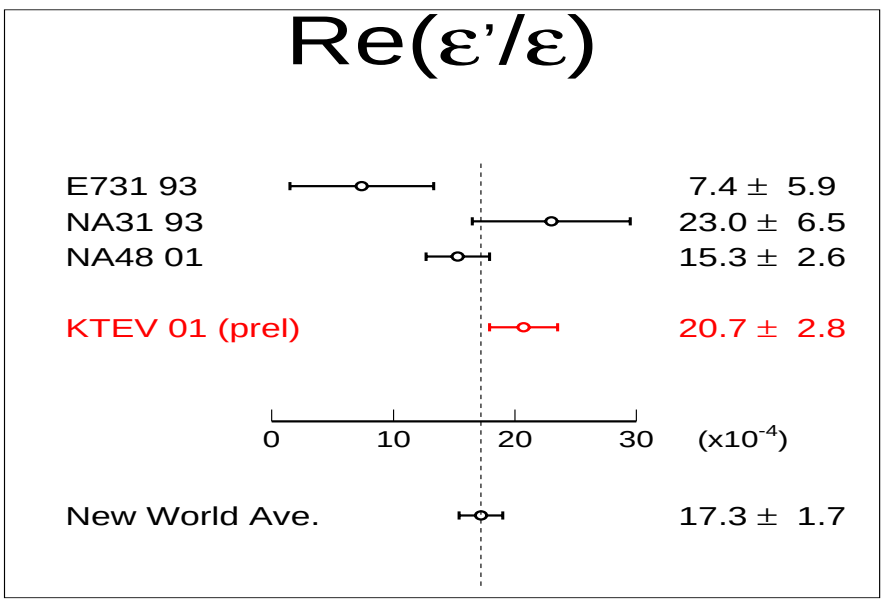

Figure 11.1: Comparison of KTeV $Re(\epsilon'/\epsilon)$ result based on 1996 and 1997 data sets with 3 most recent measurements. The measurenents are shown in units of $\times10^{-4}$.

Although recent experimental results are in reasonable agreement, the theoretical predictions of $Re(\epsilon'/\epsilon)$ range from -4$\times10^{-4}$ to $\sim$30$\times10^{-4}$. Some of the more

Group	$Re(\epsilon'/\epsilon)$ Prediction($\times 10^{-4}$)	Approach
Valencia [70]	17 ± 9	$1/N_c$ Expansion
RIKEN-BNL [71]	-4.0 ± 2.3	Quenched Lattice QCD using Domain Wall Fermions
Munich [72]	$7.7^{+6.0}_{-3.5}$ (NDR renorm.) $5.2^{+4.6}_{-2.7}$ (HV renorm.)	Phenomenological Approach
Rome [73]	$4.6^{+7.7}_{-7.2} \pm 0.4$ (HV) $8.1^{+10.3}_{-9.5} \pm 0.3$ (NDR)	Lattice QCD
Trieste [74]	22 ± 8	Chiral Quark Model
Dubna [75]	-3.2 - 3.3	Effective Chiral Lagrangian
Taiwan [76]	7 - 16	Generalized Factorization

Table 11.1: Some recent theoretical predictions of $Re(\epsilon'/\epsilon)$. The errors on the $Re(\epsilon'/\epsilon)$ predictions differ in meaning and are discussed in the references indicated.

recent Standard Model theoretical estimates using the various approaches to calculate $Re(\epsilon'/\epsilon)$ are shown in Table 11.1. Understanding the long-distance effects of the strong and electro-weak penguin diagrams on the value of $Re(\epsilon'/\epsilon)$ and the ΔI=1/2 rule pose the greatest theoretical difficulties in calculating $Re(\epsilon'/\epsilon)$ in the Standard Model. Further details can be found in references [70]- [76].

11.2 KTeV Measurements of $\Delta\phi$, Δm and τ_S

Based on the 1996 and 1997 $K_{L,S} \to \pi^0\pi^0$ and 1997 $K_{L,S} \to \pi^+\pi^-$ KTeV data sets, Δm and τ_S were measured to be (0.5262±0.0015(stat+syst))$\times 10^{10}$ $\hbar$s^{-1} and (0.8965±0.0006(stat+syst))$\times 10^{-10}$ s, respectively, as discussed in Section 10.6.1. The superweak phase, ϕ_{SW}, obtained from the KTeV measurements of Δm and τ_S is 43.38°. The KTeV measurements of Δm and τ_S are compared to other experimental measurements in Figures 11.2 and 11.3. The KTeV Δm and τ_S results are more

precise than previous experiments. Although the KTeV and PDG 2000 [45] results disagree by more than two standard deviations, the more recent measurements agree with the KTeV result.

Using the interference of K_L and K_S amplitudes in the regenerator beam, KTeV was able to measure the phase difference, $\Delta\phi$, between η_{+-} and η_{00}. Combining the 1996 and 1997 neutral mode and 1997a and 1997b charged mode data sets, $\Delta\phi$ was measured to be

$$\Delta\phi = (0.41 \pm 0.22(stat) \pm 0.48(syst))^{\circ}, \tag{11.4}$$

where the statistical error is due to both the data and Monte Carlo samples. The KTeV value for $\Delta\phi$ is consistent with CPT invariance. The KTeV measurement is compared to other measurements of $\Delta\phi$ in Figure 11.4.

The measurement of $\Delta\phi$ is equivalent to a measurement of $Im(\epsilon'/\epsilon)$ (see Equation 1.36). Hence, KTeV was able to measure both real and imaginary parts of ϵ'/ϵ at the same time by using a regenerator to produce coherent K_S and K_L in the same beam. We compare the KTeV measurements of $Re(\epsilon'/\epsilon)$ and $Im(\epsilon'/\epsilon)$ with measurements from previous Fermilab experiments, E731 and E773, in Figure 11.5. The ϵ'/ϵ measurements from all three experiments are consistent with each other and CPT conservation.

Based on the KTeV measurements of Δm, τ_S, ϕ_{+-}, ϕ_{SW} and $\Delta\phi$, we were able to set an upper limit for the K^0-$\overline{K^0}$ mass difference. The K^0-$\overline{K^0}$ mass difference, which tests CPT invariance, was measured to be

$$\begin{aligned} \frac{|m_{K^0} - m_{\overline{K^0}}|}{m_{K^0}} &= \frac{2\Delta m}{m_{K^0} sin\phi_{SW}} |\eta_{+-}| \left| \phi_{+-} - \phi_{SW} + \frac{\Delta\phi}{3} \right| \\ &< 2 \times 10^{-18}, \end{aligned} \tag{11.5}$$

at the 90% confidence level. In setting the upper limit for $\frac{|m_{K^0} - m_{\overline{K^0}}|}{m_{K^0}}$, the KTeV value for ϕ_{+-} [39], (44.12±1.36)°, and the PDG values for η_{+-} and m_{K^0} were used. The correlations between the $\Delta\phi$, ϕ_{SW} and ϕ_{+-} were not taken into account; correlations between the phase measurements lead to a slightly lower limit on the mass difference.

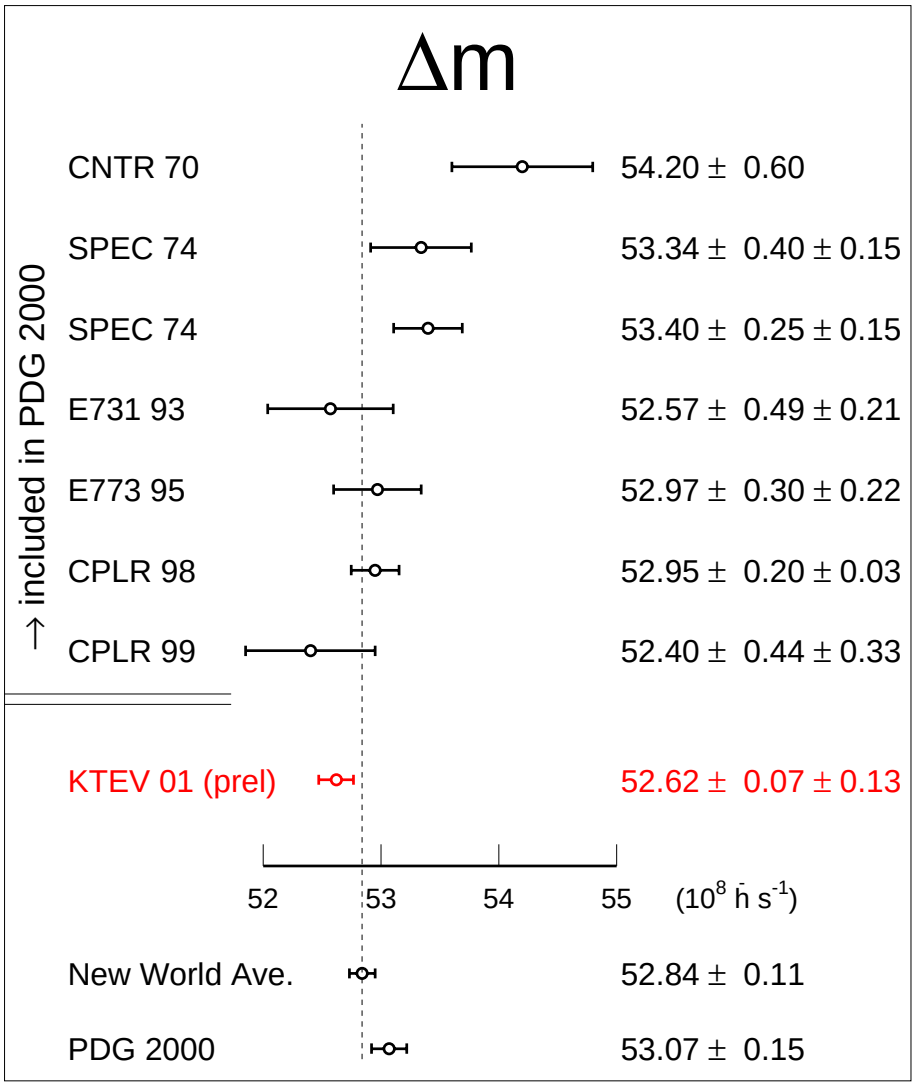

Figure 11.2: Comparison of KTeV Δm result based on 1996 and 1997 data sets with other measurements. The measurenents are shown in units of $10^8\ \hbar\ s^{-1}$.

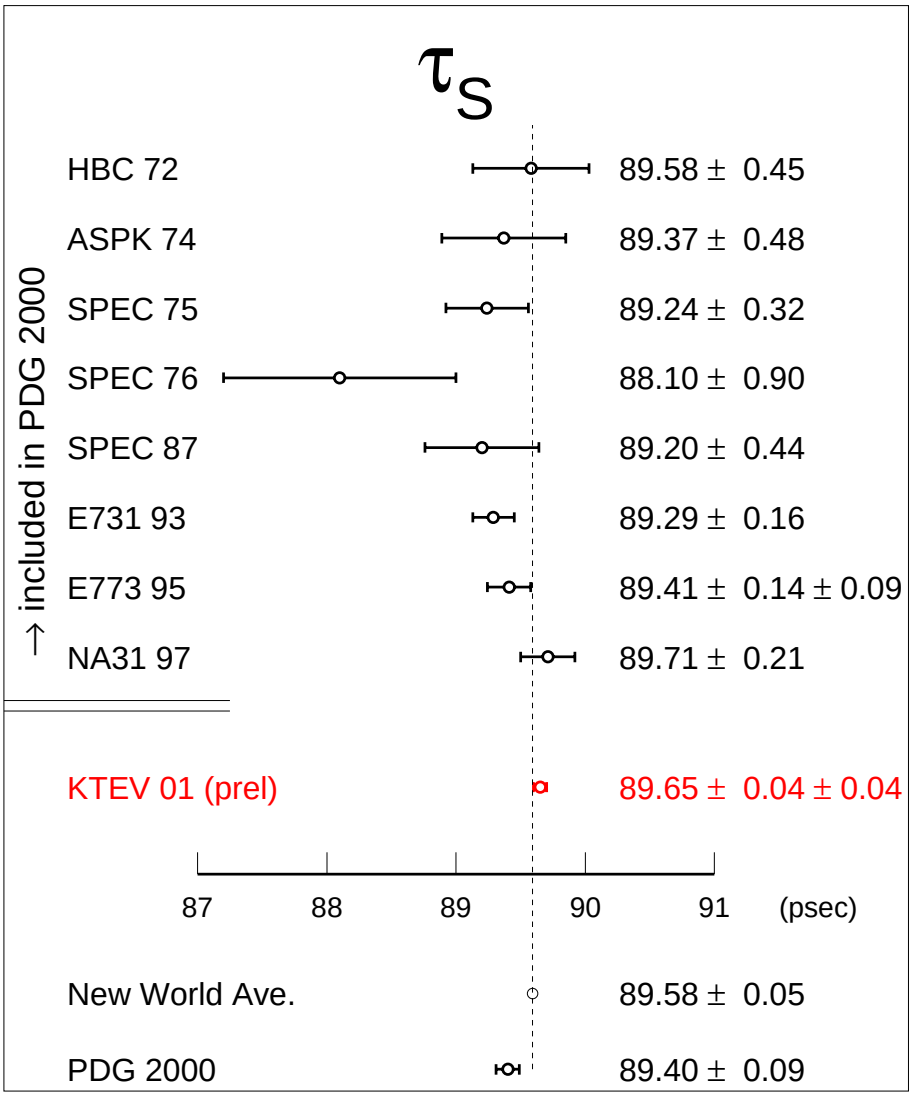

Figure 11.3: Comparison of KTeV τ_S result based on 1996 and 1997 data sets with other measurements. The measurenents are shown in units of ps.

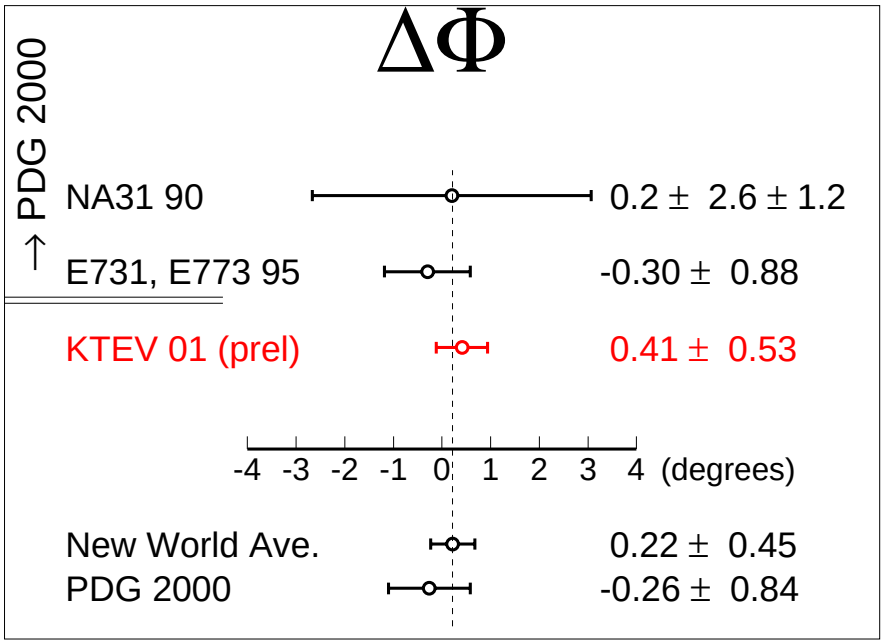

Figure 11.4: Comparison of KTeV $\Delta\phi$ result based on 1996 and 1997 data sets with other measurements. The $\Delta\phi$ measurenents are shown in units of degrees.

11.3 Concluding Remarks on CP-violation

The measurement of direct CP-violation in the kaon sector was important since it refuted non-Standard Model CP-violation mechanisms such as the superweak hypothesis [25] that only predicted indirect CP-violation, and strongly suggested that CP-violation could be explained by the Standard Model by including a non-trivial phase in the CKM matrix. The observation of direct CP-violation in the kaon sector predicted that CP-violation should exist in the B-meson sector as well. Results from the Belle [37] and Babar [38] experiments have recently observed CP-violation in B-mesons.

There is still much to look forward to in the area of CP-violation. Although CP-violation is accommodated by the Standard Model, the prediction of $Re(\epsilon'/\epsilon)$

continues to prove a theoretical challenge. A convergence of the theoretical estimates could perhaps, suggest that there are non-Standard Model contributions to direct CP-violation. In this regard, the improved precision in the measurement of $Re(\epsilon'/\epsilon)$ obtained by combining the 1996, 1997 and 1999 KTeV data sets will be important. The statistical error on $Re(\epsilon'/\epsilon)$ for the combined 1996, 1997 and 1999 KTeV data sets is expected to be 1×10^{-4}.

There are also many measurements of CP-violation in the B-sector that are currently being made. The unambiguous observation of direct CP-violation in the B-sector as well as measurements leading to the improved determination of the CKM phase δ are expected in the near future.

There are also several experiments that are looking for CP-violation in areas other than the kaon and B-sector. The search for non-zero neutron and electron electric dipole moments are ongoing while experiments to observe CP-violation in neutrinos have been proposed.

It is hoped that a better understanding of CP-violation will ultimately explain baryogenesis and the matter-antimatter asymmetry in our universe.

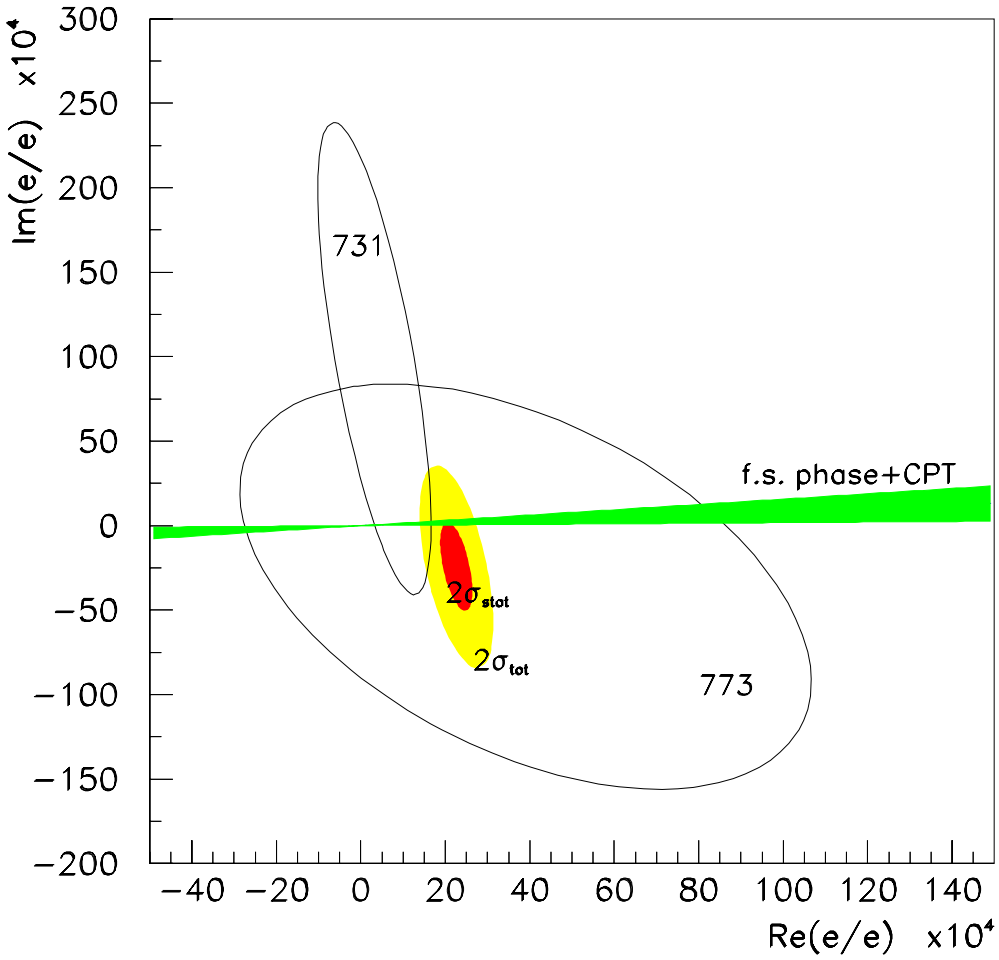

Figure 11.5: Comparison of the KTeV (1996-1997) ϵ'/ϵ measurement with measurements by Fermilab experiments, E731 and E773. The ellipses represent 2σ contours. The central ellipse representing the KTeV result is due to the (2σ) statistical error only and the outer ellipse represents the 2σ contour from the total (statistical+systematic) uncertainty. The dark band shows the expected value of $Im(\epsilon'/\epsilon)$ assuming CPT conservation. The width of the band is due to the 1σ uncertainty in the measurement of phase shifts due to the final state interactions [46].

APPENDIX A
COMMENTS ON THE RECONSTRUCTION OF ELECTROMAGNETIC CLUSTERS

In this appendix, we discuss some additional issues regarding the CsI cluster reconstruction that was performed in the analysis of the 1996 and 1997 E832 data sets. In particular, we concentrate on features in the reconstruction that may have a systematic effect on $Re(\epsilon'/\epsilon)$ and which should be investigated in future analyses.

A.1 Cluster Position Lookups

Although the position lookups were based on the cluster energy, size and region, in the 1996 and 1997 data analysis, the size of some of the clusters used in making the lookups did not correspond to the cluster size specified the lookup. For example, for a map involving the sum of energy over seven blocks, we considered a cluster which only had four blocks in a column or row. We believe that the inaccuracies in the position reconstruction of clusters due to this feature are very small.

Another feature of the position lookups was that they were made with clusters which may have had overlapping energy from neighbouring clusters since we only required clusters to be at least 7.5 cm apart. Since there were more overlaps involving high energy photons, the high energy position lookups may have been inaccurate. Although this feature could cause a bias in $Re(\epsilon'/\epsilon)$ by affecting regenerator and vacuum beam events differently, we expect the bias to be small since the Monte Carlo position lookups were made in the same way (Chapter 8). The systematic uncertainties due to biases in the cluster position determination are discussed in Chapter 9.

A.2 Transverse Energy Lookups

Although the transverse energy distribution varied with the incident particle energy[1], we used energy-independent transverse energy lookups. This could, in principle, lead to an $Re(\epsilon'/\epsilon)$ bias. However, the Monte Carlo transverse energy lookups were also independent of cluster energy, so to first order, we expect possible biases to be accounted for in the acceptance determination. Since the variation of the data and Monte Carlo transverse energy profiles with cluster energy are slightly different (especially in the blocks further away from the cluster seed), there could be second-order effects on $Re(\epsilon'/\epsilon)$ due to data-Monte Carlo differences in the treatment of overlapping clusters or clusters near the beam holes. Systematic effects due to the treatment of close clusters are discussed in Appendix C.

A.3 Readout threshold correction

Although the same readout threshold correction was used in the analysis of the 1996 and 1997 neutral mode data sets, the total energy due to blocks which were not read out was in fact different in 1996 and 1997. This can be seen in Figure A.1. There were differences between the two years in the total energy below the readout threshold because:

- the readout threshold was determined by integrating the PMT current over 228 ns in 1996 and 76 ns in 1997. As a result, for clusters with the same energy, we expect fewer channels to be read out in 1997.

- in 1996, the determination of the readout threshold and the energy calibration were performed over 228 ns, whereas in 1997, the energy calibration was performed over 114 ns. Based on this difference, we would expect the mean energy due to blocks that were not read out to be higher in 1997.

[1]The fraction of energy in the blocks far from the cluster centre varies approximately logarithmically with incident particle energy

- the DPMT calibration was different between the two years. In particular, the difference between the DPMT calibration and the pedestals measured online was not the same in the two years. This meant that the readout energy thresholds were different. By comparing the DPMT calibration with the pedestals for each channel, we observed that the readout energy threshold was higher in 1997, so the mean energy due to blocks that were not read out was expected to be higher.

Besides differences in the readout thresholds between the two years, we also expected additional differences between the data and the Monte Carlo in the total energy that was not read out. This was because the simulation did not account for pedestal fluctuations. Pedestal fluctuations tend to decrease the mean energy in of channels that are not read out, so the correction will be different

Since the threshold correction affected the energy linearity below 15 GeV, we expect that the effect of using the same threshold corrections for the 1996 and 1997 data and Monte Carlo neutral mode analyses was partly accounted for by the linearity correction which was based on the electron linearity seen in each channel. The systematic effects on $Re(\epsilon'/\epsilon)$ due to the readout threshold correction were investigated. They are discussed in detail in Chapter 9 and Appendix C.

A.4 Treatment of Close Clusters

We describe some features of our treatment of clusters which have blocks which are not part of a neighbouring cluster but nevertheless contain energy from the nearby cluster.

To subtract the energy contribution from the nearby shower, we used a map based on the transverse energy distribution of GEANT electron showers within a 13×13 small block grid. The map was independent of the cluster energy and was the same for data and Monte Carlo, even though the transverse energy profile varied with energy and the data and Monte Carlo transverse shower profiles were different. As seen in Figure A.2, the data showers had more energy than the Monte Carlo in both the central block as well as outermost ring of blocks. As a result of using a single lookup for data and Monte Carlo, the separation of close clusters was not accurate

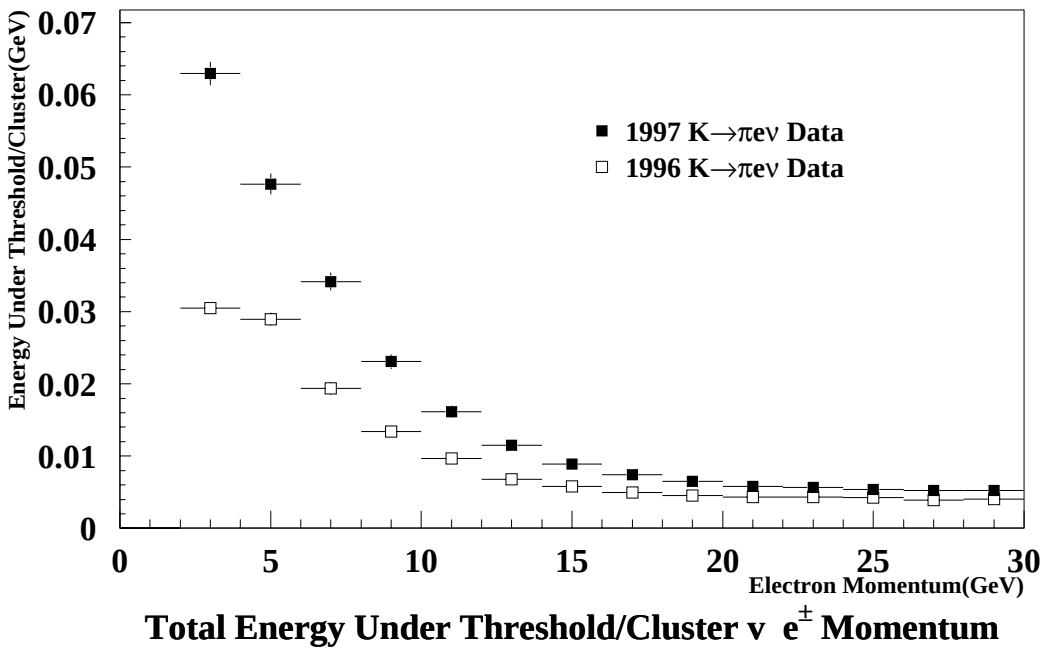

Figure A.1: Total energy below readout threshold/cluster versus $e^{\pm}$ momentum in 1996(RF Phase 1) and 1997 K_{e3} data. Only electron clusters in the small-region are considered. The errors are equal to 10% of the RMS of the distribution in each momentum bin.

at all cluster energies.

Another feature of the energy subtraction procedure was that no energy was subtracted from a block if the contribution from the neighbouring cluster was greater than the energy in the block. When a high-energy photon was near a low-energy photon, the predicted energy contribution of the high-energy photon could be higher than the energy in the outer blocks of the low energy cluster due to fluctuations in the energy of the low energy photon. As a result, the energy contribution from the high energy cluster would not be subtracted when determining the energy of the low-energy photon. As a result, the reconstructed photon energies were too high in events with photons close to each other.

Finally, it should be noted that we did not re-determine the cluster positions after subtracting the energy contribution due to nearby clusters, This could lead to a small mis-measurement of the cluster position.

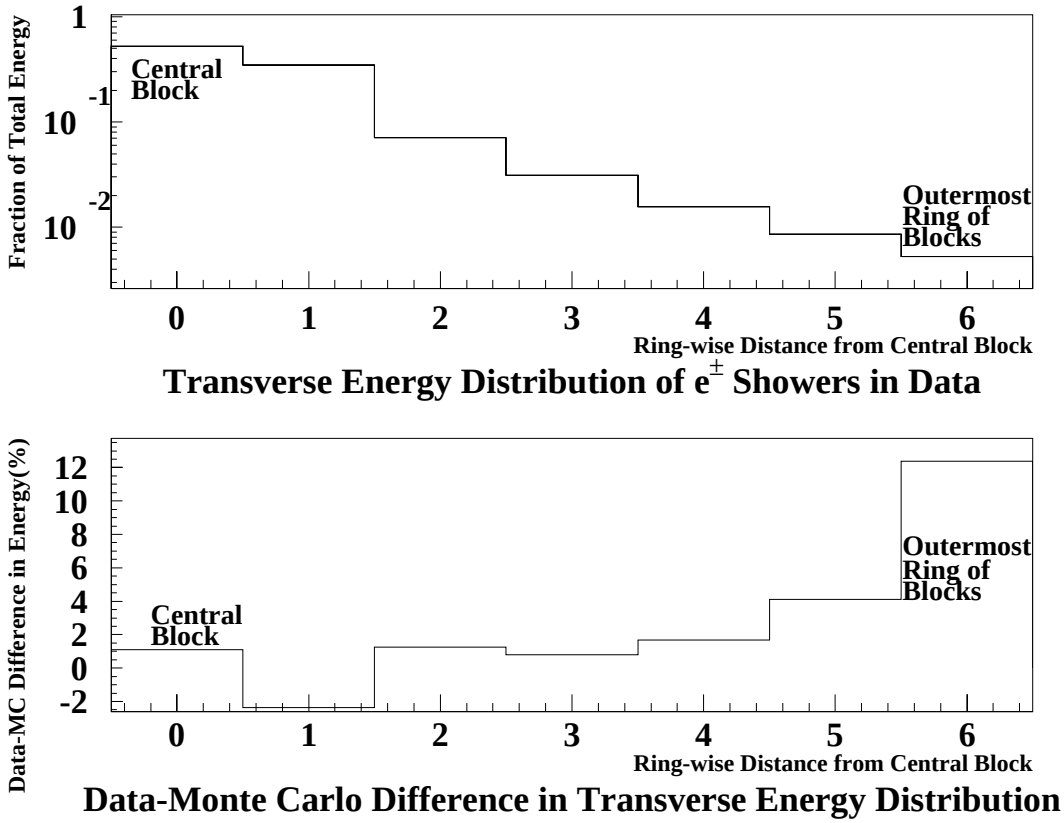

Figure A.2: Top: Transverse energy distributions of $e^{\pm}$ showers in Data. Bottom: Data-Monte Carlo difference in transverse energy distribution. The energy within each square ring of blocks is summed and then compared.

The effect of these features and the systematic uncertainties due to nearby photons are described in detail in Appendix C.

A.5 Sneaky Energy

In addition to applying the sneaky energy correction to events with two or more photons around the same beam hole, we also treated the two clusters near the same beam hole as neighboring clusters and subtracted the neighbouring energy from each cluster. This meant that too much energy was being subtracted from each photon near the hole. Although the mis-reconstruction of overlapping photon showers near the holes affected vacuum beam $2\pi^0$ events more than regenerator beam $2\pi^0$ events,

the potential bias could be reduced because the Monte Carlo events were similarly mis-reconstructed. The effect of data-Monte Carlo differences in the treatment of clusters near the beam holes is discussed in Chapter 9.

A.6 Linearity Correction

The linearity correction was determined for every channel separately. For some channels, there were not enough electrons at low energies(<10 GeV), so we extrapolated the correction using electrons at higher energies. Since the extrapolation might not accurately reflect the low-energy response, there may be non-linearities in the energy reconstruction of low-energy photons. We tried to correct for low-energy (< 5 GeV) non-linearities by comparing the reconstructed π^0 and $\pi^+\pi^-$ vertices in $K_L \to \pi^+\pi^-\pi^0$ events. This correction had no observable effect on $Re(\epsilon'/\epsilon)$, so it was not applied in the final analysis. Although there were many channels without many high-energy (>50 GeV) electrons, this was less of a concern since the mean photon energy from $K_{L,S} \to \pi^0\pi^0$ events was lower than the mean K_{e3} electron energy for a given channel.

APPENDIX B
NEUTRAL MODE ENERGY SCALE SYSTEMATICS STUDIES

In this appendix, we first discuss how the various decay modes mentioned in Section 9.2.3 were used to check the neutral mode energy scale and then describe the effect of different energy scale application schemes on these modes. We conclude this appendix by explaining how the systematic error on $Re(\epsilon'/\epsilon)$ due to the neutral mode energy scale was assigned.

B.1 Decay Modes used in Neutral Mode Energy Scale Study

In this section, we describe the decay modes that were used to study the neutral mode energy scale, and investigate to what extent these modes were useful in studying the variation of the $K_{L,S} \to \pi^0\pi^0$ energy scale along the decay region. The usefulness and drawbacks of each of the modes discussed are summarized in Table B.1.

B.1.1 Hadronic Interactions at the Regenerator

Hadronic interactions in the regenerator that produced $2\pi^0$ were used to compare the data and Monte Carlo energy scales at the regenerator. Such hadronic regenerator interactions were referred to as regenerator "junk" events. To study the data and Monte Carlo energy scales using regenerator "junk" events, we compared the data and Monte Carlo reconstructed $z_{2\pi^0}$ positions after accounting for the mean production point for regenerator "junk" events in which all four photons from the $2\pi^0$ decay escaped the regenerator.

$2\pi^0$ regenerator "junk" events were isolated by selecting well-reconstructed regenerator beam events in the kaon mass sidebands that had no extra in-time clusters and applying tight χ^2_{shape} and $\chi^2_{\pi^0}$ cuts to reduce contamination from non-photons[1].

To relate the data-Monte Carlo energy scale agreement seen with regenerator "junk" events to that of $K_{L,S} \to \pi^0\pi^0$ events, we compared the kinematic distributions for regenerator "junk" and $K_{L,S} \to \pi^0\pi^0$ events between 123 m and 128 m from the target as shown in Figures B.1 and B.2. Although the mean four-photon energy was higher for regenerator "junk" events, the distributions shown in Figures B.1 and B.2 agreed well within each 20 GeV kaon energy bin. We also compared the amount of underlying energy in regenerator "junk" and $K_{L,S} \to \pi^0\pi^0$ events and found that the additional energy due to other particles (e.g., neutrons) produced during hadronic interactions in the regenerator was negligible. The good agreement in photon energy, photon angle, minimum photon separation and underlying energy distributions between regenerator "junk" and $K_{L,S} \to \pi^0\pi^0$ modes indicated that the data and Monte Carlo $z_{2\pi^0}$ distributions for regenerator "junk" events should agree after the final energy scale had been applied.

B.1.2 $K_L \to \pi^0\pi^0\pi^0$ Decays

$K_L \to \pi^0\pi^0\pi^0$ decays were also used to check the neutral mode energy scale at the regenerator. The data and Monte Carlo reconstructed z_K distributions at the regenerator edge were compared after accounting for the effective regenerator edge for $K_L \to 3\pi^0$ events, which was 5.5 mm upstream of the downstream physical edge of the regenerator. Cluster reconstruction and energy scale corrections were identical to that in the $2\pi^0$ mode.

B.1.3 $K^* \to \pi^0 + K_S$ Decays at the Regenerator

The decay $K^* \to \pi^0 K_S$, in which the K_S decayed to $\pi^+\pi^-$ outside the regenerator, was used as a cross-check of the neutral mode energy scale at the regenerator. By

[1]Relaxation of the the χ^2_{shape} and $\chi^2_{\pi^0}$ cuts did not affect the data-Monte Carlo regenerator edge comparison significantly.

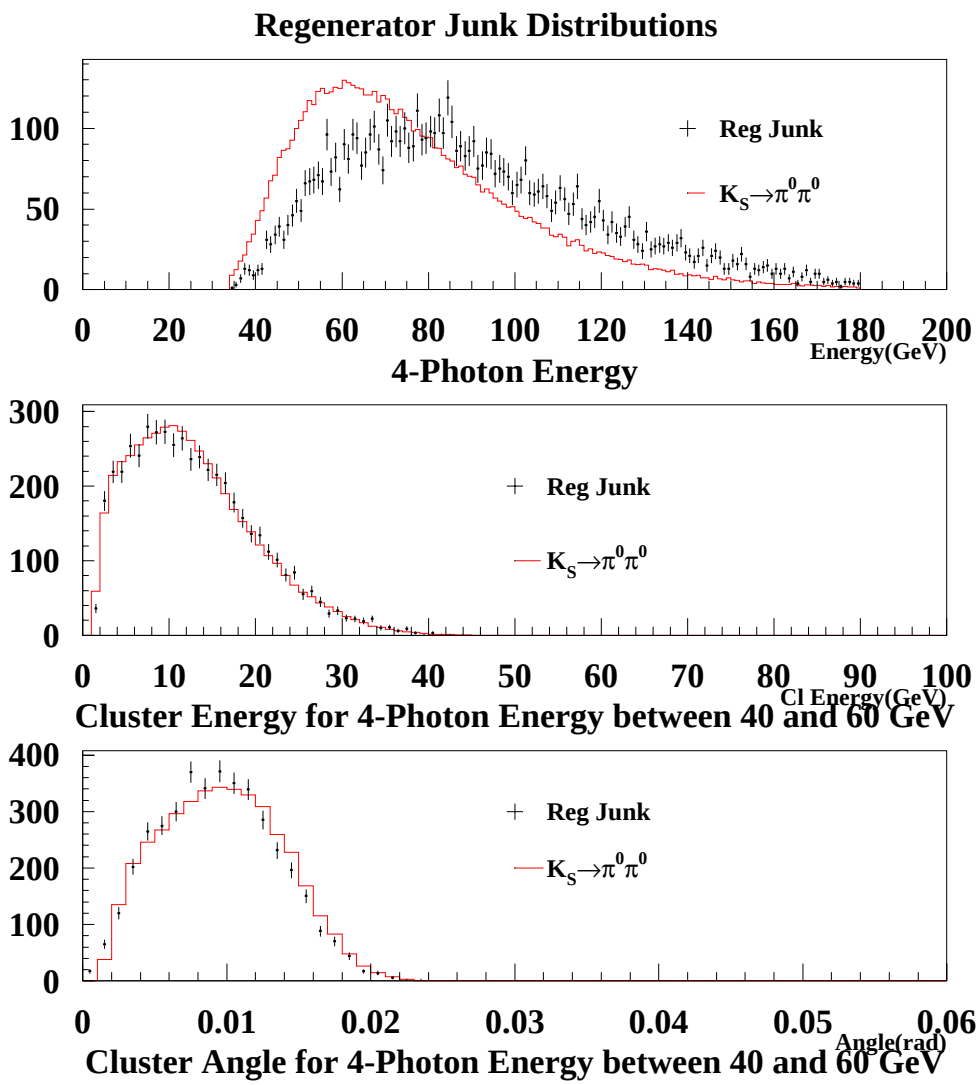

Figure B.1: Comparison of Regenerator "Junk" and with $K_{L,S} \to \pi^0\pi^0$ data distributions. The $K_{L,S} \to \pi^0\pi^0$ events chosen have a z-vertex between 123 and 128 m.

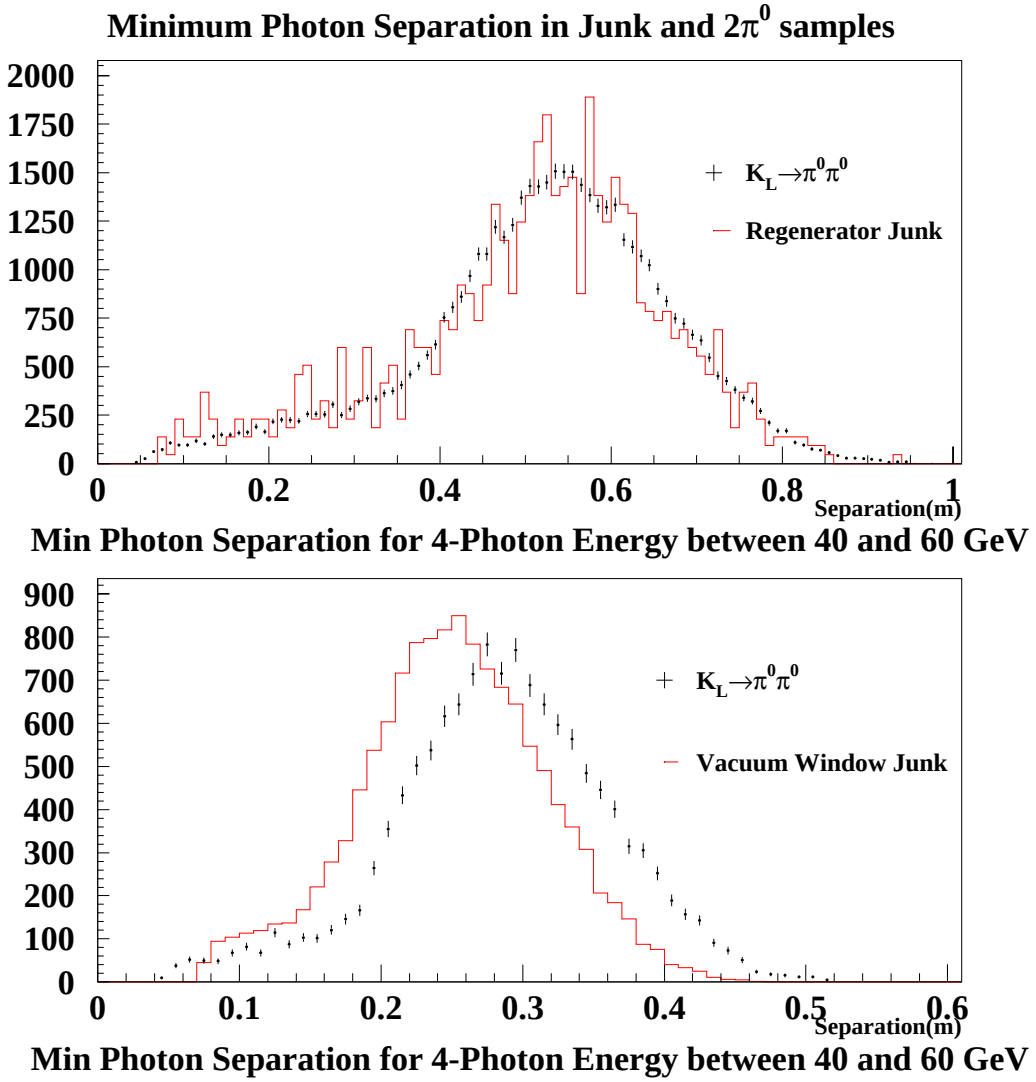

Figure B.2: Minimum Photon Separation in regenerator (top plot) and vacuum window "junk" (bottom plot) data compared with $K_{L,S} \to \pi^0\pi^0$ data. The four-photon energy was between 40 GeV and 60 GeV. The $K_{L,S} \to \pi^0\pi^0$ events chosen had a z_K-vertex between 123 m and 128 m in the top plot and a z_K-vertex between 153 and 158 m in the bottom plot. The distributions are normalized such that their areas are the same.

assuming that the invariant mass of the two photons was the π^0-mass, we measureed and compared the z-vertex formed by the photons in data and Monte Carlo.

B.1.4 Hadronic Interactions in the Vacuum Window Region

Hadronic interactions in the vacuum window region also produced events with $2\pi^0$. Such events were referred to as vacuum window "junk" events. To study the energy scale at the downstream end of the decay region, we simulated $2\pi^0$ production in the vacuum window, DC1 and the helium bags just downstream of the vacuum window and compared the reconstructed $2\pi^0$ vertex with the data in the vacuum beam. Vacuum window "junk" events were isolated using the same reconstruction and analysis cuts (other than the z_K-vertex position cut) as regenerator "junk" events.

In order to understand to what extent vacuum window "junk" events could be used to study the neutral mode energy scale at the downstream end of the decay region, we compared vacuum window "junk" and $K_{L,S} \to \pi^0\pi^0$ data distributions at z_{kaon} between 153 m and 158 m from the target as shown in Figure B.3. The vacuum window "junk" and $K_{L,S} \to \pi^0\pi^0$ distributions of four-photon energy, cluster energy and cluster angle agreed well within each 20 GeV kaon energy bin. However, as seen in Figure B.2, the vacuum window "junk" and $K_{L,S} \to \pi^0\pi^0$ events had different photon separation distributions. Based on the comparison of vacuum window "junk" and $K_{L,S} \to \pi^0\pi^0$ distributions, we conclude that vacuum window "junk" events could be used to measure the $K_{L,S} \to \pi^0\pi^0$ data-Monte Carlo energy scale at the downstream end of the decay region as long as the energy scale is not affected greatly by the separation of photons.

B.1.5 $K_L \to \pi^+\pi^-\pi^0$ Decays

In $K_L \to \pi^+\pi^-\pi^0$ decays, the π^0 mass directly depended on the neutral energy scale if the kaon decay vertex was assumed to be the reconstructed $\pi^+\pi^-$ vertex. By comparing the reconstructed π^0 mass, m_{π^0}, as a function of the reconstructed kaon vertex position in data and Monte Carlo (Figure B.4), energy scale differences between

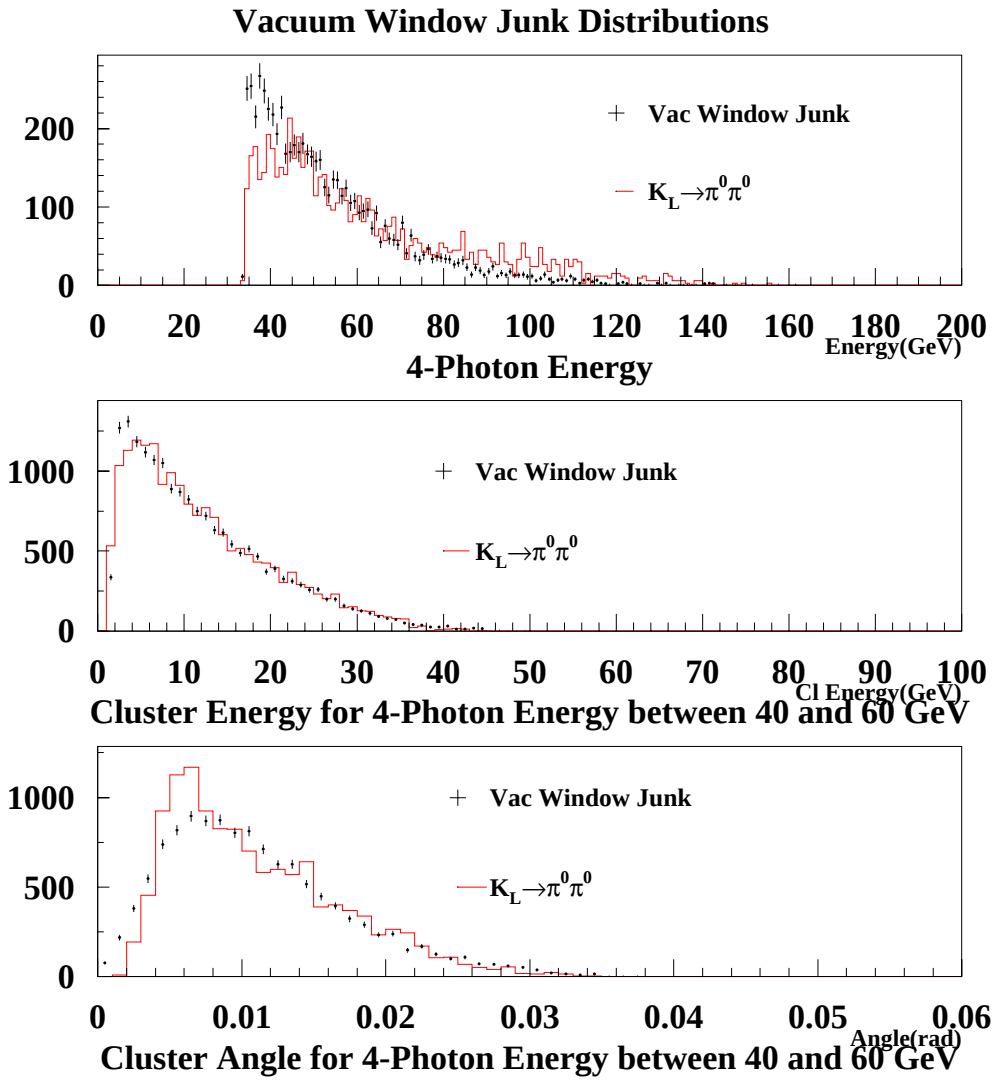

Figure B.3: Distributions of vacuum window "junk" data compared with $K_{L,S} \to \pi^0\pi^0$ data. The $K_{L,S} \to \pi^0\pi^0$ events chosen have a z_K-vertex between 153 m and 158 m.

data and Monte Carlo could be studied throughout the decay region[2]. Although $K_L \to \pi^+\pi^-\pi^0$ decays were useful in checking the neutral mode energy reconstruction over the decay volume, the $K_L \to \pi^+\pi^-\pi^0$ event sample was insensitive to energy scale differences due to close, energy-asymmetric clusters which were present in some $K_{L,S} \to \pi^0\pi^0$ events; the kinematic minimum photon separation for $K_L \to \pi^+\pi^-\pi^0$ decays was 20 cm at the calorimeter for π^0 at KTeV, and the two photons had similar energies when they were close to each other.

As seen in Figure B.4, the variation of the π^0 mass with z_K was the same in the regenerator and vacuum beams. Although there was more accidental activity in the regenerator beam, the good agreement in the π^0 mass between the regenerator and vacuum beams showed that the variation in the reconstructed π^0 mass along the decay region was not due to accidental activity but had to do with photon position or energy mis-reconstruction. Another possible explanation for the variation in the reconstructed π^0 mass was a bias in the charged vertex reconstruction, although this effect was expected to be small. Figure B.5 shows the angular and energy distributions of photons in $K_L \to \pi^+\pi^-\pi^0$ events at $\overline{z}_{kaon}$=126 m and $\overline{z}_{kaon}$=156 m. The photon angle and energy distributions were different at different regions of the decay volume; these differences could be responsible for the π^0 mass variation as a function of z_{kaon}.

B.1.6 $\eta \to \pi^0\pi^0\pi^0$ at the Vacuum Window

η mesons that were produced hadronically in the vacuum window could subsequently decay via the $\pi^0\pi^0\pi^0$ channel. By reconstructing such decays in the data and Monte Carlo, the neutral energy scale for decays at the vacuum window could be studied. This was a useful cross-check of the energy scale since like the vacuum window "junk" and $K_L \to \pi^+\pi^-\pi^0$ decays, these decays occurred at the end of the decay volume.

[2]Instead of comparing m_{π^0} between data and Monte Carlo, we could also compare the difference between the $\pi^+\pi^-$ and π^0 vertices in the data and Monte Carlo by assuming the PDG [45] value for m_{π^0}

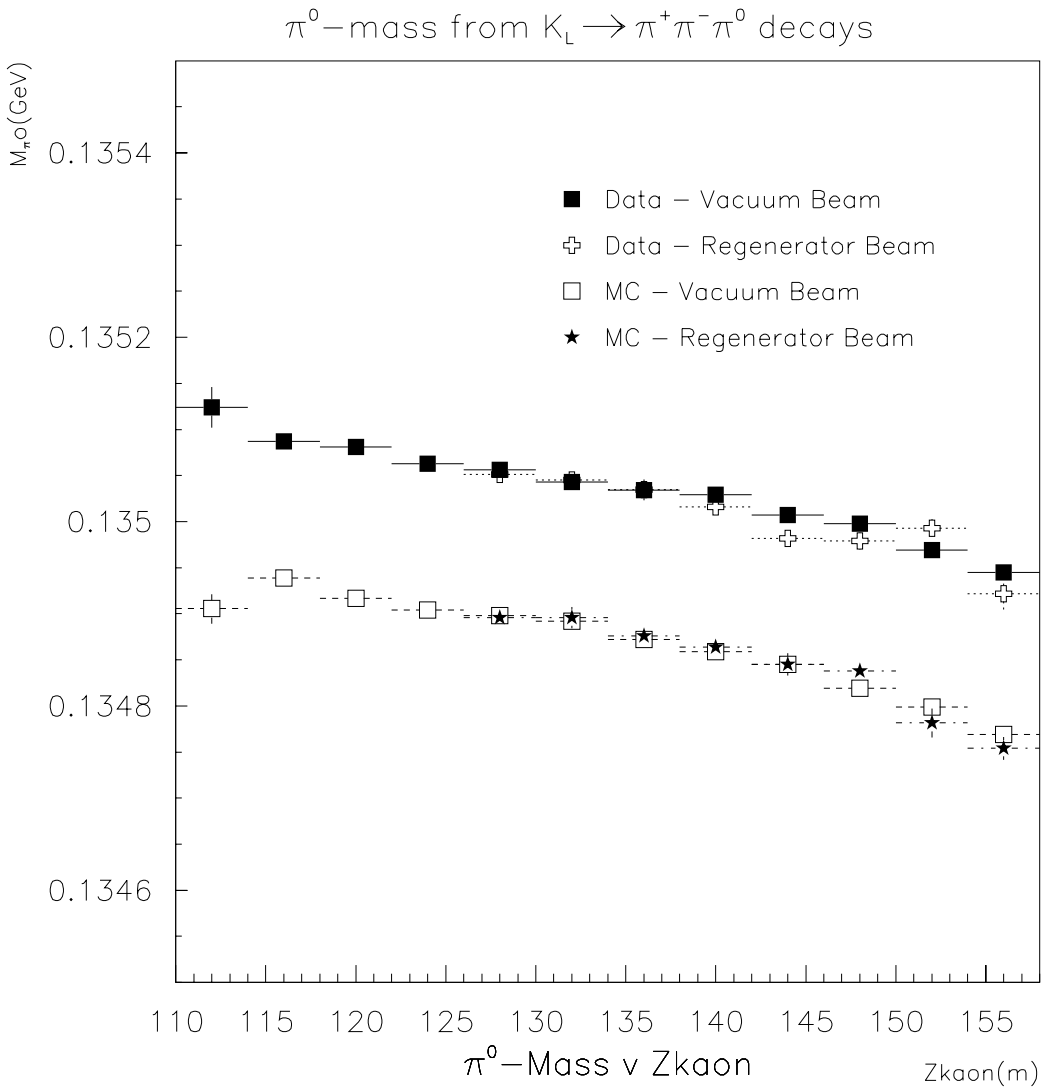

Figure B.4: Data-Monte Carlo comparison of the π^0 mass from $K_L \rightarrow \pi^+\pi^-\pi^0$ events in the Vacuum and Regenerator Beams as a function of z_{kaon}. The final energy scale based on $K_{L,S} \rightarrow \pi^0\pi^0$ events has not been applied.

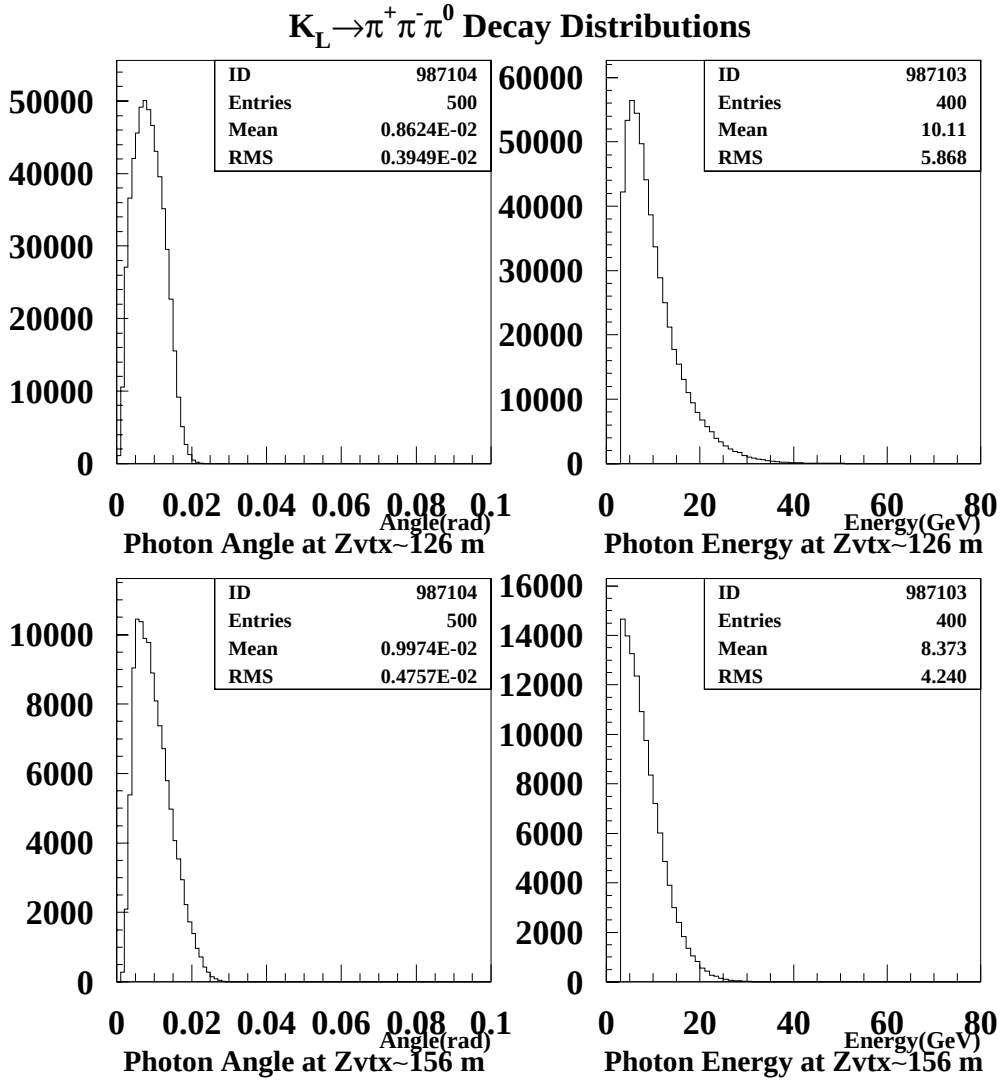

Figure B.5: Distributions of 1997 $K_L \rightarrow \pi^+\pi^-\pi^0$ data events in the vacuum beam. Top: $z_{kaon} \sim 126$ m. Bottom: $z_{kaon} \sim 156$ m.

B.1.7 $K_{L,S} \to \pi^0\pi^0$ Dalitz Decays

$2\pi^0$ Dalitz decays where one π^0 decayed to γe^+e^- and the other π^0 decayed to two photons were used to check the neutral mode energy scale. By comparing the z_{π^0}-difference between the $\pi^0 \to \gamma\gamma$ and $\pi^0 \to e^+e^-\gamma$ vertices in data and Monte Carlo, we were able to compare the data and Monte Carlo energy scales. Only regenerator beam events were used. The $\pi^0 \to e^+e^-\gamma$ vertex was determined by reconstructing the electron momenta with the spectrometer and the photon energy with the calorimeter. The $\pi^0 \to \gamma\gamma$ vertex was reconstructed as described in Section 7.2.2). We did not use the e^+e^- vertex as the π^0 vertex because the vertex resolution was poor for tracks with a small opening angle. Although the vertex resolution for the electrons was poor, the track momentum measurement was good enough to study the photon energy scale. Since there was only a small sample of $2\pi^0$ Dalitz decays in 1997, we could only compare the mean data and Monte Carlo distributions over the full regenerator beam decay region. Hence, the $2\pi^0$ Dalitz channel tested the data-Monte Carlo energy scale agreement at the average z_K, $\sim$130 m.

B.2 Data-Monte Carlo Energy Scale Comparisons

Having described the various modes used to study the neutral mode energy scale in the previous section, we now discuss the effect of the nominal energy scale correction on these modes and investigate the effect of different data-Monte Carlo energy scale corrections on the photon reconstruction and $Re(\epsilon'/\epsilon)$. We also study the effect of energy non-linearities on the data-Monte Carlo energy scale comparisons in various modes.

The data-Monte Carlo agreement between the data and Monte Carlo z-distributions in the various modes was determined after applying the nominal energy scale (Figure 7.9) to data events. As shown in Figure 9.4, the data-Monte Carlo agreement in the various modes at the regenerator edge was good but at the vacuum window, there was a data-Monte Carlo discrepancy seen in hadronic vacuum window interac-

Mode	Usefulness	Drawbacks
$K_L \to \pi^+\pi^-\pi^0$	Studied energy scale over full decay region	Insensitive to photons which were closer than 20 cm Insenstive to photons which were strongly energy-asymmetric Sensitive to Charged Vertex Reconstruction
Regenerator " "junk"	Kinematic distributions agreed with $K_{L,S} \to \pi^0\pi^0$ at a fixed 4-photon energy	Large uncertainties in determining average production point in regenerator
Vacuum Window "junk"	Explored downstream decay region	More sensitive than $K_{L,S} \to \pi^0\pi^0$ events to overlapping photons Sensitive to simulation at DC1 vacuum window, helium bags
$\eta \to 3\pi^0$	Explored downstream decay region	Kinematics different from $K_{L,S} \to \pi^0\pi^0$ events Small sample
$2\pi^0$ Dalitz	Explored region between regenerator and vacuum window Sensitive to overlapping clusters which were energy-asymmetric	Kinematics different from $K_{L,S} \to \pi^0\pi^0$ events Very small sample
$K_L \to \pi^0\pi^0\pi^0$	Sensitive to low energy	6 photons instead of 4
$K^* \to \pi^0 + K_S$	Additional cross-check at regenerator	Uncertainty over mean production point

Table B.1: Usefulness and drawbacks of using various modes to study neutral mode energy scale. The list is not exhaustive.

tions[3]. The data reconstructed (1.89±0.41) cm and (2.46±0.37) cm downstream (see Figure 9.5) of the Monte Carlo in the 1996 and 1997 data sets, respectively.

Since the nominal energy scale correction was based on the four-photon (kaon) energy rather than the photon energy, the nominal energy scale correction was not completely appropriate for modes with more or less than four photons. Therefore, we studied the effect of two other alternative energy scale corrections on the data. We studied the effect of applying a flat energy scale correction (independent of kaon energy) and a scale correction derived from the nominal scale correction but based on the photon energy. The difference in $Re(\epsilon'/\epsilon)$ between using the alternative energy scale corrections described below and the nominal (E_K-dependent) energy scale correction was 0.5×10^{-4}.

We applied a flat energy scale correction of 0.99929 to the different modes described in the previous section. The flat energy scale correction was chosen such that the data and Monte Carlo z_K-distributions agreed at the regenerator edge for $K_{L,S} \to \pi^0\pi^0$ events. After applying the flat energy scale correction to the various modes, the data-Monte Carlo agreement at the regenerator edge and vacuum window were consistent with that obtained using the nominal energy scale correction.

We also investigated the effect of an energy scale based on the photon energy. For each photon of energy, E_γ, the energy scale correction, $f_{scale}(E_\gamma)$, was given by the nominal energy scale correction for kaon energy, $E_K = 4E_\gamma$, such that

$$f_{scale}(E_\gamma) = f^{Data}_{photons}(E_K = 4E_\gamma). \tag{B.1}$$

A different scale was applied to each photon in an event. Applying the photon energy-based scale resulted in a large data-Monte Carlo disagreement at both the regenerator and vacuum window in the various modes.

In order to determine the sensitivity of the energy scale to energy and position non-linearities, we studied the data-Monte Carlo agreement in $K_{L,S} \to \pi^0\pi^0$ as well as regenerator and vacuum window "junk" events after applying several different

[3]By construction, the data-Monte Carlo agreement for $K_{L,S} \to \pi^0\pi^0$ events at the regenerator edge was exact.

energy and position-based reconstruction modifications (see Appendix C). The reconstruction modifications improved the data-Monte Carlo agreement in distributions which were affected by the energy and position linearity. After each modification, the $K_{L,S} \to \pi^0\pi^0$-based regenerator edge matching scale was applied, so that the data-Monte Carlo z_K distributions agreed at the regenerator edge in the $K_{L,S} \to \pi^0\pi^0$ mode. For each of the reconstruction modifications, the data-Monte Carlo agreement for "junk" events at the vacuum window and the regenerator edge were seen to be consistent with that obtained from the nominal analysis.

B.3 Assignment of Systematic Uncertainty

This section explains how the systematic error on $Re(\epsilon'/\epsilon)$ due to the neutral mode energy scale was assigned. Since the procedure for assigning the systematic error was the same for the 1996 and 1997 neutral modes, we first discuss the systematic error for the 1997 data set and then present the uncertainty for the 1996 data set.

Since the data-Monte Carlo z-distribution agreement at the regenerator edge ($z \sim 125\ m$) was good in all the modes, the systematic uncertainty due to the neutral mode energy scale was based on the data-Monte Carlo z-difference at the downstream end of the decay region, $z \sim 158m$. At the vacuum window region, the $\eta \to 3\pi^0$ and hadronic "junk" modes showed that the data reconstructed farther downstream than the Monte Carlo, while in $K_L \to \pi^+\pi^-\pi^0$ events the data were farther upstream of the Monte Carlo by (0.68±0.29) cm[4].

The data-Monte Carlo discrepancy due to hadronic interactions at the vacuum window, (2.46±0.37) cm (in 1997), was used to set the systematic error on $Re(\epsilon'/\epsilon)$ because it was the mode with the largest data-Monte Carlo difference. Since vacuum window "junk" events were more sensitive to the mis-reconstruction of close clusters (see Figure B.2), the data-Monte Carlo energy scale difference seen in vacuum window "junk" events might be larger than that for $K_{L,S} \to \pi^0\pi^0$ events at the downstream

[4]Data and Monte Carlo $K_L \to \pi^+\pi^-\pi^0$ events were compared after applying a flat energy scale correction to the data. The flat scale was derived from $K_{L,S} \to \pi^0\pi^0$ events but accounted for the difference between the mean photon energies in $K_L \to \pi^+\pi^-\pi^0$ and $K_{L,S} \to \pi^0\pi^0$ events.

end of the decay region. Nevertheless, we adopted a cautious approach in assigning the energy scale systematic error by using hadronic vacuum window interactions to determine the systematic uncertainty.

To determine the uncertainty, an energy scale which was a linear function of the kaon z-position was applied to $K_{L,S} \rightarrow \pi^0\pi^0$ data events. The energy scale shifted the reconstructed kaon z-vertex in data 2.64 cm upstream at the vacuum window but did not cause any change in the reconstructed z-vertex position at the regenerator edge. Based on the variation of the π^0 vertex z-position with z_K in $K_L \rightarrow \pi^+\pi^-\pi^0$ events shown in Figure 9.4, it is plausible that applying a scale which varied linearly with the kaon z-vertex position was a good estimate of the scale variation along the decay region. The wide triangular band seen in Figure 9.4 shows the range of data-Monte Carlo discrepancies that was covered by the energy scale systematic error. This linearly varying energy scale caused a change in $Re(\epsilon'/\epsilon)$ of -1.40$\times10^{-4}$, as well as an increase in the slope of the $K_{L,S} \rightarrow \pi^0\pi^0$ data-Monte Carlo z_K overlay of 0.26$\times10^{-4}$. Since the change in z_K-slope was a measure of the acceptance change, for which we assigned a separate systematic error, we subtracted the change in $Re(\epsilon'/\epsilon)$, -0.31$\times10^{-4}$, expected from the z_K-slope increase from the total change in $Re(\epsilon'/\epsilon)$ due to the linearly varying energy scale in quadrature. The systematic error on $Re(\epsilon'/\epsilon)$ due to the neutral mode energy scale was 1.37$\times10^{-4}$ in 1997.

The large systematic error assigned covered the shift in $Re(\epsilon'/\epsilon)$ due to the alternative energy scale corrections discussed in the previous section. To ensure that we were not under-estimating the systematic uncertainty, we determined the effect of matching the data and Monte Carlo $K_{L,S} \rightarrow \pi^0\pi^0$ distributions at the regenerator and upstream edge of the vacuum beam decay region (z_K <122 m) as well as the hadronic interactions at the vacuum window. The change in $Re(\epsilon'/\epsilon)$ based on this "global" fit was consistent with the assigned systematic error due to the energy scale.

The systematic uncertainty on $Re(\epsilon'/\epsilon)$ in 1996 due to the neutral mode energy scale was 1.08$\times10^{-4}$ based on the (1.89$\pm$0.41) cm data-Monte Carlo difference seen in hadronic vacuum window interactions.

It is interesting to compare the energy scale systematic error of 1.37$\times10^{-4}$ in 1997 with the 0.91$\times10^{-4}$ change in $Re(\epsilon'/\epsilon)$ that would be expected if we had assumed that

the shift of 2.64 cm at the vacuum window only affected the z_K-cut, causing a change in the number of downstream vacuum beam events. As described in Section 7.3.1, the difference arose from the fact that the simple counting scheme did not account for the effect of the neutral mode energy scale on the kaon energy distribution.

APPENDIX C
STUDIES OF ENERGY AND POSITION RECONSTRUCTION IN THE NEUTRAL MODE

Differences between the data and the Monte Carlo simulation due to the neutral mode energy and position reconstruction were seen in several $K_{L,S} \to \pi^0\pi^0$ distributions. These $K \to 2\pi^0$ distributions included:

- the variation of kaon mass with kaon energy shown in Figure C.1;
- the variation of kaon mass with the kaon vertex z-position seen in Figure C.2;
- the variation of kaon mass with average photon angle as shown in Figure C.3;
- the variation of kaon mass with minimum photon separation as seen in Figure C.4;
- the variation with kaon energy of the data-Monte Carlo difference in the reconstructed regenerator edge position as shown in Figure 7.7.

In this appendix, we discuss possible causes for these data-Monte Carlo reconstruction differences and then study the effect of these differences on $Re(\epsilon'/\epsilon)$. The assignment of the systematic uncertainty on $Re(\epsilon'/\epsilon)$ due to photon energy and position reconstruction is described at the end of this appendix.

C.1 Data-Monte Carlo Reconstruction Differences

We have mentioned several reconstruction differences between the $2\pi^0$ data and Monte Carlo in Chapters 4, 7, 8 and Appendix A. We present below some of the data-Monte Carlo reconstruction differences which could explain why the data and Monte Carlo distributions shown in Figures C.1, C.2, C.3 and C.4 were not the same.

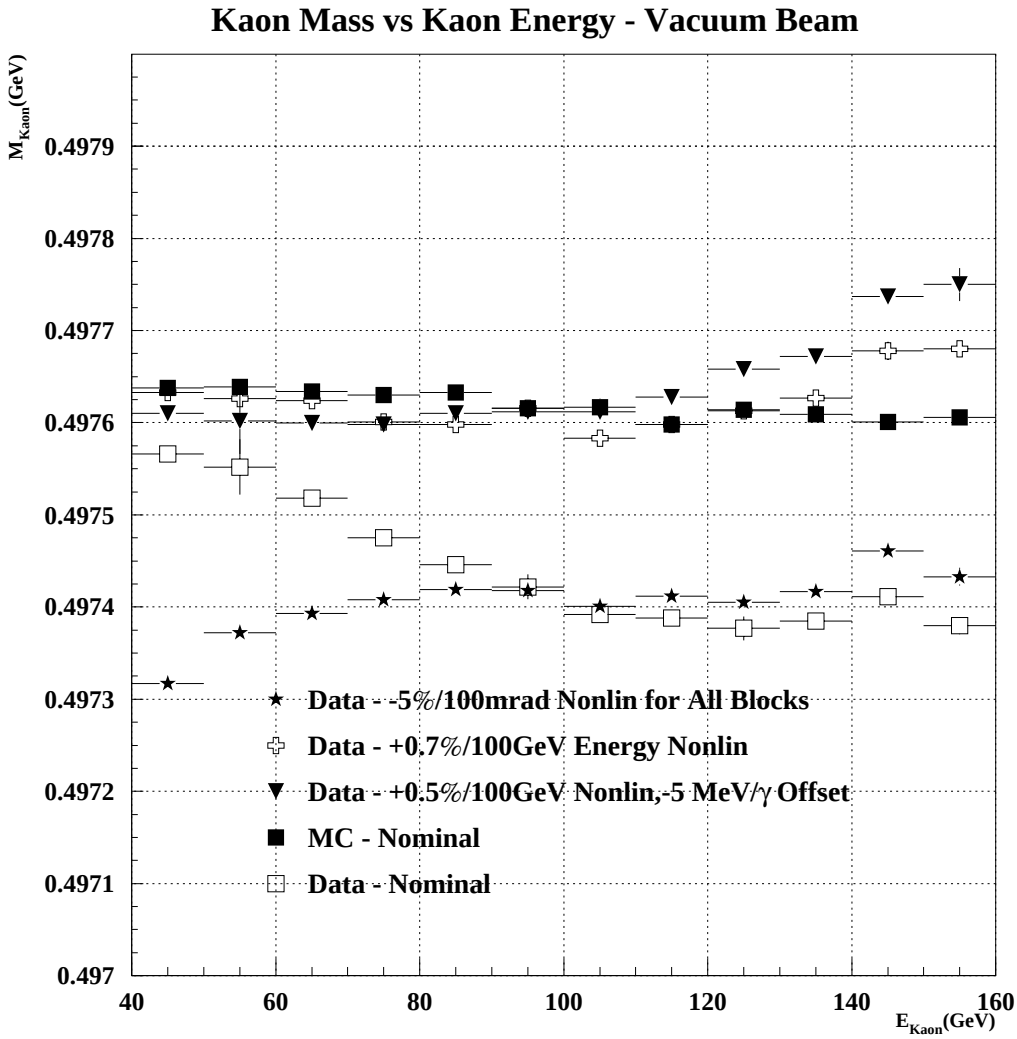

Figure C.1: Variation of kaon mass with kaon energy for vacuum beam background-subtracted $2\pi^0$ data in 1997, Monte Carlo and three of the energy nonlinearity distortions that were studied. A global change in energy scale has no effect on the kaon mass.

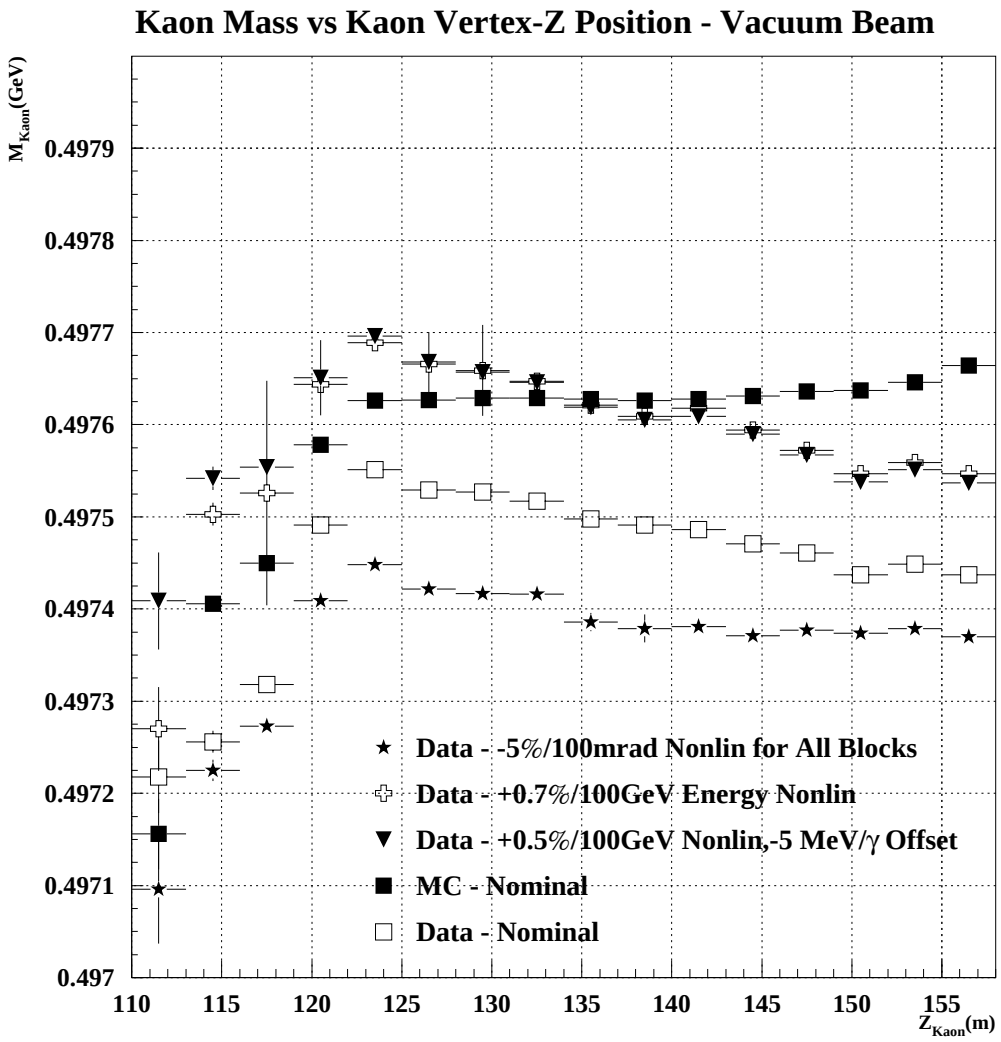

Figure C.2: Variation of kaon mass versus kaon vertex z-position for vacuum beam background-subtracted $2\pi^0$ data in 1997, Monte Carlo and the 3 of the energy non-linearity distortions that were studied.

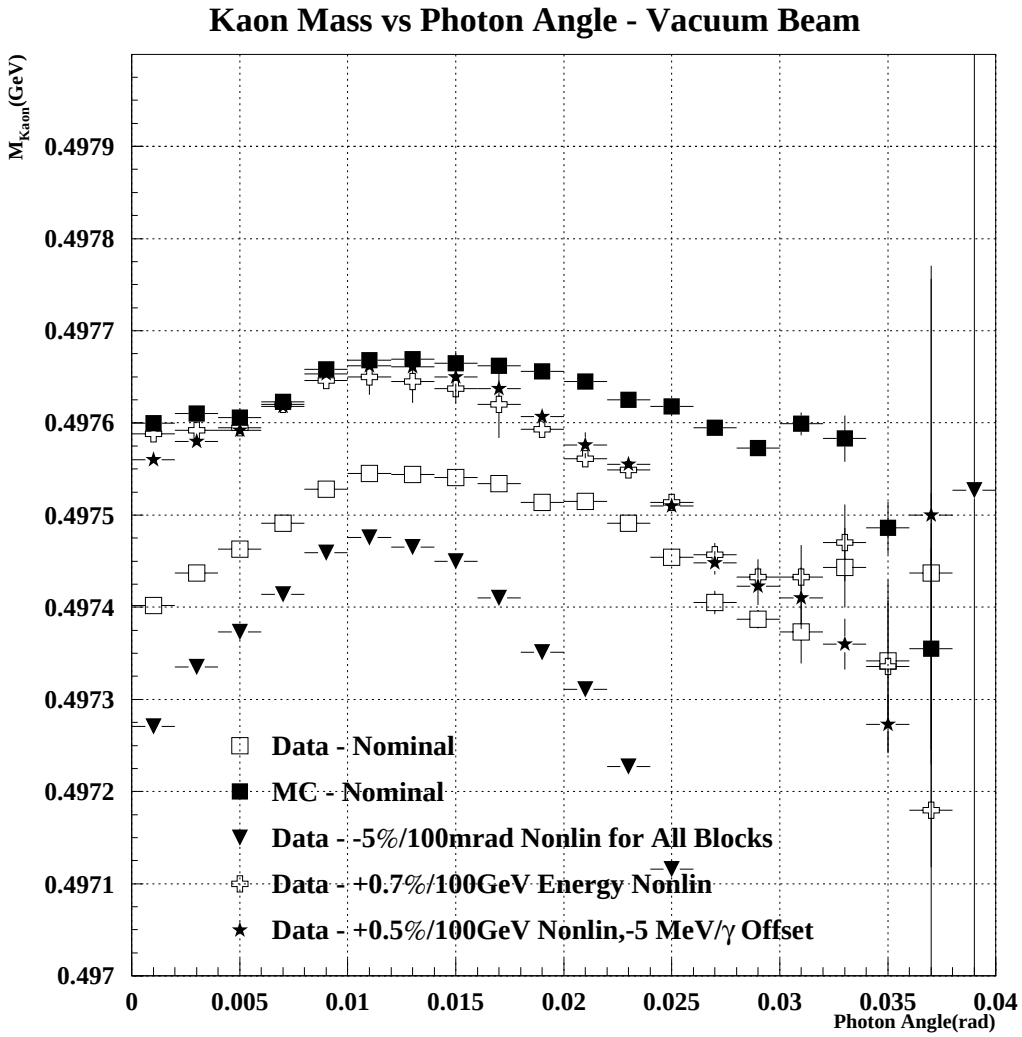

Figure C.3: Variation of Kaon mass with photon angle for background-subtracted $2\pi^0$ vacuum beam data in 1997, Monte Carlo and the 3 of the energy nonlinearity distortions that were studied.

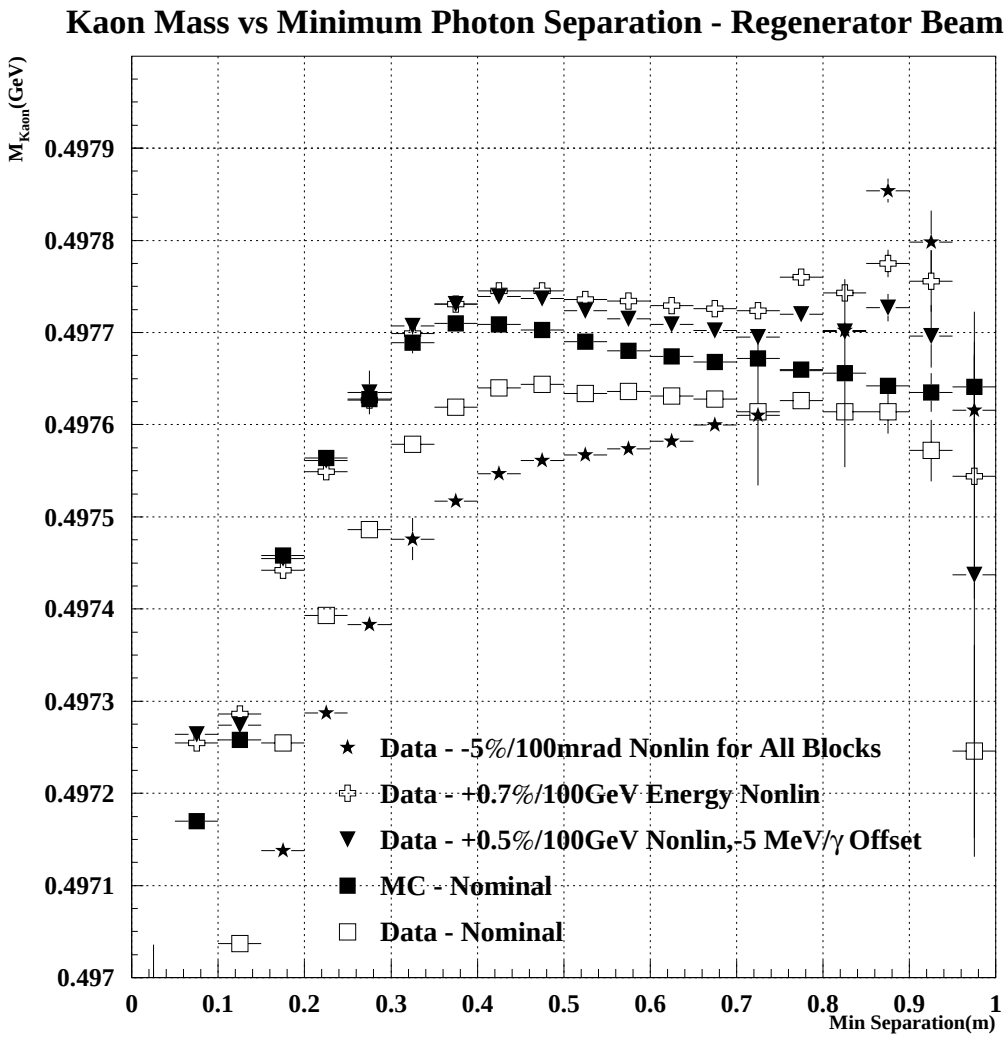

Figure C.4: Variation of kaon mass with minimum photon separation for 1997 background-subtracted vacuum beam $2\pi^0$ data, Monte Carlo and the 3 of the energy nonlinearity distortions that were studied.

- Photon energy non-linearities: Photon energy linearity differences between the data and Monte Carlo were present because the Monte Carlo did not simulate the effect of longitudinal non-uniformities in data exactly (see Section 8.4.2). Data-Monte Carlo linearity differences were also introduced by differences between the data and Monte Carlo due to the readout threshold correction ($E_{sub-thresh}$), as well as by not simulating DPMT pedestal fluctuations. The data-Monte Carlo differences in the readout threshold correction are described in Appendix A.

- Shower Depth for Photons: As seen in Section 7.2.1, a mis-reconstruction of the mean shower depth led to a mis-determination of the kaon mass and vertex z-position. Since the kaon vertex positions of data and Monte Carlo $K_{L,S} \rightarrow \pi^0\pi^0$ events were determined using the same photon shower depth, 0.17 m, data-Monte Carlo differences in the shower mean could cause differences in the reconstructed kaon mass and z-vertex. Data-Monte Carlo differences in the shower mean arose because the Monte Carlo shower position was adjusted based on photon angle, energy and position during generation (see Section 8.4.2).

- Energy mis-reconstruction due to photon incident angle: The amount of energy that was deposited in a cluster of fixed size depended on the angle at which the photon was incident on the calorimeter. Since the showers in the simulation were generated at a fixed polar angle of 8 mrad, and no cluster energy correction based on the photon incident angle was applied to the data or Monte Carlo, there were data-Monte Carlo differences in the reconstruction of $K_{L,S} \rightarrow \pi^0\pi^0$ events. Since an angle-based correction was not applied during calibration, photon-electron differences in the incident angle for a given seed block led to non-linearities in the photon energy reconstruction. In addition, since the energy linearity correction ($f_{linearity}$) was based on electrons, the angular dependance of reconstructed photon energies was complicated further. Not accounting for the photon incident angle could also result in the mis-determination of the photon position since the position lookups were made from an average distribution of photons over the small-, large- and mixed-regions. However, since both

Monte Carlo and data position lookups were made in the same way, we expect any data-Monte Carlo difference in cluster position determination to be small.

- Treatment of overlapping photons: As described in Appendix A, there were data-Monte Carlo differences in the subtraction of "neighbouring energy" from photons because the "neighbouring energy" correction used a common map for both data and Monte Carlo analyses, despite differences between the data and Monte Carlo transverse energy distributions. Furthermore, since the "neighbouring energy" correction did not "separate" energy-asymmetric photons accurately, in both data and Monte Carlo, the kaon mass varied with the minimum photon separation (see Figure C.4).

  To separate the energy from overlapping photons (i.e., clusters containing blocks that were part of more than one cluster), transverse energy maps were used (see Section 4.5.1). Separate photon-based transverse maps were used for data and Monte Carlo events to account for data-Monte Carlo differences in the transverse energy distribution. However, since the energy scale was not determined for each channel individually (.i.e., a block-wise calibration was not perfored), there could still be data-Monte Carlo differences in separating overlapping photons. Another feature of the transverse maps was that they were made with a select group of photons which had a certain angular distribution. As a result, differences in the transverse energy distribution due to photon incident angle could cause a mis-reconstruction of photons that were close together. This effect was more important in data since Monte Carlo showers were generated at a fixed polar angle.

- Momentum mis-measurement during calibration: Charged mode reconstruction features that were only present in the data could have an effect on the energy calibration via the electron momentum measurement. A momentum mis-reconstruction could affect both the neutral mode energy scale and linearity. There could also be channel-to-channel variations in the energy reconstruction due to the momenutm mis-measurement during calibration.

C.2 Determining the Effect on $Re(\epsilon'/\epsilon)$ of Data-Monte Carlo Reconstruction Differences

In order to determine the effect on $Re(\epsilon'/\epsilon)$ due to the data-Monte Carlo $K_{L,S} \to \pi^0\pi^0$ reconstruction differences discussed in the previous section, the data reconstruction was modified to improve the data-Monte Carlo agreement in some or all of the distributions shown in Figures C.1, C.2, C.3 and C.4. Some of the distortions that we applied actually caused the data-Monte Carlo agreement in some distributions to get considerably worse; we did not consider these distortions in assigning an uncertainty on $Re(\epsilon'/\epsilon)$.

We applied combinations of the following energy and position reconstruction modifications and studied their effect on the data-Monte Carlo regenerator edge. After matching the data and Monte Carlo energy scales based on the $K_{L,S} \to \pi^0\pi^0$ z_K distributions at the regenerator, we compared data-Monte Carlo z_K distributions and measured the change in $Re(\epsilon'/\epsilon)$ with respect to the nominal analysis.

- Energy non-linearity applied to each cluster. We studied the effect of data-Monte Carlo photon linearity data differences by modifying the photon energies in data such that the photon energy was given by

$$E_{\gamma,new} = E_{\gamma,old}(1 + \alpha E_{\gamma,old}), \tag{C.1}$$

  where $E_{\gamma,old}$ was the original reconstructed photon energy, $E_{\gamma,new}$ was the modified photon energy and α was the energy non-linearity. Applying an energy non-linearity to each photon in the data improved data-Monte Carlo agreement in the variation of the kaon mass with kaon energy. Energy non-linearity modifications ranging from $\alpha = 0.3\%/100$ GeV to $\alpha = 0.7\%/100$ GeV were applied. (See Figure C.1.) We observed that the data-Monte Carlo difference in the kaon mass variation with kaon energy was reduced by applying an energy non-linearity of 0.7%/100 GeV to the data. The effects of these non-linearity modifications on other distributions are seen in Figures C.2, C.3 and C.4. Although the kaon mass agreement improved after applying an energy

non-linearity of 0.7%/100 GeV, there were still some data-Monte Carlo reconstruction differences. For example, the kaon energy variation of the data-Monte Carlo regenerator edge position difference (see Figure C.13) got much worse and there was still a data-Monte Carlo difference in the kaon mass variation with z_K.

- Energy offset applied to each cluster. To investigate the effect of data-Monte Carlo differences in the readout threshold correction and the amount of accidental energy in the calorimeter, we added a fixed amount of energy, E_{extra}, to each cluster in the data such that

$$E_{\gamma,new} = E_{\gamma,old} + E_{extra}, \tag{C.2}$$

where $E_{\gamma,old}$ was the original reconstructed photon energy and $E_{\gamma,new}$ was the modified photon energy. We studied the effect of applying energy offsets ranging from $E_{extra} = -5$ MeV/photon to $E_{extra} = 3$ MeV/photon to the data. Reducing the energy of each photon by 5 MeV in combination with applying a photon energy non-linearity of 0.5%/100 GeV to the data improved the data-Monte Carlo agreement in the kaon mass as shown in Figures C.1, C.2, C.3 and C.4.

- Energy scale based on seed block. We determined a separate energy scale for each channel such that the z_{π^0} and $z_{\pi^+\pi^-}$ vertices in $K_L \to \pi^+\pi^-\pi^0$ events would agree. The procedure had to be iterated eight times until the energy scale for each block converged. The energy scale was determined separately for data and Monte Carlo events and was ~0.1% for each channel. The effect on $K_{L,S} \to \pi^0\pi^0$ events is seen in Figures C.5, C.7 and C.9. Modifying the energy scale for each seed block based on $K_L \to \pi^+\pi^-\pi^0$ events reduced the kaon mass in both data and Monte Carlo events but had a negligible impact on the data-Monte Carlo kaon mass disagreement. The $K_L \to \pi^+\pi^-\pi^0$-based modification affected the data-Monte Carlo regenerator edge position agreement as shown in Figure C.12. Although the variation of the regenerator edge position difference

with kaon energy was not affected much, the mean edge difference between data-Monte Carlo was reduced.

- Modification of photon position based on shower depth. To account for shower depth differences in data and Monte Carlo, we modified the $x-$ and y-positions of each photon based on the track-cluster differences seen in $K_L \rightarrow \pi^{\pm}e^{\mp}\nu$ events. A separate correction was applied to data and Monte Carlo. The effect of these corrections is shown in Figures C.5, C.7 and C.9. For most photons, the shift in the $x-$ and y-positions corresponded to an upstream shift in the shower depth. Not surprisingly, the net result of shifting the shower depth upstream was to reduce the kaon mass. Since the difference between the shift in the data and Monte Carlo shower depths was small, the data-Monte Carlo reconstruction differences were not affected considerably by this modification.

- Energy non-linearity based on photon angle. To try to improve the data-Monte Carlo variation of the kaon mass with photon angle, we modified the energy of each photon in the data based on the photon incident angle. The modified photon energy, $E_{\gamma,new}$, was given by

$$E_{\gamma,new} = E_{\gamma,old}(1 + \alpha\theta_{\gamma}) \tag{C.3}$$

  where $E_{\gamma,old}$ was the original reconstructed photon energy, θ_{γ} was the photon angle and α was the energy non-linearity. The effect of applying an energy non-linearity, α, of -5%/100 mrad to the data is seen in Figures C.1, C.2, C.3 and C.4. Applying a photon energy non-linearity of -5%/100 mrad to all photons changed the data distributions dramatically and made the data-Monte Carlo agreement much worse. This suggested that while the energy reconstruction was very dependent on the photon angle, any energy non-linearity based on photon angle must have either been much smaller in magnitude or must have had a more complicated form (e.g., based on the average angle of the cluster seed during calibration).

- Energy correction based on nearby clusters. An additional correction to clus-

ters that were within 35 cm of each other was added to account for data-Monte Carlo differences in the treatment of close clusters. The correction was only applied to data and was based on the data-Monte Carlo difference in the reconstructed kaon mass variation with minimum photon separation. Figure C.10 shows the data-Monte Carlo difference in the variation of the kaon mass with minimum photon separation after applying the correction. As seen in Figures C.6 and C.8, the data-Monte Carlo difference in the kaon mass improved at higher energies, where the photons were closer together, and the kaon mass variation with z_K was reduced.

Some of the reconstruction modifications that we investigated affected the data-Monte Carlo z_K difference at the regenerator edge considerably. We also observed that some of the modifications caused a small change in the slope of the data-Monte Carlo z_K overlay. Figures C.11, C.12 and C.13 show the data-Monte Carlo difference in the reconstructed regenerator edge position for the energy and position reconstruction modifications that were studied. The effect of the reconstruction modifications on $Re(\epsilon'/\epsilon)$ that were applied are presented in Table C.2.

C.2.1 Cluster Reconstruction near the Holes

Besides investigating the effect (on $Re(\epsilon'/\epsilon)$) of the data-Monte Carlo reconstruction differences mentioned in the previous section, we studied the reconstruction of clusters near the beam holes by comparing the nominal measurement of $Re(\epsilon'/\epsilon)$ to a sample that excluded events that contained two or more photons near (within 7.5 cm) the same beam hole. As described in Appendix A, too much energy was being subtracted from photons when reconstructing the energy of overlapping photons near the beam hole. Differences between the data and Monte Carlo in the treatment of photons at the beam hole could potentially cause a large bias in $Re(\epsilon'/\epsilon)$ since the photon illumination was different for regenerator and vacuum beam $K_{L,S} \to \pi^0\pi^0$ events (see Table 4.2).

The effect of not allowing photon overlaps at the beam hole is presented in Table C.1. If events with two or more clusters near the same hole were excluded,

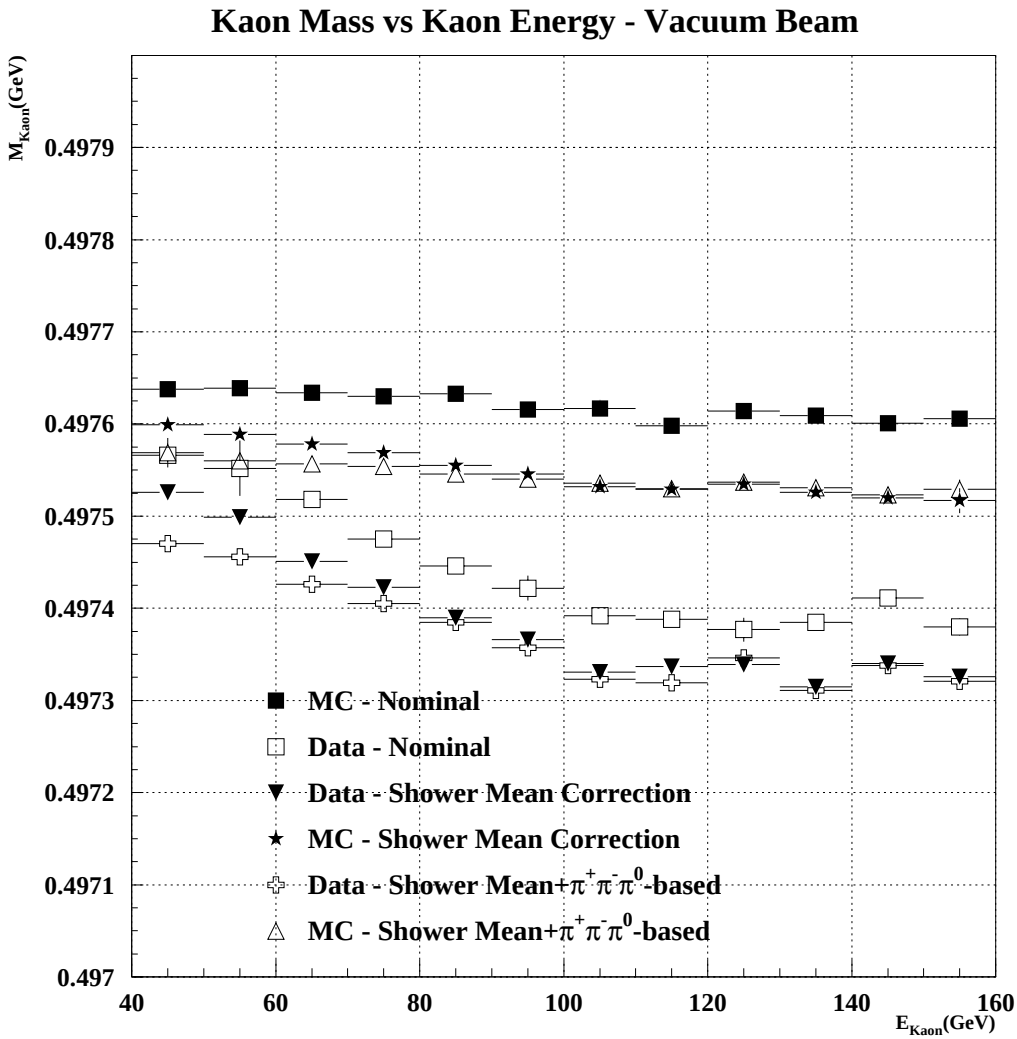

Figure C.5: Variation of kaon mass versus kaon energy for 1997 vacuum beam $2\pi^0$ background-subtracted data, Monte Carlo and distortions based on the shower mean and an blockwise energy scale determined using $K_L \to \pi^+\pi^-\pi^0$ events. Although a change in energy scale which is independent of calorimeter illumination has no effect on the kaon mass, an illumination-dependent energy scale has a small effect on the kaon mass.

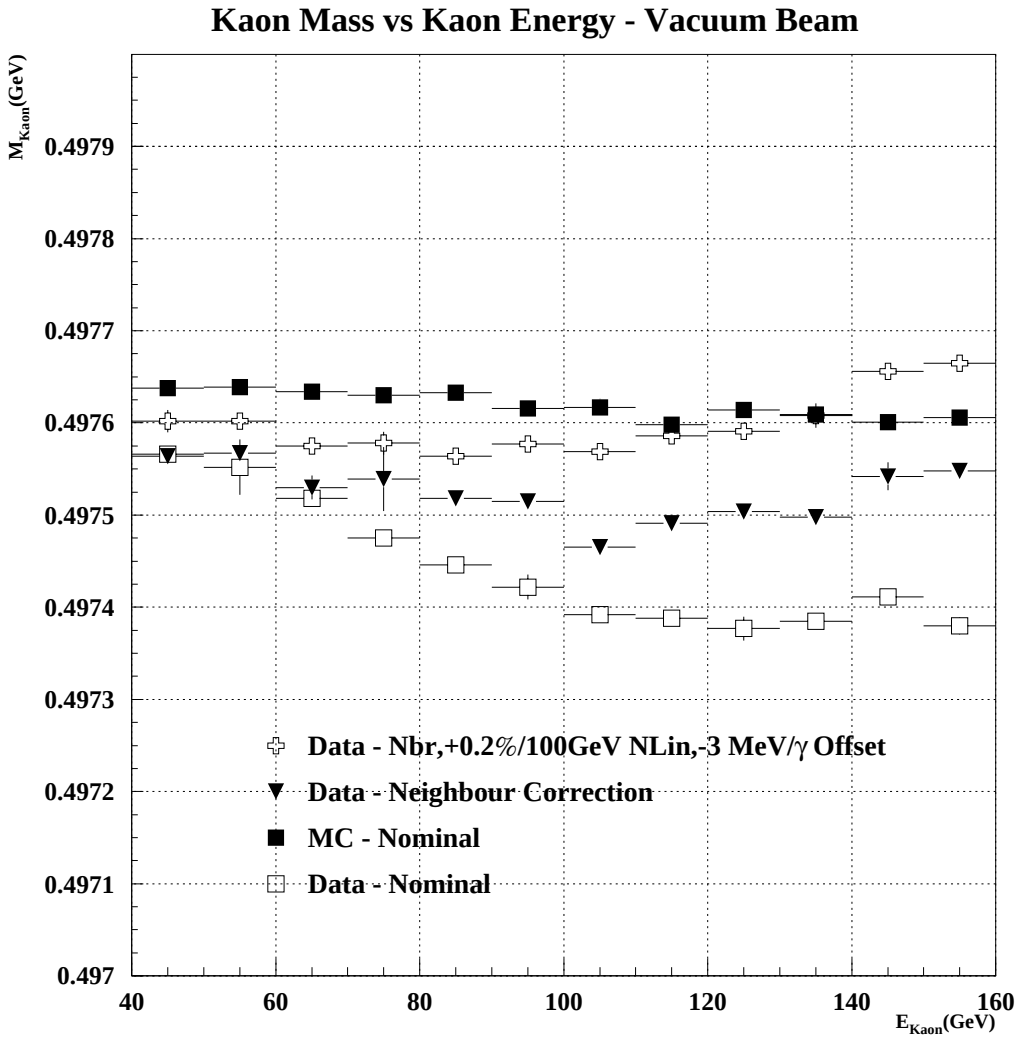

Figure C.6: Variation of kaon mass versus kaon energy for vacuum beam $2\pi^0$ background-subtracted data, Monte Carlo and distortions based on the closeness of clusters in 1997.

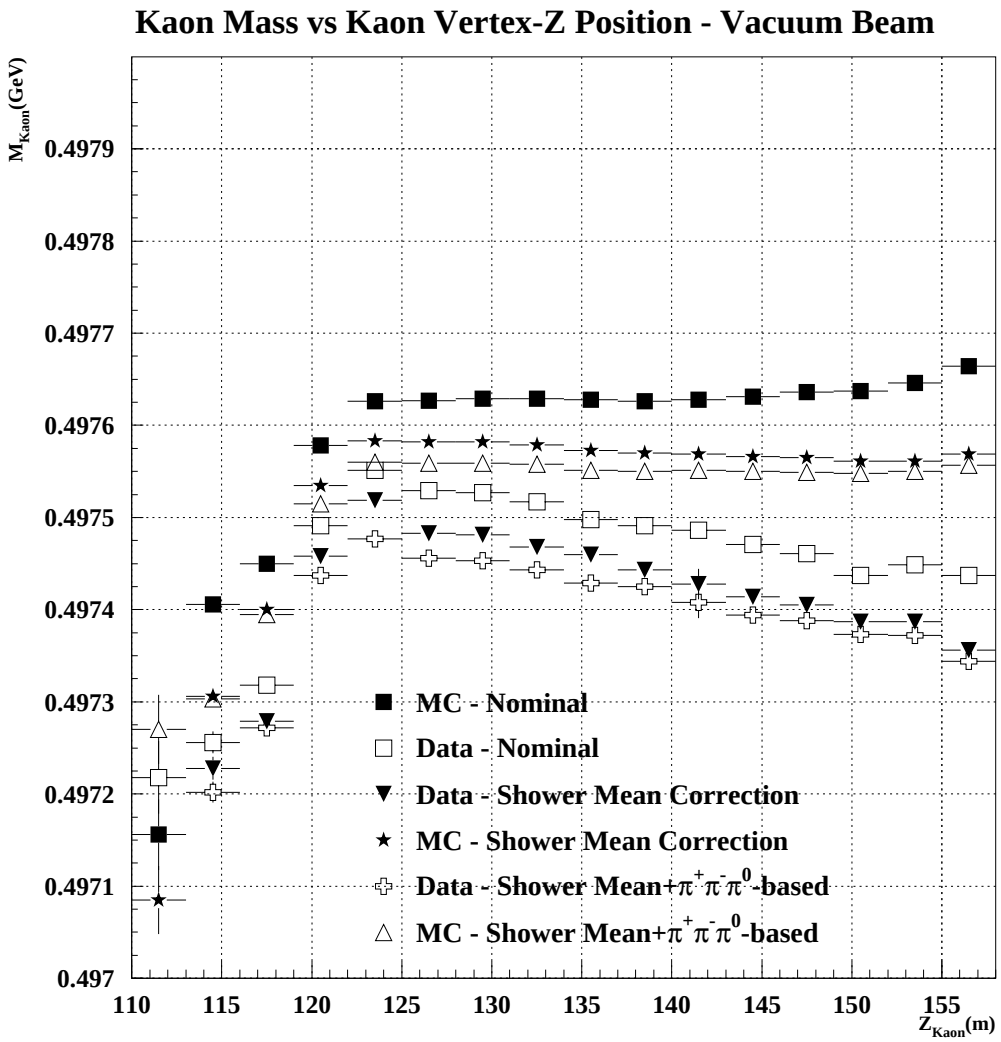

Figure C.7: Variation of kaon mass versus kaon vertex z-position for $2\pi^0$ background-subtracted vacuum beam $K_{L,S} \rightarrow \pi^0\pi^0$ data in 1997, Monte Carlo and distortions based on shower mean and $K_L \rightarrow \pi^+\pi^-\pi^0$ events.

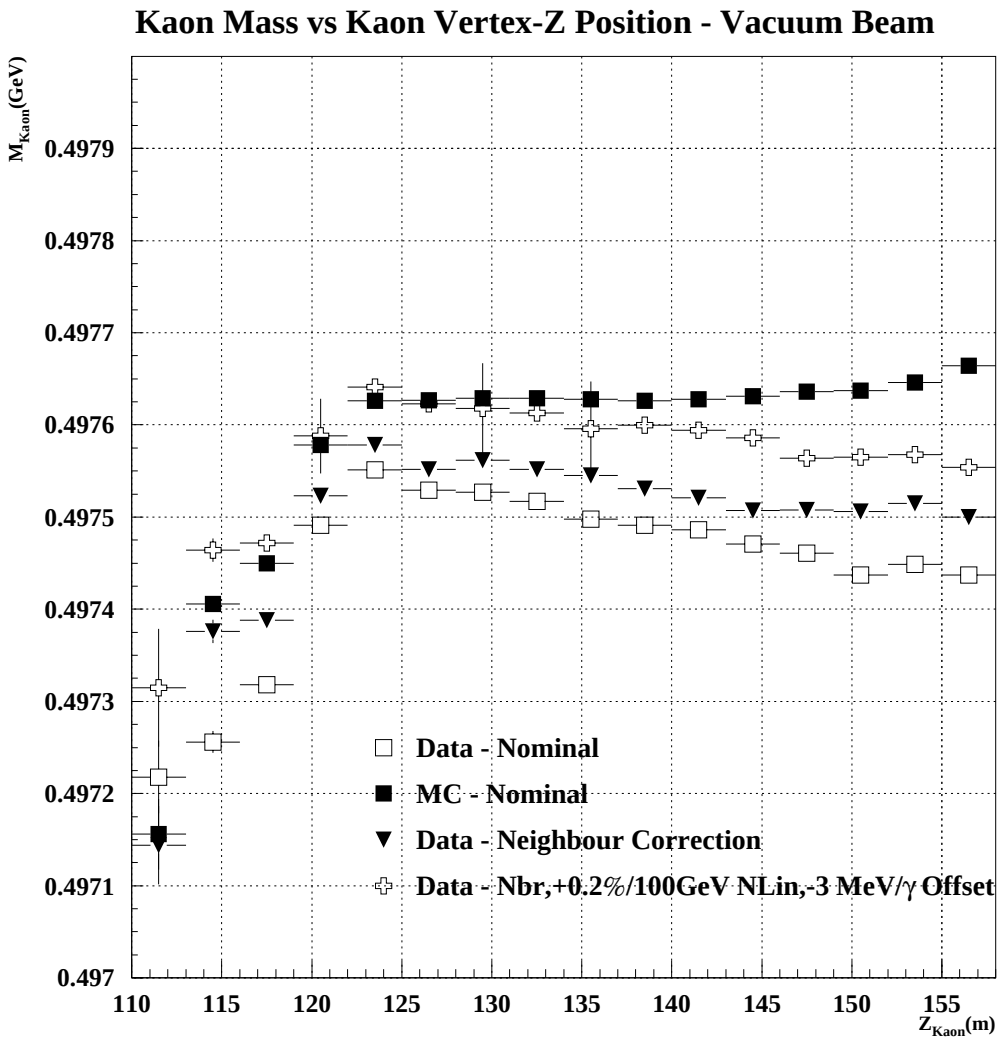

Figure C.8: Variation of kaon mass vs z_K for 1997 background-subtracted vacuum beam $2\pi^0$ data, Monte Carlo and distortions based on overlapping photons.

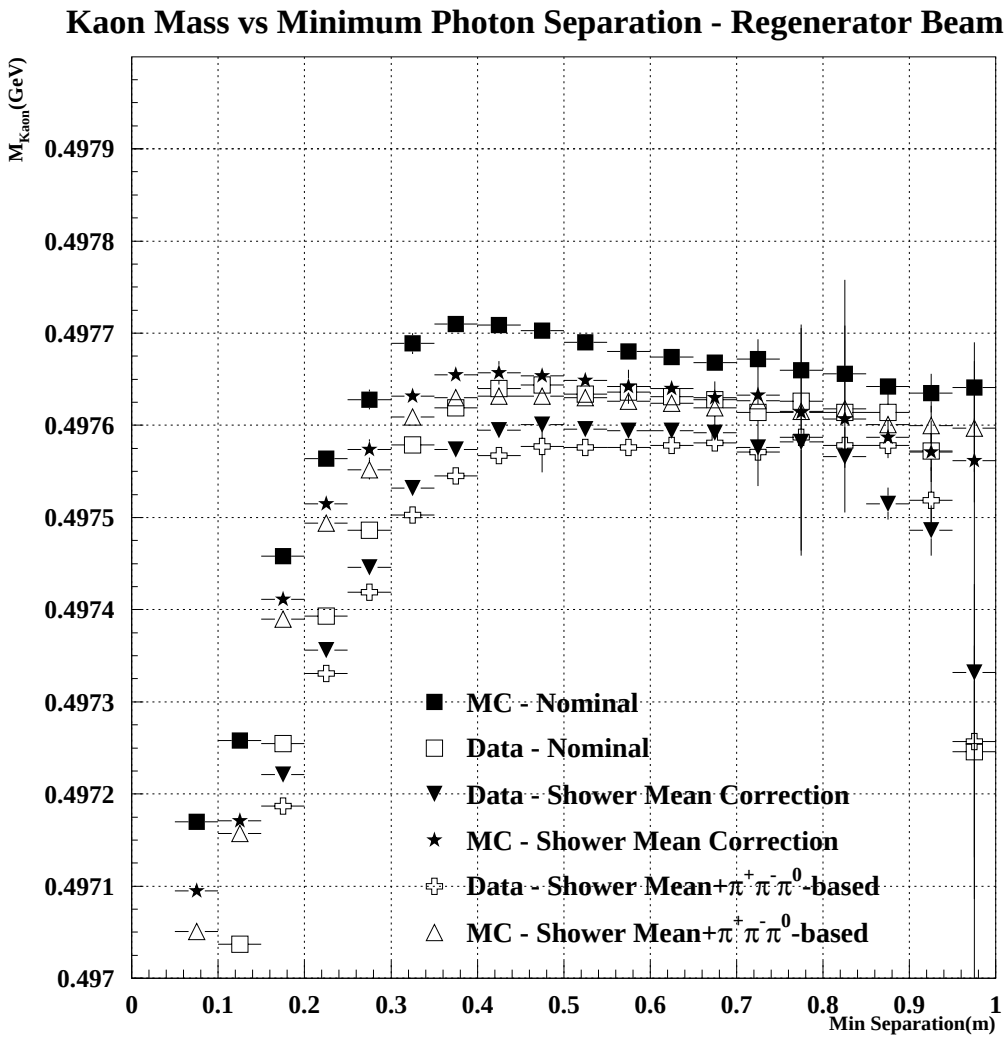

Figure C.9: Kaon mass versus minimum photon separation for 1997 background-subtracted vacuum beam $2\pi^0$ data, Monte Carlo and distortions based on shower mean and $K_L \to \pi^+\pi^-\pi^0$ events.

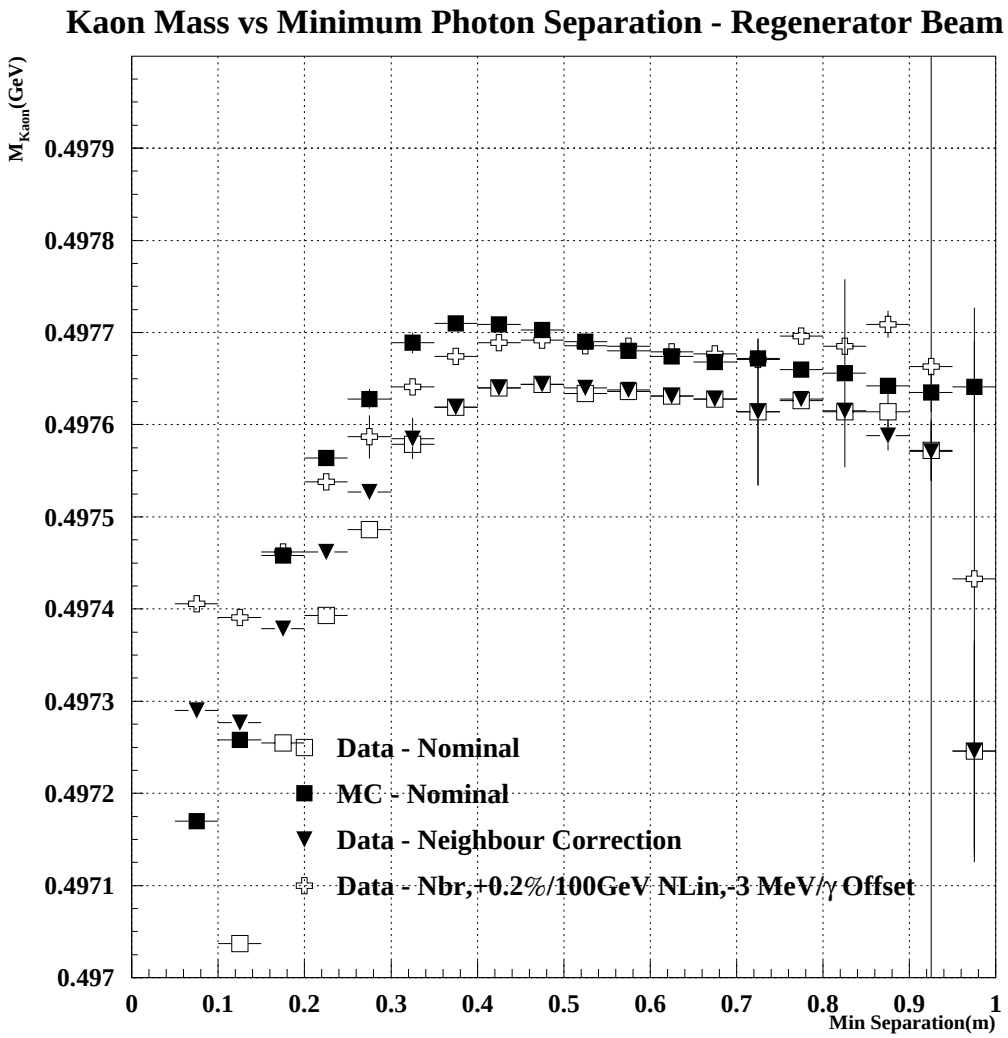

Figure C.10: Kaon mass versus minimum photon separation for 1997 background-subtracted vacuum beam $2\pi^0$ data, Monte Carlo and distortions based on overlapping photons.

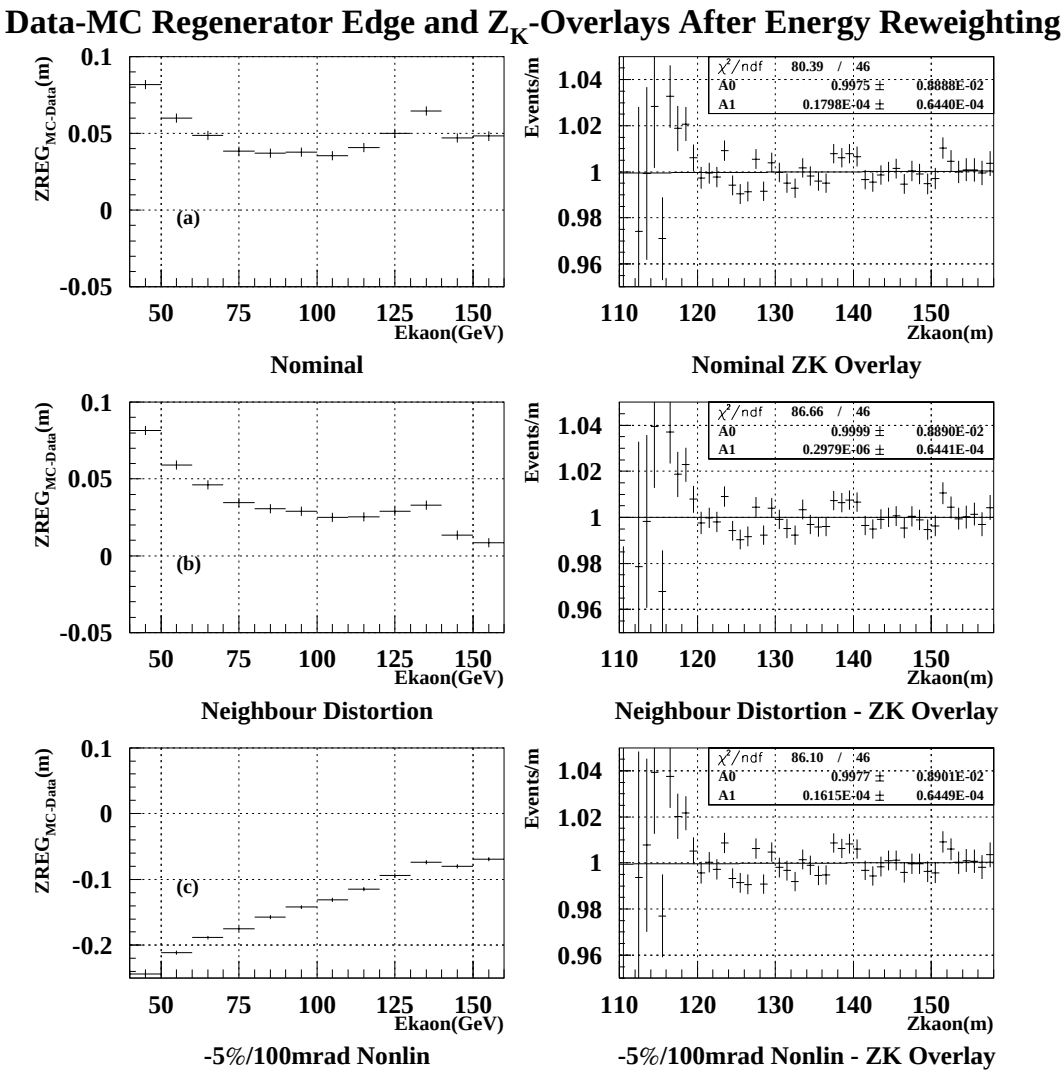

Figure C.11: Left: 1997 $2\pi^0$ Data-Monte Carlo difference in the regenerator edge position before any kaon-energy dependent scale is applied. Right: 1997 Vacuum Beam $2\pi^0$ Kaon vertex Z-overlays after energy reweighting. Presented above are distributions for (a) the nominal analysis, (b) the nearby cluster/neighbour energy distortion applied to data and (c) a photon-angle based energy non-linearity applied to data. Note: The vertical scale is different in (c)

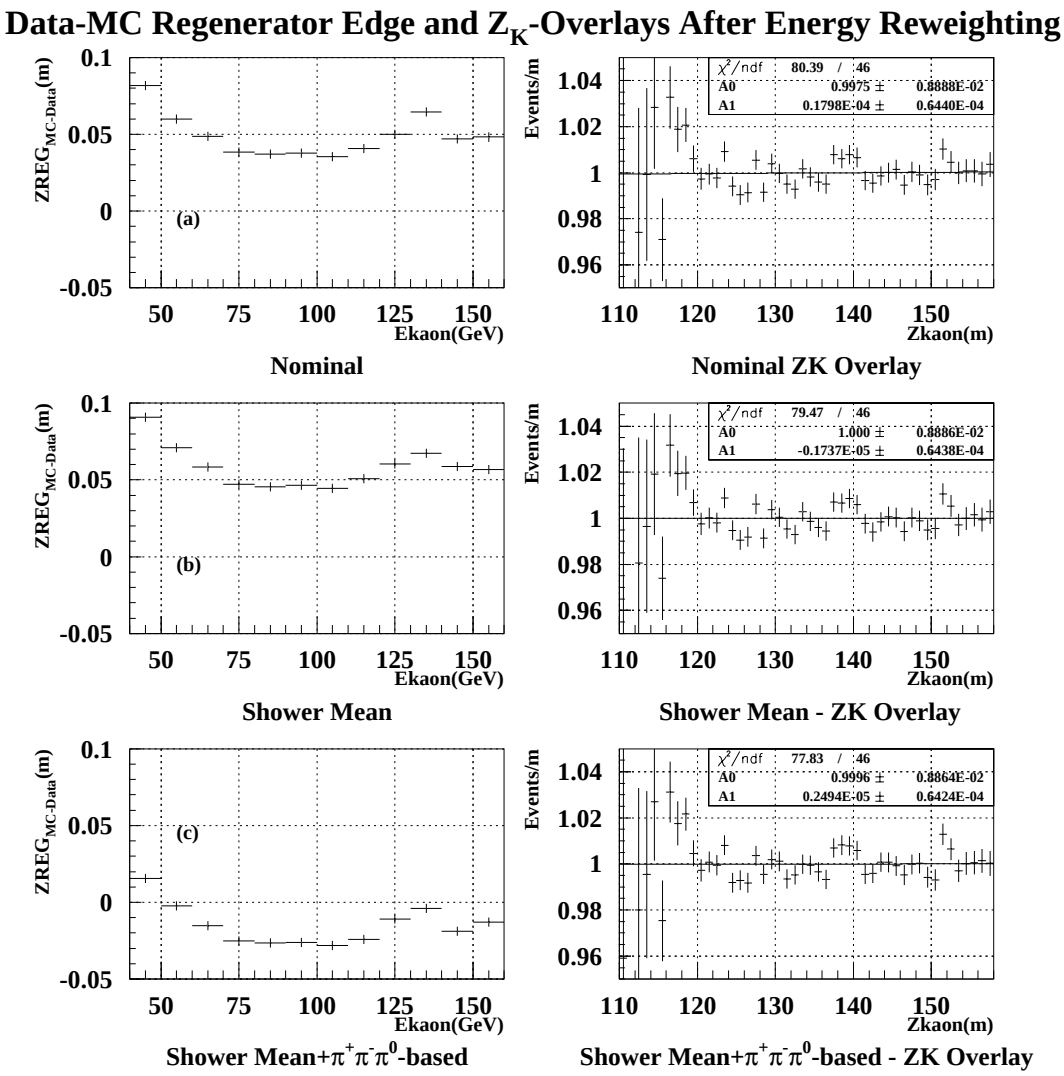

Figure C.12: Left: 1997 $2\pi^0$ Data-Monte Carlo difference in the regenerator edge position before any kaon-energy dependent scale is applied. Right: 1997 Kaon vertex data-Monte Carlo z-overlays after energy reweighting for $2\pi^0$ vacuum beam events. Presented above are distributions for (a) the nominal analysis, (b) the shower mean adjustment in data and Monte Carlo and (c) a shower mean and $K_L \to \pi^+\pi^-\pi^0$-based blockwise scale adjustment.

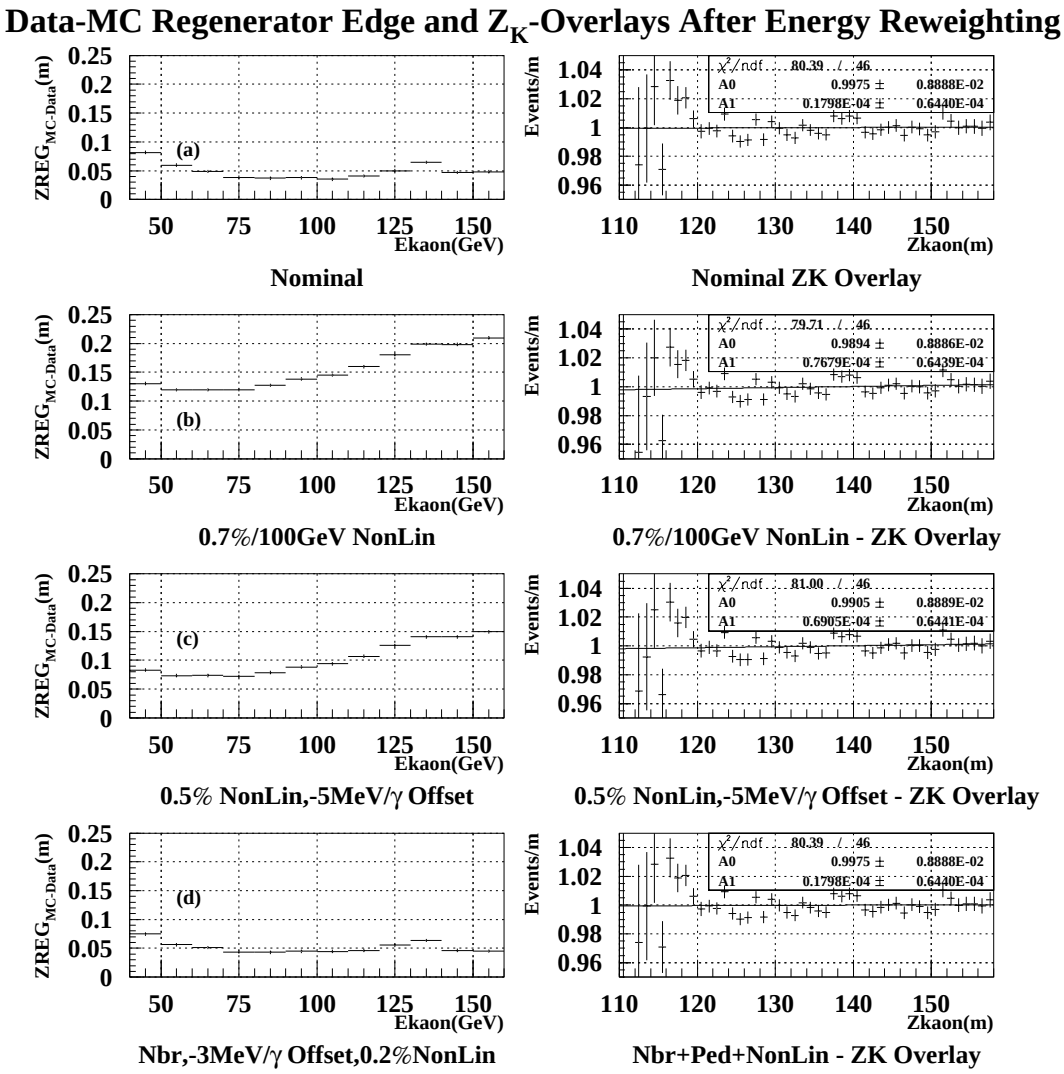

Figure C.13: Left: Data-Monte Carlo difference in the regenerator edge position before any kaon-energy dependent scale is applied. Right: Kaon vertex data-Monte Carlo Z-overlays after energy reweighting for vacuum beam $2\pi^0$ events in 1997. Presented above are distributions for the nominal analysis (a) as well as for several energy nonlinearity distortions and photon energy offsets (b),(c),(d). We observe that the distortions cause large variations of the data-Monte Carlo regenerator edge.

$Re(\epsilon'/\epsilon)$ was found to increase by $1.42 \pm 0.67 \times 10^{-4}$ with respect to the nominal measurement. The slope in the ratio of the data and Monte Carlo z_K distributions also changed by $(-0.83 \pm 0.39) \times 10^{-4}/m$, corresponding to an increase in $Re(\epsilon'/\epsilon)$ of $(1.00 \pm 0.47) \times 10^{-4}$. After subtracting the effect on $Re(\epsilon'/\epsilon)$ of the acceptance (z_K-slope) change, the change in $Re(\epsilon'/\epsilon)$ (with respect to the nominal analysis) due to cluster overlaps near the beam holes was $(0.42 \pm 0.67) \times 10^{-4}$. We also studied the effect of not allowing cluster overlaps near the beam hole on $K_L \to \pi^0\pi^0\pi^0$ events. $K_L \to \pi^0\pi^0\pi^0$ events showed a change in the data-Monte Carlo z_K agreement corresponding to a slope of $(-0.55 \pm 0.22) \times 10^{-4}/m$ when we did not allow more than one cluster near the same beam hole. The z_K-slope change for $K_L \to 3\pi^0$ events was consistent with the $K_{S,L} \to 2\pi^0$ mode.

Decay Mode	$\Delta Re(\epsilon'/\epsilon)$ ($\times 10^{-4}$) wrt Nominal Analysis	$\Delta(z_K$-slope) ($\times 10^{-4}$) wrt Nominal Analysis
$K_{S,L} \to 2\pi^0$:		
Total Change	1.42±0.67	-0.83±0.39
$\Delta Re(\epsilon'/\epsilon)$ due to $\Delta(z_K$-slope)	1.00±0.47	—
$\Delta Re(\epsilon'/\epsilon)$ after accounting for $\Delta(z_K$-slope)	0.42±0.67	—
$K_L \to 3\pi^0$:		
Change in z_K-slope	—	-0.55±0.22

Table C.1: Study of overlapping photons at the CsI beam holes. This table presents the effect of excluding events with two or more photons within 7.5 cm of the same beam hole on $K_{L,S} \to \pi^0\pi^0$ and $K_L \to \pi^0\pi^0\pi^0$ events.

Since there was no significant change in $Re(\epsilon'/\epsilon)$ due to cluster overlaps near the beam hole (after accounting for the acceptance change), and the change in the data-Monte Carlo z_K slope with respect to the nominal analysis was consistent between the $K \to 2\pi^0$ and $K \to 3\pi^0$ modes, we did not assign an additional systematic error on $Re(\epsilon'/\epsilon)$ based on the reconstruction of two or more photons near the same beam hole.

C.3 Systematic Uncertainty due to Energy and Position Mis-reconstruction in $K_{L,S} \to \pi^0\pi^0$ Events

Even though the data-Monte Carlo kaon mass agreement improved for many of the distortions that were investigated, the large changes in the data-Monte Carlo z_K-agreement at the regenerator edge indicated that the data-Monte Carlo reconstruction differences were not due to a single reconstruction feature (e.g., energy non-linearities) but instead were due to a combination of features. Nevertheless, by studying several reconstruction features and measuring their effects on $Re(\epsilon'/\epsilon)$, we bounded the possible uncertainty due to the neutral mode energy and postion reconstruction.

To determine a systematic uncertainty on $Re(\epsilon'/\epsilon)$, we added, in quadrature, the changes in $Re(\epsilon'/\epsilon)$ due to the reconstruction modifications that improved the data-Monte Carlo agreement shown in Figures C.1, C.2, C.3 and C.4. The effect of the acceptance (z_K-slope) change was not subtracted when considering the systematic error due to the neutral mode reconstruction since the change in the z_K-slope was small. The distortions that were selected are highlighted in **boldface** in Table C.2. We assigned a systematic uncertainty on $Re(\epsilon'/\epsilon)$ due to the photon energy and position reconstruction of 0.66 $\times 10^{-4}$ for the 1997 data set. The systematic uncertainty was the same for the 1996 data set because the $K_{L,S} \to \pi^0\pi^0$ data-Monte Carlo distributions showed the same level of agreement as in 1997.

Type of Nonlinearity	$\Delta Re(\epsilon'/\epsilon)(\times 10^{-4})$ (wrt) (Nom. Analysis)	Fit χ^2 (for 21 dof)	z_K-slope ($\times 10^{-4}$/m)
Nominal Analysis	—–	18.13	0.18 ± 0.64
Nonlinearity (0.7%/100 GeV)	**−0.19**	**18.56**	$\mathbf{0.77 \pm 0.64}$
Nonlinearity (0.5%/100 GeV) Offset (−5MeV/Photon)	**−0.01**	**18.31**	$\mathbf{0.69 \pm 0.64}$
Shower Mean Adjustment	0.13	18.86	0.02 ± 0.64
Shower Mean Adjustment $K_L \to \pi^+\pi^-\pi^0$-based calibration	**−0.25**	**18.51**	$\mathbf{0.02 \pm 0.64}$
Nonlinearity (-5%/100 mrad)	+1.61	21.54	0.16 ± 0.64
Energy Overlap from Nearby Clusters	0.58	17.82	0.00 ± 0.64
Energy Overlap from Nearby Clusters, Nonlinearity (0.2%/100 GeV), Offset (−3MeV/Photon)	**0.58**	**18.35**	$\mathbf{0.18 \pm 0.64}$

Table C.2: Results of $Re(\epsilon'/\epsilon)$ fit and the slope in the data-Monte Carlo z_K agreement (slope) using different reconstruction modifications. We did **not** account for the change in the data-Monte Carlo z_K-slope with respect to the nominal analysis when presenting the change in $Re(\epsilon'/\epsilon)$ due to the reconstruction modifications since the change in the data-Monte Carlo z_K-slope was small. Only modifications that are in **boldface** were considered when assigning a systematic uncertainty. The other distortions caused data-Monte Carlo agreement in certain distributions to get much worse. The fit conditions for all the fits shown in this table were slightly different from the fitting conditions used to obtain the final $Re(\epsilon'/\epsilon)$ result (see Table 10.4).

REFERENCES

[1] M. Polak and R. Trivers, *Trends Ecol. Evol.*, **9**,122, 1994.

[2] E. Heilbronner and J.D Dunitz, *Reflections on Symmetry*, Verlag Helvetica Chimica Acta, Basel, 1993.

[3] A.V. Shubnikov and V.A. Koptsik, *Symmetry in Science and Art*, Plenum Press, New York, 1974.

[4] S.J. Abas and A.S. Salman, *Symmetries of Islamic Geometrical Patterns*, World Scientific, Singapore,1994.

[5] D. Schattschneider and W. Walker, *M.C. Escher Kaleidocycles*, Ballantine Books, New York, 1977.

[6] L. Boltzmann,*Berl. Ber.*, 1897.

[7] H.A. Kramers,*Koninkl. Ned. Ak. Wet. Proc.*, **33**, 959 (1930)

[8] E.P. Wigner,*Goett. Nachr.*, 546 (1932).

[9] E.P. Wigner,*Goett. Nachr.*, 375 (1927).

[10] O. Laporte,*Zeit. f. Phys.*,**23**, 135 (1924).

[11] W. Heisenberg, *Zeitschrift f. Phys.*, **90**, 209 (1934).

[12] H.A. Kramers,*Koninkl. Ned. Ak. Wet. Proc.*, **40**, 814 (1937)

[13] J. Schwinger, *Phys. Rev.*, **91**, 713 (1953); *Phys. Rev.*, **94**, 1362 (1954).

[14] G. Lüders, *Kgl. Danske Videnskab Selskab., Matt-fys. Medd.*, **28**, 1(1954).

[15] W. Pauli,*Niels Bohr and the Development of Physics*, Pergamon Press, Elmsford, New York, 1955.

[16] C.S. Wu et al.,*Phys. Rev.*,**105**, 1413 (1957).

[17] J.I. Friedman and V.L. Telegdi, *Phys. Rev.*, **105**, 1681 (1957).

[18] R.L. Garwin, L.M. Lederman and M. Weinrich, *Phys. Rev.*,**105**, 1415 (1957).

[19] T.D. Lee, R. Oehme and C.N. Yang, *Phys. Rev.*,**106**, 340 (1957).

[20] L. Landau,*JETP***32**, 405 (1957).

[21] C.N. Yang,*Rev. Mod. Phys.*, **29**, 231 (1957).

[22] J.H Christenson,J.W. Cronin, V.L. Fitch and R. Turlay,*Phys. Rev.* , **13**, 138 (1964).

[23] V.L. Fitch,R.F. Roth,J.S Russ and W. Vernon, *Phys. Rev.*, **15**, 73-76 (1965).

[24] R.G. Sachs,*The Physics of Time Reversal*, The University of Chicago Press, Chicago, 1987.

[25] L. Wolfenstein, *Phys. Rev.*, **13**, 562 (1964).

[26] M. Kobayashi and T. Maskawa, *Prog. Theor. Phys.*, **49**, 652 (1973).

[27] F. Gilman and M.B. Wise, *Phys. Lett.*, **83B**, 83 (1979).

[28] A.D. Sakharov, *JETP Lett* **5**, 24 (1967).

[29] R.D. Peccei, *CP Violation in Particle Physics and Astrophysics*, 615-632, Editions Frontieres, Gif-Sur-Yvette Cedex, 1990.

[30] Holder et al., *Phys. Lett.*, **40B**, 141 (1972).

[31] G.D. Barr et al.,*Phys. Lett.*, **B317**, 233 (1993).

[32] L.K. Gibbons et al., *Phys. Rev. Lett.*, **70**, 1203 (1993).

[33] A. Lai et al., *Eur.Phys.J.*, **C22**, :231 (2001).

[34] A. Alavi-Harati et al., *Phys. Rev. Lett.*, **83**, 22 (1999).

[35] J. Ellis,*Nucl. Inst. Meas. Phys. Res.*, Sect. A **284**, 33 (1989).

[36] P.G. Harris et al., *Phys. Rev. Lett.*, **82**, 1999.

[37] K. Abe et al., *Phys. Rev. Lett.*, **87**, 2001.

[38] B. Aubert et al., *Phys. Rev. Lett.*, **87**, 2001.

[39] J.A. Graham, Ph.D. Thesis, University of Chicago, December 2001.

[40] M. Gell-Mann and A. Pais,*Phys. Rev.*, **97**, 1387 (1955).

[41] P.K. Kabir,*The CP Puzzle*, Academic Press, New York (1968).

[42] T.T Wu and C.N. Yang, *Phys Rev Lett.*,**13**, 380 (1964).

[43] K.M. Watson,*Phys. Rev.*.**88**, 1163(1952).

[44] F. Niebergall et al.,*Phys. Lett.*,**B49**, 103 (1974).

[45] Particle Data Group,*Review of Particle Physics*, *Eur. Phys. J.*,**C15**, 1 (2000).

[46] E. Chell and M.G. Olson,*Phys. Rev.*, **D48**, 4076 (1993).

[47] B. Schwingenheuer et al., *Phys. Rev. Lett.*, **74**, 4376 (1995).

[48] A. Apostolakis,*Phys. Lett.*, **B458**, 545 (1999).

[49] R.G. Sachs,*Phys. Rev.*,**D33**, 3283 (1986).

[50] K. Kleinknecht, *Fort. Phys.*, **21**, 57 (1973).

[51] R.A.Briere, Ph.D. Thesis, University of Chicago, June 1995.

[52] F. Gilman, *Phys. Rev. Lett.*, **171**, 1453 (1968).

[53] The KLOE Collaboration, *The KLOE Detector, Technical Proposal*, LNF 92/019 (1992).

[54] K. Arisaka et al., *KTeV Design Report*, Technical Report FN-580, Fermilab, 1992.

[55] V. Bocean et al., *Performance of the KTeV High-Energy Neutral Kaon Beam at Fermilab*, Technical Report TM-2046, Fermilab, 1998.

[56] R. Kessler, private communication.

[57] E.D. Zimmerman, Ph.D. Thesis, University of Chicago, March 1999.

[58] C. Bown et al., *Nucl. Instrum. Methods Phys. Res., Sect. A*, A **369**, 248 (1996).

[59] R. Tschirhart, private communication.

[60] T. Zimmerman,M. Sarraj, *A Second Generation Integrator and Encoder ASIC*, IEEE Trans. on Nucl. Sci., **43**. 3 (1996), 1683-1688.

[61] Z. Wei,R. Zhu, *Nucl. Instrum. Methods Phys. Res., Sect. A*, A **326**, 508 (1993).

[62] P.S.Shawhan, Ph.D. Thesis, University of Chicago, December 1999.

[63] A.J. Malensek, Fermilab Reports FN-341,FN-341A(errata),1981.

[64] L.K. Gibbons, Ph.D. Thesis, University of Chicago, August 1993.

[65] F. Carminati et al., computer code GEANT 3.15/09, CERN, Geneva, April 1992.

[66] W.R. Nelson et al., *The EGS4 Code System*, SLAC-265, Stanford Linear Accelerator Center, December 1985.

[67] R.A. Briere and B. Winstein, *Phys. Rev. Lett.*, **75**, 402 (1995).

[68] G.C. Bown, private communication.

[69] F. James and M. Roos, computer code MINUIT, CERN, Geneva, 1994.

[70] E. Pallante and A. Pich, *Nucl.Phys.* **B617**(2001) 441.

[71] T. Blum et al.,*BNL-HET-01/30*, BNL, 2001.

[72] S. Bosch et al., *Nucl.Phys.* **B565**(2000) 3.

[73] M. Ciuchini,G. Martinelli, *Nucl. Phys. Proc. Suppl.*,**99**(2001) 27.

[74] S. Bertolini et al., *Phys. Rev. D*,**63**(2001) 056009

[75] A.A. Belkov, JINR-E2-99-236, July 1999.

[76] H.Y. Cheng,*Chin.J.Phys.***38**(2000) 1044.